# ENVIRONMENTAL SOURCES AND TREATMENT STRATEGIES OF ORGANIC MICROPOLLUTANTS

# ENVIRONMENTAL SOURCES AND TREATMENT STRATEGIES OF ORGANIC MICROPOLLUTANTS

By YICHEN WU, B.Eng., M.S.

A Thesis Submitted to the School of Graduate Studies in Partial Fulfilment of the Requirements for the Degree Doctor of Philosophy

DOCTOR OF PHILOSOPHY (2022)

Chemical Engineering, McMaster University

1280 Main St W, Hamilton, Ontario L8S 4L7

TITLE: Environmental sources and treatment strategies of organic micropollutants: a case study evaluating boreal peatland soil organic composition and peat-derived pollutant leaching, and micropollutants removal using wildfire-damaged boreal peats-based sorbents and rGO nano-enabled composite membranes

AUTHOR: Yichen Wu

B.Eng. (Nanjing Tech University, China)

M.S. (Purdue University, United States)

SUPERVISOR: Dr. Charles-François de Lannoy

NUMBER OF PAGES: xxiv, 267

**Lay abstract**

Climate change, industrial manufacture, and population growth have been exacerbating the global water stress. Organic micropollutants (OMPs) are potentially toxic, persistent and can exist even at trace levels, which have been increasingly discovered and identified in natural and built systems. In this research, environmental chemistry of climate-change impacted boreal peatland soils, and their mechanistic relationships to peat soil hydrophobicity, organic substance transformations, micropollutant leaching, and impacts to downstream potable water quality was investigated as a case study. Two different innovative water treatment strategies were developed for restoring peatland resilience and enhancing water resource sustainability including treating peatland phenolic micropollutants. The first approach converted shallow layer wildfire- and drought-damaged peats into value-added porous carbons for adsorption. The second approach synthesized a novel reduced graphene oxide (rGO) nanocomposite membrane for process-intensified flow-through separation. These solutions provide novel insights for source water protection and wastewater treatment in adaption to climate change.

**Abstract**

Organic micropollutants (OMPs) in climate change affected natural environment such as wetlands, and engineered systems have brought serious concerns for water security and public health. These issues have increased the demand for better managing water resources and developing effective technologies for aqueous micropollutants removal. This thesis investigated these subjects through the following five sub-research projects.

First, boreal peatland was used as a case study for understanding how peatland fires and droughts impacts peatland resilience. Laboratory results suggested that heating and moisture condition, coupled with peat organic hydrophobic transformations, influence peat soil hydrophobicity and the resultant water-extractable pollutant leaching, which potentially threatens peatland downstream receiving waters such as potable waters by high organic loads.

Further, post-fire peat chemistry and their mechanistic relationships to leached pollutants (total organic carbon (TOC), nutrients and phenols) were elucidated through a laboratory leaching study. Increased contaminant loading was observed in post-heated peat leachates, suggesting negative effects to water treatment efficiency and an increase of treatment costs to surface waters as potable water source.

Next, peat soils damaged from extreme fires and droughts were upcycled for producing high surface area, value-added porous carbons based on a rapid, facile chemical activation approach. This application had the simultaneous benefit of peatland ecological restoration,

protecting downstream communities from heavy run-off, and using the sustainable damaged peats for effective environmental remediation though adsorption.

Moreover, a critical review of nano-enabled composite membranes for OMP removal (size-exclusion, adsorption, charge interaction, and photo- and electro-catalysis) and their respective benefits and limitations were discussed. This work brought new perspectives for next-generation nanocomposite membranes for OMP removal.

Finally, a novel, hyperbranched polyethylenimine (HPEI) crosslinked iron doped reduced graphene oxide (rGO) nanocomposite membrane was synthesized for process-intensified flow-through separation of phenolic micropollutants. Mechanisms and separation performance to phenolic micropollutant and azo dyes were investigated.

**Acknowledgements**

I would like to thank my supervisor Dr. Charles-François de Lannoy for the continuous support and guidance throughout my Ph.D. period. My research work would not have been conducted so smoothly without his funding support, valuable insights on research contents and manuscript editing, as well as encouragement and advice. His scientific curiosity, passion for discovery, critical thinking has enlightened me to perform innovative research over the past four years. I am grateful for his instrumental mentoring beyond academia to help me develop comprehensive skills for personal growth and progress.

I would also like to extend my thanks to my supervisory committee members, Dr. Robert Pelton, Dr. Todd Hoare and Dr. James Michael Waddington, for their useful suggestions and constructive criticisms on my research design which enabled me to think beyond my field to deepen my conceptual understanding and improve my research quality. Many thanks to my out-of-lab research collaborators, Dr. Ming Chen, Dr. Colin P.R. McCarter, and Dr. Xuebin Xu, who greatly contributed their knowledge to my research work.

I appreciate the staffs/technicians at Biointerfaces Institutes (BI), Canadian Center for Electron Microscopy (CCEM), and McMaster Analytical X-Ray Diffraction Facility (MAX) for their assistance on sample analyses. I acknowledge staffs and students from Prof. Robert Pelton Lab, Prof. Todd Hoare Lab, Prof. David Latulippe Lab, Prof. Greg Slater Lab, Prof. Zeinab Hosseinidoust Lab and Prof. Ayse Turak Lab for equipment training and usage. I want to thank the Graduate Assistant Michelle Whalen for her

hardworking administrative work, and Michael Clarke, Paul Gatt, Doug Keller and Tim Stephens for their technical support on my research.

Special thanks to my amazing lab members, Nan Zhang, Mohamed Elganzoury, Hye-Jin Lee, Mohamad Amin Halali, Scott Laengert, Alexander Sutherland, Daniel Osorio, Melissa Larocque, Cassandra Chidiac, Maria Ximena Ruiz-Caldas, Colin Gibson, Hannah Grewal, Erik Fréchette and Gavin Yuen, who have offered numerous supports and brought wonderful experience to me in the journey at McMaster University, which I will always remember.

It was my great pleasure to have acquainted with so many excellent colleagues and friends in Canada who gave me endless great memories and made my life enjoyable, including Lei Tian, Nan Zhang, Dongyang Li, Jinlei Li, Hongfeng Zhang, Fengyan Wang, Yuanhua Li, Lu Zhu, Gaoyin He, Xiao Wu, Dong Yang, Naveen Kumar Vasudevan, Mohamed Elganzoury, Hye-Jin Lee, Qiukui Hao family, Yan (Alice) Chen family, and those that were not mentioned. I also want to express my appreciation to my dear friends out of Canada especially Yanyao Bao, Hanghua Wang, Jie Li, Xuebin Xu and Jiale Zhu, who have accompanied me through boring and difficult moments.

Finally, I would like to dedicate my dissertation to my dear parents, grandparents and wife, who gave me the biggest love, patience and encouragement throughout my Ph.D. period.

## Table of Contents

## List of Figures and Tables

### Chapter 2



### Chapter 3

## Chapter 4



## Chapter 5



## Chapter 6

## Chapter 2 Supplementary Information



## Chapter 3 Supplementary Information



## Chapter 4 Supplementary Information

## Chapter 4 Supporting Method Article



## Chapter 6 Supplementary Information



## Chapter 2



## Chapter 4



## Chapter 5



## Chapter 2 Supplementary Information

## Chapter 3 Supplementary Information



## Chapter 4 Supplementary Information

## List of Abbreviations and Symbols

| | |
|---|---|
| **AC** | activated carbon |
| **ALD** | atomic layer deposition |
| **AOP** | advanced oxidation process |
| **APT** | attapulgite nanorod |
| **BAC** | biological activated carbon |
| **BET** | Brunauer -Emmett-Teller |
| **BPA** | bisphenol A |
| **BWF** | boreal water futures |
| **CA** | cellulose acetate |
| **CAC** | commerical activated carbon |
| **CAS** | conventional activated sludge |
| **CCEM** | Canadian Centre for Electron Microscopy |
| **CCL** | contaminant candidate list |
| **CMC** | critical micelle concentration |
| **CNC** | cellulose nanocrystial |
| **CNF** | carbon nanofiber |
| **CNT** | carbon nanotube |
| **COD** | chemical oxygen demand |
| **COF** | covalent organic framework |
| **CPB** | cetylpyridinium bromide |
| **CR** | Congo red |
| **CTAB** | cetyltremethyl ammonium bromide |

| | |
|---|---|
| **DA** | dopamine+J80:K88` |
| **DBP** | disinfection byproduct |
| **DCMD** | direct contact membrane distillation |
| **DFT** | density function theory |
| **DMAc** | dimethylacetamide |
| **DMF** | dimethylformamide |
| **DMSO** | dimethylsulfoxide |
| **DOC** | dissolved organic carbon |
| **DOM** | dissolved organic matter |
| **DS** | draw solution |
| **ECM** | electrically conductive membrane |
| **EDC** | endocrine disrupting chemical |
| **EDC** | N-(3-Dimethylaminopropyl)-N′-ethylcarbodiimide |
| **EDS** | Energy dispersive X-ray spectroscopy |
| **EU** | European Union |
| **FO** | forward osmosis |
| **FTIR** | Fourier transform – infrared spectroscopy |
| **GAC** | granular activated carbon |
| **GC-MS** | Gas chromatography – mass spectrometry |
| **GO** | graphene oxide |
| **GWC** | gravimetric water content |
| **GWF** | global water futures |
| **HNT** | halloysite nanotube |

| | |
|---|---|
| **HPEI** | hyperbranched polyethylenimine |
| **IC** | inorganic carbon |
| **IPA** | isopropanol |
| **$k_{ow}$** | octanol-water partition coefficient |
| **LBL** | layer-by-layer assembly |
| **LC-MS** | Liquid chromatography – mass spectrometry |
| **MAC** | maximum allowable concentration |
| **MB** | methylene blue |
| **MBR** | membrane bioreactor |
| **MEUF** | micellar-enhanced ultrafiltration |
| **MF** | microfiltration |
| **MI** | membrane distillation |
| **MO** | methyl orange |
| **MOF** | metal organic framework |
| **MPD** | m-phenylene diamine |
| **MWCO** | molecular weight cut-off |
| **NF** | nanofiltration |
| **NHS** | N-Hydroxysuccinimide |
| **NIPS** | non-solvent induced phase inversion |
| **NMP** | N-methyl-2-pyrrolidone |
| **NP** | nanoparticle |
| **NPE** | nonylphenol ethoxylate |
| **NRP** | non-reactive phosphorus |

| | |
|---|---|
| **nZVI** | nano zerovalent iron |
| **OMP** | organic micropollutant |
| **PA** | polyamide |
| **PAA** | poly acrylic acid |
| **PAC** | powdered activated carbon |
| **PAH** | polyaromatic hydrocarbon |
| **PAN** | polyacrylonitrile |
| **PC** | principal component |
| **PC** | polycarbonate |
| **PCA** | principal component analysis |
| **PCB** | polychlorinated biphenyl |
| **PDA** | polydopamine |
| **PES** | polyethersulfone |
| **PFC** | perfluorinated chemical |
| **PhAC** | pharmaceutical |
| **PHC** | polyhalogenated compound |
| **PIP** | piperazine |
| **PLS** | partial least squares |
| **PNP** | *p*-nitrophenol |
| **PPCP** | pharmaceutical and personal care product |
| **PSF** | polysulfone |
| **PVDF** | polyvinylidene difluoride |
| **PZC** | point of zero charge |

| | |
|---|---|
| **rGO** | reduced graphene oxide |
| **RMSE** | root-mean-square-error |
| **RO** | reverse osmosis |
| **RP** | reactive phosphorus |
| **RPIQ** | ratio of performance to inter-quartile |
| **SDS** | sodium dodecyl sulfate |
| **SEM** | Scanning electron microscopy |
| **SRT** | solid retention time |
| **TA** | tannic acid |
| **TC** | total carbon |
| **TDS** | total dissolved solid |
| **TEM** | Transmission electron microscopy |
| **TFC** | thin film composite |
| **TFN** | thin film nanocomposite |
| **TIPS** | thermally induced phase inversion |
| **TKN** | total Kjeidahl nitrogen |
| **TMC** | trimethyl chloride |
| **TMD** | transition metal dichalcogenide |
| **TMP** | transmembrane pressure |
| **TMS** | trimethylsilyl |
| **TN** | total nitrogen |
| **TOC** | total organic carbon |
| **TON** | total organic nitrogen |

| | |
|---|---|
| **TOrC** | trace organic compound |
| **TP** | total phosphorus |
| **UF** | ultrafiltration |
| **US EPA** | United States Environmental Protection Agency |
| **USGS** | United States Geological Survey |
| **VWC** | volumettric water content |
| **XPS** | X-ray photoelectron spectroscopy |
| **XRD** | X-ray powder diffraction |
| **WDPT** | water drop penetration test |
| **WWTP** | wastewater treatment plant |

**Declaration of Academic Achievement**

This Ph.D. dissertation is organized in a "sandwich style" based on published, submitted and prepared for submission articles described as follows.

**Chapter 2**: Y. Wu, N. Zhang, G. Slater, J.M. Waddington, C.-F. de Lannoy, Hydrophobicity of peat soils: Characterization of organic compound changes associated with heat-induced water repellency, Science of The Total Environment 714 (2020) 136444. https://doi.org/10.1016/j.scitotenv.2019.136444.

**Chapter 3**: Y. Wu, X. Xu, C.P. McCarter, N. Zhang, M.A. Ganzoury, J.M. Waddington, C.-F. de Lannoy, Assessing leached TOC, nutrients and phenols from peatland soils after lab-simulated wildfires: Implications to source water protection, Science of the Total Environment 822 (2022) 153579. https://doi.org/10.1016/j.scitotenv.2022.153579.

**Chapter 4**: Y. Wu, N. Zhang, C.-F. de Lannoy, Upcycling wildfire-impacted boreal peats into porous carbons that efficiently remove phenolic micropollutants, Journal of Environmental Chemical Engineering 9(4) (2021) 105305. https://doi.org/10.1016/j.jece.2021.105305.

**Chapter 4 Method Article (Appendix A.)**: Y. Wu, N. Zhang, C.-F. de Lannoy, Fast synthesis of high surface area bio-based porous carbons for organic pollutant removal, MethodsX 8 (2021) 101464. https://doi.org/10.1016/j.mex.2021.101464.

**Chapter 5**: Y. Wu, M. Chen, H.-J. Lee, M.A. Ganzoury, N. Zhang, C.-F. de Lannoy, Nanocomposite polymeric membranes for organic micropollutants (OMPs) removal: A critical review. Submitted Feb 10th 2022 to ACS ES&T Engineering.

**Chapter 6**: Y. Wu, N. Zhang, S. Laengert, G. Yuen, C.-F. de Lannoy, Bioinspired hyperbranched polyethylenimine (HPEI) cross-linked iron doped reduced graphene oxide (rGO) membrane for ultrafiltration of phenols and azo dyes from water. Pending submission to Chemical Engineering Journal.

Yichen Wu developed the methodology, conducted the investigation and formal analyses, and wrote the original manuscripts under direct supervision of Dr. Charles-François de Lannoy, who was also responsible for funding acquisition, project planning and paper reviewing. Nan Zhang, Gavin Yuen, Mohamed A. Ganzoury and Scott Laengert helped with some experiments and data analyses. Dr. Ming Chen, Dr. Xuebin Xu, Dr. Hye-Jin Lee Dr. Colin P.R. McCarter and Dr. James Michael Waddington contributed their expertise and participated in some editing for some paper chapters. All the coauthors have critically reviewed the manuscripts and provided valuable insights for possible improvements.

# Chapter 1

# Introduction

## 1.1 Background

### 1.1.1 Organic micropollutant (OMP) pollution

Increasing water stress by chemical pollution in aquatic environment is a serious concern, especially considering the rapid population growth competing for limited clean potable water resource, climate change decreasing soil moisture and compromising water quality, and growing human activities such as irrigated agriculture, food and energy industries consuming large quantities of fresh water. The development of analytical chemistry has allowed the detection and identification, and treatment of a large number of organic substances to mitigate the acute vulnerability of water shortages and contamination. However, there are still many emerging, trace contaminants, known as organic micropollutants (OMPs), that are not readily removed or degraded, and thus have been ubiquitously found in both treated wastewaters and natural waters. OMPs have complex natural (*e.g.*, forest fires) and anthropogenic origins, which have garnered substantial attention all across the globe over the recent decade due to their continuous production and discharge, potential (chronic) toxicity, bioaccumulation and persistency, even at trace levels (ng/L to μg/L) [1].

For instance, phenolic micropollutants, mainly derived from consumer product use, application of pharmaceutical drugs and pesticides, other industrial practices, and some natural processes, have been pervasively found in surface waters and treated wastewater effluents [2]. Phenols such as chlorophenols and nitrophenols can cause serious toxicity and bioaccumulation effects in living organisms [2]. Phenolic estrogens such as nonylphenol and bisphenol A, are known to cause endocrine disrupting effects [3], which

interfere with synthesis, transport, and action of natural hormones in human body. Depending on the concentration and exposure frequency, OMPs can even induce cancers and bring lethal effects to living organisms upon contact [4].

The occurrence, fate and transport, and physicochemical properties, and treatment methods of OMPs have been advancing, despite their still partly unknown ecological and environmental impacts. Nevertheless, many of these compounds have been regulated by updated environmental laws and are now properly treated by various water treatment processes.

### 1.1.2 Peatland importance, OMP pollution, and environmental implications

Peatlands are important wetlands that cover 3% of global terrestrial areas including large areas of Boreal and Arctic landscapes, which store approximately twice as much carbon as global forest biomass, and play pivotal roles for mitigating climate warming as they accumulate dead peats and other plant materials [5]. In Canada alone, peatlands occupy vast boreal plains including Alberta, Saskatchewan and Manitoba, representing 21% of its land surface [6]. Natural peatlands provide important global and regional ecological services such as carbon sequestration [7], water resource retention [8] and wildlife preservation. However, excessive peatland cultivation, draining, burning and mining activities along with climate change induced wildfires greatly add to the risk of peatland degradation, flooding and soil erosion, and greenhouse gas emissions.

Peat soils are comprised of thick organic layers in the form of partially decomposed plant remains [8, 9], and are typically classified as organic soils. Given that, peats often export

large amounts of organic carbon, nutrients and dissolved heavy metals into surface waters [10]. Peat-derived pollutants including OMPs are correlated with peat soil chemistry and their resultant hydrophobicity, which are closely impacted by climate change driven wildfires, particularly flameless smouldering fires [11]. Wildfires can impact the pollutants within peats. It is hypothesized that heat intensity, time of exposure, and depth of penetration impacts how peat-derived compounds fractionate. Less polar substances transport deeper than the polar ones under heat diffusion, and broadens the surface hydrophobic layer [12, 13]. The labile fractions can be volatilized and condensed onto deeper cooler peat soils. Besides, impacted by fire temperature, oxygen availability and peat soil moisture content, wildfires can also cause combustion, chemical transformations and degradation of peat-derived compounds, including typically from 50-100 ℃ for dehydration, above 150℃ for pyrolysis, and above 210 ℃ for oxidation reactions [14]. Occasionally, smouldering fires can reach as high as 600 ℃ [11], which may produce highly aromatic substances.

The physical and chemical changes of peat soils likely affect the types and quantities of peat-derived pollutants such as OMPs, and their subsequent release into peatland watersheds. These OMPs can be transported to surface waters, groundwaters and peatland drinking water sources during flooding and precipitation events through overland flow and peat soil media, which might cause deterioration of water and soil quality. Unfortunately, compared with the intensely studied peatland hydrological and hydrogeochemical processes, environmental implications (*e.g.*, peat as sources for aqueous pollutants) of climate change impacted boreal peatlands is substantially under investigated. As such there

is a need to more comprehensively understand of the chemical compositions of wildfire-impacted peats at the molecular scale. While peats are harvested for organic matter containing products, such as biofuels, or horticultural ingredients, wildfire-impacted boreal peats are still underappreciated for their economic potential in new fields, such as environmental remediation and energy sustainability [15]. Wildfires disturb over 25000 $km^2$ boreal regions in Canada [16], in which peatlands are the dominant lands that most affected. The fire-damaged surface peats cover large surface areas, which might incur post-fire flooding, enhanced surface drying, soil erosion risks and slowed vegetation regrowth [17]. Therefore, there is a need to study how to sustainably harvest fire-damaged boreal peats to achieve both economic and environmental benefits through advanced applications. These aspects are worth deep investigation in the future.

### 1.1.3 Conventional OMP removal technologies

OMP occurrence in many natural (*e.g.*, boreal peatland) and built systems is a great concern, which demands proper treatment. However, conventional water treatment unit operations have not historically been specifically designed for these pollutants and as such exhibit inadequate removals of OMPs. Coagulation-flocculation [18], biological treatment [19, 20], advanced oxidation [21, 22], adsorption [22, 23], and ultrafiltration (UF), nanofiltration (NF) and low pressure reverse osmosis (RO) membrane filtration [24, 25], can at best partially remove OMPs. Coagulation-flocculation employing inorganic salts or polymer agents can only eliminate some dissolved organic matter and their OMP removal (15-75%) is limited and inconsistent [26]. Biological techniques such as conventional activated sludge (CAS) processes and membrane bioreactors (MBR) are effective in removing

nutrients, some simple organic molecules, and pathogens, but these biological processes are less effective towards recalcitrant OMPs [19], such as polychlorinated biphenyls (PCBs). MBR can achieve higher removal (20-60%) to OMPs than CAS due to MBR's higher sludge retention time, higher biodiversity and greater microorganism adaptation [19, 26], but is still inadequate for the growing concentrations for OMPs. Advanced oxidation processes (AOPs) such as the Fenton reaction, UV/$H_2O_2$ oxidation, and ozonation, can degrade OMPs quickly and efficiently. However, these processes are not selective towards OMPs. In addition, the formation of the strong oxidant - hydroxyl radicals ($^{\cdot}OH$) - demands high energy and chemical input. Furthermore, AOP processes can form oxidation byproducts in water and can potentially transform OMPs into other toxic species [27], which is the subject of ongoing research. Adsorption has been widely used for aqueous OMP removal due to its ease of operation and high efficiency (up to 99%) [28], but activated carbon (AC) adsorption of OMPs faces early breakthrough, slow kinetics, and interference from other matrix substances, and AC production and regeneration can be costly [23]. These design and operational deficiencies of conventional water treatment are becoming increasingly incompatible with the growing amounts and types of OMPs (either naturally occurring or artificially synthesized) in water, demanding research advancements for new water treatment technologies.

Among these technologies, adsorption and membrane separation have been considered as relatively feasible and effective physical processes for OMP removal. Adsorption has long been used for deep treatment of municipal/industrial wastewater, and drinking water. While commercial activated carbons (CACs) have been extensively used to treat various

contaminants, the material costs remain high and CACs cannot always achieve high removal to different OMPs. As such, researchers have been attempting to develop novel sorbents as alternative solutions. On the other hand, applications of NF and RO membranes have also been rapidly growing amongst drinking water and tertiary water treatment facilities [4], which often serve as the ultimate barriers for the removal of OMPs. Because these membrane processes primarily rely on size exclusion to remove OMPs, they show strengths to remove non-biodegradable molecules. Overall, these two approaches are among the most promising OMP removal processes, but developing new materials for making novel sorbents and membranes are desired to increase the removal efficiency, and/or lower the associated costs to solve the urgent challenges of OMP pollution in aquatic environment.

### 1.2 Research objectives

The objective for this research was to facilitate OMP source identification and management in climate change impacted natural systems, and develop next-generation water treatment technologies for water sustainability in response to OMP contamination in the aqueous phase such as surface water, wastewater, and potable water. Here, this research was divided into two phases. Funded by a Global Water Futures grant, in Phase 1, a grand natural system *i.e.*, climate change impacted boreal peatland, was used as a case study, which involved the quantification of organic soil (*i.e.*, peats) chemical transformations mediated by wildfires, assessment of leachable OMPs and/or other typical pollutants and their immediate impacts to regional water systems and downstream drinking water treatment facilities. In phase 2, two novel water treatment approaches, which had the

potential to remove a variety of OMPs in different water environments, based on novel functional materials and nano-enabled composite membranes, were developed and optimized to address water pollution (*e.g.*, peatland phenolic micropollutants and/or other anthropogenic OMPs such as azo dyes in water) for enhancing water security. These strategies aimed to bring novel insights to city planners, policy makers and forestry services for wetland/stream restorations in many highly-valued, fire-recurring wildland-human interfaces in the boreal regions, and to provide alternative solutions for potable water/wastewater treatment operators to remove OMPs from other water types.

### 1.3 Research contents

Detailed phased contents for each topic are as follows: **I)** A case study modulating organic pollution in wildfire-impacted boreal peatlands, which involves (1) Characterizing organic composition and hydrophobic transformations of peats following lab-simulated wildfires; (2) Assessing water-leachable peat-derived pollutants including phenolic micropollutants though a lab-simulated batch leaching study; **II)** Developing novel water treatment approaches for aqueous OMP removal, which involves (3) Converting climate change damaged boreal peats into value-added high surface area, highly efficient porous carbon bio-sorbents for adsorption; and (4) Synthesizing a novel, 2-dimensional reduced graphene oxide (rGO) based nanocomposite membrane for enhanced flow-through separation.

### 1.4 Thesis outline

*Chapter1*

Chapter 1 provides the background and objectives of the project, and a brief overview of research details in each chapter.

*Chapter 2*

Chapter 2 investigates how forest fire might contribute to hydrophobic transformations of peat organic molecules, and thus the formation of OMPs in boreal peatlands. Peat soil chemistry is closely related with peat soil hydrophobicity, which is a common phenomenon affected by moisture content [29-31], organic content [32, 33], moss species [31] and peat fire conditions (smoldering and flaming combustions) [9, 34]. Changes in peat hydrophobicity and the resultant organic compositions have significant implications on peatland hydrological processes such as causing increased surface runoff, reduced infiltration and slowed forest recovery [35, 36]. However, very limited studies explored organic soil hydrophobic transformations and the associated environmental impacts, and this study filled the gap.

A comprehensive evaluation of duration of hydrophobicity in pre-fire and lab-simulated post-fire peats were studied. Hydrophobicity was correlated with possible heat-induced chemical transformations of peat organic substances. The pre-heat and post-heat (300 ℃) organic compositions such as fatty acids, sugars, polycyclic compounds, aromatic acids and short-chain molecules, were identified through gas chromatograph – mass spectrometry (GC-MS) and Fourier transform – infrared spectroscopy (FTIR). Heat-induced physical structural and morphological changes were identified through scanning electron microscopy (SEM) and Brunauer -Emmett-Teller (BET) measurements. Results

from this study can help understand the formation of peat-derived molecules modulated by peatland fires, so that policy makers and downstream municipalities can better monitor and manage the fire-induced peatland contaminants in soil and water systems.

*Chapter 3*

Following outcomes reached in chapter 2, chapter 3 attempts to answer what types and quantities of pre- and post-fire peat-derived pollutant groups are water-leachable following flooding or heavy precipitations, and if they are of acute concern for downstream source water quality and drinking water treatment facilities. A lab-based batch leaching study was performed to quantify the concentrations of peat leached carbons, nutrients and phenols. As fire temperature has great impacts on peat chemistry, two different heating temperatures (250 and 300°C) were adopted to prepare post-heated peats, which best simulates the samples from low-severity smouldering peat fires. Samples were stirred in batch condition at a given peat/water mass ratio over a 2-day period to simulate vigorous field leaching condition.

Changes of leached pollutants, including phenolic micropollutants, from peats treated at different heating temperature were contrasted, and their concentrations in the laboratory setting were compared with US surface water guidelines, European Union (EU) wastewater discharge limit and Canadian sewer discharge by-law limits. Principal component analysis (PCA) was used to conjecture possible leaching mechanism. Given limitations of field sampling due to risks from fire and smoke, these experimental results reported in this seminal study provided useful lab-scale data and laid a foundation for next step field

measurements and validations of peat leachable pollutants modulated by different wildfire conditions.

*Chapter 4*

Results from Chapter 2 and Chapter 3 have identified several climate change induced issues on boreal peatland. First, the existence of OMPs such as phenols and benzoic acid and its derivatives in boreal peatlands, may pose serious risks to potable water systems in the boreal communities. High concentrations of other hydrophilic molecules such as saccharides and amino acids will likely also increase the chemical oxygen demand (COD) level in receiving waters such as municipal pipelines, disturbing C: N ratio for denitrification process in water treatment plants. Second, damaged by frequent burning, shallow layer boreal peats often become hydrophobic, especially at a few centimeters below the surface, due to either movement and condensation of vapors of hydrophobic organic compounds from surface to underlying cooler layers and coat or chemically bond onto soil particles [37, 38] or condensation of the transformed organic matter, including pyrolysis products from sources such as cellulose constituents from the litter layer [12]. This would increase the chance of flooding and soil erosion, thus impeding peatland restoration.

Hence, chapter 4 aims to provide a solution for promoting peatland ecological restoration while benefiting downstream communities, including agricultural lands and municipal water systems through mitigation of flooding and aquatic organic loadings. Wildfire-damaged boreal peats were for the first time employed as carbon-rich precursors for

making bio-sorbents for efficient OMP adsorption in water through a simple $ZnCl_2$ activation approach under moderate temperature pyrolysis.

The as-prepared porous carbons were characterized by FTIR, X-ray photoelectron spectroscopy (XPS), SEM and BET measurements. The physicochemical characteristics were correlated with their high adsorption capacities towards a model micropollutant, *p*-nitrophenol (PNP). The study identified the key adsorption mechanisms, and highlighted the affiliated environmental and economic benefits of peat porous carbons compared with using other bio-based sorbents as well as commercial sorbents. This application was justified in that (i) fire-damaged surface peats can be excavated to promote peatland restoration and reduce OMP pollution introduced by themselves; (ii) the waste peats can be upcycled to produce value-added sorbents; (iii) the sorbents can remove a variety of OMPs that occurred in not only boreal peatland but also municipal and industrial wastewaters.

*Chapter 5*

Chapter 4 has demonstrated that adsorption process is versatile, effective, and insensitive to toxic pollutants [39], which motivates the study of other technologies for OMP removal. In recent years, membrane-assisted technologies have played increasingly significant roles for water purification and resource recovery in major industries [40-42]. However, some limitations exist. Conventional ultrafiltration (UF) membranes have poor rejection to small organic solutes due to large molecular weight cut-off (MWCO > 1kDa), despite of the high permeability, low energy consumption and easy automation [43]. Tight nanofiltration (NF)

membranes still cannot entirely remove small OMPs (< 500 Da) such as some pharmaceutical compounds [44-47]. NF and reverse osmosis (RO) usually rely on high operating pressure, which brings high costs.

Recently, development of next generation advanced functional polymeric composite membranes has appeared to be an attractive option to advance removal of OMPs. The embedded nanofillers on surface or in polymeric matrix helps to improve membrane characteristics so that the membranes can be tailored to remove certain OMPs at relatively low operating pressures. The topic of nanocomposite polymer membranes for OMP removal has not been comprehensively and critically reviewed as this is an emerging topic. This research hence reviewed the types of nanocomposite membranes developed (surface localized, bulk modified, and thin film nanocomposite membranes) specifically for OMP removal, their fabrication processes, and their targeted applications towards different types of OMPs. Chapter 5 systematically organizes past work, brought clarity and direction to this field, and provided future perspectives for possible improvements of OMP removal by certain nanocomposite membranes.

*Chapter 6*

Continuing the research findings from Chapter 5, chapter 6 aims to develop advanced nanocomposite membranes for OMP removal, in an attempt to overcome existing challenges faced by conventional membranes. In recent years, 2D graphene-based nanomaterials (*e.g.*, graphene oxide (GO), and reduced graphene oxide (rGO)) have gained great interest for water purification because of various advantages, such as an atomically

thin structure, good mechanical strength and large surface area [48]. This study synthesized a novel, iron-doped cross-linked rGO surface-deposited polyethersulfone (PES) membrane using hyperbranched polyethylenimine (HPEI) as crosslinker, which in comparison to conventional graphene-based membranes had higher water flux and higher hydration stability. Membrane physicochemical properties were characterized by Raman spectroscopy, FTIR, XPS, BET, SEM, transmission electron microscopy (TEM) and contact angle measurement. The as-prepared nanocomposite membranes were applied for removal of aqueous PNP micropollutant and azo dyes (methyl orange (MO) and methylene blue (MB) under dead-end mode. The effect of solute concentration, pH and filtrate volume on separation performance were investigated. This study provides an attractive alternative for micropollutants removal from water at low pressure.

*Chapter 7*

Chapter 7 summarizes the main contributions of this thesis, and provides future perspectives to foster next step researches.

## 1.5 References

[1] Y. Yang, X. Zhang, J. Jiang, J. Han, W. Li, X. Li, K.M. Yee Leung, S.A. Snyder, P.J. Alvarez, Which Micropollutants in Water Environments Deserve More Attention Globally?, Environmental Science & Technology, (2020).
[2] R.L. Ramos, V.R. Moreira, Y.A. Lebron, A.V. Santos, L.V. Santos, M.C. Amaral, Phenolic compounds seasonal occurrence and risk assessment in surface and treated waters in Minas Gerais—Brazil, Environmental Pollution, 268 (2021) 115782.
[3] Y.-H. Liu, S.-H. Zhang, G.-X. Ji, S.-M. Wu, R.-X. Guo, J. Cheng, Z.-Y. Yan, J.-Q. Chen, Occurrence, distribution and risk assessment of suspected endocrine-disrupting chemicals in surface water and suspended particulate matter of Yangtze River (Nanjing section), Ecotoxicology and environmental safety, 135 (2017) 90-97.
[4] S. Huang, J.A. McDonald, R.P. Kuchel, S.J. Khan, G. Leslie, C.Y. Tang, J. Mansouri, A.G. Fane, Surface modification of nanofiltration membranes to improve the removal of organic

micropollutants: Linking membrane characteristics to solute transmission, Water Research, 203 (2021) 117520.
[5] F. Humpenöder, K. Karstens, H. Lotze-Campen, J. Leifeld, L. Menichetti, A. Barthelmes, A. Popp, Peatland protection and restoration are key for climate change mitigation, Environmental Research Letters, 15 (2020) 104093.
[6] M. Turetsky, K. Wieder, L. Halsey, D. Vitt, Current disturbance and the diminishing peatland carbon sink, GEOPHYSICAL RESEARCH LETTERS, 29 (2002).
[7] Z.C. Yu, Northern peatland carbon stocks and dynamics: a review, Biogeosciences, 9 (2012) 4071-4085.
[8] J. Holden, Peatland hydrology and carbon release: why small-scale process matters, Philosophical Transactions of the Royal Society A: Mathematical, Physical and Engineering Sciences, 363 (2005) 2891-2913.
[9] M.R. Turetsky, B. Benscoter, S. Page, G. Rein, G.R. van der Werf, A. Watts, Global vulnerability of peatlands to fire and carbon loss, Nature Geoscience, 8 (2014) 11.
[10] F.L. Muller, S.P. Tankéré-Muller, Seasonal variations in surface water chemistry at disturbed and pristine peatland sites in the Flow Country of northern Scotland, Science of the total environment, 435 (2012) 351-362.
[11] G.M. Davies, A. Gray, G. Rein, C.J. Legg, Peat consumption and carbon loss due to smouldering wildfire in a temperate peatland, Forest Ecology and Management, 308 (2013) 169-177.
[12] S.M. Savage, Mechanism of Fire-Induced Water Repellency in Soil, Soil Science Society of America Journal, 38 (1974) 652-657.
[13] L.F. Debano, S.M. Savage, D.A. Hamilton, The Transfer of Heat and Hydrophobic Substances During Burning, Soil Science Society of America Journal, 40 (1976) 779-782.
[14] E. Pastor, I. Oliveras, E. Urquiaga-Flores, J.A. Quintano-Loayza, M.I. Manta, E. Planas, A new method for performing smouldering combustion field experiments in peatlands and rich-organic soils, International Journal of Wildland Fire, 26 (2017) 1040-1052.
[15] D. Clarke, J. Rieley, Strategy for responsible peatland management, International Peat Society Finland, 2010.
[16] C.M. Gibson, L.E. Chasmer, D.K. Thompson, W.L. Quinton, M.D. Flannigan, D. Olefeldt, Wildfire as a major driver of recent permafrost thaw in boreal peatlands, NATURE COMMUNICATIONS, 9 (2018).
[17] C. Li, R. Grayson, J. Holden, P. Li, Erosion in peatlands: Recent research progress and future directions, Earth-Science Reviews, 185 (2018) 870-886.
[18] S. Suarez, J.M. Lema, F. Omil, Pre-treatment of hospital wastewater by coagulation–flocculation and flotation, Bioresource Technology, 100 (2009) 2138-2146.
[19] S. Arriaga, N. de Jonge, M.L. Nielsen, H.R. Andersen, V. Borregaard, K. Jewel, T.A. Ternes, J.L. Nielsen, Evaluation of a membrane bioreactor system as post-treatment in waste water treatment for better removal of micropollutants, Water Research, 107 (2016) 37-46.
[20] T.L. Zearley, R.S. Summers, Removal of Trace Organic Micropollutants by Drinking Water Biological Filters, Environmental Science & Technology, 46 (2012) 9412-9419.
[21] C.P. James, E. Germain, S. Judd, Micropollutant removal by advanced oxidation of microfiltered secondary effluent for water reuse, Separation and Purification Technology, 127 (2014) 77-83.
[22] J. Altmann, A.S. Ruhl, F. Zietzschmann, M. Jekel, Direct comparison of ozonation and adsorption onto powdered activated carbon for micropollutant removal in advanced wastewater treatment, Water Research, 55 (2014) 185-193.

[23] Y. Ling, D.M. Alzate-Sánchez, M.J. Klemes, W.R. Dichtel, D.E. Helbling, Evaluating the effects of water matrix constituents on micropollutant removal by activated carbon and β-cyclodextrin polymer adsorbents, Water research, 173 (2020) 115551.
[24] K. Kimura, G. Amy, J.E. Drewes, T. Heberer, T.-U. Kim, Y. Watanabe, Rejection of organic micropollutants (disinfection by-products, endocrine disrupting compounds, and pharmaceutically active compounds) by NF/RO membranes, Journal of membrane science, 227 (2003) 113-121.
[25] Y. Yoon, P. Westerhoff, S.A. Snyder, E.C. Wert, Nanofiltration and ultrafiltration of endocrine disrupting compounds, pharmaceuticals and personal care products, Journal of Membrane Science, 270 (2006) 88-100.
[26] S. Das, N.M. Ray, J. Wan, A. Khan, T. Chakraborty, M.B. Ray, Micropollutants in wastewater: fate and removal processes, Physico-Chemical Wastewater Treatment and Resource Recovery, (2017) 75-117.
[27] A.R. Lado Ribeiro, N.F.F. Moreira, G. Li Puma, A.M.T. Silva, Impact of water matrix on the removal of micropollutants by advanced oxidation technologies, Chemical Engineering Journal, 363 (2019) 155-173.
[28] A. Almuntashiri, A. Hosseinzadeh, F. Volpin, S.M. Ali, U. Dorji, H. Shon, S. Phuntsho, Removal of pharmaceuticals from nitrified urine, Chemosphere, 280 (2021) 130870.
[29] E. Hewelke, J. Szatyłowicz, T. Gnatowski, R. Oleszczuk, Effects of Soil Water Repellency on Moisture Patterns in a Degraded Sapric Histosol, Land Degradation & Development, 27 (2016) 955-964.
[30] K. Berglund, L. Persson, Water repellence of cultivated organic soils, Acta Agriculturae Scandinavica, Section B - Soil & Plant Science, 46 (1996) 145-152.
[31] P.A. Moore, M.C. Lukenbach, N. Kettridge, R.M. Petrone, K.J. Devito, J.M. Waddington, Peatland water repellency: Importance of soil water content, moss species, and burn severity, Journal of Hydrology, 554 (2017) 656-665.
[32] A. Lachacz, M. Nitkiewicz, B. Kalisz, Water repellency of post-boggy soils with a various content of organic matter, Biologia, 64 (2009) 634-638.
[33] M. Orzechowski, S. Smólczyński, P. Sowiński, B. Rybińska, Water repellency of soils with various content of organic matter in north-eastern Poland, Soil Science Annual, 64 (2013) 30-33.
[34] J. O'Donnell, M. Turetsky, J. Harden, K. Manies, L. Pruett, G. Shetler, J. Neff, Interactive Effects of Fire, Soil Climate, and Moss on CO2 Fluxes in Black Spruce Ecosystems of Interior Alaska, Ecosystems, 12 (2009) 57-72.
[35] S.H. Doerr, R.A. Shakesby, W.H. Blake, C.J. Chafer, G.S. Humphreys, P.J. Wallbrink, Effects of differing wildfire severities on soil wettability and implications for hydrological response, JOURNAL OF HYDROLOGY, 319 (2006) 295-311.
[36] S.H. Doerr, R.A. Shakesby, R.P.D. Walsh, Soil water repellency: its causes, characteristics and hydro-geomorphological significance, EARTH-SCIENCE REVIEWS, 51 (2000) 33-65.
[37] J. Letey, Causes and consequences of fire-induced soil water repellency, Hydrological Processes, 15 (2001) 2867-2875.
[38] L.F. DeBano, The role of fire and soil heating on water repellency in wildland environments: a review, JOURNAL OF HYDROLOGY, 231 (2000) 195-206.
[39] M. Ahmaruzzaman, Adsorption of phenolic compounds on low-cost adsorbents: A review, Advances in Colloid and Interface Science, 143 (2008) 48-67.
[40] L.D. Nghiem, A. Manis, K. Soldenhoff, A.I. Schäfer, Estrogenic hormone removal from wastewater using NF/RO membranes, Journal of Membrane Science, 242 (2004) 37-45.
[41] B.C. Ricci, C.D. Ferreira, A.O. Aguiar, M.C.S. Amaral, Integration of nanofiltration and reverse osmosis for metal separation and sulfuric acid recovery from gold mining effluent, Separation and Purification Technology, 154 (2015) 11-21.

[42] T. Wang, H. Wu, S. Zhao, W. Zhang, M. Tahir, Z. Wang, J. Wang, Interfacial polymerized and pore-variable covalent organic framework composite membrane for dye separation, Chemical Engineering Journal, 384 (2020) 123347.
[43] S.G. Arhin, N. Banadda, A.J. Komakech, I. Kabenge, J. Wanyama, Membrane fouling control in low pressure membranes: A review on pretreatment techniques for fouling abatement, Environmental Engineering Research, 21 (2016) 109-120.
[44] H. Guo, L.E. Peng, Z. Yao, Z. Yang, X. Ma, C.Y. Tang, Non-polyamide based nanofiltration membranes using green metal–organic coordination complexes: implications for the removal of trace organic contaminants, Environmental science & technology, 53 (2019) 2688-2694.
[45] G. Han, T.-S. Chung, M. Weber, C. Maletzko, Low-pressure nanofiltration hollow fiber membranes for effective fractionation of dyes and inorganic salts in textile wastewater, Environmental science & technology, 52 (2018) 3676-3684.
[46] L.-x. Dong, X.-c. Huang, Z. Wang, Z. Yang, X.-m. Wang, C.Y. Tang, A thin-film nanocomposite nanofiltration membrane prepared on a support with in situ embedded zeolite nanoparticles, Separation and Purification Technology, 166 (2016) 230-239.
[47] N. Rakhshan, M. Pakizeh, Removal of triazines from water using a novel OA modified SiO2/PA/PSf nanocomposite membrane, Separation and Purification Technology, 147 (2015) 245-256.
[48] S. Dervin, D.D. Dionysiou, S.C. Pillai, 2D nanostructures for water purification: graphene and beyond, Nanoscale, 8 (2016) 15115-15131.

## Chapter 2

# Hydrophobicity of peat soils: Characterization of organic compound changes associated with heat-induced water repellency

Reprinted from *Y. Wu, N. Zhang, G. Slater, J.M. Waddington, C.-F. de Lannoy, Hydrophobicity of peat soils: Characterization of organic compound changes associated with heat-induced water repellency, Science of The Total Environment 714 (2020) 136444.*

## 2.1 Abstract

Boreal peatlands provide critical global and regional ecosystem functions including climate regulation and nutrient and water retention Wildfire represents the largest disturbance to these ecosystems. Peatland resilience depends greatly on the extent of post-fire peat soil hydrophobicity. Climate change is altering wildfire intensity and severity and consequently impacting post-fire peat soil chemistry and structure. However, research on fire-impacted peatlands has rarely considered the influence of peat soil chemistry and structure on peatland resilience. Here we characterized the geochemical and physical properties of natural peat soils under laboratory heating conditions. The general trend observed is that hydrophilic peat soils become hydrophobic under moderate heating and then become hydrophilic again after heating for longer, or at higher, temperatures. The loss of peat soil hydrophilicity initially occurs due to evaporative water loss (250 °C and 300 °C for 5 min). Gently but thoroughly dried peat soils (105 °C for 24 h) also show mass losses after heating, indicating the loss of organic compounds through thermal degradation. Gas chromatography-mass spectrometry (GC–MS) and Fourier transform-infrared (FTIR) spectroscopy were used to characterize the chemistry of unburned and 300 °C burned peat soils, and various fatty acids, polycyclic compounds, saccharides, aromatic acids, short-chain molecules, lignin and carbohydrates were identified. We determined that the heat-induced degradation of polycyclic compounds and aliphatic hydrocarbons, especially fatty acids, caused dried, hydrophobic peat soils to become hydrophilic after only 20 min of heating at 300 °C. Furthermore, peat soils became hydrophilic more quickly (20 min vs

6 h) with an increase in heat from 250 °C to 300 °C. Minimal structural changes occurred, as characterized by BET and SEM analyses, confirming that surface chemistry, in particular fatty acid content, rather than structure govern changes in peat soil hydrophobicity.

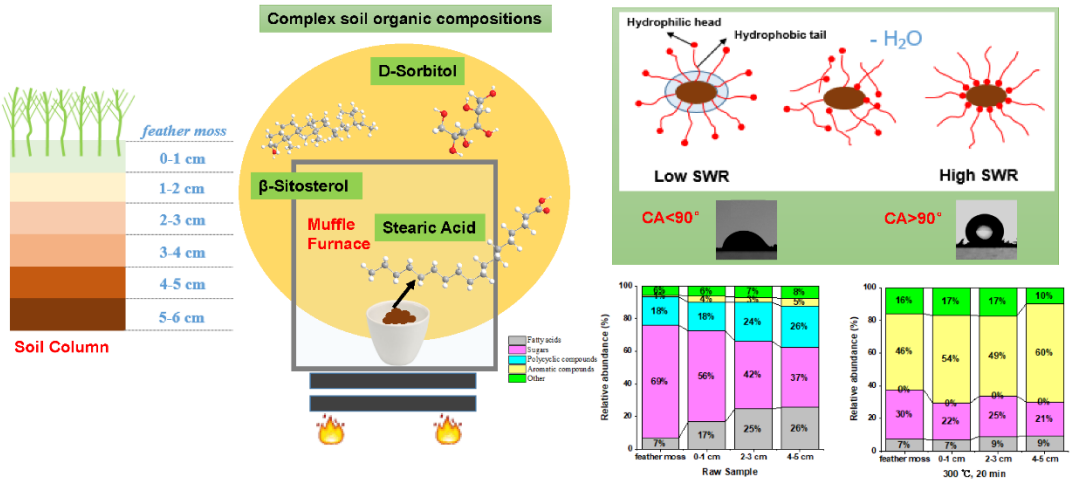


## 2.2 Introduction

Boreal peatlands represent a globally significant terrestrial carbon reservoir [1] and regional freshwater resource [2]. Wildfires are the largest disturbance affecting these ecosystems [3] and with climate change increasing the frequency and severity of boreal wildfires [4, 5], there is a critical need to examine their potential impacts on boreal soils and ecosystems [6, 7]. Wildfires can alter many soil properties [8] including their wettability. Soil hydrophobicity, characterized by reduced rate of wetting and decreased soil water retention, is frequently increased by forest fires in many soil types worldwide [9-15]. Soil hydrophobicity has significant impacts on peatland hydrological processes [12, 16-19], causing both reduced infiltration, which leads to inhibited plant

growth and slowed forest recovery, and increased overland flow, which leads to increased surface runoff and soil erosion [20-23].

Peat soils are comprised of thick organic layers in the form of partially decomposed plant remains [24, 25]. Peat soils are typically classified as organic soils, notably distinctive from mineral soils. It has been argued that mineral soil hydrophobicity is impacted by coatings and environmental conditions. Specific coatings include hydrophobic organic coatings [22, 26, 27] from plant leaf waxes [28], root exudates [29], fungal growth or microbial activity [30], and decomposing organic matter [31, 32], and their resultant soil texture [33, 34], while specific environmental conditions include variations in field soil water content [35, 36], differences in vegetation cover [37] and changes in temperature [28, 38]. In contrast to widely investigated mineral soil hydrophobicity [39, 40], comparable detailed studies for organic soils (e.g. peats) are scarce [16]. The current literature suggests that organic content [41, 42], moss species [43], in combination with moisture content [16, 43, 44], and peat fire conditions (i.e. smoldering and flaming combustions) [25, 45] play key roles in influencing peatland soil water repellency.

Fire can create [46], strengthen [11, 45, 47] and eliminate [48, 49] soil hydrophobicity. The impact of fire on soil hydrophobicity is predominantly controlled by the fire temperatures and duration [8, 15], oxygen availability (combustion vs pyrolysis) [50], and heterogeneity of heating. It has been reported that soil hydrophobicity considerably increases when heating soils between 175 and 200 °C while no significant changes have been observed below 175 °C [46]. Some reasons identified for fire-induced soil hydrophobicity include fire-induced organic structural modifications, polymerization or polycondensation

reactions [8, 51], improved hydrophobic molecular bonding [52, 53] and melting and redistribution of the interstitial waxes onto soil aggregates [21, 54]. Hydrophobicity has been observed to be eliminated by heating soils to high temperatures between 280 and 400 °C [11, 47]. The likely cause of hydrophobic elimination is the volatilization, alteration and combustion of organic compounds [55, 56], although little quantification of these changes has been performed. Peat fires are dominated by smoldering fires, coupled with flaming fires [25, 57] due to high biomass loadings in peatlands. In-vivo studies have predominantly found increased peatland soil water repellency post-fire [12, 43, 45], but some studies have also attributed wildfires to cause reduced peat soil hydrophobicity [17, 58]. Such discrepancies in studies indicate that post-fire peat soil hydrophobicity exhibits site-specific characteristics [58]. Thus, whether soils become hydrophobic as well as the extent of their hydrophobicity post-fire is a function of initial soil properties and heating conditions.

Overall, the current state of knowledge on how fire impacts organic soil hydrophobicity is incomplete and sometimes contradictory. This is likely due to the inconsistent fire parameters that have been studied, as well as the high variability in soil types, experimental conditions, and measurement techniques. This inconsistency has resulted in disagreement in the literature about how fires impact organic soil hydrophobicity [47, 59, 60]. Furthermore, there is an absence of literature on how peat soil hydrophobicity responds to different fire conditions when coupled with water content variations and heat-induced organic composition transformations. As such, there is a need for detailed studies of the physical and chemical transformations of hydrophobic organic soils by fire. A mechanistic

explanation of fire-induced organic soil hydrophobic transformations will provide a framework for understanding the empirical observations from experiments and field trials that occur under a wide range of organic peat soil types and conditions. Finally, understanding the mechanisms regulating peat soil hydrophobicity is pivotal for conserving the hydrological, ecological and biogeochemical functions of peatlands [61]. For example, such an understanding could provide insights into the optimal development of biodegradable flame retardants and peat soil hydrophobic modifiers that maintain peatland function while enhancing their resilience to forest fires.

Hence, we collected unburned boreal forest peatland topsoils, and subjected them to controlled laboratory heating conditions to approximate the impacts of forest fires. Through comprehensive geochemical and physical analyses, we identified the heat-induced transformation of organic compounds that likely alter peatsoil hydrophobicity. We propose that specifically identified hydrophobic organic compounds present on and within peatland soils play critical roles for heat-induced peat soil hydrophobicity.

## 2.3 Materials and methods

### 2.3.1 Study area and soil sampling

The boreal peatland area studied is within the Pelican Mountain research site (55°36′ N, 113°35′60″ W), in province of Alberta, Canada. The research area is characterized by a dense black spruce (Picea mariana) overstory and is surrounded by aspen forest and mixed wood stands. Ground cover moss species were typically dominated by *Sphagnum* and *feather moss* and/or lichen species.

Cores of *feather moss* (and underlying peat) were specifically collected as it is the dominant species in black spruce peatland, and previous research has determined this species to have poor water retention and high post-fire hydrophobicity [43, 62]. Cores were collected, representatively in both undisturbed control areas (i.e. natural forested peatland, high fuel load) and a FireSmart™ hand-thinned treatment areas (i.e. human activity intervened peatland, reduced fuel load) where the tree density is reduced by felling and there is a 3 m spacing between trees with no lower branches. Coring of samples were conducted from different microforms (i.e. hummocks and lawns) in these two areas to reconcile the high surface heterogeneity and incorporate various environmental conditions include different water content, depth to water table, and peat decomposition levels [63, 64]. See Table S1 for the sampling points. At each sampling point cores were taken using PVC pipes with inner diameter of 10 cm, up to 15 cm without changing the original structure from the surface live *feather moss* (4–8 cm) to the first few centimeters (with thickness > 6 cm) of peat below the living moss layer.

2.3.2 Sample preparation and bulk physical properties

Boreal peatlands are exclusively dominated by organic materials, and the vertical stratification of peat soils usually reflects the degree of organic decomposition [65]. *Feather moss*, which has no root systems [66], normally dominates the ground cover of mid to late successional boreal forest stands. Live *feather moss* is relatively uniform in structure and composition, and was directly separated from the underlying peat for later characterization. For the underlying peat (after moss removal) we prepared samples by removing large twigs, roots and wood debris embedded in the peat. Given that heat transfer

and the impacts of fire on soil rarely penetrate deeper than a few centimeters of shallow soil layers [46, 57, 67], only the first 6 cm of peat soils were retained for studying the heat-induced changes in hydrophobicity. These 6 cm thick peat soil samples were divided into 1 cm thick subsample slices (i.e. 0–1 cm. 1–2 cm, 2–3 cm, 3–4 cm, 4–5 cm and 5–6 cm).

Previous studies have shown that drying temperature (25–105 °C) during pretreatment may affect soil water repellency [68-70]. Possible causes are the changes in water contents and soil organic matters after drying [68]. However, findings regarding different soil types and pretreatment temperatures are often conflicting [44, 69, 70], and do not necessarily agree on whether soil drying treatment has an influence on the water repellency. Our laboratory tests indicate that both 25 °C air-drying and 105 °C oven drying overnight for wet peat soils led to an increase in water repellency, while 25 °C air-drying cannot guarantee sufficient removal of peat pore free water. BET vacuum drying for peat soils under 25 °C and 105 °C for 24 h removes all peat moisture, but was measured to have insignificant differences in mass losses. We thus conclude that drying temperature under our laboratory settings mainly affects peat soil hydrophobicity by changing water contents instead of causing organic matter degradations or volatilizations. Mechanical grinding of peat soils has been established to achieve homogenized chemical composition, and benefits subsequent geochemical analyses.

Therefore, all subsamples were dried in an oven at 105 °C for 24 h to equilibrium weight, and then were ground and passed through a 2 mm sieve (Fisher brand, U.S. Standard sieve, diameter 8 in.). The homogenized dried *feather moss* samples and peat soil samples were then mixed to approximate an average depth-dependent composition. For example, from

multiple peat soil cores, all 1–2 cm subdivided cores were dried, ground, and then well-mixed with each other to make one well-mixed 1–2 cm sample. The mixed averaged samples were further transferred to sealed Ziploc bags and stored for future analysis. Peat soil bulk density, peat soil gravimetric water content (GWC) and volumetric water content (VWC) of the 5 field samples for the 6 depths were determined using the following equations (Fig. S1).

$$\rho_b = \frac{m_{dry}}{V_{bulk}} \quad (1)$$

$$\theta_g = \frac{m_{wet} - m_{dry}}{m_{dry}} \quad (2)$$

$$\theta_v = \theta_g \frac{\rho_p}{\rho_{water}} \quad (3)$$

where $m_{dry}$ is the sample dry weight in an oven to constant dry weight at 105 °C; $m_{wet}$ is the sample wet weight on field; $V_{bulk}$ is the peat soil bulk volume includes volume of solids and pore space; $\rho_b$ (g/cm$^3$) is peat soil bulk density; $\rho_p$ is peat soil particle density, and here an estimated value of 1.47 g/cm$^3$ is used [43, 71]; $\theta_g$ (g/g) and $\theta_v$ (cm$^3$/cm$^3$) are peat soil GWC and VWC respectively.

2.3.3 Water repellency measurement

Peat soil water repellency on unheated and heated samples was evaluated by water drop penetration time (WDPT) tests. This test characterizes the extent of hydrophobicity on a porous surface [72] and is done by placing about 50 μL of distilled water onto a flat peat soil surface. Time was recorded from the time of initial water contact with the soil surface until the water completely penetrated the sample surface. Water repellency is classified based on the category used in other studies [43, 72-74]. Namely, hydrophilic (<5 s); slightly

hydrophobic (5–60 s); strongly hydrophobic (60–600 s); severely hydrophobic (600–3600 s) and extremely hydrophobic (>3600 s).

### 2.3.4 Laboratory heating

Prepared dried and wet (GWC = 3 g/g) samples were respectively heated in a tabletop muffle furnace (Fisher Scientific, USA) at different temperatures for different durations. 3 g $H_2O$/g soil was selected for moist samples because this reflects the median moisture level of collected field peat soils (i.e. 0.20–5.59 g/g). The internal chamber contains heating elements on all sides enabling uniform heating. The furnace is equipped with built-in vent ports on top for removing volatile compounds and water vapour. The experiments were conducted in atmospheric gas composition within the chamber, without an external air supply. The muffle furnace was preheated to the assigned temperature and the temperature was allowed to stabilize for at least 10 min before samples were introduced. For each sample, 50 mg of soils (dry weight basis) was placed in a glazed ceramic crucible (dia. 35 mm, Fisherbrand) as a flat thin layer. Samples were allowed to cool to room temperature in air and then their weights and WDPT tests were measured. As this study only considered *feather moss* peat soils and was conducted under laboratory heating conditions, the results are a first order approximation to field burning conditions, where heterogeneous moss cover, changes in oxygen content, and heating gradients contribute to the rate of change of soil hydrophobicity.

### 2.3.5 Gas chromatography-mass spectrometry (GC–MS)

#### 2.3.5.1 Extraction procedure

Polar amphiphilic solvents display desirable interfacial activity and have been shown to be most effective in removing hydrophobic compounds from water-repellent soils [26, 75, 76]. Despite some studies having shown that solvent type may affect compound conformation and molecular arrangement on surface of soil particles and induce changes in post-extraction water repellency [75, 77], IPA/$NH_3$ mixture [77-79] is widely used for the extraction of compounds from many soil types. Here we extracted the organic compounds from peat soils via a mixture of isopropanol/30% ammonia (v:v, 7:3). Approximately 50 mg of oven-dried peat soils were mixed with 1 mL isopropanol/ammonia (30%) (v:v, 7:3) solvent mixture. All samples were pre-wetted in the solvent mixture for 5 min, then the samples were sonicated in a Branson 2800 Ultrasonic Cleaner (Crystal Electronic Inc., Canada) for 15 min to allow sufficient detachment of organic molecules from the soil particles. Suspensions were collected and centrifuged in an Eppendorf Microcentrifuge 5430, (Eppendorf, Germany) at 4000 rpm for 2 min. Supernatants were used for the GC–MS analysis.

#### 2.3.5.2 Internal standards, calibration curves, and sample preparation

Expected organic compounds on soils include fatty acids, sterols, and sugars. An internal standard was used for each class of organic compound, to establish baseline concentrations measured by GC–MS. The internal standards were lauric acid (98%, Sigma-Aldrich) for fatty acids, resorcinol (99%, Fisher Chemical) for sugars/sugar alcohols, and 5-α-cholestane (97%, Sigma-Aldrich) for polycyclic compounds. Reference standards of

several organic compounds were added to soil extracts to calibrate the extent to which solvent-extracted organic compounds were analyzed by GC–MS. Together with the internal standards these determined the concentration of compounds extracted from soils. The reference standards closely approximated different classes of compounds in the solvent extracts. The reference standards were palmitic acid (98%, ACROS organics), stearic acid (97%, ACROS organics), D-sorbitol (97%, ACROS organics) and cholesterol (99%, Sigma-Aldrich).

A working reference standard (400 μg/mL) containing all the standards was prepared by mixing identical aliquots of 2 mg/mL palmitic acid, stearic acid and cholesterol in dichloromethane (DCM), 2 mg/mL D-sorbitol in dimethylformamide (DMF), and pure DCM. A series of reference standard sub stocks (10, 33.3, 50, 100, 150, 200, 300 and 400 μg/mL) were prepared by diluting this working reference standard with appropriate amounts of DCM.

A mixture of internal standard stock DCM solution for lauric acid, resorcinol and 5-α-cholestane was also prepared, of which the concentration for each chemical was 250 μg/mL. 30 μL of reference standard sub stock for each concentration (10, 33.3, 50, 100, 150, 200, 300 and 400 μg/mL), was transferred into a 250 μL glass conical insert in a 2 mL clear Robo vial, followed by adding 20 μL of the internal standard stock solution and 50 μL of MSTFA (with 1% TMCS), the derivatizing agent. A series of mixed standards (3, 10, 15, 30, 45, 60, 90 and 120 ppm) with a fixed amount (50 ppm) of internal standards for calibration were thereby established. 200 μL of soil extracts was transferred into a 250 μL glass conical insert in a 2 mL clear Robo vial. Each sample was completely evaporated

with nitrogen and reconstituted with 15 μL DCM, 10 μL internal standard stock and 25 μL MSTFA (with 1% TMCS). To ensure complete derivatization, the standards and samples were incubated at 60 °C for 1 h and then load for GC–MS analysis.

#### 2.3.5.3 Instrumentation and compounds quantification

Analytical separation and determinations of the derivatized standards and samples were performed using an Agilent 6890 series GC coupled with an Agilent 5973 series mass quadruple detector, equipped with an Agilent DB-5MS column (30 m × 0.32 mm × 0.25 μm). The system was operated using He carrier gas under constant flow (1.2 mL/min) at 70 eV ionization energy. The oven temperature was programmed to increase from 50 °C (hold 1 min) to 300 °C (hold 15 min) at an increase rate of 5 °C /min. The m/z scan range of this GC–MS is 50–800. Compounds were identified using the NIST 2011 MS library, and their respective concentration was estimated by calculation from the previously established calibration curves. Those compounds which could not be fully identified on the basis of mass spectra with a match score <800 were labelled as “unknown”.

### 2.3.6 Fourier transform infrared spectroscopy (FTIR)

To compare the structural arrangement of functional groups along the peat soil depth profile and trace the chemical transformations of organic molecules during the heating process, FTIR was performed for the unheated and heated samples by a Nicolet 6700 FT-IR spectrometer (Thermo Scientific, USA). Samples were placed directly on an ATR diamond crystal plate, and the flat press tip on the pressure arm was locked into the small

crystal. Spectral data were acquired by averaging 64 scans at 4 $cm^{-1}$ resolution over the mid-infrared range from 4000 to 525 $cm^{-1}$ and interpreted by OMNIC 8.2 software. Spectra are all presented as transmittance values.

### 2.3.7 BET and SEM characterization

Peat soil specific surface area was measured by BET $N_2$ adsorption-desorption at liquid nitrogen temperature (77 k) with a physisorption instrument (Quantahrome iQ). Soil samples were first outgassed at 105 °C under vacuum for 24 h prior to the measurements. The BET specific surface area was determined by the Brunauer-Emmet-Teller (BET) model which involves the use of the following BET equation.

$$\frac{1}{W\left(\frac{P_0}{P}-1\right)} = \frac{1}{W_m B} + \frac{B-1}{W_m B}\left(\frac{P}{P_0}\right) \quad (4)$$

where W is the weight of gas adsorbed at a relative pressure of $P/P_0$; $W_m$ is the weight of adsorbate (nitrogen) constituting a monolayer of surface coverage; B represents a BET constant which is related to the energy of adsorption in the first adsorbed layer and indicates the magnitude of the adsorbent/adsorbate interactions. The $P/P_0$ ranged from 0.05 to 0.35 in the adsorption isotherm, which was used to calculate the specific surface area based on the multipoint BET method.

Pre- and post-burned peat soil's microstructure was characterized by Scanning Electron Microscopy (SEM). The measurements were performed using a JEOL 6610LV tungsten filament equipped SEM, or a JEOL JSM-7000F, a Schottky field emission gun equipped

SEM under high vacuum, depending on the required resolution of the images. All samples were coated with 15 nm of gold prior to SEM characterization.

## 2.4 Results and discussion

### 2.4.1 Pre and post-burn peat soil hydrophobicity

#### 2.4.1.1 Effect of water content

Soil moisture content has long been considered an important factor responsible for the highly variable and irregular patterns of soil hydrophobicity [36, 46, 80]. According to the water drop permeation (WDPT) tests presented in Fig. 1, peat soil hydrophobicity decreases non-linearly with gravimetric water content (GWC). There is a sharp cut-off in water content that transforms peat soils from hydrophobic to hydrophilic. For example, water does not easily infiltrate *feather moss* peat soils with low water content (<0.3 g/g), but easily infiltrates soils with high water content (>0.8 g/g). Small differences in peat soil water content lead to dramatic changes in water infiltration behavior. We observed that this critical soil GWC threshold increased with increasing soil depth. The threshold ranged from between 0.3 and 0.7 g water/g soil for *feather moss* layers (surface) to between 0.8 and 1.0 g water/g soil for deep peat soil layers (4–5 cm below surface). The marked moisture content threshold, known as a narrow transition range, between hydrophobic to hydrophilic soils has been reported as the critical GWC, which has been observed for not only mineral soils [29, 39, 81], but also peat soils [16, 43]. For instance, Moore et al. [43] found that *feather moss* peats exhibit a threshold-like GWC of <1.4 g/g, and this coincided with poor water retention, frequently tolerated desiccation and high hydrophobicity under field conditions. The water within peats can change soil hydrophobicity by altering organic

molecular arrangements in soil particles during the interactions. This difference in threshold reflects the differences in organic matter quantity and polarity.

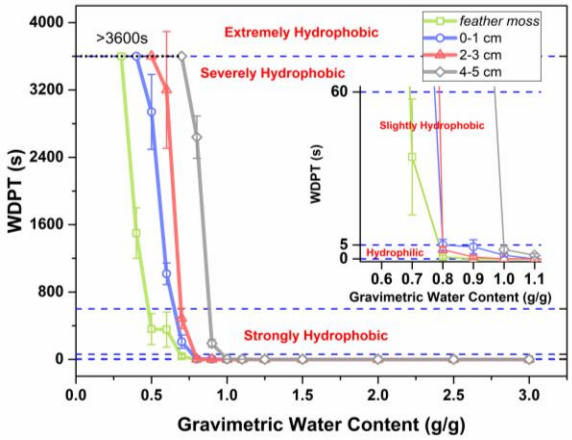


**Fig. 1.** The relationship between hydrophobicity and moss and peat soil gravimetric water content from the study site. The inset indicates the GWC ranges in which peat soils become hydrophilic.

As demonstrated in Fig. 1, peat soils can demonstrate extreme hydrophobicity even when they contain considerably higher GWC (e.g. 0.8 g/g for deep soils). This implies that water content alone does not govern peat soil water repellency. The conformation and reorientation of organic matter within the peat soil in the wetting cycle may partly explain this phenomenon. It is assumed that when GWC is low, the polar ends of amphiphilic molecules remain associated through hydrogen bonds and are forced to attach to soil particles while the non-polar ends, e.g. methyl or methylene groups, orient outwards, leading to water repellency [22, 82]. Under higher GWC, the molecular polar groups which include hydroxyl and carboxylic groups will interact with water molecules rather than each other and/or with soil particles. The soil-organic bonds weaken, rendering the surfaces hydrophilic [22, 83].

#### 2.4.1.2 Heating kinetics

The heating temperature is critical in determining post-fire soil hydrophobicity [21, 47]. Of the boreal forested peatlands, smoldering and flaming fires are the two common forms of peat fires [25, 57]. Smoldering fires, known as flameless burning of biofuels (e.g. peats), can impregnate into deep layers of organic soils and persist for long periods (i.e. up to months or longer) despite rainfalls [84]. Smoldering fires have peak temperatures ranging from 400 to 600 °C [57, 85]. In comparison, flaming fires require continuous ignitions and as such occur less frequently in northern peatlands [57, 86]. Temperatures reached during flaming fires above ground can be very high (i.e. sometimes as high as 1500 °C) [57]. However, shallow soil layers rarely exceed 300 to 500 °C [57].

Because peat burning (oxidative combustion as opposed to pyrolysis) usually takes place between 250 and 300 °C [57], dried and wet (GWC = 3 g/g) peat soils were heated respectively at 250 °C and 300 °C to simulate a field peat soil wildfire event. Fig. 2 shows that both moist (GWC = 3 g/g) and dried soils lose water mass and become hydrophobic within the first 5 min of heating, regardless of temperature. Initially wettable moist samples rapidly became extremely hydrophobic. It has been suggested that moisture can accelerate heat transfer in soils as a result of water's higher thermal conductivity over air [87]. Nevertheless, heated wet soils do not exceed 95 °C until the complete vaporization of water [88, 89]. Given these low temperatures within the first 5 min, we deduced that the substantial weight loss in the wet samples in the first 5 min (Fig. 2a and d) is primarily attributed to water vaporization and not the volatilization and/or combustion of organic compounds within the soils. Changes in water content lead to marked soil hydrophobicity

within 5 min. This is likely a result of both water loss and the vaporization-induced changes in conformation and orientation of organic molecules. After the initial 5 min, heat-induced mass loss within the samples is likely a result of soil organic matter decomposition, chemical transformation, and volatilization. During this time, specific classes of organic compounds are lost from soils, which directly impacts soil hydrophobicity.

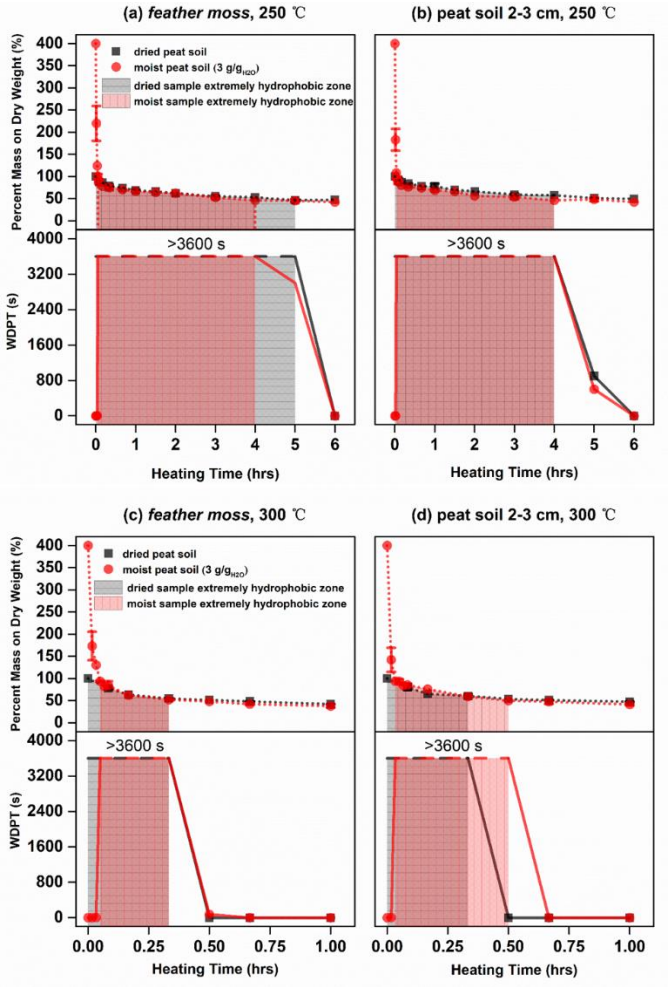


**Fig. 2.** Heating kinetics of dried and moist peat soils: (a) 250 °C for *feather moss*, (b) 250 °C for 2-3 cm peat soil; (c) 300 °C for *feather moss*, (d) 300 °C for 2-3 cm peat soil.

The temperature to which peat soils are exposed governs the persistence of soil hydrophobicity. After substantial heating, soils can lose their hydrophobicity. As shown

in Fig. 2, soils heated to 250 °C required significantly more time (4.5–6 h) to destroy their hydrophobicity than soils heated to 300 °C (25–30 min). Soils changed drastically from hydrophobic to hydrophilic after heating for these times (4.5–6 h and 25–30 min), such that these time points were termed threshold points. Their hydrophobicity was eliminated at the threshold point, making the peat soils wettable once more, probably due to hydrophobic organic compound removal.

In addition, we examined the impact of a wide range of temperatures on the rate of hydrophobicity loss, to evaluate the range of common peat fire temperatures. Samples were heated up to 24 h because studies have shown that peat fires are often sustained for several minutes up to several hours or longer [84]. The total mass of peat soils that was evaluated was small (50 mg) for each experiment. This mass covered a thin layer (approximately 2–3 mm) in the ceramic heating crucible and as such it was expected that these peat soils were uniformly heated in bulk. Therefore, there was no attempt to identify heat propagation through the peat soil depth profile during heating. It is expected that heat propagation would be hindered in dried peat soils. This study focused on heat generated from external sources such as smoldering fires, rather than heat propagated through thermal conduction. Given that no oxygen was pumped into the furnace during the heating, the oxygen availability would differ between the peat soil surface (i.e. direct contact to oxygen) and within the peat soil bulk (i.e. limited diffusive oxygen transport). Both combustion and pyrolysis conditions exist within our crucible. However, we hypothesize that the oxygen availability difference is minimal, given the small mass added in the crucible.

Fig. 3 demonstrates the minimum time for dried peat soils to lose their hydrophobicity when heated at various temperatures ranging from 225 to 350 °C. The time point at which peat soil hydrophobicity is eliminated ranges greatly from 14 to 20 h at 225 °C to only a few minutes at 350 °C. We also observed that deeper peat soils lose their hydrophobicity more quickly than shallower peat soils for the same heating temperature. Shallower peat soils are more decomposed but have nearly the same particle size distribution (Fig. S2), suggesting that their chemical composition may influence their heat-induced loss of hydrophobicity. This difference in hydrophobicity loss as a function of depth within the soil may be due to the differences in soil composition Therefore, we conclude that the hydrophobicity of peat soils is primarily affected by their chemical composition, moisture content and the heating temperature and exposure time to which they are subjected.

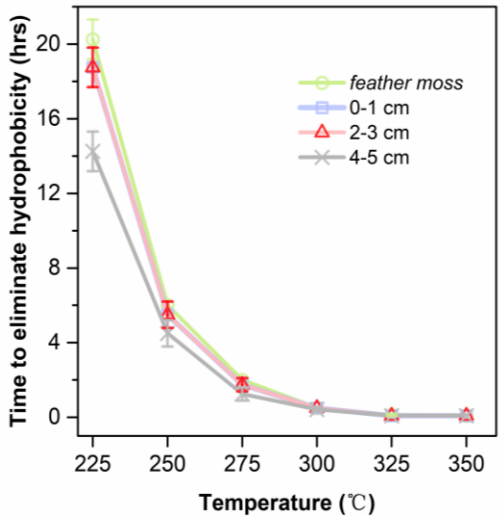


**Fig. 3.** Minimum time to eliminate dried peat soil hydrophobicity under laboratory heating under different temperatures. WDPT tests were measured based on duplicates of samples.

### 2.4.2 GC-MS quantification

In this study, we extracted various hydrophilic and hydrophobic organic compounds from peat soils using an isopropanol/30% ammonia 7:3 ($IPA/NH_3$) mixed solvent. Fig. 4, Fig. 5, Fig. 6, Fig. S3 and Fig. S4 show the relative abundances and quantitative amounts of major extractable compounds from peat soils using $IPA/NH_3$.

#### 2.4.2.1 Fatty acids

Straight-chain n-fatty acids ($C_{16}$-$C_{26}$) were detected in this study, where there is an even-over-odd number predominance of the homologues in all samples (Fig. 4a). However, the respective concentration of each alkanoic acid differ quantitatively among samples from different depths and of different heating duration. In the unheated raw samples, the surface *feather moss* extracts were characterized by a high content of short-chain ($<C_{20}$) fatty acids, specifically $C_{16:0}$ palmitic acid, $C_{18:0}$ stearic acid, $C_{18:1}$ oleic acid and $C_{18:2}$ linoleic acid. The relative abundance of these even-numbered fatty acids decreased at lower depths in the peat soil. This may be due to an attenuation of microbial hydrolysis activities [90] or arbuscular fungi input [91]. Long-chain ($>C_{20}$) even-numbered fatty acids are also predominant in all extracts. The majority of *feather moss* fatty acids measured in the samples were $C_{22}$, $C_{24}$ and $C_{26}$, which coincides with previously measured results of $C_{24}$ dominance in other moss types, such as *Sphagnum* [92]. The long-chain fatty acids ($>C_{20}$), on the other hand, may be from above ground plant species [93]. The decomposed peat soils contain similar amounts of long-chain fatty acids, which are likely from plant root biopolymers such as suberin [94] or from above ground epicuticular plant waxes [90].

Fatty acids were also extracted from peat soils that were heated to 300 °C for 5 min and 20 min (Fig. 4b, c). Laboratory heating data presented in Fig. 4 indicate that while variable changes of fatty acids were found, there is only a mild decrease of fatty acids regardless of chain length for soils heated for 5 min. Results show that 5 min of heating at 300 °C thermally breaks down 21%, 35%, 33% and 36% (avg. 31%) of total fatty acids for *feather moss*, peat soil 0–1 cm, peat soil 2–3 cm and peat soil 4–5 cm, respectively (Fig. 4b). The proportion of fatty acids within soils heated for 5 min fluctuates slightly (i.e. +5%, −5%, −8% and −14%) (Fig. 6). However, these changes are insufficient to eliminate peat soil hydrophobicity. After 20 min of heating to 300 °C, however, causes the thermal breakdown of 86%, 89%, 91% and 89% (avg. 89%) of the fatty acids from *feather moss*, 0–1 cm, 2–3 cm and 4–5 cm peat soil depths, respectively (Fig. 4c). The proportion of fatty acids among all organic species declined throughout heating measurements (Fig. 6). The hydrophilic tendency of peat soils after 20 min of heating is also associated with the disappearance of long-chain fatty acids ($>C_{20}$) and the significant decrease of short-chain fatty acids ($<C_{20}$). This agrees with earlier studies that demonstrated long-chain fatty acids are more susceptible to thermal degradation, and upon heating fatty acid chain length decreases [95]. We hypothesize that these long-chain fatty acids have higher degradation rates than short-chain fatty acids, and can degrade into short chain molecules in the heating process. The significant losses of these hydrophobic fatty acids (up to 89% of initial concentration) after only 20 min of heating is correlated with a return of soil hydrophilicity. This supports the hypothesis that fatty acids are critical in contributing to pre- and post-fire peat soil hydrophobicity.

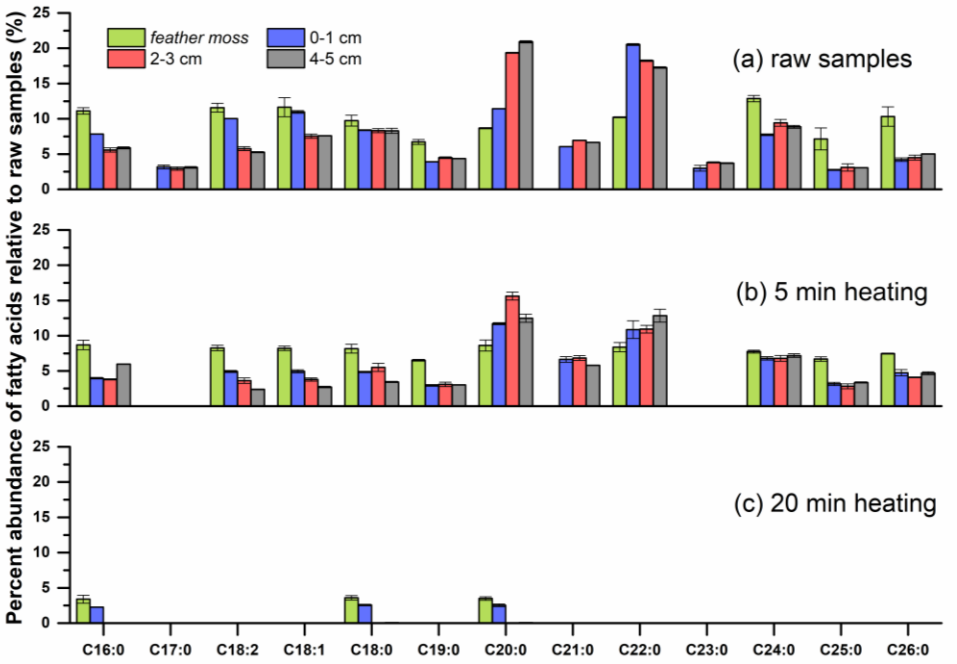


**Fig. 4.** Changes in percent abundance of fatty acids relative to raw samples under 300 °C laboratory heating for peat soils from different depth. All runs were measured in triplicates.

2.4.2.2 Polycyclic compounds

Complex polycyclic compounds were found in all extracts with variable relative abundance and are frequently found in many soils [96] including peatlands [97]. Steroids and triterpenoids were found in considerable amounts at all depths (Fig. S3a). These compounds are primarily dominated by cholesterol and *β*-sitosterol derivatives, which mainly occur in the membranes of plants and microorganisms. The presence of abundant *β*-sitosterol ($C_{29}$) may indicate plant [26] or fungi origins [91]. Other steroids such as campasterol ($C_{28}$) and α-amyrin ($C_{30}$) are also thought to be associated with vascular plants and fungi [98]. Significant amounts of dehydroabietic acid, a widely found diterpene resin acid, was also found in soil extracts and gives strong evidence to indicate microbial activity within humic acids [99]. Polycyclic compounds are typically hydrophobic

compounds. In particular, *β*-sitosterol alone and in combination with similar water-insoluble phytosterols may significantly add to soil hydrophobicity.

As shown in Fig. S3b, there was considerable degradation of polycyclic compounds in peat soils after 5 min of heating at 300 °C. 58%, 28%, 45% and 30% (avg. 40%) of polycyclic compounds were lost within *feather moss*, 0–1 cm, 2–3 cm and 4–5 cm peat soil depths, respectively. The proportion of polycyclic compounds among all organic compounds in peat soils was also measured to decrease after 5 min of heating to 300 °C (Fig. 6). The relative proportion of polycyclic compounds and fatty acids among all organic compounds for each of the 4 peat soils at 5 min heating are similar (Fig. 6), therefore it is uncertain which of these classes of compounds have a greater impact on heat-induced soil hydrophobicity. Of note, none of the polycyclic compounds were detected after 20 min heating, implying that polycyclic compounds have low heat resistance in terms of heat duration and may have been volatized during the heating process [95]. While fatty acids are usually more volatile and easier to degrade into other carbon forms, the polycyclic compounds might have lower affinity in peat soils under heating and are thus less stable in peat soils. The complete loss of these polycyclic compounds after 20 min coincides with the loss of hydrophobicity of peat soils after this amount of time at 300 °C. This may indicate that the presence of polycyclic compounds within peat soils plays a critical role in soil hydrophobicity, and their heat-induced elimination also contributes to soil hydrophilicity.

#### 2.4.2.3 Sugars

The focus of this work was to identify how peat soil hydrophilicity is impacted by the quantity of monosaccharides, disaccharides and sugar alcohols and less important to quantify the exact sugar structures. Exhaustive isolation and identification of carbohydrates from plants and soils by GC–MS is challenging. Reducing sugars of tautomeric forms in trimethylsilyl (TMS) derivatives produces many peaks that are challenging to identify [100]. Most monosaccharides such as pentoses and hexoses present two GC peaks because of their 1α- and 1β-reconfiguration of OH group on the pyrano or furano ring [101, 102], and some open-ring compounds (i.e. ketols and aldols) may present together with their cyclic isomers, making it complicated to quantify the concentrations of individual sugars [102]. Moreover, the high similarities of mass spectrometric fragments from sugars or sugar alcohols from the same groups greatly increases the ambiguity of the identified individual compound [101, 102] in the case that there is no prior knowledge of sugar retention times from sugar standards. This is the case even if sugar alcohols and anhydrosacharides do not display isomers in the chromatogram. Hence, the GC peaks were summed together, and a single value is presented in Fig. 5 for total isomeric compositions of the sugar types, i.e. $C_5H_{10}O_5$, $C_6H_{12}O_6$, etc. For additional specificity, most probable sugars are listed for certain peaks based on NIST library confidence scores.

Raw peat soil samples were found to contain various amounts of monosaccharides ($C_5$ and $C_6$), disaccharides ($C_{12}$), sugar alcohols ($C_5$-$C_7$), sugar acids ($C_4$ and $C_6$) and levoglucosan (Fig. 5a). Among them, monosaccharides and disaccharides are the most abundant compounds in the samples, which are considered to be from vegetation and

microorganisms [26]. Primary candidates for these saccharides include $C_5$ sugars (arabinose, xylose, etc.), $C_6$ sugars (glucose, mannose, fructose, etc.) and $C_{12}$ sugars (sucrose, trehalose, mannobiose, etc.). In addition, the monosaccharide abundance increases with depth whereas the disaccharide abundance decreases with depth. This may imply an increasingly prevalent oligo or polysaccharides utilization by subsurface microbes along the depth profile [103]. The ratio of $C_6/C_5$ sugar is >2, suggesting fairly important microbial contributions under the moss layer [94]. The extremely high sucrose abundance in the *feather moss* extracts agrees with the results in other studies that various moss species can uptake multiple dissolved sugars [104] and some types can most preferentially utilize sucrose to increase growth [105]. The sharp decline of total sugar content from the *feather moss* layer to the decomposed peat soils may be explained by the decrease of exogenous sugar uptake by peat moss [104]. Saccharidic polyols such as arabitol, sorbitol and pinitol are much less abundant in all measured samples [26, 106].

The sugar distribution in the samples changed markedly upon heating for 5 min producing much higher concentrations of levoglucosan (Fig. 5b). Levoglucosan is produced from burning biomass and is a pyrolysis product formed from the thermal depolymerization of structural polysaccharides, such as cellulose [107, 108]. The concentration and relative abundance of monosaccharides decrease for all measured depths, suggesting that their decomposition and volatilization from particulate organic matter occurs at the same rate. The change in disaccharide content as a function of heating, on the other hand is uncorrelated with depth, as demonstrated in Fig. 5. The disaccharide content of *feather moss* and 0–1 cm samples decreased in total content, while that of 2–

3 cm and 4–5 cm sample depths increased in total content. We speculate that these newly produced disaccharides may form from the hydrolysis of residual refractory polysaccharides found throughout the raw soil samples. The concentration of all compounds dramatically decreased (down 95%, 93%, 91% and 89% for *feather moss*, 0–1 cm, 2–3 cm and 4–5 cm peat soil, respectively) after 20 min of heating (Fig. 5c), and only small amounts of $C_5$ and $C_{12}$ sugars and levoglucosan were observed to remain. This suggests that the absolute amount of the distribution of sugars is important in governing hydrophilicity.

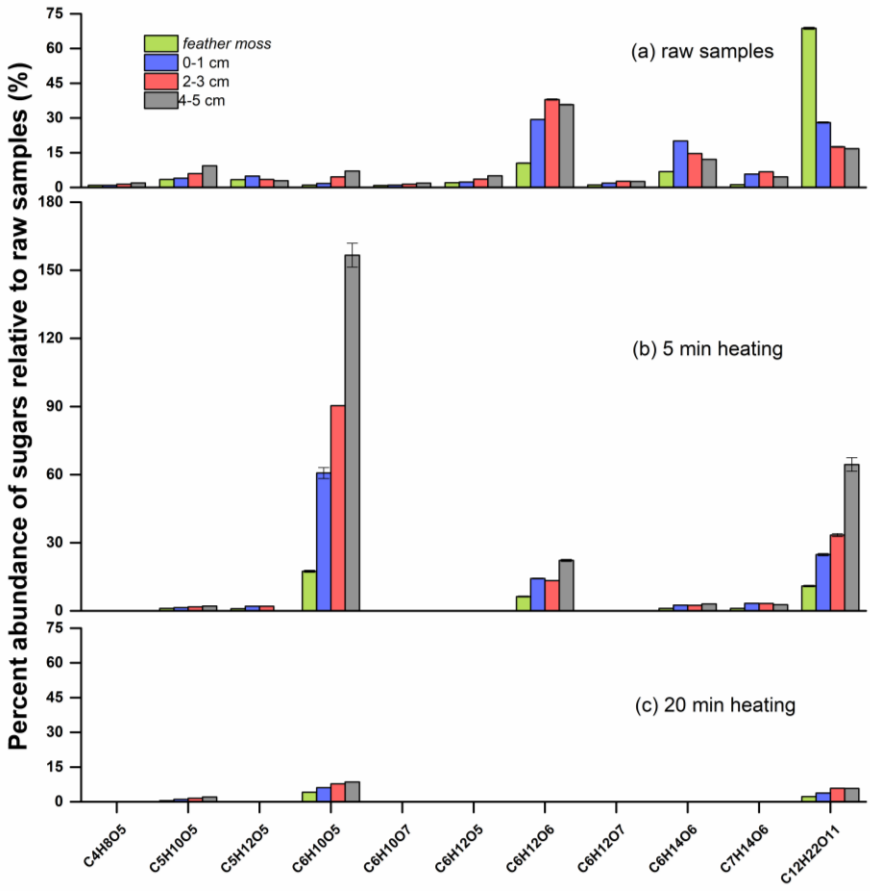


**Fig. 5.** Changes in percent abundance of sugars relative to raw samples under 300 °C laboratory heating for peat soils from different depth. All runs were measured in triplicates.

#### 2.4.2.4 Aromatic acids and short-chain molecules

As with all organic compounds studied in these peat soils, the concentration of aromatic compounds decreased with increasing heating time (Fig. S4). Interestingly, both the relative abundance of the aromatic compounds and the diversity of types of aromatic compounds increased with increased heating time. For example, we measured an increase in the number of benzoic acid derivatives carrying carbonyl, hydroxyl and methoxy groups. The production of these aromatic acids upon heating may be attributed to the combustion of polysaccharides, phenolic hydrolysis and/or depolymerization of lignin [26, 95]. The impact of this increased relative abundance and increased diversity on soil hydrophobicity was not evident, however it may have an impact on post-fire peatland recovery. It was also observed that short-chain polar molecules, such as short-chain carboxylic acids and amino acids, follow the general trend of decreasing abundance with heating at all depths.

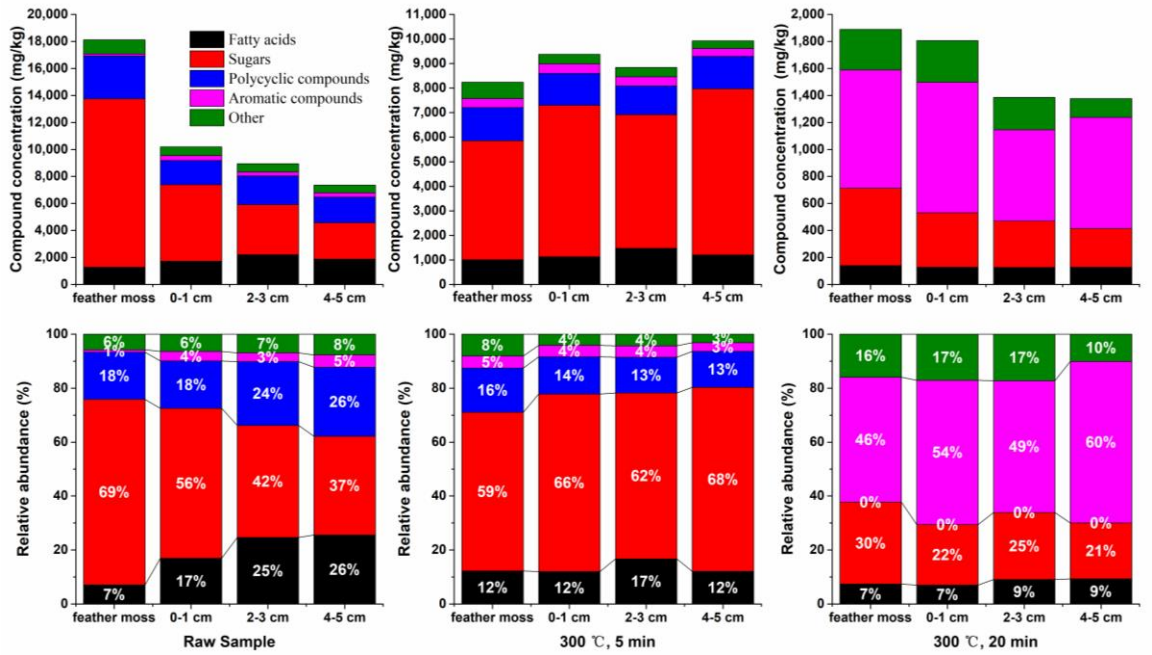


**Fig. 6.** Percent and total contents of compound groups from unheated and heated peat soil extracts for different depths.

### 2.4.3 FTIR characterization

FTIR spectra were obtained of peat soil samples heated to 300 °C for various durations to identify changes in chemical functional groups. Representative FTIR spectra are shown in Fig. 7. All the unheated peat soil samples exhibit a broad peak at 3335 $cm^{-1}$. This is ascribed to the O—H stretching vibrations [109], of carbohydrates such as cellulose. The prominent twin peaks near 2920 and 2850 $cm^{-1}$ represent the asymmetric and symmetric stretching of aliphatic hydrocarbons [110, 111], which are found in plant wax or lipids. The band occurring near 1730 $cm^{-1}$ is possibly assigned to the C═O stretching of carbonyl groups from ketones, aldehydes and organic acids [112]. The peak at 1610 $cm^{-1}$ indicates aromatic C═C stretching and asymmetric C—O stretching of carboxylic groups [111, 113], and can represent the presence of lignins, aromatic compounds or aliphatic carboxylates [109]. The small peak near 1514 $cm^{-1}$ may reflect aromatic lignin-derivatives

[114]. The small shoulders near 1420 and 1370 $cm^{-1}$ in the fingerprint region are probably caused by C—H and O—H deformations of phenolic structures, and may indicate characteristics of structural carbohydrates [115]. The light band at 1315 $cm^{-1}$ shows the $CH_2$ wagging and mainly appears in crystalline cellulose [116]. The band near 1242 $cm^{-1}$ is ascribed to the C—O stretching of phenolic OH groups [115] or represent specific structural polysaccharides such as cellulosic material [115, 117]. The small peak at 1150 $cm^{-1}$ indicates the C-O-C asymmetric stretching in cellulose and hemi-cellulose [118]. The intense peak near 1030 $cm^{-1}$ is associated with C—O stretching and confirms the presence of carbohydrate or polysaccharide structures [110, 119]. It should also be noted that despite the similarities of the transmittance bands among the different samples, slight peak variability exists due to sample composition variations resulting from the heterogeneous nature of peat soil organic matter.

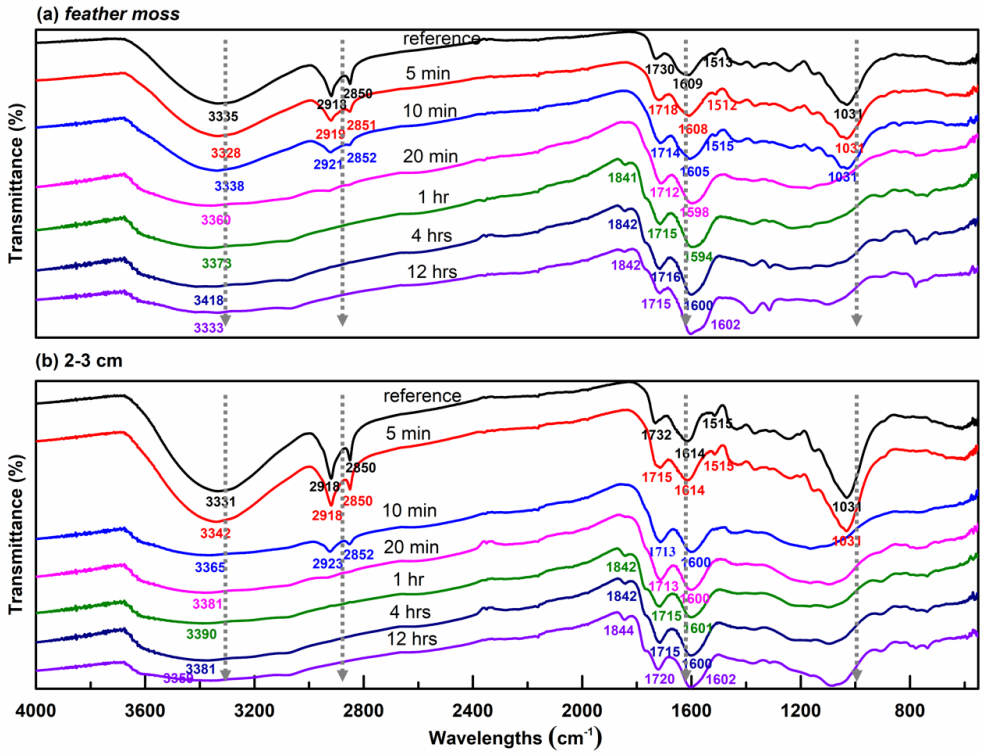


**Fig. 7.** FTIR spectra of (a) surface *feather moss* and (b) decomposed peat soils at 2-3 cm depth under 300 °C laboratory heating. Samples were oven-dried for 24 hrs in an oven at 105 °C prior to characterization and heating.

Laboratory heating was conducted for up to 12 h to comply with aforementioned typical peat fire durations. Results presented in Fig. 7 show the changes in functional groups as a function of heating time. Based on kinetic heating experiments, peat soils remain highly hydrophobic when heated <20 min. At 5 and 10 min, there are only small decrease of hydroxyl groups at 3330 $cm^{-1}$ peak, and some small decrease in the long-chain aliphatic hydrocarbons twin peaks at 2920 and 2850 $cm^{-1}$. There are more significant peak losses near 1420, 1368, 1315, 1242 and 1150 $cm^{-1}$. These peak losses likely indicate the combustion of cellulose and structural carbohydrates. Peat soil hydrophobicity has a sharp decrease at 20 min of heating. It is observed that the 3330 $cm^{-1}$ hydroxyl group becomes less intense, reflecting the persistent thermal dehydration of saccharides or polycyclic

compounds. This is also in consistency with the pronounced diminishing of signal band at 1030 $cm^{-1}$. The dramatic elimination of the twin peaks at 2920 and 2850 $cm^{-1}$ occurs especially after 20 min of heating, indicating the irreversible fragmentation of long-chain aliphatic hydrocarbons. The reduction of peaks at 3330, 2920, 2850 and 1030 $cm^{-1}$ are correlated with significant decreases in peat soil water repellency, thus we deduce that the presence of aliphatic hydrocarbons (i.e. fatty acids), saccharides and polycyclic compounds significantly contribute to peat soil hydrophobicity.

After 20 min heating, hydrophilic peat soils continue to undergo chemical transformations as observed in the FTIR spectra, however these chemical transformations do not alter their hydrophilicity. With extended heating to up to 12 h, the transmittance band at around 1730 $cm^{-1}$ is shifted to the right by approximately 15 units. It is probable that 20 min of heating thermally degraded organic constituents included hemicellulose, and that some labile organic compounds undergo chemical transformations to form new carbonyl groups [120, 121]. The peak 1610 $cm^{-1}$ is shifted slightly to lower wavenumbers during longer heating periods and this may be related to the increased proportion of aromatic structures [121]. The loss of peaks at around 1514 $cm^{-1}$ upon extended heating could reflect the degradation of free lignocellulose and humic substances [122]. Due to the complexity of organic compounds involved, it is challenging to precisely identify functional groups associated with vibrational modes within the fingerprint zone. However, the continuous attenuation of small signal bands from 1430 to 1150 $cm^{-1}$ and the elimination of many peaks in between supports the hypothesis that unstable organic compounds are thermally degraded after 20 min of heating. An additional small but sharp peak near

1842 $cm^{-1}$ appears after 1 h of heating. This might be related to the C═O stretching from newly produced cyclic carbonate groups [123, 124].

### 2.4.4 BET and SEM characterization

The specific surface area of the peat soils are summarized in Table 1. BET $N_2$ adsorption measurements of peat soil surface area was low (1.46 $m^2/g$). Heating at 300 °C for 5 min led to a slight increase in surface area (3.71 $m^2/g$), and heating for 20 min resulted in a larger surface area (11.77 $m^2/g$). The standard deviations of the acquired surface areas from multiple peat soil samples increased with extended heat duration, indicating greater structural variability with longer heating times. No attempts have been made to analyze more samples due to the poor reproducibility of specific surface areas for different heated samples. This lack of reproducibility is reflective of the inconsistent organic matter consumptions/transformations and structural changes, which are possibly related to the naturally variability of peat soils in their nano and micro surface areas, and may also be caused by variations in soil layer thickness in the heating crucibles, uneven heat conduction in the furnace, and the high sample composition heterogeneity.

**Table 1** BET surface area of the unheated and heated peat soils.

| **Sample** | **BET Surface Area ($m^2/g$)** | | |
|---|---|---|---|
| | **raw*** | **300°C, 5 min*** | **300°C, 20 min**** |
| *feather moss* | 1.51±0.72 | 6.41±5.48 | 11.54±7.76 |
| 0-1 cm | 1.50±0.72 | 2.76±2.17 | 12.42±12.33 |
| 2-3 cm | 1.45±0.60 | 2.79±0.65 | 11.22±5.77 |
| 4-5 cm | 1.38±0.70 | 2.87±1.80 | 11.90±8.54 |
| **averaged** | **1.46** | **3.71** | **11.77** |

Note: *: data calculated based on measurements of 4 different samples; **: data calculated based on measurements of 3 different samples. For burned samples, each sample was prepared by mixing three burned samples operated following the same procedure whose initial weight before heating was 0.05 g. All samples were dried in an oven at 105 °C for 24 hrs before heating treatment.

Electron microscopy images (Fig. 8) indicate the morphological structures of the unheated and 300 °C heated peat soils. While BET measurements probed nanoporous materials (d < 1000 nm), SEM was able to analyze the presence of large pores or voids (d > 1 μm). The unheated *feather moss* fragments have no observable void pores on the relatively smooth surface and no visible pores appear on the heated sample surface (Fig. 8 1a and 1b). Peat soil pulverization leads to fragmentation of original peat structures at the micro-scale (Fig. 8 1a and 1b), but has insignificant impacts on its nano-scale structures (Fig. 8 1c and 2c). High resolution SEM images of the raw *feather moss* and decomposed peat soils (without grinding) (Fig. 8 1c and 2c) further support the BET results that the *feather moss* peat soils have low nano- and microporosity. There were no discernable morphological changes (Fig. 8 2a and 2b) of deeper peat soil surface areas at the micrometer scale, suggesting that while significant chemical changes were quantified, no significant physical macroscopic changes occurred after 300 °C heating for 20 min. As expected, the small changes in BET surface area were not observable in SEM imaging.

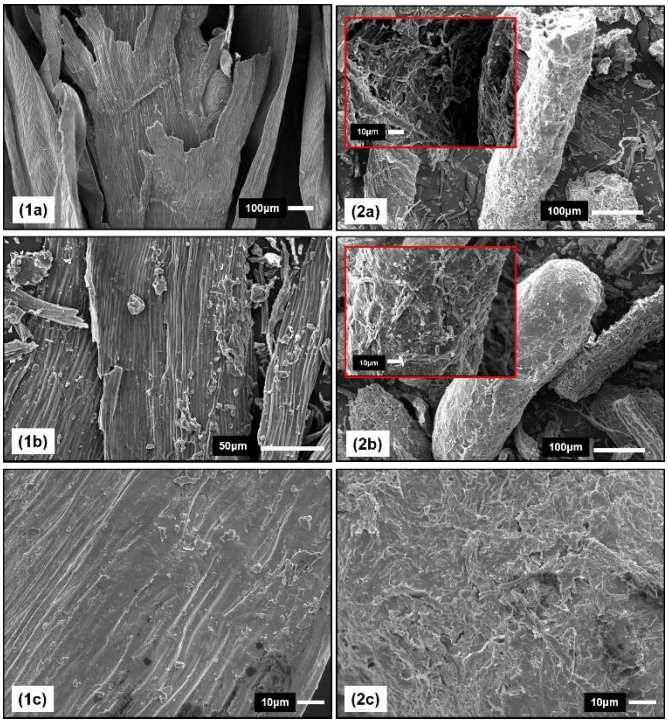


**Fig. 8.** SEM secondary electron images (SEI) of the unheated and heated peat soils: (1a) unheated *feather moss*, (1b) *feather moss* heated at 300 °C for 20min; (2a) unheated 2-3 cm peat soil (the inset zoomed in 10×), (2b) 2-3 cm peat soil heated at 300 °C for 20min (the inset zoomed in 10×); (1c) unheated *feather moss* without grinding, (2c) unheated 2-3 cm peat soil without grinding. Micrographs of 1a, 1b, 2a and 2b were operated at 10kV using a JEOL 6610LV SEM instrument, micrographs of 1c and 2c were operated at 5kV using a JEOL JSM-7000F SEM instrument.

The structural changes of peat soils are found to be minimal and therefore less likely to have an impact on the changes of soil hydrophobicity during heating processes as compared to the concurrent soil chemical changes and moisture variations. These results suggest that hydrophobicity is mostly associated with changes in the organic compound compositions. Hydrophobic organic compounds coated on peat soil particles are primarily responsible for heat-induced peat soil hydrophobicity.

## 2.5 Conclusion

This study investigated the factors controlling peat soil hydrophobicity through laboratory heating of peat soils obtained from an experimental field site in Pelican Mountain, AB,

Canada. We conclude that the hydrophobicity of boreal peat soils is primarily affected by their chemical composition, moisture content and the burning conditions to which they are subjected (temperature and exposure time). The presence of water within peats can change soil hydrophobicity by altering organic molecular arrangements in soil particles during interactions. Peat soils become hydrophobic within 5 min of heating (250 °C & 300 °C) primarily due to conformation and reorientation of organic molecules caused by water vaporization rather than organic compound combustion. Heating for longer times, however, caused soils to become hydrophilic again. This was likely due to thermal degradation/volatilization of hydrophobic fatty acids and polycyclic structured materials, the loss of which eliminated hydrophobicity. Peat soils exposed to heat can cause the fragmentation of long-chain alkyl molecules, polycyclic structured materials and hydrophilic sugars. Hydrophobic substances, especially long-chain fatty acids, are considered most significant in contributing to pre- and post-fire peat soil hydrophobicity. Degradation of organic compounds at lower temperatures (250 °C) occurred after 4.5–6 h, while those compounds degraded within only 25–30 min after heating at higher temperatures (300 °C). Peat soils are non-porous at the nanoscale (<1000 nm), and the structural changes of peat soils are found to be less significant than the chemical changes and moisture variations for the changes of soil hydrophobicity during heating processes.

As this study only considered *feather moss* peat soils and was conducted under laboratory heating conditions, this first order approximation neglects the influence that heterogeneous moss cover, changes in oxygen content, and heating gradients have on the rate of change of soil hydrophobicity. Moreover, while our findings related to fire-induced peat soil

chemical transformations and the pattern of peat soil hydrophobicity can feasibly be applied to most peat soils across the boreal peatlands, we suggest these findings be limited to boreal peatland applications. As such, we do not believe this study provides a good reference for tropical peatlands where severe peat fires have also been observed [125, 126]. Tropical peats are substantially different from boreal peat soils in their organic compositions, physical structures, and surface coverage, i.e. tropical peats typically have large amounts of course woody debris covering their surface, which resists burning [125]. We encourage a similar approach to investigating tropical peat water repellency dynamics. Further, this study did not investigate the impact of high molecular weight organic compounds, such as cellulose and lignin, which are refractory and difficult to quantify. The impact of heat and fire on these compounds will likely also have an impact on soil hydrophobicity and is worthy of further study. In particular, large pieces of plant matter were removed from the soil, and these components likely play a role in fire-induced changes to peat soil hydrophobicity.

### 2.6 Environmental significance

Global climate change is expected to increase drought and wildfire across Canada's boreal forests [58]. Changes to wildfire frequency and intensity will in turn alter peat soil chemistry. This study's first order approximations to the way field burning conditions impacts peat soils provide strong evidence that increased fire severity will have significant impacts on peat soil organic composition and distribution. In particular, we have demonstrated that changes to peat soil chemistry as a result of high temperatures and/or

longer heat exposure cause hydrophobic peat soils to become hydrophilic while losing many of the organic molecules that control peat soil water retention.

Wildfires can pose risks to boreal peatland watersheds, causing deteriorated source water quality and increased costs for drinking water supply facilities [127]. This study identifies the organic compounds likely present in peat soils before and after a forest fire. Our comprehensive chemical analysis provides an organic molecule fingerprint of the leachates (e.g. hydrophilic benzoic compounds and carboxylic acids) in the runoff that enter source waters and drinking water facilities downstream of forest fires. Knowledge of these chemical compounds and their concentrations will inform environmental assessors and water treatment operators of what compounds will be found in downstream systems after forest fires, thereby enabling them to more effectively protect source waters and implement effective treatment in drinking water treatment systems. For example, our analysis suggests that after severe fires (peat soils exposed to 300 °C heating for 20 min) aromatic compounds account for a significant proportion of organic content (> 50%) implying that runoff will also contain higher concentrations of aromatic compounds.

Further, we argue that this research may inform peat soil management and optimized fuel treatment applications. For example, tillage in agricultural and horticultural peat soils (in formerly drained peatlands) often causes discernible changes of peat soil properties, leading to reduced organic mass level and reduced water holding capacity [126, 128]. Results from our study strongly supports a focus on peatland reclamation in these managed/degraded peatlands. Peatland soil water retention and hydrophobicity likely can be regulated by controlling the organic composition of the peat soil, adjusting the rate of

irrigation, and even potentially adding post-burn peat soils to peatlands in order to modify peat soil hydrophobicity. The severity and ignition of forest fire events may also be controlled by regulating peat soil hydrophobic-hydrophilic alterations during drought cycles, effectively controlling peat soil water content. This would be especially relevant at the wildland-urban and wildland-industry interface [129]. Fuel reduction (tree removal, tree mulching) is currently a common approach to reducing wildfire risk in peatlands with high fuel loads (e.g. black spruce peatlands) [62]. Altering or controlling the organic content of peat soils could be an additional forest fuel reduction method to mitigating wildfires and smoldering [130]. We advocate for future research that explores developing organic peat soil additives/coatings to control the chemical composition, and thereby the water content, of post-burned peat soils.

Draining and burning events in boreal peatlands changes peat soil hydrophobicity, which can lead to massive environmental costs at regional scales. This research provides guidelines for when boreal peat soils become hydrophobic/hydrophilic at various forest fire temperatures. As such, this research will guide policy makers, forestry services and downstream municipalities to better estimate and predict the peatland hydrophobic transformations and consequently develop appropriate boreal landscape management strategies (e.g. fuel treatments, wetland restoration, stream restoration, etc.) to protect the wildland-society interface from the impacts of wildfire.

## 2.7 Acknowledgements

The research is funded by the CF-REF Global Water Futures program as part of the Boreal Water Futures (BWF) initiative. We would like to thank Patrick Deane and Sophie

Wilkinson in the McMaster Ecohydrology Lab for peat soil sample collection and delivery. We greatly acknowledge Jennie Kirby in Dr. Greg Slater's lab for offering GC–MS instrument and operational support, and the Canadian Centre for Electron Microscopy (CCEM) at McMaster University for providing the electron microscopy equipment.

## 2.8 References

[1] Z.C. Yu, Northern peatland carbon stocks and dynamics: a review, BIOGEOSCIENCES, 9 (2012) 4071-4085.
[2] J.R. Xu, P.J. Morris, J.G. Liu, J. Holden, Hotspots of peatland-derived potable water use identified by global analysis, NATURE SUSTAINABILITY, 1 (2018) 246-253.
[3] M. Turetsky, K. Wieder, L. Halsey, D. Vitt, Current disturbance and the diminishing peatland carbon sink, GEOPHYSICAL RESEARCH LETTERS, 29 (2002).
[4] M. Flannigan, B. Stocks, M. Turetsky, M. Wotton, Impacts of climate change on fire activity and fire management in the circumboreal forest, GLOBAL CHANGE BIOLOGY, 15 (2009) 549-560.
[5] M.D. Flannigan, K.A. Logan, B.D. Amiro, W.R. Skinner, B.J. Stocks, Future area burned in Canada, CLIMATIC CHANGE, 72 (2005) 1-16.
[6] J.W. Harden, S.E. Trumbore, B.J. Stocks, A. Hirsch, S.T. Gower, K.P. O'Neill, E.S. Kasischke, The role of fire in the boreal carbon budget, GLOBAL CHANGE BIOLOGY, 6 (2000) 174-184.
[7] M.R. Turetsky, E.S. Kane, J.W. Harden, R.D. Ottmar, K.L. Manies, E. Hoy, E.S. Kasischke, Recent acceleration of biomass burning and carbon losses in Alaskan forests and peatlands, NATURE GEOSCIENCE, 4 (2011) 27-31.
[8] G. Certini, Effects of fire on properties of forest soils: a review, OECOLOGIA, 143 (2005) 1-10.
[9] L.F. DeBano, Water repellent soils: a state-of-the-art, USDA Forest Service, 1981.
[10] L. DeBano, Water repellency in soils: a historical overview, Journal of hydrology, 231 (2000) 4-32.
[11] S.H. Doerr, W.H. Blake, R.A. Shakesby, F. Stagnitti, S.H. Vuurens, G.S. Humphreys, P. Wallbrink, Heating effects on water repellency in Australian eucalypt forest soils and their value in estimating wildfire soil temperatures, INTERNATIONAL JOURNAL OF WILDLAND FIRE, 13 (2004) 157-163.
[12] N. Kettridge, R.E. Humphrey, J.E. Smith, M.C. Lukenbach, K.J. Devito, R.M. Petrone, J.M. Waddington, Burned and unburned peat water repellency: Implications for peatland evaporation following wildfire, JOURNAL OF HYDROLOGY, 513 (2014) 335-341.
[13] S.A. Lewis, J.Q. Wu, P.R. Robichaud, Assessing burn severity and comparing soil water repellency, Hayman Fire, Colorado, HYDROLOGICAL PROCESSES, 20 (2006) 1-16.
[14] M.E. Varela, E. Benito, E. de Blas, Impact of wildfires on surface water repellency in soils of northwest Spain, HYDROLOGICAL PROCESSES, 19 (2005) 3649-3657.

[15] L.M. Zavala, A.J.P. Granged, A. Jordan, G. Barcenas-Moreno, Effect of burning temperature on water repellency and aggregate stability in forest soils under laboratory conditions, GEODERMA, 158 (2010) 366-374.
[16] E. Hewelke, J. Szatylowicz, T. Gnatowski, R. Oleszczuk, Effects of Soil Water Repellency on Moisture Patterns in a Degraded Sapric Histosol, LAND DEGRADATION & DEVELOPMENT, 27 (2016) 955-964.
[17] N. Kettridge, M.C. Lukenbach, K.J. Hokanson, K.J. Devito, R.M. Petrone, C.A. Mendoza, J.M. Waddington, Severe wildfire exposes remnant peat carbon stocks to increased post-fire drying, SCIENTIFIC REPORTS, 9 (2019).
[18] N. Kettridge, M.C. Lukenbach, K.J. Hokanson, C. Hopkinson, K.J. Devito, R.M. Petrone, C.A. Mendoza, J.M. Waddington, Low Evapotranspiration Enhances the Resilience of Peatland Carbon Stocks to Fire, GEOPHYSICAL RESEARCH LETTERS, 44 (2017) 9341-9349.
[19] M.C. Lukenbach, K.J. Devito, N. Kettridge, R.M. Petrone, J.M. Waddington, Burn severity alters peatland moss water availability: implications for post-fire recovery, ECOHYDROLOGY, 9 (2016) 341-353.
[20] H.W. Chau, A. Biswas, V. Vujanovic, B.C. Si, Relationship between the severity, persistence of soil water repellency and the critical soil water content in water repellent soils, GEODERMA, 221 (2014) 113-120.
[21] S.H. Doerr, R.A. Shakesby, W.H. Blake, C.J. Chafer, G.S. Humphreys, P.J. Wallbrink, Effects of differing wildfire severities on soil wettability and implications for hydrological response, JOURNAL OF HYDROLOGY, 319 (2006) 295-311.
[22] S.H. Doerr, R.A. Shakesby, R.P.D. Walsh, Soil water repellency: its causes, characteristics and hydro-geomorphological significance, EARTH-SCIENCE REVIEWS, 51 (2000) 33-65.
[23] A. Jordan, L. Martinez-Zavala, N. Bellinfante, Heterogeneity in soil hydrological response from different land cover types in southern Spain, CATENA, 74 (2008) 137-143.
[24] J. Holden, Peatland hydrology and carbon release: why small-scale process matters, PHILOSOPHICAL TRANSACTIONS OF THE ROYAL SOCIETY A-MATHEMATICAL PHYSICAL AND ENGINEERING SCIENCES, 363 (2005) 2891-2913.
[25] M.R. Turetsky, B. Benscoter, S. Page, G. Rein, G.R. van der Werf, A. Watts, Global vulnerability of peatlands to fire and carbon loss, NATURE GEOSCIENCE, 8 (2015) 11-14.
[26] I. Atanassova, S.H. Doerr, Organic compounds of different extractability in total solvent extracts from soils of contrasting water repellency, EUROPEAN JOURNAL OF SOIL SCIENCE, 61 (2010) 298-313.
[27] K.A. Mainwaring, C.P. Morley, S.H. Doerr, P. Douglas, C.T. Llewellyn, G. Llewellyn, I. Matthews, B.K. Stein, Role of heavy polar organic compounds for water repellency of sandy soils, ENVIRONMENTAL CHEMISTRY LETTERS, 2 (2004) 35-39.
[28] E.B. Rueda, M. Rodriguez-Alleres, E.V. Teijeiro, Environmental Factors Governing Soil Water Repellency Dynamics in a Pinus Pinaster Plantation in NW Spain, LAND DEGRADATION & DEVELOPMENT, 27 (2016) 719-728.
[29] L.W. Dekker, S.H. Doerr, K. Oostindie, A.K. Ziogas, C.J. Ritsema, Water repellency and critical soil water content in a dune sand, SOIL SCIENCE SOCIETY OF AMERICA JOURNAL, 65 (2001) 1667-1674.
[30] N. Tessler, L. Wittenberg, N. Greenbaum, Soil water repellency persistence after recurrent forest fires on Mount Carmel, Israel, INTERNATIONAL JOURNAL OF WILDLAND FIRE, 22 (2013) 515-526.
[31] E. de Blas, M. Rodriguez-Alleres, G. Almendros, Speciation of lipid and humic fractions in soils under pine and eucalyptus forest in northwest Spain and its effect on water repellency, GEODERMA, 155 (2010) 242-248.

[32] N.T. Jimenez-Morillo, J.E. Spangenberg, A.Z. Miller, A. Jordan, L.M. Zavala, F.J. Gonzalez-Vila, J.A. Gonzalez-Perez, Wildfire effects on lipid composition and hydrophobicity of bulk soil and soil size fractions under Quercus suber cover (SW-Spain), ENVIRONMENTAL RESEARCH, 159 (2017) 394-405.
[33] D.F. Scott, Soil wettability in forested catchments in South Africa; as measured by different methods and as affected by vegetation cover and soil characteristics, JOURNAL OF HYDROLOGY, 231 (2000) 87-104.
[34] X.Y. Wang, Y. Zhao, R. Horn, Soil Wettability as Affected by Soil Characteristics and Land Use, PEDOSPHERE, 20 (2010) 43-54.
[35] J. Poulenard, J.C. Michel, F. Bartoli, J.M. Portal, P. Podwojewski, Water repellency of volcanic ash soils from Ecuadorian paramo: effect of water content and characteristics of hydrophobic organic matter, EUROPEAN JOURNAL OF SOIL SCIENCE, 55 (2004) 487-496.
[36] E.S. Vogelmann, J.M. Reichert, J. Prevedello, C.O.B. Consensa, A.E. Oliveira, G.O. Awe, J. Mataix-Solera, Threshold water content beyond which hydrophobic soils become hydrophilic: The role of soil texture and organic matter content, GEODERMA, 209 (2013) 177-187.
[37] J.F. Mao, K.G.J. Nierop, M. Rietkerk, J.S.S. Damste, S.C. Dekker, The influence of vegetation on soil water repellency-markers and soil hydrophobicity, SCIENCE OF THE TOTAL ENVIRONMENT, 566 (2016) 608-620.
[38] M.O. Goebel, J. Bachmann, M. Reichstein, I.A. Janssens, G. Guggenberger, Soil water repellency and its implications for organic matter decomposition - is there a link to extreme climatic events?, GLOBAL CHANGE BIOLOGY, 17 (2011) 2640-2656.
[39] S.H. Doerr, A.D. Thomas, The role of soil moisture in controlling water repellency: new evidence from forest soils in Portugal, JOURNAL OF HYDROLOGY, 231 (2000) 134-147.
[40] N.T. Jimenez-Morillo, J.A. Gonzalez-Perez, A. Jordan, L.M. Zavala, J.M. de la Rosa, M.A. Jimenez-Gonzalez, F.J. Gonzalez-Vila, Organic Matter Fractions Controlling Soil Water Repellency in Sandy Soils From the Doñana National Park (Southwestern Spain), LAND DEGRADATION & DEVELOPMENT, 27 (2016) 1413-1423.
[41] A. Lachacz, M. Nitkiewicz, B. Kalisz, Water repellency of post-boggy soils with a various content of organic matter, BIOLOGIA, 64 (2009) 634-638.
[42] M. Orzechowski, S. Smólczynski, P. Sowinski, B. Rybinska, Water repellency of soils with various content of organic matter in north-eastern Poland, Soil Science Annual, 64 (2013) 30.
[43] P.A. Moore, M.C. Lukenbach, N. Kettridge, R.M. Petrone, K.J. Devito, J.M. Waddington, Peatland water repellency: Importance of soil water content, moss species, and burn severity, JOURNAL OF HYDROLOGY, 554 (2017) 656-665.
[44] K. Berglund, L. Persson, Water repellence of cultivated organic soils, ACTA AGRICULTURAE SCANDINAVICA SECTION B-SOIL AND PLANT SCIENCE, 46 (1996) 145-152.
[45] J.A. O'Donnell, M.R. Turetsky, J.W. Harden, K.L. Manies, L.E. Pruett, G. Shetler, J.C. Neff, Interactive Effects of Fire, Soil Climate, and Moss on CO2 Fluxes in Black Spruce Ecosystems of Interior Alaska, ECOSYSTEMS, 12 (2009) 57-72.
[46] L.F. DeBano, The role of fire and soil heating on water repellency in wildland environments: a review, JOURNAL OF HYDROLOGY, 231 (2000) 195-206.
[47] L.F. Debano, J. Krammes, Water repellent soils and their relation to wildfire temperatures, Hydrological Sciences Journal, 11 (1966) 14-19.
[48] A.J.P. Granged, A. Jordan, L.M. Zavala, M. Munoz-Rojas, J. Mataix-Solera, Short-term effects of experimental fire for a soil under eucalyptus forest (SE Australia), GEODERMA, 167-68 (2011) 125-134.

[49] P.R. Robichaud, R.D. Hungerford, Water repellency by laboratory burning of four northern Rocky Mountain forest soils, JOURNAL OF HYDROLOGY, 231 (2000) 207-219.
[50] R. Bryant, S.H. Doerr, M. Helbig, Effect of oxygen deprivation on soil hydrophobicity during heating, INTERNATIONAL JOURNAL OF WILDLAND FIRE, 14 (2005) 449-455.
[51] E.V. Ponomarenko, D.W. Anderson, Importance of charred organic matter in Black Chernozem soils of Saskatchewan, CANADIAN JOURNAL OF SOIL SCIENCE, 81 (2001) 285-297.
[52] S. Savage, Mechanism of fire-induced water repellency in soil, Soil Science Society of America Journal, 38 (1974) 652-657.
[53] S.M. Savage, C. Heaton, J. Osborn, J. Letey, Substances Contributing to Fire-Induced Water Repellency in Soils, SOIL SCIENCE SOCIETY OF AMERICA PROCEEDINGS, 36 (1972) 674-&.
[54] C.M.M. Franco, P.J. Clarke, M.E. Tate, J.M. Oades, Hydrophobic properties and chemical characterisation of natural water repellent materials in Australian sands, JOURNAL OF HYDROLOGY, 231 (2000) 47-58.
[55] L. DeBano, S. Savage, D. Hamilton, The transfer of heat and hydrophobic substances during burning, Soil Science Society of America Journal, 40 (1976) 779-782.
[56] J.C. Neff, J.W. Harden, G. Gleixner, Fire effects on soil organic matter content, composition, and nutrients in boreal interior Alaska, CANADIAN JOURNAL OF FOREST RESEARCH, 35 (2005) 2178-2187.
[57] G. Rein, N. Cleaver, C. Ashton, P. Pironi, J.L. Torero, The severity of smouldering peat fires and damage to the forest soil, CATENA, 74 (2008) 304-309.
[58] M.C. Elmes, D.K. Thompson, J.S. Price, Changes to the hydrophysical properties of upland and riparian soils in a burned fen watershed in the Athabasca Oil Sands Region, northern Alberta, Canada, CATENA, 181 (2019).
[59] J.G. Cawson, P. Nyman, H.G. Smith, P.N.J. Lane, G.J. Sheridan, How soil temperatures during prescribed burning affect soil water repellency, infiltration and erosion, GEODERMA, 278 (2016) 12-22.
[60] C.R. Stoof, D. Moore, C.J. Ritsema, L.W. Dekker, Natural and Fire-Induced Soil Water Repellency in a Portuguese Shrubland, SOIL SCIENCE SOCIETY OF AMERICA JOURNAL, 75 (2011) 2283-2295.
[61] F. Rezanezhad, J.S. Price, W.L. Quinton, B. Lennartz, T. Milojevic, P. Van Cappellen, Structure of peat soils and implications for water storage, flow and solute transport: A review update for geochemists, CHEMICAL GEOLOGY, 429 (2016) 75-84.
[62] S.L. Wilkinson, P.A. Moore, D.K. Thompson, B.M. Wotton, S. Hvenegaard, D. Schroeder, J.M. Waddington, The effects of black spruce fuel management on surface fuel condition and peat burn severity in an experimental fire, CANADIAN JOURNAL OF FOREST RESEARCH, 48 (2018) 1433-1440.
[63] M.K. Nungesser, Modelling microtopography in boreal peatlands: hummocks and hollows, ECOLOGICAL MODELLING, 165 (2003) 175-207.
[64] R. Pouliot, L. Rochefort, E. Karofeld, Initiation of microtopography in re-vegetated cutover peatlands: evolution of plant species composition, APPLIED VEGETATION SCIENCE, 15 (2012) 369-382.
[65] D.J. Kroetsch, X.Y. Geng, S.X. Chang, D.D. Saurette, Organic soils of Canada: Part 1. Wetland Organic soils, CANADIAN JOURNAL OF SOIL SCIENCE, 91 (2011) 807-822.
[66] S. Natalia, V.J. Lieffers, S.M. Landhäusser, Effects of leaf litter on the growth of boreal feather mosses: implication for forest floor development, Journal of vegetation science, 19 (2008) 253-260.

[67] J.M. Aznar, J.A. Gonzalez-Perez, D. Badia, C. Marti, At What Depth Are The Properties of a Gypseous Forest Topsoil Affected By Burning?, LAND DEGRADATION & DEVELOPMENT, 27 (2016) 1344-1353.
[68] L.W. de Jonge, O.H. Jacobsen, P. Moldrup, Soil water repellency: Effects of water content, temperature, and particle size, SOIL SCIENCE SOCIETY OF AMERICA JOURNAL, 63 (1999) 437-442.
[69] L.W. Dekker, C.J. Ritsema, Variation in water content and wetting patterns in Dutch water repellent peaty clay and clayey peat soils, CATENA, 28 (1996) 89-105.
[70] L.W. Dekker, C.J. Ritsema, K. Oostindie, O.H. Boersma, Effect of drying temperature on the severity of soil water repellency, SOIL SCIENCE, 163 (1998) 780-796.
[71] T.E. Redding, K.J. Devito, Particle densities of wetland soils in northern Alberta, Canada, CANADIAN JOURNAL OF SOIL SCIENCE, 86 (2006) 57-60.
[72] S.H. Doerr, On standardizing the 'water drop penetration time'and the 'molarity of an ethanol droplet'techniques to classify soil hydrophobicity: a case study using medium textured soils, Earth Surface Processes and Landforms: The Journal of the British Geomorphological Group, 23 (1998) 663-668.
[73] E.B.A. Bisdom, L.W. Dekker, J.F.T. Schoute, Water repellency of sieve fractions from sandy soils and relationships with organic material and soil structure, GEODERMA, 56 (1993) 105-118.
[74] L. Martinez-Zavala, A. Jordan-Lopez, Influence of different plant species on water repellency in Mediterranean heathland soils, CATENA, 76 (2009) 215-223.
[75] S.Y. Cheng, S.H. Doerr, R. Bryant, C.J. Wright, Effects of Isopropanol/Ammonia Extraction on Soil Water Repellency as Determined by Atomic Force Microscopy, SOIL SCIENCE SOCIETY OF AMERICA JOURNAL, 74 (2010) 1541-1552.
[76] J.L. Roy, W.B. McGill, Flexible conformation in organic matter coatings: An hypothesis about soil water repellency, CANADIAN JOURNAL OF SOIL SCIENCE, 80 (2000) 143-152.
[77] C.T. Llewellyn, S.H. Doerr, P. Douglas, C.P. Morley, K.A. Mainwaring, Soxhlet extraction of organic compounds associated with soil water repellency, ENVIRONMENTAL CHEMISTRY LETTERS, 2 (2004) 41-44.
[78] S.H. Doerr, C.T. Llewellyn, P. Douglas, C.P. Morley, K.A. Mainwaring, C. Haskins, L. Johnsey, C.J. Ritsema, F. Stagnitti, G. Allinson, A.J.D. Ferreira, J.J. Keizer, A.K. Ziogas, J. Diamantisf, Extraction of compounds associated with water repellency in sandy soils of different origin, AUSTRALIAN JOURNAL OF SOIL RESEARCH, 43 (2005) 225-237.
[79] M. Ma'Shum, M. Tate, G. Jones, J. Oades, Extraction and characterization of water–repellent materials from Australian soils, Journal of Soil Science, 39 (1988) 99-110.
[80] K. Taumer, H. Stoffregen, G. Wessolek, Determination of repellency distribution using soil organic matter and water content, GEODERMA, 125 (2005) 107-115.
[81] L.W. Dekker, C.J. Ritsema, How water moves in a water repellent sandy soil: 1. Potential and actual water repellency, Water Resources Research, 30 (1994) 2507-2517.
[82] M. Mashum, V.C. Farmer, ORIGIN AND ASSESSMENT OF WATER REPELLENCY OF A SANDY SOUTH AUSTRALIAN SOIL, AUSTRALIAN JOURNAL OF SOIL RESEARCH, 23 (1985) 623-626.
[83] D.J. Horne, J.C. McIntosh, Hydrophobic compounds in sands in New Zealand - extraction, characterisation and proposed mechanisms for repellency expression, JOURNAL OF HYDROLOGY, 231 (2000) 35-46.
[84] X.Y. Huang, G. Rein, Downward spread of smouldering peat fire: the role of moisture, density and oxygen supply, INTERNATIONAL JOURNAL OF WILDLAND FIRE, 26 (2017) 907-918.

[85] G.M. Davies, A. Gray, G. Rein, C.J. Legg, Peat consumption and carbon loss due to smouldering wildfire in a temperate peatland, FOREST ECOLOGY AND MANAGEMENT, 308 (2013) 169-177.
[86] S.R. Lin, P.Y. Sun, X.Y. Huang, Can peat soil support a flaming wildfire?, INTERNATIONAL JOURNAL OF WILDLAND FIRE, 28 (2019) 601-613.
[87] N.H. Abu-Hamdeh, R.C. Reeder, Soil thermal conductivity: Effects of density, moisture, salt concentration, and organic matter, SOIL SCIENCE SOCIETY OF AMERICA JOURNAL, 64 (2000) 1285-1290.
[88] D. Badia, S. Lopez-Garcia, C. Marti, O. Ortiz-Perpina, A. Girona-Garcia, J. Casanova-Gascon, Burn effects on soil properties associated to heat transfer under contrasting moisture content, SCIENCE OF THE TOTAL ENVIRONMENT, 601 (2017) 1119-1128.
[89] G.S. Campbell, J.D. Jungbauer, W.R. Bidlake, R.D. Hungerford, PREDICTING THE EFFECT OF TEMPERATURE ON SOIL THERMAL-CONDUCTIVITY, SOIL SCIENCE, 158 (1994) 307-313.
[90] K. Quenea, C. Largeau, S. Derenne, R. Spaccini, G. Bardoux, A. Mariotti, Molecular and isotopic study of lipids in particle size fractions of a sandy cultivated soil (Cestas cultivation sequence, southwest France): Sources, degradation, and comparison with Cestas forest soil, ORGANIC GEOCHEMISTRY, 37 (2006) 20-44.
[91] D.F.W. Naafs, P.F. van Bergen, S.J. Boogert, J.W. de Leeuw, Solvent-extractable lipids in an acid andic forest soil; variations with depth and season, SOIL BIOLOGY & BIOCHEMISTRY, 36 (2004) 297-308.
[92] M. Baas, R. Pancost, B. van Geel, J.S.S. Damste, A comparative study of lipids in Sphagnum species, ORGANIC GEOCHEMISTRY, 31 (2000) 535-541.
[93] G. Almendros, J. Sanz, F. Velasco, Signatures of lipid assemblages in soils under continental Mediterranean forests, EUROPEAN JOURNAL OF SOIL SCIENCE, 47 (1996) 183-196.
[94] K.G.J. Nierop, P. Buurman, Composition of soil organic matter and its water-soluble fraction under young vegetation on drift sand, central Netherlands, EUROPEAN JOURNAL OF SOIL SCIENCE, 49 (1998) 605-615.
[95] I. Atanassova, S.H. Doerr, Changes in soil organic compound composition associated with heat-induced increases in soil water repellency, EUROPEAN JOURNAL OF SOIL SCIENCE, 62 (2011) 516-532.
[96] D.F.W. Naafs, P.F. van Bergen, M.A. de Jong, A. Oonincx, J.W. de Leeuw, Total lipid extracts from characteristic soil horizons in a podzol profile, EUROPEAN JOURNAL OF SOIL SCIENCE, 55 (2004) 657-669.
[97] A. Ramata-Stunda, Z. Petrina, P. Mekss, G. Kizane, B. Silamikele, I. Muiznieks, V. Nikolajeva, Microbiological characterization and sterilization-induced changes in the profile of the hydrophobic organic substances in Latvian balneological peat, INTERNATIONAL JOURNAL OF ENVIRONMENTAL SCIENCE AND TECHNOLOGY, 12 (2015) 2371-2380.
[98] N.J. Day, K.E. Dunfield, J.F. Johnstone, M.C. Mack, M.R. Turetsky, X.J. Walker, A.L. White, J.L. Baltzer, Wildfire severity reduces richness and alters composition of soil fungal communities in boreal forests of western Canada, Global change biology, 25 (2019) 2310-2324.
[99] K. Lehtonen, K. Hanninen, M. Ketola, Structurally bound lipids in peat humic acids, ORGANIC GEOCHEMISTRY, 32 (2001) 33-43.
[100] M.L. Sanz, M. Diez-Barrio, J. Sanz, I. Martinez-Castro, GC Behavior of disaccharide trimethylsilyl oximes, JOURNAL OF CHROMATOGRAPHIC SCIENCE, 41 (2003) 205-208.
[101] B. Mechri, M. Tekaya, H. Cheheb, M. Hammami, Determination of Mannitol Sorbitol and Myo-Inositol in Olive Tree Roots and Rhizospheric Soil by Gas Chromatography and Effect of

Severe Drought Conditions on Their Profiles, JOURNAL OF CHROMATOGRAPHIC SCIENCE, 53 (2015) 1631-1638.
[102] P.M. Medeiros, B.R.T. Simoneit, Analysis of sugars in environmental samples by gas chromatography-mass spectrometry, JOURNAL OF CHROMATOGRAPHY A, 1141 (2007) 271-278.
[103] X. Lin, M.M. Tfaily, S.J. Green, J.M. Steinweg, P. Chanton, A. Imvittaya, J.P. Chanton, W. Cooper, C. Schadt, J.E. Kostka, Microbial Metabolic Potential for Carbon Degradation and Nutrient (Nitrogen and Phosphorus) Acquisition in an Ombrotrophic Peatland, APPLIED AND ENVIRONMENTAL MICROBIOLOGY, 80 (2014) 3531-3540.
[104] R.G. Jorgensen, G.M. Richter, Composition of carbon fractions and potential denitrification in drained peat soils, JOURNAL OF SOIL SCIENCE, 43 (1992) 347-358.
[105] L.E. Graham, E. Kim, P. Arancibia-Avila, J.M. Graham, L.W. Wilcox, Evolutionary and ecophysiological significance of sugar utilization by the peat moss Sphagnum compactum (Sphagnaceae) and the common charophycean associates Cylindrocystis brebissonii and Mougeotia sp. (Zygnemataceae), AMERICAN JOURNAL OF BOTANY, 97 (2010) 1485-1491.
[106] A. Caseiro, I.L. Marr, M. Claeys, A. Kasper-Giebl, H. Puxbaum, C.A. Pio, Determination of saccharides in atmospheric aerosol using anion-exchange high-performance liquid chromatography and pulsed-amperometric detection, JOURNAL OF CHROMATOGRAPHY A, 1171 (2007) 37-45.
[107] X.L. Bai, R.C. Brown, Modeling the physiochemistry of levoglucosan during cellulose pyrolysis, JOURNAL OF ANALYTICAL AND APPLIED PYROLYSIS, 105 (2014) 363-368.
[108] E.C. Hopmans, R.A.L. dos Santos, A. Mets, J.S.S. Damste, S. Schouten, A novel method for the rapid analysis of levoglucosan in soils and sediments, ORGANIC GEOCHEMISTRY, 58 (2013) 86-88.
[109] R.R.E. Artz, S.J. Chapman, A.H.J. Robertson, J.M. Potts, F. Laggoun-Defarge, S. Gogo, L. Comont, J.R. Disnar, A.J. Francez, FTIR spectroscopy can be used as a screening tool for organic matter quality in regenerating cutover peatlands, SOIL BIOLOGY & BIOCHEMISTRY, 40 (2008) 515-527.
[110] C. Cocozza, V. D'Orazio, T.M. Miano, W. Shotyk, Characterization of solid and aqueous phases of a peat bog profile using molecular fluorescence spectroscopy, ESR and FT-IR, and comparison with physical properties, ORGANIC GEOCHEMISTRY, 34 (2003) 49-60.
[111] J. Niemeyer, Y. Chen, J.M. Bollag, Characterization of Humic Acids, Composts, and Peat by Diffuse Reflectance Fourier-Transform Infrared Spectroscopy, SOIL SCIENCE SOCIETY OF AMERICA JOURNAL, 56 (1992) 135-140.
[112] M.M. Tfaily, W.T. Cooper, J.E. Kostka, P.R. Chanton, C.W. Schadt, P.J. Hanson, C.M. Iversen, J.P. Chanton, Organic matter transformation in the peat column at Marcell Experimental Forest: Humification and vertical stratification, JOURNAL OF GEOPHYSICAL RESEARCH-BIOGEOSCIENCES, 119 (2014) 661-675.
[113] L.P.C. Romao, J.R. Lead, J.C. Rocha, L.C. de Oliveira, A.H. Rosa, A.G.R. Mendonca, A. de Souza Ribeiro, Structure and properties of Brazilian peat: Analysis by Spectroscopy and Microscopy, JOURNAL OF THE BRAZILIAN CHEMICAL SOCIETY, 18 (2007) 714-720.
[114] V. Maksimova, L. Klavina, O. Bikovens, A. Zicmanis, O. Purmalis, Structural Characterization and Chemical Classification of Some Bryophytes Found in Latvia, CHEMISTRY & BIODIVERSITY, 10 (2013) 1284-1294.
[115] L. Gandois, A.R. Cobb, I.C. Hei, L.B.L. Lim, K. Abu Salim, C.F. Harvey, Impact of deforestation on solid and dissolved organic matter characteristics of tropical peat forests: implications for carbon release, BIOGEOCHEMISTRY, 114 (2013) 183-199.

[116] C.M. Popescu, M.C. Popescu, G. Singurel, C. Vasile, D.S. Argyropoulos, S. Willfor, Spectral characterization of eucalyptus wood, APPLIED SPECTROSCOPY, 61 (2007) 1168-1177.
[117] P.Q. Yu, H. Block, Z. Niu, K. Doiron, Rapid characterization of molecular chemistry, nutrient make-up and microlocation of internal seed tissue, JOURNAL OF SYNCHROTRON RADIATION, 14 (2007) 382-390.
[118] M. Traore, J. Kaal, A.M. Cortizas, Differentiation between pine woods according to species and growing location using FTIR-ATR, WOOD SCIENCE AND TECHNOLOGY, 52 (2018) 487-504.
[119] F. Girardello, R. Guegan, V.I. Esteves, I.J.R. Baumvol, M.M.D. Sierra, J.S. Crespo, A.N. Fernandes, M. Giovanela, Characterization of Brazilian Peat Samples by Applying a Multimethod Approach, SPECTROSCOPY LETTERS, 46 (2013) 201-210.
[120] R.A. Kotilainen, T.J. Toivanen, R.J. Alen, FTIR monitoring of chemical changes in softwood during heating, JOURNAL OF WOOD CHEMISTRY AND TECHNOLOGY, 20 (2000) 307-320.
[121] I. Simkovic, P. Dlapa, S.H. Doerr, J. Mataix-Solera, V. Sasinkova, Thermal destruction of soil water repellency and associated changes to soil organic matter as observed by FTIR spectroscopy, CATENA, 74 (2008) 205-211.
[122] E. Smidt, K.U. Eckhardt, P. Lechner, H.R. Schulten, P. Leinweber, Characterization of different decomposition stages of biowaste using FT-IR spectroscopy and pyrolysis-field ionization mass spectrometry, BIODEGRADATION, 16 (2005) 67-79.
[123] W.M. Doane, B.S. Shasha, E.I. Stout, C.R. Russell, C.E. Rist, Reaction of starch with carbohydrate trans-carbonates, CARBOHYDRATE RESEARCH, 8 (1968) 266-&.
[124] W. Doane, B. Shasha, E. Stout, C. Russell, C. Rist, A facile route to trans cyclic carbonates of sugars, Carbohydrate Research, 4 (1967) 445-451.
[125] T. Hirano, K. Kusin, S. Limin, M. Osaki, Carbon dioxide emissions through oxidative peat decomposition on a burnt tropical peatland, GLOBAL CHANGE BIOLOGY, 20 (2014) 555-565.
[126] J. Jauhiainen, S.E. Page, H. Vasander, Greenhouse gas dynamics in degraded and restored tropical peatlands, MIRES AND PEAT, 17 (2016).
[127] F.N. Robinne, K.D. Bladon, U. Silins, M.B. Emelko, M.D. Flannigan, M.A. Parisien, X.L. Wang, S.W. Kienzle, D.P. Dupont, A Regional-Scale Index for Assessing the Exposure of Drinking-Water Sources to Wildfires, FORESTS, 10 (2019).
[128] D.W. Hallema, J.A. Lafond, Y. Périard, S.J. Gumiere, G. Sun, J. Caron, Long-term effects of peatland cultivation on soil physical and hydraulic properties: Case study in Canada, Vadose Zone Journal, 14 (2015) vzj2014. 2010.0147.
[129] F.N. Robinne, K.D. Bladon, C. Miller, M.A. Parisien, J. Mathieu, M.D. Flannigan, A spatial evaluation of global wildfire-water risks to human and natural systems, SCIENCE OF THE TOTAL ENVIRONMENT, 610 (2018) 1193-1206.
[130] K. Hirsch, V. Kafka, C. Tymstra, R. McAlpine, B. Hawkes, H. Stegehuis, S. Quintilio, S. Gauthier, K. Peck, Fire-smart forest management: A pragmatic approach to sustainable forest management in fire-dominated ecosystems, FORESTRY CHRONICLE, 77 (2001) 357-363.

# Chapter 3

## Assessing leached TOC, nutrients and phenols from peatland soils after lab-simulated wildfires: Implications to source water protection

## 3.1 Abstract

Pollutant leaching from wildfire-impacted peatland soils (peat) is well-known, but often underestimated when considering boreal ecosystem source water protection and when treating source waters to provide clean drinking water. Burning peat impacts its physical properties and chemical composition, yet the consequences of these transformations to source water quality through pollutant leaching has not been studied in detail. We combusted near-surface boreal peat under simulated peat smoldering conditions at two temperatures (250 ℃ and 300 ℃) and quantified the concentrations of the leached carbon, nutrients and phenols under 5 g peat $L^{-1}$ RO water suspensions from a 2-day leaching period. For the conditions studied, measured water quality parameters exceeded US surface water guidelines and even exceeded EU and Canadian wastewater/sewer discharge limits including chemical oxygen demand (COD) (125 mg/L), total nitrogen (TN) (15 mg/L), total phosphorus (TP) (2 mg/L). Phenols were close to or higher than the suggested water supply standard established by US EPA (1 mg/L). Leached carbon, nitrogen and phosphorus mainly came from the organic fraction of peats. Heating peats to 250℃ promoted the leaching of carbon-related pollutants, whereas heating to 300 ℃ enhanced the leaching of nutrients. Modulated by different heating conditions, post-heated peats likely contribute higher loads of pollutants to receiving waters than pre-heated peats, which implied fire-damaged boreal peats in field might be a critical but underappreciated factor for water pollution. A simplified PLS model based on other easily measured parameters provided an easy way for determining the stress of COD and phenols pollution in bulk water phase. Conclusions from this lab study suggested an urgency for better managing

potable water security in fire-dominated forested peatlands through comprehensive molecular diagnosis of peat leachable micropollutants by for instance liquid chromatography–mass spectrometry (LC-MS) and field measurements of aquatic pollutants downstream peatland watersheds post different fire conditions.

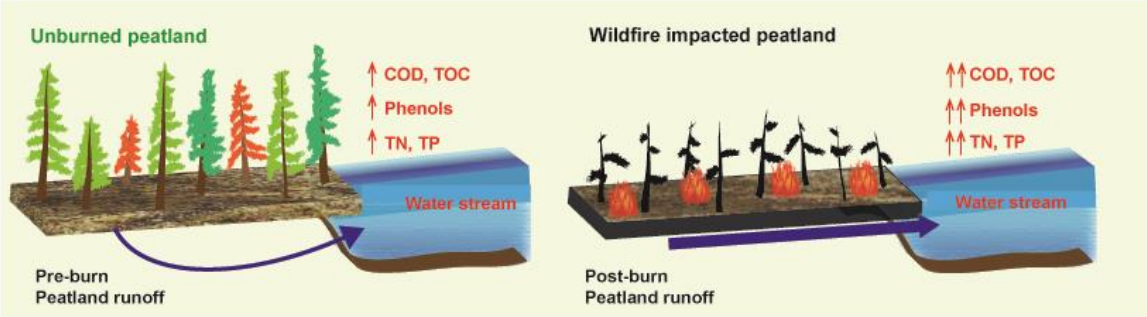


### 3.2 Introduction

Boreal peatlands represent an estimated 15-30 % (~500-600 Gt) of the global terrestrial carbon [1], 9-16 % (~8-15 Gt) of global soil organic nitrogen pool [2, 3], store approximately 10% of the world's non-glacier freshwater resource [4], and play key roles in regulating regional carbon and nutrient cycling. Peatlands in Canada account for over 90% of wetland area and ~14% of the land area [5], where runoff from these areas can impact drinking water sources for local communities, including Indigenous and First Nations communities [6]. The peatland processes that control downstream water quality are governed by a delicate balance of interactions between the hydrological, biogeochemical, and ecological conditions [7]. Wildfires disrupt this balance and can cause deleterious impacts to drinking water quality [8]. As more people continue to live and/or work in the boreal region [9], increased peatland draining and mining activities for agriculture, forestry and bioenergy [10], and climate change extending wildfire seasons as

well as increasing peat fire frequency and severity [11], a better mechanistic understanding of pollutant generation from peat fires in boreal landscapes is becoming increasingly critical.

A variety of compounds with direct peat-origin negatively impact the drinking water quality of water from peatland watersheds. Peatlands are major sources for dissolved organic matter (DOM) to downstream water sources, with up to 10-30 % net carbon uptake transported out from boreal watersheds in the form of dissolved organic carbon (DOC) [12], which is equivalent to a mean DOC export of 6.3 g $m^{-2}$ $yr^{-1}$ [13]. Drained peatlands (~15 % of world's peatlands) cumulatively release a total of 80.8 Gt carbon and 2.3 Gt nitrogen [10]. High DOC loads can cause browning of surface waters [14], and impact water quality by changing the bioavailability of coexisting heavy metals and organic pollutants [15], while also contributing to the formation of carcinogenic disinfection byproducts (DBPs) during drinking water chlorination [16]. While boreal peatlands tend to be nutrient-limited [17], peats can tightly sequester nitrogen and phosphorus in organic complexes [18], and the resultant leached nutrients into fluvial and lacustrine ecosystems can lead to eutrophication, oxygen reduction, and biodiversity loss [19]. This phenomenon has been observed in drained peatlands [20, 21] and headwater streams [19], as well as those impacted by peatland wildfire [22]. While there is a general understanding of nutrient export following peatland wildfires, the chemical origin, concentration, and synthesis routes of phenolic compounds from peatlands have not been studied. It has been suggested for example that decomposed *Sphagnum* mosses can contribute to phenols [23], but no quantification of this has been done yet [24]. *Sphagnum* polyphenols have found to

critically regulate peatland microbial community growth to favor peat accumulation [23]. Nonetheless, the necessity of treating peat-leached aquatic phenolic compounds cannot be overlooked, despite of the positive ecological roles of peat phenols, as phenols are micropollutants that cause toxicity and odor in water at trace levels [25] and contribute to DBPs in potable water disinfection [26]. Yet, phenols have been rarely measured in peatland runoff studies.

Wildfires, the largest recurring disturbances in boreal peatlands, often occur at low temperatures (< 300 ℃) through smoldering [1], which involves simultaneous pyrolysis and oxidation reactions [27]. Generally, only minor proportions of the near-surface peat along with low-growing vegetation are directly consumed via burning, while the majority of shallow peats are subject to low-severity heating that extends from the upper surface [28]. Previous studies have identified how peat heated to different temperatures undergoes complex physicochemical changes, gaining different morphology, hydrophobicity, and chemical composition [29]. Burn-induced peat physicochemical changes alters the composition of soil carbon and macronutrient availability [22], which impacts the mobility of solutes from within the peats to pore water. Solute mobility directly alters water quality in receiving surface waters [30]. Climate change is increasing the susceptibility of boreal peatlands to wildfire due to warmer and drier conditions [1]. As such, there is a critical research need to provide land managers, land users and downstream potable water utilities with knowledge of the concentration and cycling of surface runoff pollutants from wildfire-disturbed peatlands [1, 11].

Lab-based heating is an established method to simulate peat fires [25, 28, 29, 31], which provides a realistic solution to overcome existing limitations of accessing fire-dominated peatlands (*e.g.*, risks from creeping smoke, carbon monoxide, methane as well as risks from fire and heat), and enabled extrapolation to how peat fire conditions affect peat chemistry (thus pollutant leaching). A heating temperature range between 250 – 300 ℃ is characteristic in many boreal peatland forests [32], and was hence used in this study to prepare the lab-simulated post-heated peats. In this study, we focused on the organic compound leaching from near-surface peat, which are the most disturbed by peat fires. Furthermore, these peats can be readily saturated by water (up to 80%) when precipitation and flooding events occur [33]. Lab-simulated leaching is a simplified scenario that mimics field leaching conditions while eliminating environmental confounding factors (*e.g.*, farming irrigation and overland flow), and allows controlled identification of peats' leaching potential and their immediate impacts to source water quality.

This study is the first of its kind to quantify leaching of organic pollutants from fire-impacted peats, and while these controlled conditions are not perfectly reflective of field conditions, they are reasonable starting conditions for this seminal study. Therefore, as a necessary first step towards this research, the objectives of this study were to 1) investigate the effect of wildfires on peatland water quality through laboratory peat leaching studies; 2) analyze the statistical relations between various leached pollutants under different heating conditions to infer leaching mechanisms; and 3) estimate potential environmental impacts to source waters for potable use.

## 3.3 Methods

### 3.3.1 Study site and sampling

*Sphagnum*-dominated columns were extracted from a forested peatland located at the Pelican Mountain FireSmart Fuel Management Research Site (55.701636, -113.578543, Fig. S1), Alberta, Canada. The forest stand is dominated by black spruce (*Picea mariana*) with some tamarack (*Larix laricina*). Shrub cover includes an abundance of Labrador tea (*Rhododendron groenlandicum*), while the ground was characterized by *Sphagnum* mosses (*S. fuscum, S. capillifolium, S. magellanicum*) and feather mosses (*Pleurozium schreberi*, *Hylocomium splendens*, and *Ptilium crista-castrensis*). Pedochemical characteristics of the pristine *Sphagnum* and *feather moss* peats samples were examined through elemental analyses (Table S1) and identification of peat carbon and oxygen bonds by Fourier transform infrared spectroscopy (FTIR) (Fig. S2).

Five peat coring locations were randomly selected within the naturally undisturbed area, and the first 10 cm of intact peats were collected in PVC pipes (dia. 10 cm) (preserved in the original morphology protected by PVC pipes to limit potential compression), sealed with plastic wrap, transported to the lab and frozen in a conventional freezer. The collected field peats were *Sphagnum* dominated, with no or few *feather moss* peats included. Because, in general, the shallow peat layers are the most affected by wildfires, the top 5 cm of peat were segmented with a knife and air-dried until the peat reached a steady-state weight. Embedded large wood debris, plant roots and twigs were manually removed, prior to experimentation.

### 3.3.2 Experimental setup

The air-dried peat was randomly assigned to one of three treatments (n = 5 per treatment): raw peat (R), peat heated at 250 ℃ (B250), and peat heated at 300 ℃ (B300). The 5 field collected peat samples were air-dried in a fume hood for 2 days until a steady state weight was achieved. This produced 5 pre-heated raw peats (R) (2.5 g for each sample) for the leaching test. The lab-simulated post-heated peats (B250 and B300) were prepared via heating the air-dried peats in a muffle furnace (Cole Parmar, USA). This setup reflected the heat generation from external sources including peat smoldering fires, which transform peat compounds based on different oxygen availability mainly through oxidation, volatilization and/or some combustion (mainly occurring at the surface) and pyrolysis reactions (mainly occurring within the bulk) [29]. Briefly, for each of the 5 air-dried peat samples, a 0.5 g peat sample was placed onto a separate porcelain crucible (V = 100 mL, CoorsTek), which was then heated at 250 or 300 ℃ for 30 min. The process was repeated several times until the combined weight of the corresponding post-heated peat sample exceeded 2.5 g. This produced 10 post-heated peat samples (2.5 g for each of the 5 B250 samples, and 2.5 g for each of the 5 B300 samples) for the leaching test.

To determine the leachable compounds, the peat (2.5 g), either unheated or heated, was mixed with reverse osmosis (RO) water in glass Mason jars (vol. 500 mL) to make 5 g peat $L^{-1}$suspensions, and stirred at 300 rpm at 20℃ for 2 days to allow for a sufficiently long contact time to achieve the pollutant partition equilibrium. The choice to use RO water was to establish a baseline of maximum leaching potential, as well as to enhance the reproducibility of experiments using complicated and variable real peat samples. This

experimental design reflects, to the first order, pollutant leaching to potable water sources from climate change-impacted peatlands, where leaching can be high due to increased intensity and duration of rainfalls and/or flooding following long dry spells [34]. Leachates were collected through vacuum filtration using glass microfiber membranes (pore size 1.6 μm, Whatman) prior to chemical characterization. Freshly prepared leachates from pre- and post-heated peats were labelled as R-n and BT-n respectively, where R, represents the raw unheated peats, B indicates the burned peats, T (℃) is the heating temperature (T = 250 or 300), and n indicates the distinct sample number (n = 1-5).

### 3.3.3 Chemical characterization

Total carbon (TC), total organic carbon (TOC), inorganic carbon (IC), pH, chemical oxygen demand (COD), total nitrogen (TN), nitrate ($NO_3$-N), ammonia ($NH_3$-N), total phosphorus (TP, measured and reported in its orthophosphate form, $PO_4^{3-}$), reactive phosphorus (RP, measured and reported in its orthophosphate form, $PO_4^{3-}$) and phenols of the leachates were measured in parallel. Total organic nitrogen (TON) and non-reactive phosphorus (NRP, shown as $PO_4^{3-}$) were calculated by subtracting $NH_3$-N and $NO_3$-N from TN (given nitrite concentration was negligible), and subtracting RP from TP, respectively.

The pH of all water samples was determined using a pH meter (Thermo Scientific, USA). Total carbon (TC), total organic carbon (TOC) and inorganic carbon (IC) were measured using a TOC-L analyzer (Shimadzu, Japan). Chemical oxygen demand (COD) (USEPA reactor digestion method, Hach method 8000), total nitrogen (TN) (Persulfate digestion method, Hach Method 10208), nitrate (shown as $NO_3^-$-N) (Chromotropic acid method, Hach method 10020), ammonia ($NH_3$-N) (Salicylate method, Hach method 10205), total

phosphorus (TP, measured as orthophosphate, $PO_4^{3-}$) (USEPA PhosVer 3 with acid persulfate digestion method, Hach method 8190), reactive phosphorus (RP, measured as $PO_4^{3-}$) (USEPA PhosVer 3 (Ascorbic acid) method, Hach method 8048), and phenols (USEPA 4-aminoantipyrine method, Hach method 10266) were measured by standard Hach testing kits and analyzed using a Hach DR3900 Spectrophotometer. Non-reactive phosphorous (NRP) was calculated from NRP = TP – RP. Sample digestions were conducted in a Hach DRB200 Thermostat. Analytical method principles for measuring COD, TN, nitrate, ammonia, TP, RP and phenols using Hach methods were provided in the Supplementary Material.

Field collected pristine peats were also characterized by elemental analyses, FTIR and scanning electron microscopy (SEM) for identifying the original solid phase physicochemical characteristics. Elemental compositions were examined by an elemental analyzer (UNICUBE, elementar, Germany). FTIR spectra were obtained by a Nicolet 6700 FT-IR spectrometer (Thermo Scientific, USA) over the mid-infrared range from 4000 to 525 $cm^{-1}$ at 4 $cm^{-1}$ resolutions for a total of 32 scans. Scanning electron microscopy (SEM) of *Sphagnum* peat was obtained by a JEOL JSM-7000 F SEM equipment, with a 7 nm platinum (Pt) coated on sample surface.

### 3.3.4 Statistical analyses

Correlation analysis and analysis of variance (ANOVA) were conducted in Excel 2013 using XLSTAT module. Pairwise comparisons in ANOVA were based on Duncan test, with a confidence interval of 95% for the differences between the categories (see Table S2

for parameters). Principal component Analysis (PCA) and Partial Least Squares (PLS) were implemented in MATLAB R2016a software.

Principal component analysis (PCA) is among the most widely used data dimension reduction algorithms, which maps the n-dimensional features to a new k-dimensional orthogonal feature, known as the principal component (PC). The first several PCs contain the majority of the information in the large data set. The first (F1), the second (F2) and the third (F3) PCs explain the leachate pollutant characteristics, where the cumulative variability increases with PCs. Because the largely differed value of each feature (*i.e.*, each column of the matrix) will likely lead to large proportions of error when projecting into a low-dimensional space, data of each feature was first standardized by subtracting the mean for each feature and then dividing by the standard deviation, such that their sizes are within the same range.

PLS is an inverse multivariate statistical method that provides a direct relationship between a dependent variable **X** and a response variable y via maximizing covariance y and **X** [35]. PLS was adopted because it can handle multi-dimensional and collinear data sets. PLS modeling helps to identify the correlation among various leachate parameters, and rapidly quantify the important indicators (*i.e.*, COD and phenols, based on some simple leachate indicators). The root-mean-square-error (RMSE), ratio of performance to inter-quartile (RPIQ), and determination coefficient ($R^2$) were used to evaluate the performance of models.

$$\mathrm{RMSE} = \sqrt{\frac{1}{n}\sum_{i=1}^{n}\left(y_i - \hat{y}_i\right)^2} \quad (1)$$

$$\mathrm{RPIQ} = \frac{Q3 - Q1}{\mathrm{RMSE}} \quad (2)$$

$$R^2 = 1 - \frac{\sum_{i=1}^{n}\left(y_i - \hat{y}_i\right)^2}{\sum_{i=1}^{n}\left(y_i - \bar{y}\right)^2} \quad (3)$$

Where $y_i$ and $\hat{y}_i$ are the measured and predicted values of $i^{th}$ samples, respectively; $\bar{y}$ is the mean of the measured values; n is the number of samples; and Q1 and Q3 are the $1^{st}$ and $3^{rd}$ quartile of samples, respectively. High values of $R^2$ and RPIQ, along with a low RMSE value indicate a robust and accurate model.

### 3.4 Results and discussion

3.4.1 Leachate water quality characterization

Leachates extracted from raw peats (R), and those burned at 250℃ (B250) and 300℃ (B300) were assessed for various water quality factors. The chemistry of peat leachates was significantly altered after simulated burning by heating (see Table S1 for full ANOVA analyses). Average COD and TC (dominated by TOC, > 94.6% (Fig. 2a)) in the leachates was the highest for B250 (Fig. 1a and Fig. 1b, 397.1 and 150.4 mg/L, respectively) (for p-values given as: $pCOD_{raw\text{-}250} = pTC_{raw\text{-}250} < 0.05$, $pCOD_{250\text{-}300} < 0.05$, $pTC_{250\text{-}300} < 0.05$), suggesting that low temperature heating increased the organic pollutant leachability and mobility. Peats heated to higher temperature (300℃) promoted greater leaching of nutrients including total nitrogen, TN ($pTN_{raw\text{-}250}$, $pTN_{250\text{-}300}$ and $pTN_{raw\text{-}300} < 0.05$) and

total phosphorous, TP ($pTP_{raw-300}$ and $pTP_{250-300} < 0.05$), as well as phenols ($pPhenol_{raw-250}$ and $pPhenol_{raw-300} < 0.05$), with average concentrations of TN, TP, and phenols leached from B250 and B300 rising from 214.8 to 414.0 mg/L, 12.7 to 23.9 mg/L, and 4.42 to 4.43 mg/L, respectively (Fig. 1c, Fig. 1d, and Fig. 1e). TN and TP were dominated by total organic nitrogen, TON (> 98.4%) and reactive phosphorous, RP (78.6%), respectively (Fig. 2b and Fig. 2c).

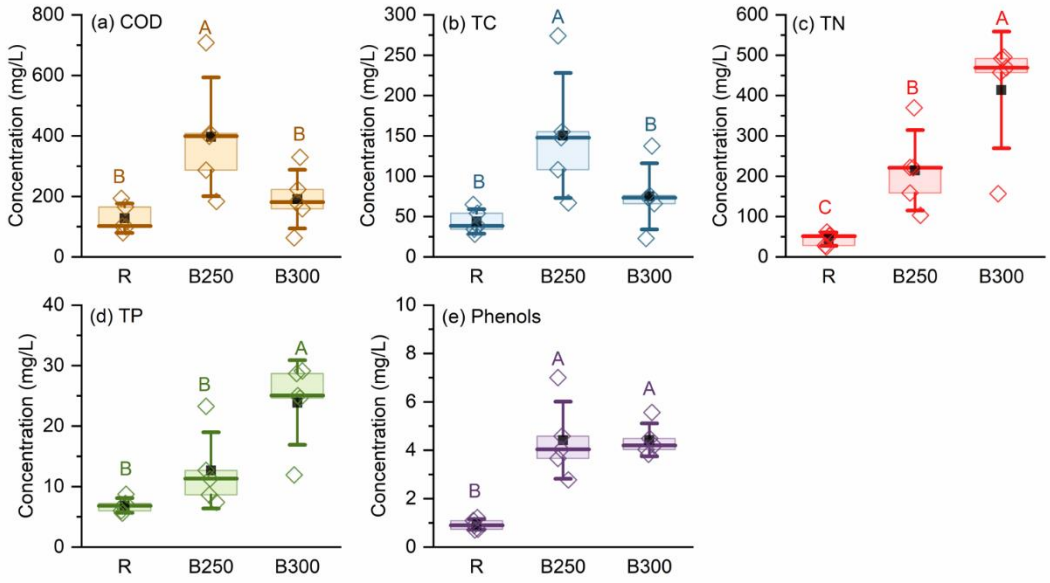


**Fig. 1.** Box plots with ANOVA post-hoc analyses indicating concentration of (a) COD; (b) TC; (c) TN; (d) TP and (e) Phenols in pre- and post-heat peat soil leachates. R, B250 and B300 represent the leachates (n=5 per treatment, as indicated by the scattered open diamonds) extracted from raw peats, 250°C heat-treated peats and 300°C heat-treated peats, respectively. Mean values are shown in black solid squares. The top and bottom of the boxes indicates the upper and lower quartile, respectively. The horizontal lines in bold represent the median. The whiskers indicate the standard deviation. 1 mg/L aqueous pollution loading is equivalent to 0.2 mg/g water-extractable compound from peat soil.

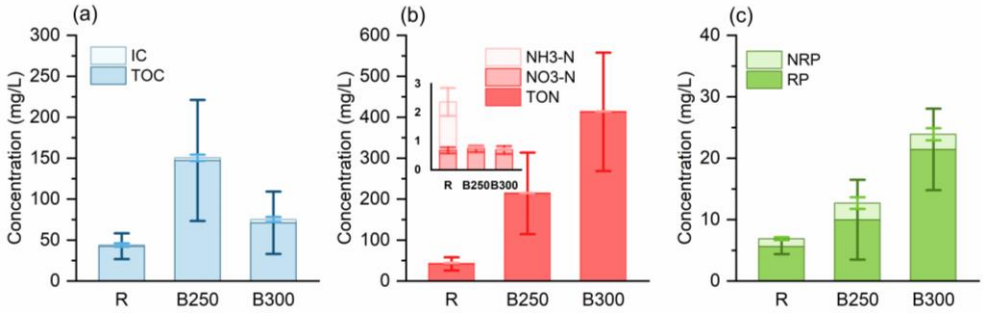


**Fig. 2.** Stacked column charts indicating the average of sub-category pollutant concentrations of (a) TC; (b) TN; and (c) TP, of the extracts (n=5 per treatment) from raw peats (R), 250℃ heat-treated peats (B250) and 300℃ heat-treated peats (B300), respectively. Error bars represent standard errors of the mean based on leachates from 5 peat cores per treatment, and 2 parallel measurements per peat sample leachate. 1 mg/L aqueous pollution loading equivalents to 0.2 mg/g water-extractable compound from peat soil.

Source surface waters require proper water treatment to be used as drinking water, but only a small fraction of surface water pollutants is monitored and treated under current regulations. In Canada for instance, the Guideline for Canadian Drinking Water Quality lists the maximum acceptable concentrations (MACs) for many heavy metals, anions and inorganic and organic chemicals (including certain chlorophenols), but many peat-derived organic pollutants such as polyphenols and benzoic acid and its derivatives [29], are not monitored. Peat leaching provides an increased type and loading of organic and nutrient pollutants, which cannot be fully detected and treated by current affordable drinking water treatment processes. This has brought challenges for drinking water source protection and treatment in the boreal communities including on First Nations reserves, despite increasing construction of water treatment systems [36].

Here we evaluate the peat leachate characteristics using surface water and wastewater discharge guidelines from other well-regulated regions for comparison (Table S3). We found that many parameters, including COD, TN, TP, TKN and phenols exceeded the

values suggested by these guidelines. Average COD from all treatments exceeded the urban wastewater discharge limits set by European Union (EU) (125 mg/L) [37] and water quality objective values for inland surface waters established in some states of United States (US) (5 – 90 mg/L). Post-heated peat leachate phenols concentrations greatly exceeded Canadian local by-law limits (1 mg/L) and US EPA suggested limits for water supply (1 mg/L) [38]. Post-heated peat leachate TN and TP concentrations were much higher than EU limits (15 mg/L for TN, 2 mg/L for TP) [37]. Worth noting, TON alone represented major constituents of total Kjeldahl nitrogen (TKN), and the concentrations for B250 and B300 exceeded Canadian local by-law limits (100 mg/L).

Although the lab results were not designed to mimic field peat mass and water volume conditions, the measured exceedances from this study over the US, European Union (EU) and Canadian water quality guidelines (Table S3) suggested that leachates from peats could be a significant source of organic pollution to receiving water bodies in the boreal region. Following peatland fires and peat-leaching events, these surface waters are likely to be of poor water quality with respect to COD, phenols, TN, and TP. We note that the mobility of these leachates in peat and subsequent hydrochemical connectivity with receiving surface waters is relatively unknown. Nevertheless, elevated leachate concentrations for post-heating peats observed here suggests that increasing contaminated runoff from boreal wildfires may be of particular concern for surface waters that are sourced as potable waters for municipalities and First Nations communities.

### 3.4.2 Correlations between types of leachates and temperature

The previous chapter characterized how heating temperature affects types and concentrations of leached peat pollutants, while this chapter investigates the relationships between various pollutants that leach from peats by identifying internal correlations. A Pearson p correlation heatmap is presented in Fig. 3, and the r values are summarized in Table S4. COD measured in the leachate was highly correlated with the presence of TOC ($r = 0.998$, $p < 0.001$), phenols ($r = 0.746$, $p < 0.01$), IC ($r = 0.625$, $p < 0.05$) and IN ($r = 0.556$, $p < 0.05$). TN and TP have demonstrated significant relevance to each other ($r = 0.882$, $p < 0.001$). TN was positively correlated with the leaching of TON ($r = 1$, $p < 0.0001$), phenols ($r = 0.676$, $p < 0.01$), and RP ($r = 0.862$, $p < 0.001$), whereas TP was positively correlated with the leaching of RP ($r = 0.94$, $p < 0.001$), phenols ($r = 0.563$, $p < 0.05$), and TON ($r = 0.882$, $p < 0.001$). Unexpectedly, ammonia leaching gave a negative correlation with TN, TP and phenols ($p < 0.05$ for all). The variables in Fig. 1, were positively correlated to leachate pH.

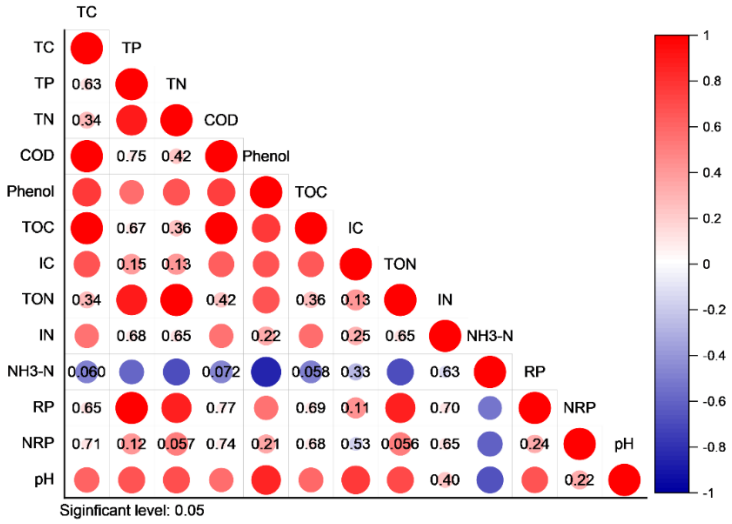


**Fig. 3.** Pearson correlation plot of p values of the water quality variables. Larger circles with darker red/blue color suggest a smaller p value and thus a stronger correlation. Red circles = positive correlation, blue circles = negative correlation. Circles without labels ($p<0.05$) indicate that a statistically significant effect was observed.

The first three principal components represented the main characteristics of the leachates, and the explained variances of F1, F2 and F3 accounted for 87.7% of the total variance (Fig. S3). Briefly, F1 distinguished between the leachate characteristics from unheated and heated peats (R vs B250 and B300) (Fig. 4a and Fig. 4b), where heating alone impacted the leachate composition. Heating temperature (B250 or B300) separated along F2, where higher carbon leachate was related to 250°C heating and higher nutrient fluxes were related to 300°C heating (Fig. 4a and Fig. 4c). Ammonia was associated with R, however the concentrations remained low. Post-fire peats increased pH and phenols concentrations in leachates regardless of heating temperature. We thus argue that peat fire temperatures likely control leachate chemical composition, and should be accounted for in predicting downstream water quality.

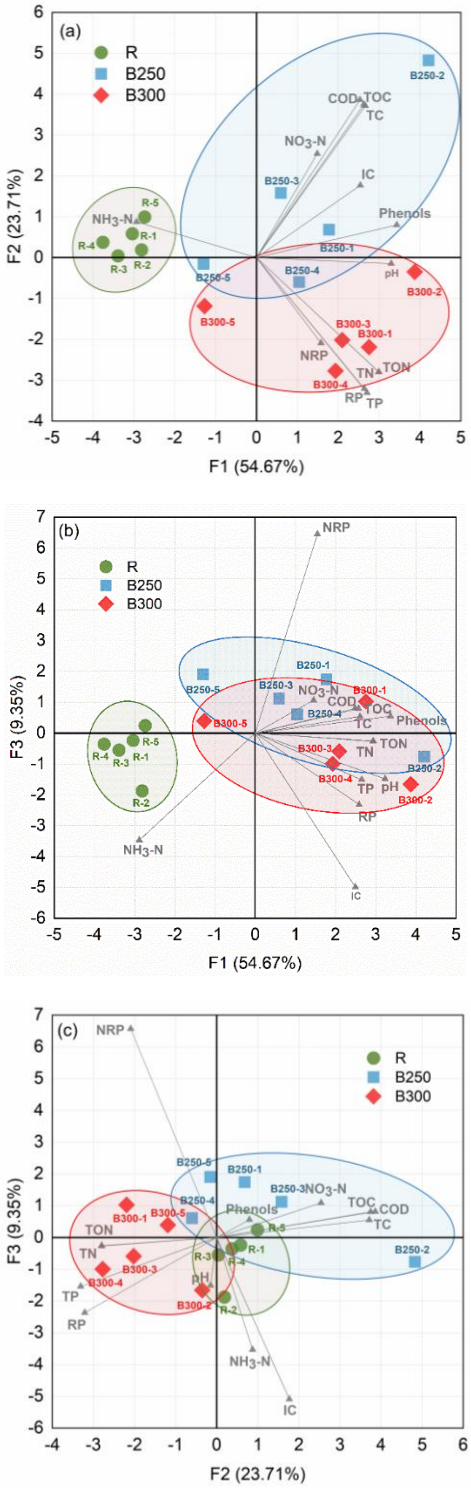


**Fig. 4.** Principle component analysis (PCA), reflected by the relationship between (a) F1 and F2; (b) F1 and F3; and (c) F2 and F3, of water chemistry for leachates extracted from raw peats (R), 250℃ heat-treated peats (B250) and 300℃ heat-treated peats (B300), respectively. Shaded green,

blue, and red colored areas indicate the clusters for R, B250 and B300, respectively. Vectors in grey refer to PC loadings of the corresponding variables.

### 3.4.3 Pollutant leaching mechanisms

The peat samples investigated in this study well represented live and/or semi-decomposed near-surface *Sphagnum*-dominated peat above the deep mineral layer, containing a high organic fraction primarily represented by leaf and stem carbon. Peat soils are rich in organic carbons, as supported by FTIR spectra (Fig. S2), including macromolecules (*e.g.*, lignin, hemicellulose and carbohydrates) [39, 40] and small molecules (*e.g.*, organic acids, phenols, and furan derivatives) [29, 40, 41]. The high COD and TC contents in leachates were directly related to these peat substances, which may dissolve or transport as particulate matter into aqueous phase (Table S5). Post-heated peats leached higher TOC concentrations (Fig. 2a). Carbon leaching significantly enhanced from B250 and this was partly related to the changes of the types of organic matter (OM) that leached from the post-heated peats. In addition to oxidizing and volatilizing some labile OM, pyrolytic processes can transform polyaromatic hydrocarbons [1], and chemically degrade biopolymers into smaller molecules [42]. The altered peat compositions may contribute more carbon into leachates through direct dissolution or attachment on soil particulates (< 1.6 μm) that entered into pore water (Table S5). Hotter fires cause more complete combustion, reducing the quantity of organic carbon that can be leached. This might explain why B300 had lower carbon-related pollution compared with B250. Detected phenols may come from peat polyphenols (*e.g.*, cinnamic aicd derivatives) [43] and post-decomposition transformed free phenolic products (*e.g.*, phenolcarboxylic acids, catechols and flavonols) [44]. *Sphagnum* contains weakly bounded water-soluble phenols in cell

walls [45], which can be readily released into water through the unique, large pore openings, as shown in the SEM image (Fig. S4). Elevated phenols leaching from post-heated peats might be related to the concentration of condensed phenolic compounds. There is very little literature discussing phenols and their mobility from peat, despite the importance of removing phenols in water treatment processes.

Leached nutrients were found to increase following heat treatment of peats. *Sphagnum*, the keystone species in many peatlands, may accumulate N through biological $N_2$ fixation, and N and C metabolisms collectively control amino acid biosynthesis [46]. Organic N can be taken up and assimilated by peats [47], and subsequently released when the peat is heated and the organic structure breaks down. Although the elemental analyses (Table S1) indicated that N element (< 1%) only took up a small fraction within boreal peats, the TN content in peat leachates was comparatively high. This may indicate the high water solubility and high mobility of peat nitrogen-containing molecules. By contrast, despite that C elemental content (48 – 49%) in boreal peats was high, many carbon-based compounds such as peat biopolymers and light hydrophobic polycyclic compounds typically have low extractive capacities in water, thus making minor contributions to TOC. It was also probable that some peat C leached out in the form of TON, which represented the primary fraction of TN (Fig. 2b). As the heating temperature increases, it is likely that the sharp increase in TN was driven by thermal depolymerization of organic N (*e.g.*, proteins) into more fugitive fractions. Burning peat causes the formation of N-heterocycles, including pyrroles [42], pyridine and its alkyl derivatives (*e.g.*, picolines) [41]. These refractory molecules cannot be sufficiently oxidized by dichromate during COD digestion

[48], suggesting that COD values underestimate the real level of organic pollutants in leachates.

Peat organic phosphorous typically tightly binds with organic compounds. The P-containing molecule adenosine triphosphate (ATP) is well-known to be vitally important for energy transfer in peat cells. The increased TP in B250 and B300 leachates may be related to fire's effect in converting organic P into more mobile orthophosphates (RP) [49]. B300 leachate had significantly higher TP and lower TC than B250, suggesting that greater volatilization of the carbon fraction reduces the phosphorous organic binding, making it more readily able to transform into RP. Heating at higher temperature for sufficiently long duration (up to several hours or longer) can decrease peat soil hydrophobicity [29], allowing more partition of RP into the water phase (Fig. 2c). It is also possible that P leaching is associated with redox sensitive Fe or Mn minerals, however this might not be a main cause because leachates from post heat-treated peats only had slightly increased pH (Table S5). The pH increase was attributed to the destruction of soil acidic organic matter and accumulation of base cations and trace metals [50] liberated from the burned peat [42]. While many field-scale studies observed no increase of pH in-situ post-fire after days or weeks [30, 51], this could be a result of distinct time/spatial scale differences between studies. Further, the buffering capacity of peatlands likely minimizes the pH impact on downgradient aquatic systems, therefore field measurements of post-fire peat leachates and the source pH would be valuable to further validate these findings.

### 3.4.4 Implications and future perspectives

This study was informative for a better understanding of pollutants leaching from *Sphagnum*-dominated peats from fire-recurring boreal peatlands. This chapter aims to elaborate on how laboratory findings might differ from field situation, and to reasonably extrapolate the conclusions obtained from the laboratory batch leaching test to assess how these changes might impact downstream source water quality and drinking water treatment. The lab-simulated heating and batch leaching set-ups best mimicked vigorous peat pollutant leaching impacted by low-severity peat fires (250 – 300 ℃) following intense flooding or rainfalls. This simplified setting however excluded the external contaminants due to precipitation, overland flow and irrigation, nor investigated other chemical compounds leached from other vegetations such as the black spruce. We recommend taking into account these factors to design field leaching tests under prescribed fires in the future.

Firstly, our lab-based results implied that that large-water flow events (*e.g.*, spring freshet and heavy rainfalls) coupled with peat fires could lead to high concentration of DOC and nutrients, which were consistent with some of the field findings [52, 53], despite that in reality the field peat leachates have more complex transport pathways into source waters from interconnected streams and wetlands. Although waters receiving peatland runoff have been measured to have low nutrients and high organic carbon [54], a clear increase of nutrients in laboratory post-heated peat leachates implied that special care should be paid to post-fire peatland nutrients monitoring, as excess levels of nutrients in field leachates may ultimately transport to source waters as runoff, leading to eutrophication, algal blooms, and oxygen loss, fish kills and other ecosystem disruptions [55, 56]. Impacted water

sources require greater treatment for drinking water, which increases costs associated with removing odor, taste and toxins.

Secondly, the lab study confirmed the high DOM concentration in peat leachates, which brought urgent needs for next step peatland heavy metal assessments, especially for those areas in vicinity to peatland mining areas. As peatlands are known to be sinks for inorganic mercury (Hg) and sources of methylmercury (MeHg) [57], changes to peats post-fire causing greater leachate carbon may increase the production and subsequent export of bioavailable MeHg from burned peatlands into source waters. Although the upper layer of peats in naturally undisturbed peatlands are less impacted by atmospheric deposition of heavy metals from anthropogenic dust particles [58], peat-leached organic substances could still serve as strong chelators for the dissolved metal species such as copper (Cu), lead (Pb) and iron (Fe) that already present in receiving surface waters and downstream water treatment utilities, often resulting in an increased mobility of heavy metals during DOC transport process [59]. The contaminated peat leachates, thus, can be critical non-point sources of pollution to surface waters, posing risks for potable water users.

Thirdly, we note that the leachable material obtained in this study describes the mobile fraction and does not necessarily represent the overall output to receiving surface waters in peatland watersheds, as a variety of hydrological and biogeochemical processes will impact these constituents along their flow paths to surface waters [7, 60, 61]. For instance, increases in peat hydrophobicity [29] will decrease deep percolation of precipitation and increase runoff [62]. This change in the routing of water may increase the export of the derived leachates from sloped peatlands, thus transporting greater loads of leached

contaminants quickly to aquatic systems. In any case, post-fire local community water treatment costs often increase when the drinking water sources are subject to peat-derived contamination. We suggest to consider *in-situ* peat soil chemistry and hydrological conditions for better adjusting hydraulic loads and upgrading processing units in the boreal water treatment utilities.

Finally, this lab study demonstrated that heating temperature is a critical factor affecting leachate water chemistry, which motivates an investigation of how field peat fire temperatures impact peat runoff water quality, and thus the downstream water treatment process. Heavily polluted source waters make water treatment more difficult and thus more expensive. The differences in DOM and nutrient composition generated at different heating temperatures could impact drinking water treatability, including determining the level of denitrification required, and interfering with chlorination disinfection through the formation of organic chloramines [63]. Influent flows with widely fluctuating concentrations may lead to poor treatment efficiency within small-scale water treatment plants in boreal communities [8]. Furthermore, differences in post-heated leachate composition could impact interacting processes, such as organic-metal complexation and mobility or Hg methylation [50], further altering downstream water quality and treatment cost. We advocate to look into these phenomena through establishing prescribed burning on peatland regions.

### 3.4.5 COD and phenols prediction

Adequate water treatment in response to peat fires would benefit from pollutants prediction based on some easily measured water quality parameters. For instance, COD measurements

may be difficult for small-scale water operators in boreal watersheds and other peatland dominated watersheds, and measurements of total phenols are rare across drinking water treatment plants and infrequent even at large drinking water treatment facilities. Because COD and phenols were strongly correlated to other leachate parameters (Fig. 3), the calibration and validation of the PLS model sets showed promising performance for both COD and phenols prediction (Fig. 5) for boreal derived pollutants. High variable importance in the projection (VIP) scores for COD occurred with TC, TN, TOC and TON predictors (Fig. S5a), while VIPs for phenols occurred with TC, TN, COD, TOC and TON predictors (Fig. S5b). Leached COD and phenols mainly came from organic carbon, but successful prediction of their leached concentration on the basis of TON alone provides a reasonable assumption that C-based pollutants (*e.g.*, phenols) have similar leaching pathways as N-based pollutants.

The PLS model hence provided a novel methodology for water quality modeling in boreal peatlands, but further study is required including validation by long-term field measured water pollution data, and model optimization through incorporating other potential predictors such as sulfur and heavy metals. Since the lab-based leaching study was an ideal condition neglecting the effects of precipitation, evaporation, overland flow, snow-melting, and/or anthropogenic inputs of new pollutants, the PLS model requires proper modification to match the hydrological and geochemical conditions of different boreal peatland watersheds. In general, these statistical findings indicate that simple measurements, such as TOC, can be used by water treatment operators downstream of peat-dominated

watersheds for estimating phenols or COD content immediately after a peatland fire event, which often coincides with limited sampling capacity.

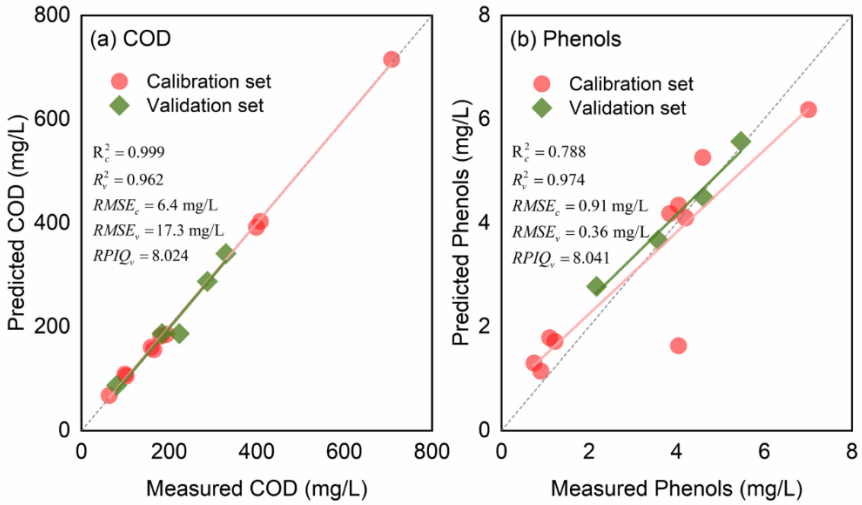


**Fig. 5.** Goodness of fit of PLS models for prediction of (a) COD; and (b) Phenols. The grey dashed lines refer to 1:1 line. The pink and green lines are the regression lines for the calibration set and validation set, respectively.

### 3.5 Conclusions

This seminal study measured the leaching of TOC, nutrients and phenols from pre- and post-heated boreal peatland soils under lab conditions using real boreal peats exposed to conditions that approximated to first order burn conditions in the field. The results presented in this study are indicative of the impacts of leachable peat pollutants associated with low-temperature peat fires. Fresh peat leachates collected from 5 g peat $L^{-1}$ RO water suspensions have considerable COD, TN, TP, TKN and phenols concentrations after a 2-day batch leaching process, that exceeded well-established surface water and wastewater discharge guidelines from Canada, US and EU (Table S3), and sources of these contaminants primarily came from TC and organic fractions of TN and TP. Post-heated peats showed markedly higher leaching potential of TOC, nutrients and phenols as a result

of altered peat soil chemistry and solute mobility. We recommend to identify the peat leachate chemistry at molecular level by liquid chromatography–mass spectrometry (LC – MS) in future studies, which might help validating the chemical transformation of post-heated peat leachable organic compounds such as N-containing amino acids and pyrroles. Moreover, we provided a simplified PLS model for predicting COD and phenols based on data of other peatland common aqueous pollutants, yet more studies are required for optimization including tracing additional pollutants (*e.g.*, sulfur and Hg) and correcting model fittings for different peatland sites. Overall, this pioneering study expanded the understanding on how peat heating influences leachable peat compounds at lab-scale level, and will advance a more in-depth field validation of post-burn peatland potable water quality in adaption to climate change, as well as a holistic peatland leaching evaluation combining prescribed burning including intense flammable fires at higher temperatures (> 300 ℃). The results of this study will alert land users and downstream water operators to better monitor, manage, and predict the leaching of peat-derived pollutants, with a special focus on the leaching of post-fire peat-derived phenols, which are of acute concern for downstream potable water treatment processes.

### 3.6 Acknowledgements

This work was supported by the Global Water Futures (GWF) program and Boreal Water Futures (BWF) program. Scanning electron microscopy (SEM) was performed at Canadian Centre for Electron Microscopy (CCEM). We acknowledge Dr. Sophie Wilkinson and Patrick Deane in the McMaster Ecohydrology Lab for field sample collections.

## 3.7 References

[1] M.R. Turetsky, B. Benscoter, S. Page, G. Rein, G.R. Van Der Werf, A. Watts, Global vulnerability of peatlands to fire and carbon loss, Nature Geoscience, 8 (2015) 11-14.
[2] J. Limpens, M.M. Heijmans, F. Berendse, The nitrogen cycle in boreal peatlands, in: Boreal peatland ecosystems, Springer, 2006, pp. 195-230.
[3] Y. Gong, J. Wu, Vegetation composition modulates the interaction of climate warming and elevated nitrogen deposition on nitrous oxide flux in a boreal peatland, Global Change Biology, 27 (2021) 5588-5598.
[4] J. Xu, P.J. Morris, J. Liu, J. Holden, Hotspots of peatland-derived potable water use identified by global analysis, Nature Sustainability, 1 (2018) 246-253.
[5] J. Levison, M. Larocque, V. Fournier, S. Gagné, S. Pellerin, M. Ouellet, Dynamics of a headwater system and peatland under current conditions and with climate change, Hydrological Processes, 28 (2014) 4808-4822.
[6] S. Osterwalder, K. Bishop, C. Alewell, J. Fritsche, H. Laudon, S. Åkerblom, M.B. Nilsson, Mercury evasion from a boreal peatland shortens the timeline for recovery from legacy pollution, Scientific reports, 7 (2017) 1-9.
[7] C.P.R. McCarter, F. Rezanezhad, W.L. Quinton, B. Gharedaghloo, B. Lennartz, J. Price, R. Connon, P. Van Cappellen, Pore-scale controls on hydrological and geochemical processes in peat: Implications on interacting processes, Earth-Science Reviews, 207 (2020) 103227.
[8] C.A. Emmerton, C.A. Cooke, S. Hustins, U. Silins, M.B. Emelko, T. Lewis, M.K. Kruk, N. Taube, D. Zhu, B. Jackson, Severe western Canadian wildfire affects water quality even at large basin scales, Water Research, 183 (2020) 116071.
[9] S.A. Nitoslawski, A.T.M. Chin, A. Chan, I.F. Creed, J.W. Fyles, J.R. Parkins, M.L. Weber, Demographics and social values as drivers of change in the Canadian boreal zone, The Boreal 2050 project: a road map towards sustainability of the boreal zone, 01 (2019) 377-392.
[10] H. Liu, D. Zak, F. Rezanezhad, B. Lennartz, Soil degradation determines release of nitrous oxide and dissolved organic carbon from peatlands, Environmental Research Letters, 14 (2019) 094009.
[11] K. Nelson, D. Thompson, C. Hopkinson, R. Petrone, L. Chasmer, Peatland-fire interactions: A review of wildland fire feedbacks and interactions in Canadian boreal peatlands, Science of The Total Environment, 769 (2021) 145212.
[12] M. Palviainen, E. Peltomaa, A. Laurén, N. Kinnunen, A. Ojala, F. Berninger, X. Zhu, J. Pumpanen, Water quality and the biodegradability of dissolved organic carbon in drained boreal peatland under different forest harvesting intensities, Science of The Total Environment, (2021) 150919.
[13] T. Moore, Dissolved organic carbon in a northern boreal landscape, Global Biogeochemical Cycles, 17 (2003).
[14] H.A. de Wit, S. Valinia, G.A. Weyhenmeyer, M.N. Futter, P. Kortelainen, K. Austnes, D.O. Hessen, A. Räike, H. Laudon, J. Vuorenmaa, Current browning of surface waters will be further promoted by wetter climate, Environmental Science & Technology Letters, 3 (2016) 430-435.
[15] H. Kang, M.J. Kwon, S. Kim, S. Lee, T.G. Jones, A.C. Johncock, A. Haraguchi, C. Freeman, Biologically driven DOC release from peatlands during recovery from acidification, Nature communications, 9 (2018) 1-7.
[16] J.P. Ritson, M. Bell, N.J. Graham, M.R. Templeton, R.E. Brazier, A. Verhoef, C. Freeman, J.M. Clark, Simulated climate change impact on summer dissolved organic carbon release from peat and surface vegetation: Implications for drinking water treatment, Water research, 67 (2014) 66-76.

[17] J. Luan, J. Wu, S. Liu, N. Roulet, M. Wang, Soil nitrogen determines greenhouse gas emissions from northern peatlands under concurrent warming and vegetation shifting, Communications biology, 2 (2019) 1-10.
[18] G. Chiapusio, V.E. Jassey, F. Bellvert, G. Comte, L.A. Weston, F. Delarue, A. Buttler, M.L. Toussaint, P. Binet, Sphagnum species modulate their phenolic profiles and mycorrhizal colonization of surrounding andromeda polifolia along peatland microhabitats, Journal of chemical ecology, 44 (2018) 1146-1157.
[19] H. Marttila, S.-M. Karjalainen, M. Kuoppala, M.L. Nieminen, A.-K. Ronkanen, B. Kløve, S. Hellsten, Elevated nutrient concentrations in headwaters affected by drained peatland, Science of the total environment, 643 (2018) 1304-1313.
[20] M. Koskinen, T. Tahvanainen, S. Sarkkola, M.W. Menberu, A. Laurén, T. Sallantaus, H. Marttila, A.-K. Ronkanen, M. Parviainen, A. Tolvanen, Restoration of nutrient-rich forestry-drained peatlands poses a risk for high exports of dissolved organic carbon, nitrogen, and phosphorus, Science of the Total Environment, 586 (2017) 858-869.
[21] M. Nieminen, T. Sallantaus, L. Ukonmaanaho, T.M. Nieminen, S. Sarkkola, Nitrogen and phosphorus concentrations in discharge from drained peatland forests are increasing, Science of the Total Environment, 609 (2017) 974-981.
[22] C. van Beest, R. Petrone, F. Nwaishi, J.M. Waddington, M. Macrae, Increased Peatland Nutrient Availability Following the Fort McMurray Horse River Wildfire, Diversity, 11 (2019) 142.
[23] V.E. Jassey, G. Chiapusio, P. Binet, A. Buttler, F. Laggoun-Défarge, F. Delarue, N. Bernard, E.A. Mitchell, M.L. Toussaint, A.J. Francez, Above-and belowground linkages in Sphagnum peatland: Climate warming affects plant-microbial interactions, Global Change Biology, 19 (2013) 811-823.
[24] N. Walpen, G.J. Getzinger, M.H. Schroth, M. Sander, Electron-donating phenolic and electron-accepting quinone moieties in peat dissolved organic matter: quantities and redox transformations in the context of peat biogeochemistry, Environmental science & technology, 52 (2018) 5236-5245.
[25] Y. Wu, N. Zhang, C.-F. de Lannoy, Upcycling wildfire-impacted boreal peats into porous carbons that efficiently remove phenolic micropollutants, Journal of Environmental Chemical Engineering, 9 (2021) 105305.
[26] Y. Pan, Y. Wang, A. Li, B. Xu, Q. Xian, C. Shuang, P. Shi, Q. Zhou, Detection, formation and occurrence of 13 new polar phenolic chlorinated and brominated disinfection byproducts in drinking water, Water research, 112 (2017) 129-136.
[27] X. Huang, G. Rein, Smouldering combustion of peat in wildfires: Inverse modelling of the drying and the thermal and oxidative decomposition kinetics, Combustion and Flame, 161 (2014) 1633-1644.
[28] N.E. Flanagan, H. Wang, S. Winton, C.J. Richardson, Low-severity fire as a mechanism of organic matter protection in global peatlands: Thermal alteration slows decomposition, Global change biology, 26 (2020) 3930-3946.
[29] Y. Wu, N. Zhang, G. Slater, J.M. Waddington, C.-F. de Lannoy, Hydrophobicity of peat soils: Characterization of organic compound changes associated with heat-induced water repellency, Science of The Total Environment, 714 (2020) 136444.
[30] K. Burd, C. Estop-Aragonés, S.E. Tank, D. Olefeldt, Lability of dissolved organic carbon from boreal peatlands: interactions between permafrost thaw, wildfire, and season, Canadian Journal of Soil Science, 100 (2020) 503-515.
[31] Y. Wu, N. Zhang, C.-F. de Lannoy, Fast synthesis of high surface area bio-based porous carbons for organic pollutant removal, MethodsX, 8 (2021) 101464.

[32] G. Rein, N. Cleaver, C. Ashton, P. Pironi, J.L. Torero, The severity of smouldering peat fires and damage to the forest soil, CATENA, 74 (2008) 304-309.
[33] F. Rezanezhad, J.S. Price, W.L. Quinton, B. Lennartz, T. Milojevic, P. Van Cappellen, Structure of peat soils and implications for water storage, flow and solute transport: A review update for geochemists, Chemical Geology, 429 (2016) 75-84.
[34] V.E. Jassey, C. Signarbieux, Effects of climate warming on Sphagnum photosynthesis in peatlands depend on peat moisture and species-specific anatomical traits, Global change biology, 25 (2019) 3859-3870.
[35] P. Geladi, B.R. Kowalski, Partial least-squares regression: a tutorial, Analytica chimica acta, 185 (1986) 1-17.
[36] A.M. Klasing, Make it Safe: Canada's Obligation to End the First Nations Water Crisis, Human Rights Watch, 2016.
[37] C.D. UWWTD, 91/271/EEC concerning urban waste water treatment, 1991, L, 135 40-52.
[38] S. Álvarez-Torrellas, M. Martin-Martinez, H. Gomes, G. Ovejero, J. García, Enhancement of p-nitrophenol adsorption capacity through N2-thermal-based treatment of activated carbons, Applied Surface Science, 414 (2017) 424-434.
[39] M.R. Turetsky, R.K. Wieder, C.J. Williams, D.H. Vitt, Organic matter accumulation, peat chemistry, and permafrost melting in peatlands of boreal Alberta, Écoscience, 7 (2000) 379-392.
[40] R.A. Bourbonniere, Review of water chemistry research in natural and disturbed peatlands, Canadian water resources journal, 34 (2009) 393-414.
[41] D.S. Kosyakov, N.V. Ul'yanovskii, T.B. Latkin, S.A. Pokryshkin, V.R. Berzhonskis, O.V. Polyakova, A.T. Lebedev, Peat burning–An important source of pyridines in the earth atmosphere, Environmental Pollution, 266 (2020) 115109.
[42] H. Knicker, How does fire affect the nature and stability of soil organic nitrogen and carbon? A review, Biogeochemistry, 85 (2007) 91-118.
[43] L. Bragazza, C. Freeman, High nitrogen availability reduces polyphenol content in Sphagnum peat, Science of the Total Environment, 377 (2007) 439-443.
[44] G. Naumova, A. Tomson, N. Zhmakova, N. Makarova, T. Ovchinnikova, Phenolic compounds of sphagnum peat, Solid Fuel Chemistry, 47 (2013) 22-26.
[45] V.E. Jassey, G. Chiapusio, E.A. Mitchell, P. Binet, M.-L. Toussaint, D. Gilbert, Fine-scale horizontal and vertical micro-distribution patterns of testate amoebae along a narrow fen/bog gradient, Microbial Ecology, 61 (2011) 374-385.
[46] D.J. Weston, C.M. Timm, A.P. Walker, L. Gu, W. Muchero, J. Schmutz, A.J. Shaw, G.A. Tuskan, J.M. Warren, S.D. Wullschleger, Sphagnum physiology in the context of changing climate: emergent influences of genomics, modelling and host–microbiome interactions on understanding ecosystem function, Plant, cell & environment, 38 (2015) 1737-1751.
[47] L. Bragazza, J. Limpens, Dissolved organic nitrogen dominates in European bogs under increasing atmospheric N deposition, Global Biogeochemical Cycles, 18 (2004).
[48] L. Li, S. Zhang, G. Li, H. Zhao, Determination of chemical oxygen demand of nitrogenous organic compounds in wastewater using synergetic photoelectrocatalytic oxidation effect at TiO2 nanostructured electrode, Analytica chimica acta, 754 (2012) 47-53.
[49] B.J. Cade-Menun, S.M. Berch, C.M. Preston, L. Lavkulich, Phosphorus forms and related soil chemistry of Podzolic soils on northern Vancouver Island. II. The effects of clear-cutting and burning, Canadian Journal of Forest Research, 30 (2000) 1726-1741.
[50] C. Ackley, S.E. Tank, K.M. Haynes, F. Rezanezhad, C. McCarter, W.L. Quinton, Coupled hydrological and geochemical impacts of wildfire in peatland-dominated regions of discontinuous permafrost, Science of The Total Environment, 782 (2021) 146841.

[51] C. Evans, I. Malcolm, E. Shilland, N. Rose, S. Turner, A. Crilly, D. Norris, G. Granath, D. Monteith, Sustained biogeochemical impacts of wildfire in a mountain lake catchment, Ecosystems, 20 (2017) 813-829.
[52] K. Burd, S.E. Tank, N. Dion, W.L. Quinton, C. Spence, A.J. Tanentzap, D. Olefeldt, Seasonal shifts in export of DOC and nutrients from burned and unburned peatland-rich catchments, Northwest Territories, Canada, Hydrology and Earth System Sciences, 22 (2018) 4455-4472.
[53] D.H. Vitt, Functional characteristics and indicators of boreal peatlands, in: Boreal peatland ecosystems, Springer, 2006, pp. 9-24.
[54] I. Tjerngren, M. Meili, E. Björn, U. Skyllberg, Eight Boreal Wetlands as Sources and Sinks for Methyl Mercury in Relation to Soil Acidity, C/N Ratio, and Small-Scale Flooding, Environmental Science & Technology, 46 (2012) 8052-8060.
[55] A.A. Mamuji, J.L. Rozdilsky, Wildfire as an increasingly common natural disaster facing Canada: understanding the 2016 Fort McMurray wildfire, Natural Hazards, 98 (2019) 163-180.
[56] F.-N. Robinne, K.D. Bladon, U. Silins, M.B. Emelko, M.D. Flannigan, M.-A. Parisien, X. Wang, S.W. Kienzle, D.P. Dupont, A Regional-Scale Index for Assessing the Exposure of Drinking-Water Sources to Wildfires, Forests, 10 (2019) 384.
[57] J. Fritsche, S. Osterwalder, M.B. Nilsson, J.r. Sagerfors, S. Åkerblom, K. Bishop, C. Alewell, Evasion of elemental mercury from a boreal peatland suppressed by long-term sulfate addition, Environmental science & technology letters, 1 (2014) 421-425.
[58] B. Smieja-Król, B. Fiałkiewicz-Kozieł, J. Sikorski, B. Palowski, Heavy metal behaviour in peat–A mineralogical perspective, Science of the total environment, 408 (2010) 5924-5931.
[59] J. Rothwell, K.G. Taylor, E. Ander, M. Evans, S. Daniels, T. Allott, Arsenic retention and release in ombrotrophic peatlands, Science of the Total Environment, 407 (2009) 1405-1417.
[60] T. Broder, H. Biester, Hydrologic controls on DOC, As and Pb export from a polluted peatland–the importance of heavy rain events, antecedent moisture conditions and hydrological connectivity, Biogeosciences, 12 (2015) 4651-4664.
[61] L.E. Brown, J. Holden, S.M. Palmer, K. Johnston, S.J. Ramchunder, R. Grayson, Effects of fire on the hydrology, biogeochemistry, and ecology of peatland river systems, Freshwater Science, 34 (2015) 1406-1425.
[62] K. Smettem, C. Rye, D. Henry, S. Sochacki, R. Harper, Soil water repellency and the five spheres of influence: A review of mechanisms, measurement and ecological implications, Science of The Total Environment, (2021) 147429.
[63] X. Yang, C. Fan, C. Shang, Q. Zhao, Nitrogenous disinfection byproducts formation and nitrogen origin exploration during chloramination of nitrogenous organic compounds, Water Research, 44 (2010) 2691-2702.

# Chapter 4

## Upcycling wildfire-impacted boreal peats into porous carbons that efficiently remove phenolic micropollutants

## 4.1 Abstract

Activated carbons have been widely used for water treatment due to their large surface area and structural stability. Their high cost has motivated the development of sustainable bio-based sorbents. However, their industrial acceptance within the water industry is limited by lower surface areas and poorer adsorptive capacities as compared with commercial sorbents. We herein report a green, high performance porous carbon produced from boreal peats for organic micropollutant removal. Boreal peatlands are increasingly damaged due to climate change-induced wildfires and droughts, which lead to increased run-off and impeded forest regrowth. Fire-impacted peatland soils therefore were excavated and converted into value-added porous carbons through $ZnCl_2$ activation at low temperature (400 – 600 °C). These products have significantly higher surface areas (> 1377 $m^2/g$) than commercial activated carbon Norit GSX (965 $m^2/g$). Adsorption of *p*-nitrophenol, a micropollutant, onto the porous carbons is efficient, and superior to that of Norit GSX and most sorbents reported in the literature. Adsorption mainly occurred through multi-layer chemisorption and was impacted by the electron donor-acceptor complexes mechanism, π-π interactions and steric effects. Because of the massive environmental and economic benefits, peat porous carbons are strong candidates for use in large-scale water treatment facilities.

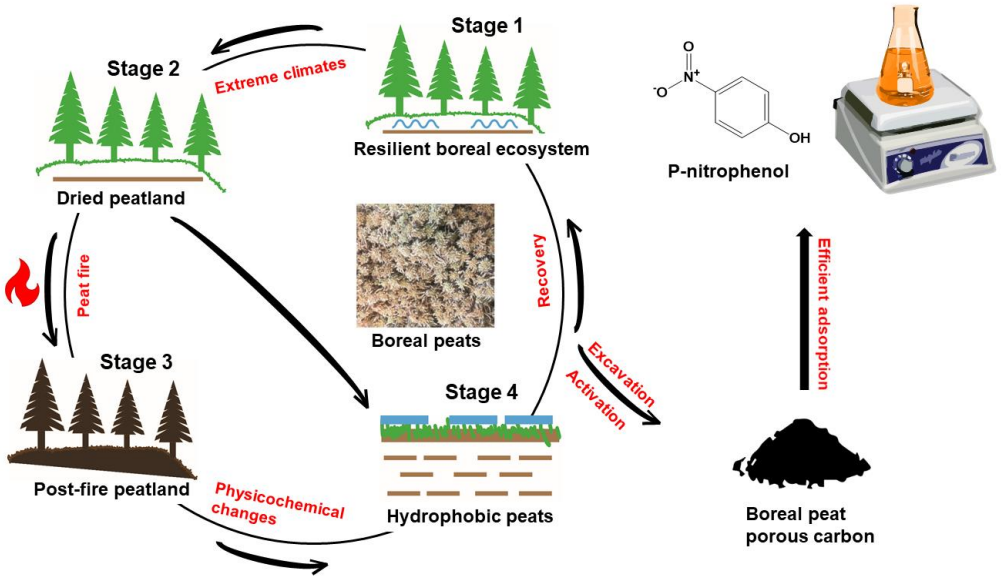


## 4.2 Introduction

Water pollution by organic micropollutants has garnered immense global awareness in recent years over the adverse impacts to ecosystems and human health [1]. Treated wastewater effluents contribute over 300 million tons of micropollutants into natural waters per year [2]. These pollutants, such as pharmaceuticals, steroid hormones, pesticides and other industrial chemicals, are characterized by their wide distribution and diversity in water systems. Nitro-aromatic compounds, such as nitrophenols, are commonly detected hazardous micropollutants in aquatic environments, due to extensive consumer product use (e.g. cosmetics, drugs and pesticides), industrial practices (e.g. oil refining, petrochemical processing, coal conversion, textile and dye production, paper milling) and natural processes (e.g. plant matter decomposition and microorganism metabolic processing) [3, 4]. Because of their taste, odor, toxicity and persistence, even at ppb levels, many phenolic compounds have been regulated as priority pollutants in the United States, Canada and the

European Union [5, 6]. The US-EPA recommends a maximum concentration of 1 ppm of total phenolic compounds in water supplies [7]. Increasingly stringent environmental regulations necessitate the improvement of water treatment techniques.

Widely investigated techniques for removing hazardous organic micropollutants include advanced oxidation processes [8], electrochemical oxidation [9], membrane processes [10], biological treatment [11], and adsorption [12]. Adsorption has been extensively used because of the versatility, effectiveness, simple operation, low initial cost and robustness to toxic pollutants [3]. Adsorption processes capture aqueous pollutants through electrostatic interactions, chemical reactions and hydrophobic interactions, depending on the chemistry of sorbents and sorbates [13]. activated carbons (ACs) are known for their high surface area, highly porous structure, surface oxygenated functionalities and good mechanical property [14], and hence are widely selected as adsorptive materials for water purification. However, commercial activated carbons (CACs) are increasingly undesirable because they are obtained from non-renewable carbonaceous materials (e.g. coals, and petroleum coke) [14]. Traditional production is energy intensive and thus costly, involving pyrolysis steps (typically 300–900 °C) using physical (e.g. using steam or $CO_2$, >700 °C) or chemical activation (e.g. using $H_3PO_4$, $ZnCl_2$, or KOH, commonly between 300 and 700 °C). Further, the surface areas of traditional CACs usually range from 500 to 1500 $m^2/g$ [15], but there has been a demand to develop more efficient materials with higher specific surface areas (up to or higher than 2000 $m^2/g$) and tailored microstructures [16].

Previous studies can only partially solve these challenges. Many inexpensive carbon-based sorbents (e.g. biochars and ACs) have been prepared using renewable biomass wastes, including agricultural wastes (e.g. corn stover [17], corn hull [17], rice husk [18], wheat straw [19], bagasse [19], peanut shell [20], coconut shell [20], potato peel [21]), forestry residues (e.g. bamboo [20], pine needles [22], eucalyptus bark [23], oak wood [17], palm shell [24]), livestock wastes (e.g. cattle manure [25]), and some biopolymers (e.g. cellulose and Kraft lignin). However, many upcycled bio-products (with or without further modification) often have lower surface areas than CACs, and they oftentimes give lower adsorptive capacities towards pollutants, including small organic micropollutants. For instance, rice husk AC achieved a maximum adsorption capacity nearly 6 times lower than CAC for phenol (56 mg/g vs 322.5 mg/g) [12, 18]. Magnetized palm shell AC had 163.3 mg/g removal towards methylene blue [24], much inferior to using CAC (i.e. 980.3 mg/g) [26]. Moreover, many agro-forestry wastes have low yield and their collection is costly and labor intensive. Thus, while environmentally viable, the novelty and usefulness of bio-based sorbents are restricted by their unsuitable origins, poor adsorption capacities and low economic benefits.

Boreal peatlands occupy 3% of the world's land area and store more than 25% of the Earth's terrestrial carbon [27]. Peatlands are widely distributed over nearly 4,000,000 $km^2$ in North America and Eurasia [27]. They are also increasingly impacted by climate change (Graphical abstract, Stage 1). As a result of climate change-induced impacts to boreal temperatures and precipitation events, boreal peatlands are increasingly damaged by wildfires and droughts (Graphical abstract, Stage 2 and 3), as demonstrated by the

surprising peat fires that have raged across Russia, Canada, and other subarctic regions in the past few years [28]. Shallow organic layers of peats, which are comprised of live moss and partially decayed plant matter, are typically the most affected by recurring droughts and wildfires. Impacts to peats include combustion, smoldering, and desiccation, leading to elevated water repellency for these damaged shallow layer peats which leads to severe flooding, soil erosion and inhibited forest recovery (Graphical abstract, Stage 4) [29]. The most frequently encountered peat fires in the boreal are low-severity burns that can ignite above-ground vegetation but only yield minor loss of underlying peats to combustion [30]. Rather than fully combust, peat is most often heated between 300 and 500 °C by low-severity fires (e.g. smoldering), which transforms its chemical composition [29, 31]. The increasing smoldering of peat is problematic from an ecological and climate perspective, as peatlands represent the largest soil organic carbon sink on Earth, with an estimated 427 Gt of carbon stored in boreal peatlands across the globe, 150 Gt of which is stored in Canada alone [32, 33].

Excavation of the climate change-impacted peats can promote water retention in burned forests while reducing peat fire events in boreal ecosystems [29]. Access through logging roads to the vast areas of pre- and post-burned damaged peat soils makes their excavation relatively simple. However, damaged peatland soils are left untreated on the forest floor due to a lack of practical uses. We have identified that the carbon-rich nature of peats make them ideal candidates for producing carbon-based sorbents, which have applications in environmental remediation and water treatment. Pyrolysis of smoldering-heated peats can lock in the carbon stored within these peats, while also producing a valuable product that

can replace less sustainably sourced porous carbons. We herein report for the first time the environmental application of climate-impacted peatland soils. Based on a rapid and facile chemical activation step, these materials can be readily converted into high surface area porous carbons, for effective purification of organic-polluted water. Their relevance to adsorption of a notorious phenolic micropollutant (*p*-nitrophenol) in water and the advantages over a CAC sorbent (Norit GSX) and conventional bio-based sorbents is also investigated.

## 4.3 Material and methods

### 4.3.1 Materials and reagents

*Feather moss* and *sphagnum* peatland soils were collected from the undisturbed boreal spruce forested peatland in the Pelican Mountain research site (55°36' N, 113°35' W) in Alberta, Canada. Intact peats (up to 15 cm depth) were cored in PVC pipes (dia. 10 cm), sealed with plastic films, and transported to the lab. The boundary between the live moss and the decomposed peat in the peat columns for *feather moss* was clear, but for *sphagnum* was indiscernible. Thus, we retained the live *feather moss* and the entire 15 cm *sphagnum* for investigation. For consistency in this study, twigs and wood debris were manually removed. Cellulose, corn starch, $ZnCl_2$ (anhydrous, >97%), steam-activated CAC, Norit GSX and 1.0 M HCl solution were purchased from Sigma-Aldrich.

Drought-dried peat soils were simulated by 105 °C oven-drying overnight and sieved to less than 2 mm size. Post-burned peat soils were simulated by heating in a muffle furnace at 300 °C for 30 min. The heat treatment did not combust the samples and could well-mimic the low-severity fires that damaged the majority of peatland soils. Cellulosic

materials and carbohydrates represent important biopolymers within surface peats, so cellulose and corn starch were used as pure components for comparison. Starch is typically unsuitable for directly making porous carbons because it swells and bursts with heat treatment to form foam like structures, which do not contribute to an increase in total surface area. Hence, corn starch was stabilized at 220 °C for 16 h to promote dehydration of reactive hydroxyl groups which are the primary moiety on starch polymer chains, pulverized by a coffee grinder, and sieved to less than 2 mm size. Cellulose was not further treated. *Feather moss*, *sphagnum*, corn starch, cellulose, burned *feather moss*, burned *sphagnum* and stabilized starch were respectively labelled as Fm, Sph, CS, CL, BFm-300, BSph-300 and BCS-220.

### 4.3.2 Synthesis approach

In a typical experiment, the precursors were well-mixed with $ZnCl_2$ powders (m/m 1:3) and directly heat-treated in a tube furnace under inert $N_2$ flow (100 mL/min) at 400 or 600 °C for 1 hr. $ZnCl_2$ was chosen for chemical activation, because it only demands moderate heating temperature, and could be readily impregnated with precursors during the thermal treatment. This showed some strengths over many other activation agents. For example, KOH activation is typically done at high temperature, up to 800–1000 ℃ [34], which is energy-intensive and could cause corrosion to the reactor. $H_3PO_4$ activation can be accomplished at lower temperatures (< 600 ℃ [34]), but would require an additional aqueous impregnation step prior to activation, because $H_3PO_4$ is commonly stored as a solution. Furthermore, $ZnCl_2$ activation helps to limit macroporosity and maximize microporosity [35], which is beneficial for the adsorption of small organic

pollutants from water. An impregnation ratio of 1: 3 (precursor: $ZnCl_2$) was selected because this is a reasonable ratio enhancing the formation of micro- and mesopores over heat treatment [36]. The tube furnace temperature was preset to 200 °C prior to the experiments. After the activation, those samples treated at 400 °C were removed from the chamber, whereas those treated at 600 °C were left inside the chamber for natural cooling under $N_2$ flow for a further 20 min before removing them. The post-treatment samples were washed with 1.0 M HCl and DI water, then oven-dried at 105 °C overnight. Each test was done in triplicate. Porous carbons manufactured from Fm, Sph, BFm-300, BSph-300, BCS-220 and CL were respectively labelled as FmZC-T, SphZC-T, BFmZC-T, BSphZC-T, BCSZC-T and CLZC-T, where T refers to the temperature applied.

### 4.3.3 Material characterization

Elemental analyses were performed by an elemental analyzer (UNICUBE, elementar, Germany). Sulfanilamide was used as a calibration standard for the instrument. 2 mg of samples were loaded into tin capsules in a carousel for sequential analyses. CHNS mode was chosen and O content was measured by weight difference. Zeta potential ($\zeta$) was determined by a zeta potential analyzer (ZetaPlus, Brookhaven Instruments, USA). $pH_{PZC}$ was obtained by plotting zeta potential as a function of pH and identifying the pH at which zeta potential crosses zero at the x-axis.

Brunauer-Emmet-Teller (BET) specific surface area was measured by $N_2$ adsorption-desorption isotherms, using a gas sorption analyzer (Autosorb iQ, Quantachrome Instruments, USA). Samples were degassed at 105 °C for 24 h prior to physisorption. Total pore volume ($V_{tot}$) was estimated based on the density function theory (DFT) method.

Micropore surface area ($S_{Micro}$) and micropore volume ($V_{Micro}$) were calculated based on the t-plot method of de Boer and Horvath-Kawazoe (HK) method, respectively. Mesopore surface area ($S_{Meso}$) and mesopore volume ($V_{Meso}$) were respectively obtained by subtracting $S_{Micro}$ from $S_{BET}$, and $V_{Micro}$ from $V_{tot}$. The pore size distribution and pore widths of the samples were characterized by the slit pore, non-local density functional theory (NLDFT) equilibrium model. Samples' structure and surface morphology were characterized by a JEOL JSM-7000 F SEM equipment. Sample surface coating was 7 nm of platinum (Pt).

Infrared spectra was identified by a Nicolet 6700 FT-IR spectrometer (Thermo Scientific, USA). Spectra were recorded within the mid-infrared range from 4000 to 525 $cm^{-1}$ at 4 $cm^{-1}$ resolution for a total of 64 scans. X-ray Photoelectron Spectroscopy (XPS) was used to characterize surface elemental species and possible chemical environment/molecular bonding of carbon atoms. X-ray beam was set at 25 W and 15 kV and the beam size was 100 μm in diameter. The photoelectron take-off angle (angle between analyzer axis and sample surface) was 45º. The pass energy for survey scan and C1s high resolution scan spectra were 224 eV and 26 eV respectively. In the C1s peak fitting analyses, background was approximated by Shirley method, and all the binding energies were calibrated with respect to the C1s peak at 284.8 eV. Powder X-ray Diffraction (XRD) patterns were obtained from 10° to 70° in 2-theta with a Cu diffractometer operating at 40 kV and 40 mA with a step time of 600 s to determine the crystal structure and amorphous nature.

### 4.3.4 Adsorption studies

Batch adsorption tests were conducted at 20 °C on the basis of phosphate-buffered (pH = 7 ± 0.3, molarity = 20 mM) synthetic *p*-nitrophenol wastewater (20–2000 mg/L). The neutral condition for the batch tests is within the pH ranges of surface waters, most municipal wastewaters and some industrial wastewaters under real condition. The buffer solution was prepared by adding 1.165 g $NaH_2PO_4 \cdot H_2O$ and 3.097 g $Na_2HPO_4 \cdot 7H_2O$ into 1 L DI water. Before adsorption, calibration curve for *p*-nitrophenol was established at the maximum wavelength of 400 nm.

Phosphate-buffered *p*-nitrophenol solutions (20–2000 mg/L) were dosed with selected sorbents (10 mg) and stirred at 200 rpm at 20 °C for 24 hrs to reach equilibrium. This maximum range was chosen to mimic the highest concentrations found in some wastewaters. The solutions after adsorption were filtered, diluted if necessary, and analyzed by UV–vis spectrophotometer at 400 nm. Experiments were conducted in triplicate for high concentration samples (i.e. 1000 and 2000 mg/L) to minimize the possible errors. Experimental data were fitted into Freundlich, Langmuir and Redlich-Peterson isotherms by 1stOpt software.

Phosphate-buffered *p*-nitrophenol solutions (20 mg/L) were dosed with selected sorbents (10 mg) and stirred at 200 rpm at 20 °C for different time durations (0–4 h). Suspensions were filtered and measured by UV–vis spectrophotometer. Preliminary experiments indicated that 4 h adsorption can achieve 98% removal of *p*-nitrophenol, and 24 hrs was sufficient to reach equilibrium. Data collected were fitted with Lagergren pseudo-first-order model, Ho & Mckay pseudo-second-order model [37] and Weber-Morris intra-

particle diffusion model [38]. The models for isotherm and kinetic adsorption can be found in the Supplementary Material. The fitted determination coefficient ($R^2$) could well reflect the variance about the mean [39], and was used to evaluate the fitting degree for the isotherm and kinetic models.

## 4.4 Results and discussion

Laboratory simulated drought-dried and post-fire peatland soils were activated and analyzed for their ability to act as high surface-area sorbents for the adsorption of *p*-nitrophenol micropollutant from wastewaters. Porous carbons made from peats were compared with those made from the primary constituents of peat - cellulose and starch as well as with commercially available activated carbon.

### 4.4.1 Physicochemical properties of bio-based porous carbons

#### 4.4.1.1 Elemental compositions

The organic content of the collected fresh surface peats were extremely high (>99%), as determined by burning the samples at 550 °C for 4 h in a muffle furnace. XPS full scan spectra (Fig. S2) also confirmed that no mineral elements were found in the samples. Table S1 indicates the organic elemental compositions present in all tested materials. As expected, C, H and O accounted for the majority of the total elemental content (> 98%). 300 °C heated boreal peat *feather moss* (BFm-300) and *sphagnum* (BSph-300) and 220 °C heat-stabilized corn starch (BCS-220) had an increase in C content and concurrently a decrease in O and H content compared to their respective precursors (Fm, Sph and CS), due to dehydration and partial combustion of organic matter. Bio-based porous carbons rendered much higher C contents (76.6–93.6%) than their precursors (41.4–61.3%). This is because $ZnCl_2$ acted

as a Lewis acid which contributed to selective stripping of O and H to $H_2O$ and $H_2$, rather than hydrocarbons from the aromatic/phenolic structures [40, 41]. As shown in the van Krevelen diagram, Fig. 1, H/C ratios varied depending on biomass type (1.44–1.88). The values for boreal peats were fairly close to 1.5, which approximated the composition of unburned fuel materials, such as cellulose and lignin [41]. The decrease of H/C and O/C ratios for heat-treated materials indicated chemical changes, in particular decarboxylation (i.e. loss of $CO_2$ and/or CO) and demethylation (i.e. loss of $CH_3$) [42]. The H/C ratios of all sorbents were less than 0.5 and this accorded with most pyrolysis-based materials [41]. During synthesis, both dehydration and chemical changes (decarboxylation & demethylation) through crosslinking condensation reactions would occur, which got intensified at higher temperature. Hence, the 600 °C activated materials exhibited higher carbonization degree and fewer oxygenated functionalities due to cleavage and cracking of weak oxygenated bonds within solid structures [42]. This was supported by reduced molar ratios of O/C and H/C at 600 °C, which also suggested a higher aromaticity and heating value (low H/C), and lower polarity and hydrophilicity (low O/C) [43]. Meanwhile, the H/C values less than 0.2 implied the formation of "black carbon", which likely contained highly porous polyaromatic structures and graphitic carbon fractions [44]. Norit GSX had the minimal H/C value ($< 0.1$), suggesting soot and lignite compositions and graphite-like structures [41].

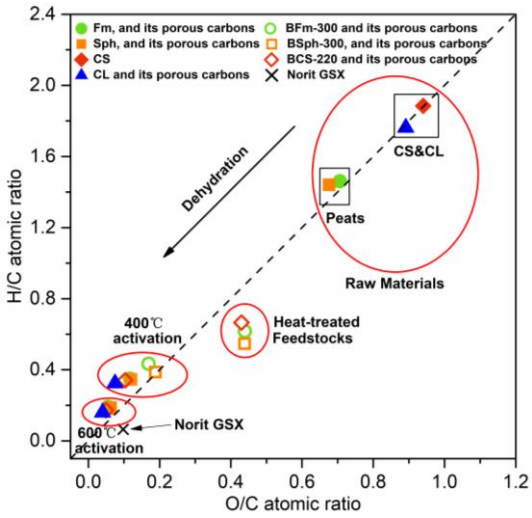


**Fig. 1.** van Krevelen diagram of elemental ratios (H/C vs O/C) for raw feedstocks and different sorbents.

#### 4.4.1.2 Point of zero charge ($pH_{PZC}$)

Surface charge of the sorbents at a range of pHs were controlled by the protonation/deprotonation of surface functional groups [45]. The bio-based porous carbons demonstrated acidic character ($3 < pH_{PZC} < 4$), and with an increase in activation temperature, $pH_{PZC}$ values slightly increased due to slight variations in surface charge and oxygen complexes. When $pH < pH_{PZC}$, $\zeta$ is positive (surface charge becomes positive). Thus, the HCl washing ($pH = 1 < pH_{PZC}$) likely led to the protonation of hydrated surface functional groups (e.g. –COOH) with the concurrent loss of residual minerals ($ZnCl_2$) used for pore formation. The adsorption experiment was conducted in neutral condition ($pH = 7 > pH_{PZC}$), hence the negatively charged surface of sorbents likely favored the adsorption of cationic species.

#### 4.4.1.3 Surface chemistry and functional groups

Table S2 provides FTIR assignments of boreal peats and the corresponding porous carbons. Results identified that the boreal peats contain hydroxyl groups, aliphatic hydrocarbons, carbonyl groups, aromatic carbon structures, carboxylic groups, which are related to the lignin and cellulosic structures, and small organic molecules. This was confirmed by the characteristic peaks at around 3340 $cm^{-1}$ (O–H), 2920 and 2850 $cm^{-1}$ ($CH_2$), 1720 $cm^{-1}$ (C=O), 1610 $cm^{-1}$ (C=C) and 1030 $cm^{-1}$ (C–O). Fm and Sph precursors, however, had a few differences in their chemical compositions. As shown in Fig. S1a and S1b, Fm had sharper twin peaks near 2920 and 2850 $cm^{-1}$ than Sph. This suggested stronger C–H stretching of alkyl chains, thus indicating more abundant plant lipids, such as fatty acids [46]. Fm had the C=O vibration at 1731 $cm^{-1}$, which was likely caused by ketones, aldehydes and aromatic esters [47]. Sph had the C=O vibration shifted to 1716 $cm^{-1}$. This may suggest the presence of carboxylic acids [46]. The laboratory-simulated burned peats had significant peak losses. Their hydroxyl peak (broad beak close to 3340 $cm^{-1}$) was greatly reduced, while carbonyl groups (shifted to 1711–1716 $cm^{-1}$) and aromatic carbon stretching (shifted to 1597–1601 $cm^{-1}$) remained predominant. ACs prepared at 400 °C retained the carbonyl groups (1694–1699 $cm^{-1}$) and the oxygen-containing aromatics (1558–1590 $cm^{-1}$) such as quinones. These bands were shifted by a few units to the right due to heat-induced chemical transformations of labile organic compounds (the biologically active fraction of soil) to form new carbonyl groups [48], and the increased level of aromaticity through $ZnCl_2$ activation. With an increase of activation temperature to 600 °C, Porous carbons lost more carbonyl groups but still preserved the aromatic C=C

vibrational bands (shifted to 1557–1574 $cm^{-1}$), while their relative intensity became lower. This indicates the deposition of carbonyl-containing groups as a result of losing organic matters, and the destruction of highly aromatic functionalities. C-O stretching from aromatic ethers, esters, alcohols or phenols (1228–1251 $cm^{-1}$) also appeared for porous carbons prepared at both temperatures [49]. CS (α-glucose) and CL (β-glucose) precursors are isomers and displayed similar FTIR peak patterns (Fig. S1c and S1d). Characteristic bands included 3297, 3330 $cm^{-1}$ (O–H), 2929, 2892 $cm^{-1}$ (C–H), 1645 $cm^{-1}$ (C–O), and 996, 1026 $cm^{-1}$ (C–O). After heating and activation, CS and CL samples had many diminished functional groups across a broad range, but an increase in new carbonyl compounds (1699–1713 $cm^{-1}$), aromatic ring structures (1557–1607 $cm^{-1}$) and aromatic ether or esters (1170–1258 $cm^{-1}$).

XPS survey spectra (Fig. S2) in the binding energy ranging from 0 to 1100 eV supported that carbon and oxygen were the primary elements present in the investigated samples due to the appearance of characteristic peaks (e.g. O1s and C1s). The distinct C1s peaks were further deconvoluted to show the possible carbon species and estimate the relative composition of major carbon surface functional groups identified from FTIR. Fig. 2 reveals the fractions of different carbon groups of the total carbon groups on surfaces. The high resolution C1s spectra can be found in Fig. S3. C1 regions can be fitted into up to four carbon states corresponding to: 1) C-C that from either amorphous or aromatic (graphitic) carbon (284.8 eV), 2) C-OH/C–O–C from phenolic groups, alcohols and ethers (286.0 eV), 3) C=O/O–C=O from lactone, carboxyl or ester groups (288.5 eV) and 4) the π-π* graphitic shake-up satellite peak from aromatic rings (291.0 eV) [50]. Of note, the peak positions

shifted slightly among samples because of the effects of neighboring atoms present on their surfaces. The proportion of each carbon species was obtained by determining the contribution of curve areas for individual carbon state to the total curve area. From the C1s curve fitting (Fig. 2), all final products had elevated fractions of amorphous carbon content (284.8 eV), nearing 60% or higher, which was expected for activated carbons. Regardless of the products, C–O and C-O-C were much more abundant than C=O and O–C=O amongst the oxygenated carbons (i.e. carbon species at 286.0 and 288.5 eV), which can also be verified by comparing the corresponding FTIR peak intensities (Fig. S1). It is presumed that C=O and O–C=O were formed during $ZnCl_2$ activation. For any one as-prepared product, the fraction of C=O and O–C=O as a function of the overall C bonding tend to increase slightly with activation temperature. This may signify the improved extraction of molecular hydrogen and hydroxyl groups during $ZnCl_2$ activation at higher temperature. Moreover, the π-π* peak at 291.0 eV appeared for all sorbents. The fraction of this carbon species increased with activation temperature for all samples except one (the heat stabilized corn starch derived products), which suggests higher temperatures led to the formation of more delocalized π conjugation from aromatic C structures.

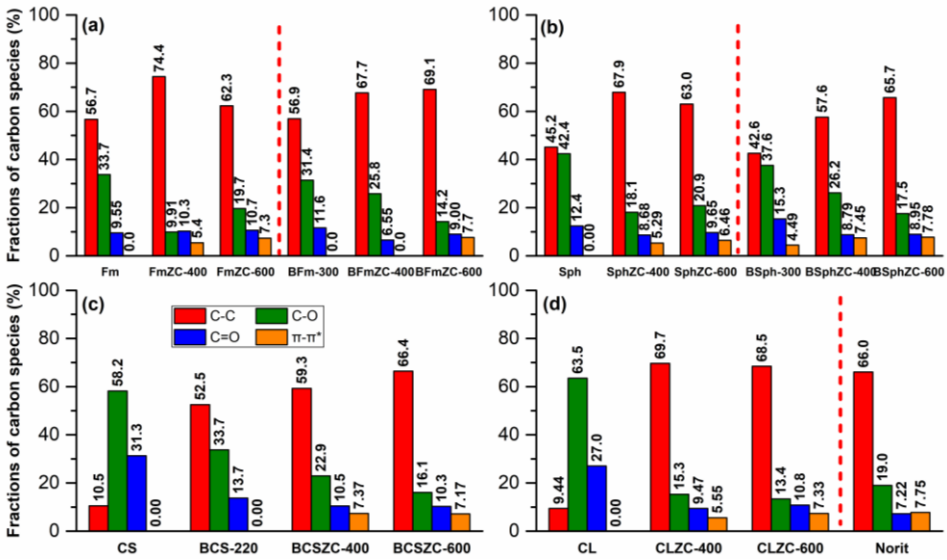


**Fig. 2.** XPS percentage fractions of different carbon groups of C1s fittings for (a) *feather moss* and its derived porous carbons, (b) *sphagnum* and its derived porous carbons, (c) corn starch and its derived porous carbons, (d) cellulose and its derived porous carbons, and Norit GSX.

#### 4.4.1.4 Surface area, pore volume and pore size

BET surface area, pore size and pore volume were summarized in Table 1. Precursor materials (raw boreal peats, corn starch, cellulose, heat-treated boreal peats and corn starch) exhibited extremely low surface areas. $ZnCl_2$ in-situ activation contributed to particle swelling, release of evaporative organic matter (e.g. tar) and development of new pores [51], thereby remarkably increasing the BET surface areas (1377–2527 $m^2/g$), which greatly exceeded that of Norit GSX (965 $m^2/g$). Surface area and pore structures are related to temperature and $ZnCl_2$ impregnation ratio [40, 52]. Generally, surface area increases with an increase of $ZnCl_2$ to feed stock impregnation ratio within a limited range (e.g. 0–2) and activation temperature (e.g. $< 450$ °C), but tends to decrease if $ZnCl_2$ is used in excess (e.g. 2–4) and the activation temperature is high (e.g. $> 450$ °C) [52]. Nonetheless, the trend is not always consistent across the literature and is dependent on the type of the starting feedstocks and the activation method used. Our study showed that higher

temperature activation gave rise to lower BET surface areas, lower micropore surface areas and lower micropore volumes for most bio-based porous carbons except for those prepared from pre-burned (300 °C heat-treated) boreal peats.

**Table 1** Surface area, pore volume and particle size of feedstocks and different sorbents.

| Precursor type | Material | $S_{BET}$ ($m^2/g$) | $S_{Micro}$[a] ($m^2/g$) | $S_{Meso}$ ($m^2/g$) | $V_{tot}$[b] ($cm^3/g$) | $V_{Micro}$[c] ($cm^3/g$) | $V_{Meso}$ ($cm^3/g$) | $V_{Micro}$ (%) | PW[d] (nm) |
|---|---|---|---|---|---|---|---|---|---|
| boreal peats | Fm | 1.3 | — | — | — | — | — | — | 2.647 |
| | FmZC-400 | 1989 | 1091 | 898 | 1.110 | 0.801 | 0.309 | 72.1 | 1.614 |
| | FmZC-600 | 1605 | 555 | 1050 | 1.226 | 0.650 | 0.576 | 53.0 | 1.614 |
| | Sph | 9.6 | — | — | — | — | — | — | 2.647 |
| | SphZC-400 | 1783 | 867 | 916 | 1.052 | 0.726 | 0.326 | 69.0 | 1.614 |
| | SphZC-600 | 1731 | 616 | 1115 | 1.240 | 0.702 | 0.538 | 56.6 | 1.614 |
| 300 ℃ simulated burned boreal peats | BFm-300 | 10.5 | — | — | — | — | — | — | 2.647 |
| | BFmZC-400 | 1383 | 1144 | 239 | 0.612 | 0.559 | 0.052 | 91.4 | 1.614 |
| | BFmZC-600 | 1719 | 1357 | 362 | 0.774 | 0.568 | 0.206 | 73.3 | 1.614 |
| | BSph-300 | 14.3 | — | — | — | — | — | — | 2.647 |
| | BSphZC-400 | 1377 | 1158 | 219 | 0.601 | 0.559 | 0.043 | 92.9 | 1.614 |
| | BSphZC-600 | 1875 | 1391 | 484 | 0.879 | 0.769 | 0.110 | 87.5 | 1.614 |
| 220 ℃ stabilized corn starch | CS | 2.0 | — | — | — | — | — | — | 2.769 |
| | BCS-220 | 1.9 | — | — | — | — | — | — | 2.647 |
| | BCSZC-400 | 1923 | 1484 | 439 | 0.872 | 0.774 | 0.098 | 88.8 | 1.614 |
| | BCSZC-600 | 1711 | 1456 | 255 | 0.705 | 0.688 | 0.017 | 97.6 | 1.614 |
| cellulose | CL | <1 | — | — | — | — | — | — | — |
| | CLZC-400 | 2527 | 435 | 2092 | 1.668 | 0.994 | 0.675 | 59.6 | 1.614 |
| | CLZC-600 | 2050 | 281 | 1769 | 1.321 | 0.819 | 0.502 | 62.0 | 3.627 |
| commercial AC | Norit GSX | 965 | 704 | 261 | 0.667 | 0.393 | 0.275 | 58.9 | 1.543 |

a. Micropore surface area ($S_{Meso}$) was calculated based on t-plot method, $S_{Meso}=S_{BET}-S_{Micro}$.
b. Total pore volume ($V_{tot}$) was determined based on the DFT method.
c. Micropore volume ($V_{Micro}$) was determined using the H-K method. $V_{Meso}=V_{tot}-V_{Micro}$.
d. Pore width (PW) was measured using DFT method.

The increased porous characteristics at 400 °C may be explained by $ZnCl_2$'s dehydration effects for promoting charring and aromatization of the carbons [52]. 600 °C activation, however, may cause partial shrinkage of the char, realignment of carbon structures and pore coalescence due to sintering effects under the selected impregnation mass ratio (i.e.

$ZnCl_2$/precursor = 3) [51]. The possible destruction of micropores and formation of mesopores may result in decreased surface area and increased pore volume. Increases in pore volume within a material were matched by a decrease in microporosity due to pore enlargement. Significantly, porous carbons synthesized from 300 °C heat-treated boreal peats had the opposite trend, i.e. micropore surface area increased at higher temperatures. This is probably because the impregnated amount of $ZnCl_2$ for these precursors was not excessive, and therefore $ZnCl_2$ continued to assist the formation of new pores and widening of existing pores even at elevated temperatures.

BET $N_2$ adsorption/desorption isotherms were also studied. Based on the IUPAC classifications, the precursors displayed type II isotherms (Fig. S4) suggesting macroporous characteristics (pores > 50 nm) for unrestricted adsorption. Porous carbons derived from heat-treated boreal peats and corn starch exhibited strong type I isotherms (Fig. 3a–c). Micropore filling and therefore high uptake at low relative pressures (< 0.1) were observed, followed by low slope (nearly horizontal) plateaus at higher relative pressures. This is indicative of microporous materials with narrow pore size distributions and small external surface areas (low mesoporosity) (Fig. 3d–f) [23, 24]. The higher microporosity for these porous carbons may be the result of less tar formation and light organic matter volatilization from the heat-stabilized carbon materials as compared to their raw counterparts during the synthesis. By contrast, type IV isotherms well-matched the curve shapes for porous carbons derived from raw boreal peats and cellulose (Fig. 3a–c), where characteristic hysteresis loops appeared appreciably at high relative pressure values (0.40–0.95) due to pore condensation, suggesting mesoporous structures [18]. In these

materials, pore widening rather than micropore formation dominated the porosity [52]. Cellulose derived porous carbons (Fig. 3c) had hysteresis loop shapes close to type H2 & H4, suggesting slit pores and/or unwell-defined pore sizes and shapes, which existed primarily in the small mesopore ranges (2–4.5 nm) (Fig. 3f). These materials' structures were comparable to Norit GSX, in which the isotherm was close to type IV. Particularly, 400 °C prepared boreal peats porous carbons had hysteresis loop slopes close to type H4 (narrow slit pores, including those in the micropore regions), whereas 600 °C prepared boreal peats porous carbons demonstrated shapes close to type H3 (slit pores with wide size distributions resulting from plate-like particles) (Fig. 3a–b). Type H3 and type H4 hysteresis loops supported the presence of slit-pores of these materials. Overall, from BET analysis, boreal peats and cellulose derived sorbents displayed similar porous structures to Norit GSX, while burned boreal peats and heat-stabilized corn starch derived sorbents exhibited substantially higher microporosity.

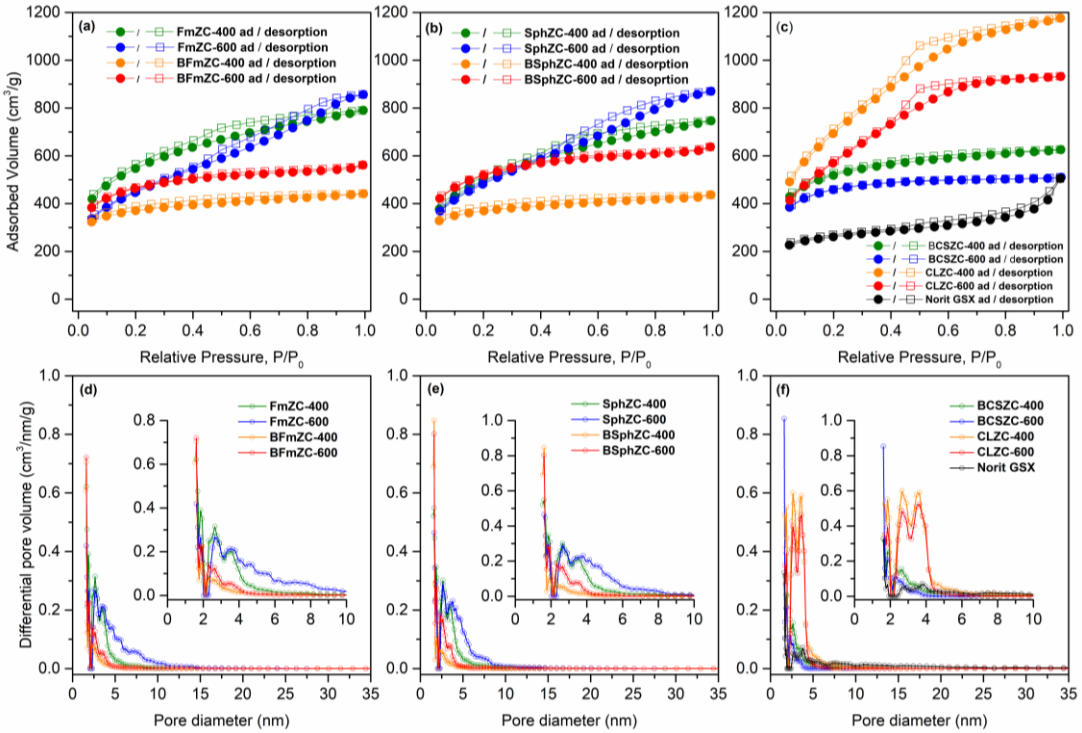


**Fig. 3.** BET $N_2$ adsorption-desorption isotherms and pore size distributions of tested adsorbents and (a, c) *feather moss* porous carbons, (b, d) *sphagnum* porous carbons, (c, f) corn starch porous carbons, cellulose porous carbons and Norit GSX.

#### 4.4.1.5 Textural and morphological properties

Fig. 4 shows the XRD profile of various studied materials. Two broad diffraction peaks emerged at 2θ around 22.6° and 44.1°, which were assigned to the diffuse graphite planes of the (002) and (100) planes respectively, implying a turbostratic structure (out-of-alignment basal planes) of disordered carbon (random layer lattice structure) [53]. As to porous carbon products, with the rise of activation temperature, the (002) band at 22.6° became sharper and less wide, while the (100) band intensity at 44.1° slightly increased. Such patterns suggest an increase of crystallite size, graphitic structure and aromatic layers [53]. Besides, boreal peats and their derived porous carbons as well as Norit GSX exhibited a narrow but sharp crystalline peak at varied intensities at 2θ around 26.5°. This

is characteristic for highly graphitized fractions with good crystallinity and degree of order, which also became enhanced at higher activation temperature (i.e. 600 °C) [54]. Thus, these materials were mainly amorphous, but contained some graphitized microcrystals within their structures. The curved layers of carbon within the amorphous structures of the synthesized porous carbons contained distorted aromatic carbon rings and defective regions, which reduced carbon stacking density and led to high surface area, beneficial for adsorption applications [55].

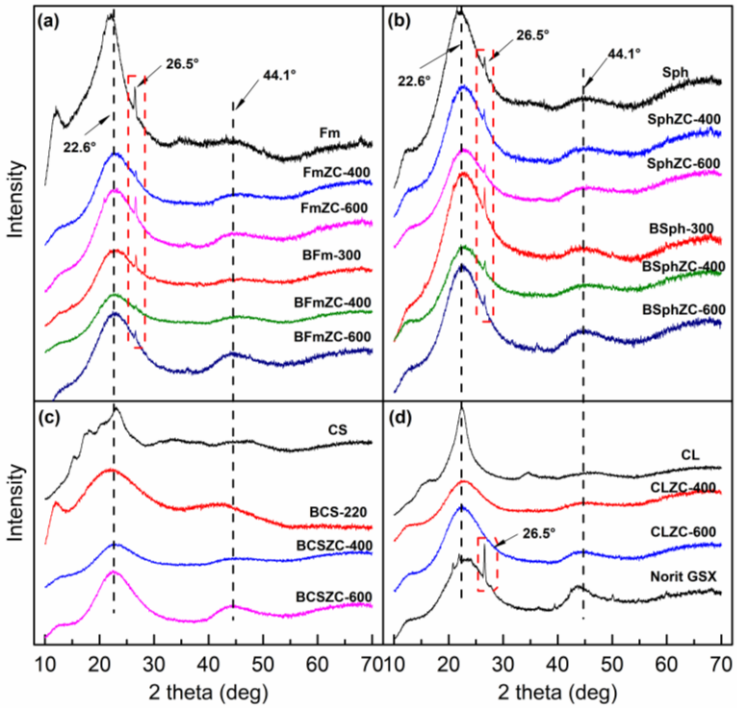


**Fig. 4.** XRD patterns of (a) *feather moss* and its derived porous carbons, (b) *sphagnum* and its derived porous carbons, (c) corn starch and its derived porous carbons, (d) cellulose and its derived porous carbons, and Norit GSX.

Figs.5 and S5 indicate the morphology of samples by SEM images. SEM analysis probes large micrometer (>1 μm) pore structures on the materials, and is a useful supplement to BET characterization to extend the range of morphological analysis from nanometer to

micrometer sized pores. BET probes the pore characteristics at the nanoscale, i.e. identifying the micropores (≤ 2 nm) and the mesopores (2–50 nm), but does not measure micrometer-sized pores. *Feather moss* contained no observable micrometer size-scale pores on the surfaces of the flat lateral walls (Fig. S5a1), but *sphagnum* contained large pore openings (> 10 μm) of the dead cells at the exterior leaf and suggested more complex internal arrangements (Fig. 5a1). Following heat treatment at 300 °C for 30 min, considerable volatilization and thermal degradation of peat constituents may occur, and the peat grains became more fragmented with mild shrinkage of the micrometer size surface pores (Figs. 5ba and S5b1). Pyrolysis in the tube furnace led to more irregular textures and textures for the carbon matrix, such as increased peat fragments, surface heterogeneity and enlarged micrometer sized cavities (Fig. 5a2, a3, b2, b3; Fig. S5a2, a3, b2 and b3). In addition, the hybrid transverse sections of peat fragments indicated highly porous network structures of peat stem internal regions after chemical activation (see the small images in Fig. 5a2, a3, b2, b3; Fig. S5 a2, a3, b2 and b3), which could be synergistically attributed to their original internal structures and $ZnCl_2$'s effects on pore development and enlargement inside cell walls. Pristine corn starch material had irregular spherical topography and smooth surface with particle size between 10 and 20 μm (Fig. S5c1), yet 220 °C stabilization of it destroyed the original morphology and led to collapse of the particles possibly due to thermal dehydration and melting of crystallites (Fig. S5c2). Untreated cellulose had well-separated fibers in flat rod shapes, with diameters ranging from 10 to 30 μm, and lengths between 200 and 500 μm (Fig. S5d1). After $ZnCl_2$ activation, the BCS-220 and CL derived porous carbons formed big chunks at micrometer scales.

While BET has probed the existence of considerable nanometer sized pores, no clear micrometer sized pores were observed on the material surfaces. The surface morphology for BCS-220 derived porous carbons (Fig. S5c3 and S5c4) were rough, while CL derived porous carbons (Fig. S5d2 and S5d3) were finer and smoother. All the synthesized products after acid treatment, drying and manual pulverization had a particle size greater than 100 µm. Nonetheless, the commercial Norit GSX (Fig. S5e) had the smallest particle size of all, which was typically less than 30 µm.

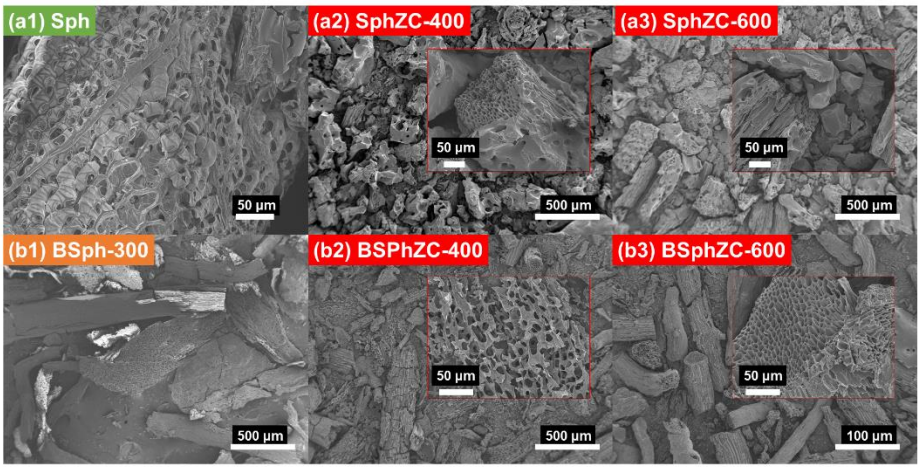


**Fig. 5.** SEM images of pre- and post-heat *sphagnum* precursors and their derived sorbents. All micrographs were obtained at 5 eV.

### 4.4.2 Adsorptive characteristics of *p*-nitrophenol on activated carbons

#### 4.4.2.1 Adsorption isotherms

Nonlinear increase of adsorption quantity was observed with increase of equilibrium concentration (Fig. 6a-b). Isotherm model fitting results obtained by 1stOpt software are summarized in Table S3, and generally, both Freundlich and Redlich-Peterson models provided good correlations for the equilibrium data (Fig. 6c-d), while Langmuir model afforded the poorest fit. Because the equilibrium data conformed poorly to the Langmuir

isotherm especially for high concentration ranges where multilayer adsorption could occur, the authentic maximum adsorption capacities were underestimated at some degree by the $q_m$ values acquired by this model. Nevertheless, using the Langmuir model, the fitted data demonstrated highly favorable adsorption behaviors for the produced porous carbons because $R_L \ll 1$ and the calculated $q_m$ values were typically larger than that for Norit GSX. Surprisingly, the obtained $q_m$ for the biomass-derived porous carbons were also notably higher than many other sorbents ever published in terms of treating aqueous *p*-nitrophenol, as can be seen in Table 2.

Using the Freundlich isotherm, $k_F$ increased with activation temperature of the sorbent products, which related directly to elevated adsorption capacity. The magnitude of 1/n reflects favorability of adsorption and all n values are greater than 1, suggesting favorable adsorption conditions [56]. In addition, n values became larger with an increase of activation temperature, signifying a decreased degree of surface heterogeneity for the obtained porous carbons [56]. It is also worth noting that the three parameter Redlich-Peterson model gave the best fit for all adsorption experiments and can best describe the *p*-nitrophenol adsorption behaviors. Hence, it is supposed that *p*-nitrophenol adsorption involves adsorption by formation of multi-layers on relatively heterogeneous carbon surfaces.

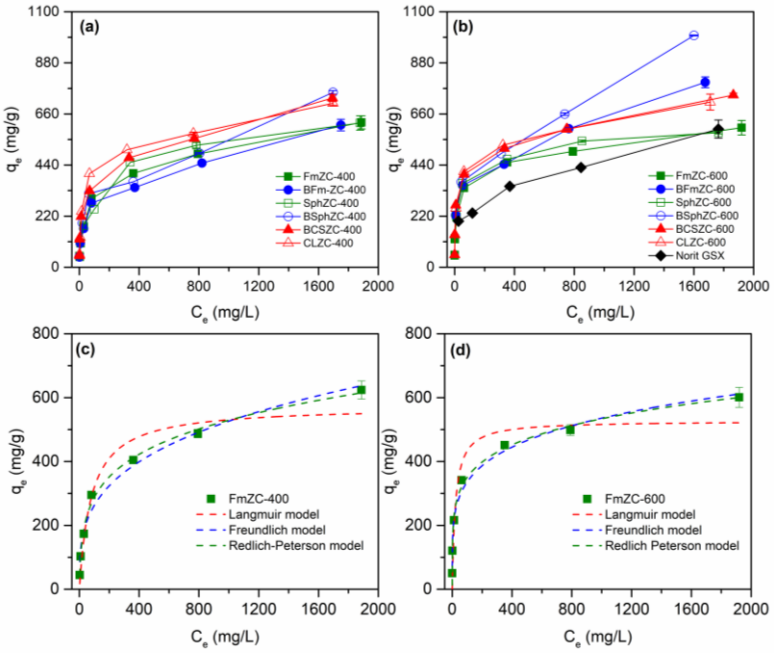


**Fig. 6.** Adsorption isotherms of *p*-nitrophenol onto representative bio-sorbents at 20 ºC. (a) 400 ºC produced porous carbons, (b) 600 ºC produced porous carbons; and representative isotherm fitting curves for (c) FmZC-400, (d) FmZC-600. Triplicate analyses were done for $C_0$=1000 and 2000 mg/L samples.

**Table 2** Comparison of maximum adsorption capacity for *p*-nitrophenol on different sorbents.

| Adsorbent | Sorption capacity (mg/g) | Reference |
|---|---|---|
| Metal-organic frameworks (MOFs) | 193 | [57] |
| Montmorillonite clay | 122 | [58] |
| Polymeric resin | 348 | [59] |
| Nanographite oxide (NGO) | 267 | [56] |
| Multi-walled carbon nanotube (MWCNT) | 32 | [60] |
| Activated carbon fiber (ACF) | 385 | [61] |
| Activated carbon (AC) | 526 | [12] |
| Cocoa shell activated carbon | 167 | [62] |
| **Biomass-derived porous carbons[a]** | **527-859** | **this study** |

a: sorption capacity is based on Langmuir model fittings, the actual maximum sorption capacities are higher. When $C_0$=~2000 mg/L, the sorption capacities range from 580-998 $m^2$/g.

### 4.4.2.2 Adsorption kinetics

Adsorption kinetics indicates the rate efficiency of each sorbent. Adsorption of *p*-nitrophenol onto various sorbents is controlled by mass transfer of adsorbate molecules in

the bulk phase (i.e. external boundary layer), diffusive transport on the sorbent surfaces and inner pores in the solid phase, and adsorption onto surface adsorptive sites [63]. The rate at which adsorption occurs is closely related to the characteristics of the adsorbate, adsorbent and the liquid phase. The adsorption kinetics (Fig. 7a) were markedly different between Norit GSX and the biomass porous carbons. At initial *p*-nitrophenol concentration of 20 mg/L, except for the test applied on Norit GSX, *p*-nitrophenol adsorption occurred rapidly at the early stage of adsorption within the first 30 min, then the adsorption gradually gave way to slower uptake rates until reaching a plateau attained after several hours. In comparison, a sharp increase of adsorption amount was achieved for *p*-nitrophenol adsorption on Norit GSX within less than 5 min approaching adsorption equilibrium very quickly and the subsequent adsorption was extremely slow. The difference of kinetic rates may be attributed to the difference in carbon surface chemistry and pore structure. The fractional uptake of *p*-nitrophenol was characterized by the intra-particle diffusion model. From Fig. 7b, the data indicated a region of sharp rise followed by a plateau region. The sharp rise process was mainly associated with diffusive transport of adsorbate, and was restricted by pore structures of the porous carbons, whereas the subsequent less sharp plateau region was retarded by formerly adsorbed molecules [64]. Because the uptake of *p*-nitrophenol was initially very fast and then gradually became slower, it is probable that *p*-nitrophenol transport initially diffused into larger pores (e.g. macro and mesopores) and then entered the micropores of the porous carbons which possessed heterogeneous pore shapes and sizes [63]. Therefore, external transport and film diffusion rather than internal transport are the dominant mechanisms in the adsorption process.

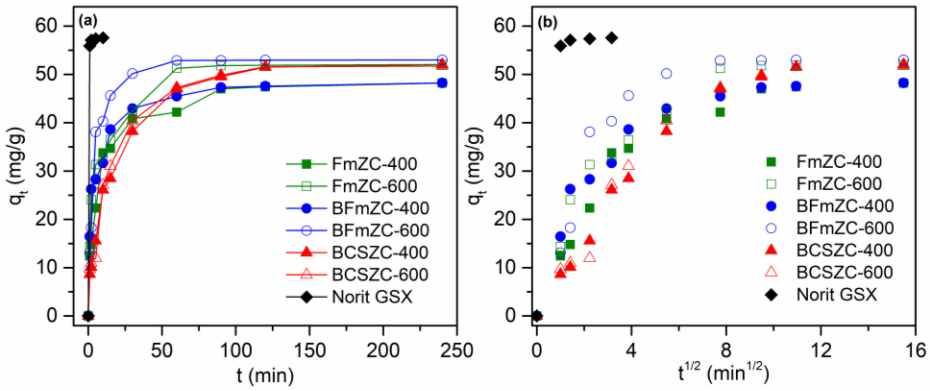


**Fig. 7.** Adsorption kinetics of *p*-nitrophenol onto selected sorbents at 20 ºC. (a) Adsorption amount as a function of time; (b) Intra-particle diffusion data of adsorption kinetics. Triplicate analyses were done for each sample.

The fitted parameters for several kinetic models can be found in Table S4. Pseudo-first-order model gave poor fittings as indicated by low $R^2$ values and large variances between $q_{exp}$ (experimental) and $q_e$ (theoretical) values, while a better fit was achieved by a pseudo-second-order model for all sorbents studied ($R^2 > 0.99$). This may be owing to the low molecular weight of the adsorbate and the small size of the sorbents [64]. These findings suggest that the adsorption was not controlled by pore diffusion. Instead, the rate-limiting step may be surface adsorption coupled with chemisorption involving valency forces through electron transfers between sorbent and sorbate phases [37]. Moreover, the calculated $k_2q_e$, known as the inverse of the half-life of adsorption process [64], can describe the rate of uptake. In this study, for the porous carbons fabricated from the same precursor, increasing activation temperature led to increased $k_2q_e$ values, suggesting promoted adsorption rates. However, the $k_2q_e$ values of the produced porous carbons (0.098–0.397 $min^{-1}$) were orders of magnitudes lower than that of Norit GSX (34.6 $min^{-1}$). Typically, CACs have been widely used in single-stage contact systems in WWTPs, which

involves mixing, contact adsorption and/or gravity precipitation within the same unit. The solid retention time (SRT) can be as long as days (e.g. 2–4 days) to allow for sufficient adsorption [65]. Thus, although these biomass-derived porous carbons had lower uptake rates, their kinetics may be acceptable for water and wastewater treatment unit operations. Moreover, they demonstrated great strengths in terms of treating high concentration *p*-nitrophenol wastewater streams (e.g. industrial wastewater) as evidenced by their high adsorption capacities.

#### 4.4.2.3 Adsorption mechanisms

Several mechanistic explanations have been proposed to influence the adsorptive properties of *p*-nitrophenol onto the porous carbons prepared at two temperatures. Firstly, it is presumed that the aromatic ring of *p*-nitrophenol, and potentially other phenolic contaminants, served as electron acceptors and interacted with the surface aromatic hydrocarbons, carbonyl and other oxygen groups of the porous carbons which acted as electron donors. This interaction is described by the electron donor-acceptor complexes mechanism [63]. This mechanism played important roles for *p*-nitrophenol adsorption onto the 400 °C activated products due to more abundant oxygenated functionalities. These oxygenated groups provided ideal active sites for hydrogen-bonding formation, which enhanced *p*-nitrophenol adsorption [56], but they also competed with water adsorption, which may impede adsorption. However, we argue that this competitive effect was not significant, because most of these groups, such as C=O groups located in the internal layers of the porous carbons, occurred infrequently on sample surfaces (as is supported by FTIR). Furthermore, the surface aromatic hydrocarbons would be expected to promote *p*-

nitrophenol adsorption [62]. The *p*-nitrophenol molecules are known to become Lewis acids due to protonation ($pH < pK_a = 7.15$ [58]), at the phosphate buffer-controlled aqueous pH near 7, while the porous carbon surfaces have many negatively charged sites ($pH > pH_{PZC}$). The adsorption therefore was also controlled by electrostatic attractions. Secondly, the π-π bonds, as indicated from XPS analyses, led to charge transfer and electrostatic interactions between the π-electrons in *p*-nitrophenol and the basal planes of graphite layers in the porous carbons. We hypothesize that this mechanism favored the *p*-nitrophenol adsorption onto the 600 °C activated products because these sorbents had more intensified delocalized π conjugation in the aromatic carbons. For instance, 600 °C activated porous carbons prepared from the heat-treated boreal peats (i.e. BFmZC-600 and BSphZC-600) exhibited the highest $q_m$ for *p*-nitrophenol (Table S3) among the sorbents, and this might be related to their high fractions of π-π satellite peaks (Fig. S3). These interactions may lead to high *p*-nitrophenol uptake [64]. The high affinity observed for the adsorption may also be attributed to the low electron density of phenolic aromatic rings because the nitro group attached at the para position served as a strong electron withdrawing group [63]. Thirdly, steric effects may have some impacts on adsorption capacity of *p*-nitrophenol. Due to the irregular pore structures at nanometer scales produced during $ZnCl_2$ activation, molecular diffusion of *p*-nitrophenol could be hindered from migrating into those low-sized micropores and inner pores, hence limiting the adsorption capacity. The existence of too large nanometer pores, on the other hand, causes weak adsorption of *p*-nitrophenol. In our study, the DFT pore size distributions of the sorbents lied primarily in the micropore (0–2 nm) and low mesopore ranges (i.e. 2–10 nm), which

closely fit the molecular size of *p*-nitrophenol (i.e. 0.66 × 0.43 nm) [66]. Such narrow pores, especially the micropores, may favor strong physical interactions between these molecules and the carbon surfaces [67]. Our study indicated that equally high removal of *p*-nitrophenol can be achieved using various porous carbons obtained at two differed activation temperatures. This can be explained by two different dominant mechanisms involved with each porous carbon. When treating specific organic wastewater streams, we advocate matching the characteristics of the contaminants with the adsorption mechanisms (electrostatic vs. π-interactions) of the sorbents to maximize contaminant adsorption.

### 4.4.3 Environmental and economic benefits

The global market size for ACs accounted for $4.72 billion in 2018 [68], and is poised to grow at a considerable rate for separation and purification industries due to their adsorptive characteristics to numerous pollutants. By 2026, the market is expected to reach $14.21 billion, a 300% increase in market size in 8 years [69]. The biggest hurdle for scaling in industries is the cost for production and regeneration. Coal-based ACs are environmentally unsustainable and expensive ($1190–$16,343 per ton) [70]. Granular activated carbons (GACs), for example, consume approximately 80 MJ/kg energy during production [71], which is a result of energy-intensive thermal activation. Regeneration of exhausted ACs uses as much as 50% of the energy used in AC production and causes a 10% loss in AC weight during each regeneration cycle [71]. Conventional biomass derived sorbents (e.g. biochars) are much cheaper ($96–$2512 per ton) [72], and provide environmental benefits, such as energy coproduction and biowaste valorization [73]. But as discussed, many bio-

based sorbents failed to compete against commercial CACs due to their substantially lower adsorption capacity.

Our study revealed that peatland soil derived porous carbons are cost and performance competitive eco-friendly alternatives to traditional sorbents. According to United States Geological Survey (USGS) National Minerals Information Center, the price for marketable peats is around $30 per ton [74], which is much cheaper than other biomass materials. Climate change damaged boreal peats, however, do not have a market value because they are generally considered of no economic use (e.g. horticultural purpose). Excavation of fire-impacted hydrophobic surface peats provides an environmental benefit through peatland ecological restoration. Furthermore, excavation is additionally beneficial to downstream communities, including peatland agricultural lands and municipal water systems, as the removal of burned peatlands mitigates flooding and aquatic organic loading to downstream water systems. Wildfires are the biggest disturbance in boreal peatlands, impacting over 25,000 $km^2$ of Canada's land mass per year [75]. Therefore, the annual generation and storage of fire- and drought-impacted ground-layer peat soils are considerable. The increasing prevalence of peatland fires in Russia and other parts of subarctic Eurasia will further increase the presence of damaged peatlands. Currently, there is no need to consider the regeneration of pollutant-saturated peat-based sorbents after use due to precursor abundance. However, the regeneration and reuse of the chemical agents from the effluents after product rinsing process would be our future perspective, as it could reduce the activating agent costs for consecutive cycles of AC production, and reduce byproduct waste. Finally, the rapid and facile activation route (< 600 °C) for these abundant

boreal peats offers an alternate feedstock to coal. Their huge accumulation each year, coupled with their perceived lack of value poses an interesting economic opportunity for future use as porous carbon sorbents.

## 4.5 Conclusions

This study investigated using a novel boreal peatland soil derived porous carbons for the separation and recovery of the phenolic micropollutant, *p*-nitrophenol, in simulated wastewaters. We introduced a one-step, low temperature (< 600 °C) facile $ZnCl_2$ activation approach for rapid conversion of naturally abundant pre- and post-burn damaged boreal peatland soils into micro- and mesoporous carbons. Peat-based sorbents exhibited much higher specific surface areas (> 1377 $m^2/g$) and higher adsorption of aqueous *p*-nitrophenol (maximum adsorption capacities > 530 mg/g), greatly exceeding many other sorbents found in the literature. Chemical sorption with the electron donor-acceptor complexes mechanism, π-π interactions and steric effects dominate the adsorption. The novelty and significance of this work lies in the fact that these damaged peatland soils are value-added, and their recycling for environmental applications are doubly beneficial for both peatland environmental remediation and as an alternative to replace coal-based CACs for micropollutants removal in water.

## 4.6 Acknowledgements

The research is funded by the CF-REF Global Water Futures (GWF) program as part of the Boreal Water Futures (BWF) initiative. We would like to thank Patrick Deane and Sophie Wilkinson in the McMaster Ecohydrology Lab for peats collection, and Dr. Hatem Zurob for offering the tube furnace. We acknowledge the Canadian Centre for Electron

Microscopy (CCEM) at McMaster University for providing the SEM equipment and McMaster Analytical X-Ray Diffraction Facility (MAC) for offering the XRD equipment. We also thank Zeynel Bayindir for giving technical assistance on XPS analyses.

## 4.7 References

[1] Y.L. Luo, W.S. Guo, H.H. Ngo, L.D. Nghiem, F.I. Hai, J. Zhang, S. Liang, X.C.C. Wang, A review on the occurrence of micropollutants in the aquatic environment and their fate and removal during wastewater treatment, SCIENCE OF THE TOTAL ENVIRONMENT, 473 (2014) 619-641.
[2] Y.R. Tong, P.J. McNamara, B.K. Mayer, Adsorption of organic micropollutants onto biochar: a review of relevant kinetics, mechanisms and equilibrium, ENVIRONMENTAL SCIENCE-WATER RESEARCH & TECHNOLOGY, 5 (2019) 821-838.
[3] M. Ahmaruzzaman, Adsorption of phenolic compounds on low-cost adsorbents: A review, ADVANCES IN COLLOID AND INTERFACE SCIENCE, 143 (2008) 48-67.
[4] W.W. Anku, M.A. Mamo, P.P. Govender, Phenolic compounds in water: sources, reactivity, toxicity and treatment methods, Phenolic compounds-natural sources, importance and applications, (2017) 419-443.
[5] M.L. Davi, F. Gnudi, Phenolic compounds in surface water, WATER RESEARCH, 33 (1999) 3213-3219.
[6] U.E.P. Agency, Guidelines establishing test procedures for the analysis of pollutants under the Clean Water Act, Fed. Reg., 49 (1984) 43234-43442.
[7] S. Alvarez-Torrellas, M. Martin-Martinez, H.T. Gomes, G. Ovejero, J. Garcia, Enhancement of p-nitrophenol adsorption capacity through N-2-thermal-based treatment of activated carbons, APPLIED SURFACE SCIENCE, 414 (2017) 424-434.
[8] M. Kallel, C. Belaid, T. Mechichi, M. Ksibi, B. Elleuch, Removal of organic load and phenolic compounds from olive mill wastewater by Fenton oxidation with zero-valent iron, CHEMICAL ENGINEERING JOURNAL, 150 (2009) 391-395.
[9] P. Canizares, J. Lobato, R. Paz, M.A. Rodrigo, C. Saez, Electrochemical oxidation of phenolic wastes with boron-doped diamond anodes, WATER RESEARCH, 39 (2005) 2687-2703.
[10] X.F. Sun, C.W. Wang, Y.B. Li, W.G. Wang, J. Wei, Treatment of phenolic wastewater by combined UF and NF/RO processes, DESALINATION, 355 (2015) 68-74.
[11] P. Praveen, K.C. Loh, Simultaneous extraction and biodegradation of phenol in a hollow fiber supported liquid membrane bioreactor, JOURNAL OF MEMBRANE SCIENCE, 430 (2013) 242-251.
[12] M. Ahmaruzzaman, D.K. Sharma, Adsorption of phenols from wastewater, JOURNAL OF COLLOID AND INTERFACE SCIENCE, 287 (2005) 14-24.
[13] J.Y. He, Y.L. Li, X.G. Cai, K. Chen, H.J. Zheng, C.M. Wang, K.S. Zhang, D.Y. Lin, L.T. Kong, J.H. Liu, Study on the removal of organic micropollutants from aqueous and ethanol solutions by HAP membranes with tunable hydrophilicity and hydrophobicity, CHEMOSPHERE, 174 (2017) 380-389.
[14] A. Nasrullah, B. Saad, A.H. Bhat, A.S. Khan, M. Danish, M.H. Isa, A. Naeem, Mangosteen peel waste as a sustainable precursor for high surface area mesoporous activated carbon: Characterization and application for methylene blue removal, JOURNAL OF CLEANER PRODUCTION, 211 (2019) 1190-1200.

[15] C.Y. Yin, M.K. Aroua, W. Daud, Review of modifications of activated carbon for enhancing contaminant uptakes from aqueous solutions, SEPARATION AND PURIFICATION TECHNOLOGY, 52 (2007) 403-415.
[16] K.R. Li, M.H. Zhou, L. Liang, L.L. Jiang, W. Wang, Ultrahigh-surface-area activated carbon aerogels derived from glucose for high-performance organic pollutants adsorption, JOURNAL OF COLLOID AND INTERFACE SCIENCE, 546 (2019) 333-343.
[17] T.Y. Zhang, W.P. Walawender, L.T. Fan, M. Fan, D. Daugaard, R.C. Brown, Preparation of activated carbon from forest and agricultural residues through CO2 activation, CHEMICAL ENGINEERING JOURNAL, 105 (2004) 53-59.
[18] L.J. Kennedy, J.J. Vijaya, K. Kayalvizhi, G. Sekaran, Adsorption of phenol from aqueous solutions using mesoporous carbon prepared by two-stage process, CHEMICAL ENGINEERING JOURNAL, 132 (2007) 279-287.
[19] S. Maiti, S. Purakayastha, B. Ghosh, Production of low-cost carbon adsorbents from agricultural wastes and their impact on dye adsorption, CHEMICAL ENGINEERING COMMUNICATIONS, 195 (2008) 386-403.
[20] J.J. Zhou, D.W. Li, Y. Wang, Y.Y. Tian, Z.B. Zhang, L. Wei, W. Feng, Effect of the Feedstock Type on the Volumetric Low-Pressure CO2 Capture Performance of Activated Carbons, ENERGY & FUELS, 32 (2018) 12711-12720.
[21] J. Moreno-Piraján, L. Giraldo, Activated carbon obtained by pyrolysis of potato peel for the removal of heavy metal copper (II) from aqueous solutions, Journal of Analytical and Applied Pyrolysis, 90 (2011) 42-47.
[22] A. Damaj, G.M. Ayoub, M. Al-Hindi, H. El Rassy, Activated carbon prepared from crushed pine needles used for the removal of Ni and Cd, DESALINATION AND WATER TREATMENT, 53 (2015) 3371-3380.
[23] P. Patnukao, P. Pavasant, Activated carbon from Eucalyptus camaldulensis Dehn bark using phosphoric acid activation, BIORESOURCE TECHNOLOGY, 99 (2008) 8540-8543.
[24] K.T. Wong, N.C. Eu, S. Ibrahim, H. Kim, Y. Yoon, M. Jang, Recyclable magnetite-loaded palm shell-waste based activated carbon for the effective removal of methylene blue from aqueous solution, JOURNAL OF CLEANER PRODUCTION, 115 (2016) 337-342.
[25] Q.R. Qian, M. Machida, H. Tatsumoto, Preparation of activated carbons from cattle-manure compost by zinc chloride activation, BIORESOURCE TECHNOLOGY, 98 (2007) 353-360.
[26] M. Rafatullah, O. Sulaiman, R. Hashim, A. Ahmad, Adsorption of methylene blue on low-cost adsorbents: A review, JOURNAL OF HAZARDOUS MATERIALS, 177 (2010) 70-80.
[27] M.R. Turetsky, B. Benscoter, S. Page, G. Rein, G.R. van der Werf, A. Watts, Global vulnerability of peatlands to fire and carbon loss, NATURE GEOSCIENCE, 8 (2015) 11-14.
[28] A. Witze, The Arctic is burning like never before--and that's bad news for climate change, Nature, 585 (2020) 336-338.
[29] Y. Wu, N. Zhang, G. Slater, J.M. Waddington, C.-F. de Lannoy, Hydrophobicity of peat soils: Characterization of organic compound changes associated with heat-induced water repellency, Science of The Total Environment, 714 (2020) 136444.
[30] N.E. Flanagan, H. Wang, S. Winton, C.J. Richardson, Low-severity fire as a mechanism of organic matter protection in global peatlands: Thermal alteration slows decomposition, Global change biology, 26 (2020) 3930-3946.
[31] G. Rein, N. Cleaver, C. Ashton, P. Pironi, J.L. Torero, The severity of smouldering peat fires and damage to the forest soil, CATENA, 74 (2008) 304-309.
[32] J. Leifeld, L. Menichetti, The underappreciated potential of peatlands in global climate change mitigation strategies, NATURE COMMUNICATIONS, 9 (2018).

[33] Z.C. Yu, Northern peatland carbon stocks and dynamics: a review, BIOGEOSCIENCES, 9 (2012) 4071-4085.
[34] J. Bedia, M. Peñas-Garzón, A. Gómez-Avilés, J.J. Rodriguez, C. Belver, A review on the synthesis and characterization of biomass-derived carbons for adsorption of emerging contaminants from water, C, 4 (2018) 63.
[35] Y.X. Li, X. Zhang, R.G. Yang, G.Y. Li, C.W. Hu, The role of H3PO4 in the preparation of activated carbon from NaOH-treated rice husk residue, RSC ADVANCES, 5 (2015) 32626-32636.
[36] N.R. Khalili, M. Campbell, G. Sandi, J. Golas, Production of micro- and mesoporous activated carbon from paper mill sludge - I. Effect of zinc chloride activation, CARBON, 38 (2000) 1905-1915.
[37] Y.S. Ho, G. McKay, Pseudo-second order model for sorption processes, PROCESS BIOCHEMISTRY, 34 (1999) 451-465.
[38] W.J. Weber Jr, J.C. Morris, Kinetics of adsorption on carbon from solution, Journal of the sanitary engineering division, 89 (1963) 31-59.
[39] N. Ayawei, A.N. Ebelegi, D. Wankasi, Modelling and Interpretation of Adsorption Isotherms, JOURNAL OF CHEMISTRY, 2017 (2017).
[40] S. Ucar, M. Erdem, T. Tay, S. Karagoz, Preparation and characterization of activated carbon produced from pomegranate seeds by ZnCl2 activation, APPLIED SURFACE SCIENCE, 255 (2009) 8890-8896.
[41] K.Z. Qian, A. Kumar, K. Patil, D. Bellmer, D.H. Wang, W.Q. Yuan, R.L. Huhnke, Effects of Biomass Feedstocks and Gasification Conditions on the Physiochemical Properties of Char, ENERGIES, 6 (2013) 3972-3986.
[42] W. Suliman, J.B. Harsh, N.I. Abu-Lail, A.M. Fortuna, I. Dallmeyer, M. Garcia-Perez, Influence of feedstock source and pyrolysis temperature on biochar bulk and surface properties, BIOMASS & BIOENERGY, 84 (2016) 37-48.
[43] M. Ahmad, S.S. Lee, A.U. Rajapaksha, M. Vithanage, M. Zhang, J.S. Cho, S.E. Lee, Y.S. Ok, Trichloroethylene adsorption by pine needle biochars produced at various pyrolysis temperatures, BIORESOURCE TECHNOLOGY, 143 (2013) 615-622.
[44] T.A.J. Kuhlbusch, M.O. Andreae, H. Cachier, J.G. Goldammer, J.P. Lacaux, R. Shea, P.J. Crutzen, Black carbon formation by savanna fires: Measurements and implications for the global carbon cycle, JOURNAL OF GEOPHYSICAL RESEARCH-ATMOSPHERES, 101 (1996) 23651-23665.
[45] J.A. Menendez-Diaz, I. Martin-Gullon, Types of carbon adsorbents and their production, in: T.J. Bandosz (Ed.) ACTIVATED CARBON SURFACES IN ENVIRONMENTAL REMEDIATION, 2006, pp. 1-47.
[46] R.R.E. Artz, S.J. Chapman, A.H.J. Robertson, J.M. Potts, F. Laggoun-Defarge, S. Gogo, L. Comont, J.R. Disnar, A.J. Francez, FTIR spectroscopy can be used as a screening tool for organic matter quality in regenerating cutover peatlands, SOIL BIOLOGY & BIOCHEMISTRY, 40 (2008) 515-527.
[47] C. Cocozza, V. D'Orazio, T.M. Miano, W. Shotyk, Characterization of solid and aqueous phases of a peat bog profile using molecular fluorescence spectroscopy, ESR and FT-IR, and comparison with physical properties, ORGANIC GEOCHEMISTRY, 34 (2003) 49-60.
[48] I. Simkovic, P. Dlapa, S.H. Doerr, J. Mataix-Solera, V. Sasinkova, Thermal destruction of soil water repellency and associated changes to soil organic matter as observed by FTIR spectroscopy, CATENA, 74 (2008) 205-211.
[49] A.C. Lua, T. Yang, Characteristics of activated carbon prepared from pistachio-nut shell by zinc chloride activation under nitrogen and vacuum conditions, JOURNAL OF COLLOID AND INTERFACE SCIENCE, 290 (2005) 505-513.

[50] P. Liu, W.J. Liu, H. Jiang, J.J. Chen, W.W. Li, H.Q. Yu, Modification of bio-char derived from fast pyrolysis of biomass and its application in removal of tetracycline from aqueous solution, BIORESOURCE TECHNOLOGY, 121 (2012) 235-240.
[51] K. Mohanty, M. Jha, B.C. Meikap, M.N. Biswas, Preparation and characterization of activated carbons from Terminalia arjuna nut with zinc chloride activation for the removal of phenol from wastewater, INDUSTRIAL & ENGINEERING CHEMISTRY RESEARCH, 44 (2005) 4128-4138.
[52] J.A. Yang, K.Q. Qiu, Development of high surface area mesoporous activated carbons from herb residues, CHEMICAL ENGINEERING JOURNAL, 167 (2011) 148-154.
[53] T.H. Liou, Development of mesoporous structure and high adsorption capacity of biomass-based activated carbon by phosphoric acid and zinc chloride activation, CHEMICAL ENGINEERING JOURNAL, 158 (2010) 129-142.
[54] A. Dandekar, R.T.K. Baker, M.A. Vannice, Characterization of activated carbon, graphitized carbon fibers and synthetic diamond powder using TPD and drifts, CARBON, 36 (1998) 1821-1831.
[55] Z.L. Zhu, A.M. Li, L. Yan, F.Q. Liu, Q.X. Zhang, Preparation and characterization of highly mesoporous spherical activated carbons from divinylbenzene-derived polymer by ZnCl2 activation, JOURNAL OF COLLOID AND INTERFACE SCIENCE, 316 (2007) 628-634.
[56] B. Zhang, F. Li, T. Wu, D.J. Sun, Y.J. Li, Adsorption of p-nitrophenol from aqueous solutions using nanographite oxide, COLLOIDS AND SURFACES A-PHYSICOCHEMICAL AND ENGINEERING ASPECTS, 464 (2015) 78-88.
[57] B.J. Liu, F. Yang, Y.X. Zou, Y. Peng, Adsorption of Phenol and p-Nitrophenol from Aqueous Solutions on Metal-Organic Frameworks: Effect of Hydrogen Bonding, JOURNAL OF CHEMICAL AND ENGINEERING DATA, 59 (2014) 1476-1482.
[58] M. El Ouardi, M. Laabd, H. Abou Oualid, Y. Brahmi, A. Abaamrane, A. Elouahli, A.A. Addi, A. Laknifli, Efficient removal of p-nitrophenol from water using montmorillonite clay: insights into the adsorption mechanism, process optimization, and regeneration, ENVIRONMENTAL SCIENCE AND POLLUTION RESEARCH, 26 (2019) 19615-19631.
[59] C.H. Hong, W.M. Zhang, B.C. Pan, L. Lv, Y.Z. Han, Q.X. Zhang, Adsorption and desorption hysteresis of 4-nitrophenol on a hyper-cross-linked polymer resin NDA-701, JOURNAL OF HAZARDOUS MATERIALS, 168 (2009) 1217-1222.
[60] X.E. Shen, X.Q. Shan, D.M. Dong, X.Y. Hua, G. Owens, Kinetics and thermodynamics of sorption of nitroaromatic compounds to as-grown and oxidized multiwalled carbon nanotubes, JOURNAL OF COLLOID AND INTERFACE SCIENCE, 330 (2009) 1-8.
[61] D.Y. Tang, Z. Zheng, K. Lin, J.F. Luan, J.B. Zhang, Adsorption of p-nitrophenol from aqueous solutions onto activated carbon fiber, JOURNAL OF HAZARDOUS MATERIALS, 143 (2007) 49-56.
[62] F. Ahmad, W. Daud, M.A. Ahmad, R. Radzi, Using cocoa (Theobroma cacao) shell-based activated carbon to remove 4-nitrophenol from aqueous solution: Kinetics and equilibrium studies, CHEMICAL ENGINEERING JOURNAL, 178 (2011) 461-467.
[63] A. Kumar, S. Kumar, S. Kumar, D.V. Gupta, Adsorption of phenol and 4-nitrophenol on granular activated carbon in basal salt medium: Equilibrium and kinetics, JOURNAL OF HAZARDOUS MATERIALS, 147 (2007) 155-166.
[64] Q.S. Liu, T. Zheng, P. Wang, J.P. Jiang, N. Li, Adsorption isotherm, kinetic and mechanism studies of some substituted phenols on activated carbon fibers, CHEMICAL ENGINEERING JOURNAL, 157 (2010) 348-356.
[65] M. Boehler, B. Zwickenpflug, J. Hollender, T. Ternes, A. Joss, H. Siegrist, Removal of micropollutants in municipal wastewater treatment plants by powder-activated carbon, WATER SCIENCE AND TECHNOLOGY, 66 (2012) 2115-2121.

[66] Z.B. Wu, X.Z. Yuan, H. Zhong, H. Wang, G.M. Zeng, X.H. Chen, H. Wang, L. Zhang, J.G. Shao, Enhanced adsorptive removal of p-nitrophenol from water by aluminum metal-organic framework/reduced graphene oxide composite, SCIENTIFIC REPORTS, 6 (2016).
[67] S. Haydar, M.A. Ferro-Garcia, J. Rivera-Utrilla, J.P. Joly, Adsorption of p-nitrophenol on an activated carbon with different oxidations, CARBON, 41 (2003) 387-395.
[68] G. Ravenni, G. Cafaggi, Z. Sárossy, K.R. Nielsen, J. Ahrenfeldt, U. Henriksen, Waste chars from wood gasification and wastewater sludge pyrolysis compared to commercial activated carbon for the removal of cationic and anionic dyes from aqueous solution, Bioresource Technology Reports, 10 (2020) 100421.
[69] A.A. Ahmad, A.T.M. Din, N.K.E. Yahaya, A. Khasri, M.A. Ahmad, Adsorption of basic green 4 onto gasified Glyricidia sepium woodchip based activated carbon: Optimization, characterization, batch and column study, Arabian Journal of Chemistry, 13 (2020) 6887-6903.
[70] Z.M. Yunus, A. Al-Gheethi, N. Othman, R. Hamdan, N.N. Ruslan, Removal of heavy metals from mining effluents in tile and electroplating industries using honeydew peel activated carbon: A microstructure and techno-economic analysis, JOURNAL OF CLEANER PRODUCTION, 251 (2020).
[71] H.A. Alhashimi, C.B. Aktas, Life cycle environmental and economic performance of biochar compared with activated carbon: A meta-analysis, RESOURCES CONSERVATION AND RECYCLING, 118 (2017) 13-26.
[72] R.M. Campbell, N.M. Anderson, D.E. Daugaard, H.T. Naughton, Financial viability of biofuel and biochar production from forest biomass in the face of market price volatility and uncertainty, APPLIED ENERGY, 230 (2018) 330-343.
[73] K.A. Thompson, K.K. Shimabuku, J.P. Kearns, D.R.U. Knappe, R.S. Summers, S.M. Cook, Environmental Comparison of Biochar and Activated Carbon for Tertiary Wastewater Treatment, ENVIRONMENTAL SCIENCE & TECHNOLOGY, 50 (2016) 11253-11262.
[74] J. Ober, Mineral commodity summaries 2018. Mineral commodity summaries. Reston, in, 2018.
[75] C.M. Gibson, L.E. Chasmer, D.K. Thompson, W.L. Quinton, M.D. Flannigan, D. Olefeldt, Wildfire as a major driver of recent permafrost thaw in boreal peatlands, NATURE COMMUNICATIONS, 9 (2018).

# Chapter 5

## Nancomposite polymeric membranes for organic micropollutants (OMPs) removal: A critical review

## 5.1 Abstract

The prevalence of organic micropollutants (OMPs) and their persistence in water supplies have raised serious concerns for drinking water safety and public health. Conventional water treatment technologies, including adsorption and biological treatment, are known to be insufficient in treating OMPs, and have demonstrated poor selectivity towards a wide range of OMPs. Pressure-driven membrane filtration has the potential to remove many OMPs detected in water with high selectivity as membranes' molecular weight cut-off (MWCO), surface charge, and hydrophilicity can be easily tailored to targeted OMP's size, charge and octanol-water partition coefficient ($K_{ow}$). Over the past 10 years, polymeric (nano)composite microfiltration (MF), ultrafiltration (UF) and nanofiltration (NF) membranes have been extensively synthesized and studied for their ability to remove OMPs. This review discusses the fate and transport of emerging OMPs in water, an assessment of conventional membrane-based technologies (NF, reverse osmosis (RO), forward osmosis (FO), membrane distillation (MD) and UF membrane-based hybrid processes) for their removal, and a comparison to the state-of-the-art nano-enabled membranes with enhanced selectivity towards specific OMPs in water. Nano-enabled membranes for OMP treatment are further discussed with respect to their permeability, enhanced properties, limitations, and future improvements.

## 5.2 Introduction

Organic micropollutants (OMPs), such as endocrine disrupting chemicals (EDCs), pharmaceutical and personal care products (PPCPs), and other trace organic compounds (TOrCs), are an emerging concern in the water supply of developed and developing

countries alike. OMPs are defined as natural or synthetic compounds that can be present in water at trace levels (ng/L to μg/L) [1]. Despite many emerging OMPs have still unknown impacts to ecology and human health, the increased OMP quantities has raised global concern about their toxicity, bioaccumulation and persistence [2, 3], leading to updated environmental guidelines and laws in developed societies. The United States Environmental Protection Agency (US EPA) publishes a contaminant candidate list (CCL) of unregulated contaminants that potentially require future regulation for public water system every 5 years [4]. Canada identified certain substances including nonylphenol ethoxylates (NPEs) to be assessed on a priority basis [5]. The European Union (EU) has updated a watch list of substances, such as several azole pharmaceuticals and pesticides, for union-wide monitoring in surface waters in 2020 [6].

Membrane-assisted technology has played an increasingly significant role for water purification and resource recovery. Nanofiltration (NF) and reverse osmosis (RO) processes typically provide adequate water flux and simultaneous rejection of organic molecules and multivalent salts. While rejection to organic solutes can be high (> 90%), NF membranes (pore size 0.5 -2 nm, molecular weight cut-off (MWCO) 200 – 2000 Da) cannot fully remove small-sized OMPs (*e.g.*, <500 Da for some antibiotics and EDCs, 200-400 Da for most pesticides) [7-9]. While RO membranes have denser membrane structures and therefore generally higher OMP removal rates, uncharged OMPs can readily dissolve and diffuse through RO membranes [10]. NF (6 – 10 bar) and RO (14 – 70 bar) processes are energy-intensive due to high feed pressure requirements [11], and suffer from membrane fouling, resulting in decreased flux and decreased selectivity for OMP removal.

Microfiltration (MF) and ultrafiltration (UF) are more economical membrane filtration processes due to high permeability, low energy consumption and easy automation [12]. These membranes however poorly remove OMPs due to large pore size. The MWCO of UF membranes (1-100 kDa), for example, greatly exceeds that of most OMPs (<1 kDa) [13]. Alternatively, combining MF or UF process with other treatment measures (*e.g.*, powdered activated carbon/ultrafiltration (PAC/UF) process and micellar-enhanced ultrafiltration (MEUF)) can enhance OMP removal. However, the additional units/agents applied largely increase water treatment plants' operating costs and plant footprint.

The recent development of nanocomposite polymeric membranes is an attractive option to increase process intensification while achieving high OMP removal. These advanced functional membranes contain nanomaterial modifiers that enhance the polymeric membranes' physicochemical properties (*e.g.*, hydrophobicity, surface charge, pore size) to help to adsorb/reject/degrade specific OMPs during filtration or within membrane reactor. Nanocomposite polymeric membranes can be prepared by: 1. Coating nanomaterials onto the surface of conventional membranes, 2. integrating nanomaterials into the Membrane matrix, 3. sandwiching nanomaterials between the membrane and a polymer thin film, or 4. Embedding nanomaterials into a polymer thin film on the membrane.

Current review papers have described technological advances of OMP removal in wastewater [14-16], with some focused on applying membrane-based technologies [13, 17-19]. However, there is a dearth of reviews on the synthesis and application of state-of-the-art nanocomposite polymeric membranes for OMP treatment. Given a large increase in the

number of publications in this field over the past 10 years (Figure 1), we provide a systematic overview and novel perspective of the research advancements on nanocomposite polymeric membranes and their applications for OMP removal form water, to inspire researchers to better design next-generation membranes for environmental applications.

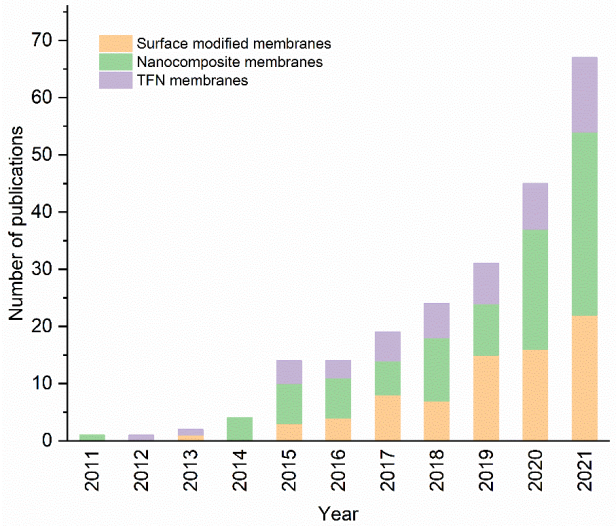


**Fig. 1.** Total number of publications (2011 – 2021) for organic micropollutants removal using nanocomposite polymeric membranes.

### 5.3 Occurrence and transport of OMPs in water

With increased anthropogenic activities, more and more substances have been recognized and monitored as OMPs. Typical OMPs include steroidal hormones, pesticides and biocides and their degradation products, plasticizers (*e.g.*, phthalates), polyhalogenated compounds (PHCs) (*e.g.*, polychlorinated biphenyls (PCBs) and perfluorinated chemicals (PFCs)), disinfection byproducts (DBPs), pharmaceuticals (PhACs)( *e.g.*, antibiotics and anti-inflammatory drugs), personal care products (*e.g.*, cosmetics and fragrances), industrial chemicals (*e.g.*, phenols and synthetic dyes), and combustion byproducts (*e.g.*, polyaromatic hydrocarbons (PAHs)). A summary of representative OMPs, their physical

properties, and measured concentrations in the aquatic environments is presented in Table 1.

**Table 1** Commonly studied OMPs in water and their physical properties.

| Category | Subclass | Example | Physical Properties | | | | | Reported Concentrations (ng/L) | | |
|---|---|---|---|---|---|---|---|---|---|---|
| | | | MW (Da) | S [a] (mg/L) | $pK_a$ | $LogK_{ow}$ | Ref. | Surface Water [c] | Effluent [d] | Ref. |
| Endocrine disrupting chemicals (EDCs) | Steroid hormones | estrone (E1) | 270 | 30 | 10.34 | 3.13 - 3.43 | [20] | 1.8 | 0.1 - 15.3 | [21, 22] |
| | | 17-β-estradiol (E2) | 272 | 13 | 10.46 | 2.69 - 4 | [20] | 0.56 | 0.6 - 5.8 | [21, 22] |
| | | estriol (E3) | 288 | 13 | 10.38 | 2.81 | [20] | 3.7 | 0.4 - 6.8 | [21, 22] |
| | | testosterone | 288 | 23.4 | | 3.32 | [23] | 0.01 | ND | [21, 24] |
| | | 17-α-ethinylestradiol (EE2) | 296 | 4.7-19 | 10.4 | 3.67 - 4.2 | [20] | | < 106 | [25] |
| | | progesterone | 314 | 8.81 | | 3.87 | [23] | < 0.01 | ND | [21, 24] |
| | Pesticides | carbendazim | 191 | 8 | 4.2 | 1.52 | [26] | | | |
| | | simazine | 202 | 6.2 | 1.6 | 2.2 | [27] | 0.2 - 488.8 | 26.3 | [28, 29] |
| | | atrazine | 216 | 34.7 | 1.7 | 2.7 | [27] | 0.9 - 5170 | 4.2 | [28, 29] |
| | | diuron | 233 | 42 | 2,68 | 2.7 | [13, 27] | 1.4 - 1362 | 61.7 | [28, 29] |
| | | diazinon | 304 | 40 | 2.6 | 3.81 | [3] | 0.6 - 276 | 21.4 | [28, 29] |
| | Phenolic estrogens | octylphenol (OP) | 206 | 12.6 | 10.39 | 4.12 | [30] | < 226 | | [31] |
| | | nonylphenol (NP) | 220 | 6.35 | 10.25 | 5.99 | [3] | < 2760 | 13.4 - 471.6 | [31] |
| | | bisphenol A (BPA) | 228 | 120 | 9.6 | 3.32 | [3] | < 2470 | < 1840 | [25, 31] |
| | Phthalates | dimethyl phthalate (DMP) | 194 | 4000 [b] | | 1.6 | [32] | | 0.062 | [32] |
| | | dibutyl phthalate (DBP) | 278 | 15 [b] | | 4.83 | [33] | < 4430 | 0.54 | [32, 33] |
| | | diethylhexyl phthalate (DEHP) | 391 | < 1 [b] | | 8.71 | [33] | < 5000 | 1.6 | [32, 33] |
| | Polychlorinated biphenyls (PCBs) | 2-chlorobiphenyl | 189 | | | 4.56 | [34] | | | |
| | | 4,4'-dichlorobiphenyl | 223 | | | 5.28 | [34] | | | |
| | Perfluorinated chemicals (PFCs) | perfluorooctanoic acid (PFOA) | 414 | 3400 | 2.5 | 6.28 | [35] | 0.21 - 4.2 | 255 | [29, 36] |
| | | perfluorooctane sulfonate (PFOS) | 500 | 519 | -3.27 | | [37, 38] | 0.04 - 6.9 | 62.5 | [29, 36] |
| Pharmaceutically active compounds (PhACs) | Antibiotics | sulfamethoxazole | 253 | 610 | 5.6 | 0.89 | [23] | 8.3 | 280 | [29, 39] |
| | | sulfamethazine | 278 | 430 | 7.4; 2.65 | 0.28 | [40] | | 12 | [24] |
| | | norfloxacin | 319 | 161000 | 5.77 | -1.03 | [41, 42] | | 1.6 - 260.4 | [22] |
| | | ciprofloxacin | 331 | | 10.58; 8.7; 6.14; 3.01 | 0.28 | [43] | 5.4 - 448.1 | 67 | [24, 28] |
| | | enrofloxacin | 360 | | 9.86; 7.59; 6.19; 3.85 | 0.7 | [44] | | 0.4 - 2.6 | [22] |
| | | cefadroxil | 363 | | 9.64; 7.37; 2.48 | -0.08 | [44] | | | |
| | | amoxicillin | 365 | | 9.6; 7.4; 2.4 | | [45] | < 2.08 - 223 | 20 - 1340 | [46] |

| | | | | | | | | | | |
|---|---|---|---|---|---|---|---|---|---|---|
| | | cephalexin | 365 | | 6.88; 2.56 | 0.076 | [43] | | | |
| | | tetracycline | 444 | 231 | 3.3 | -1.3 | [23] | 1.1 - 4278.7 | 0.8 - 6000 | [46] |
| | | erythromycin | 734 | 459 | 8.9 | 3.06 | [3, 13] | 0.84 | 6.5 - 2350 | [39, 46] |
| | Analgesic and anti-inflammatory drugs | acetaminophen | 151 | 14000 | 9.4 | 0.46 | [26] | 1.7 | 79 | [24, 39] |
| | | ibuprofen | 206 | 21 | 4.9 | 3.97 | [47] | 22 | 460 | [24, 39] |
| | | naproxen | 230 | 51.1 | 4.2 | 3.18 | [3, 13] | 1.4 | 26.7 | [29, 39] |
| | | diclofenac | 296 | 2.37 | 4.15 | 4.51 | [48] | 8.7 | 49.5 | [29, 39] |
| | Blood lipid regulators | carbamazepine | 236 | 17.7 | < 2 - 2.45; 7 | 2.18 - 2.93 | [40] | 4.9 | 832 | [29, 39] |
| | | bezafibrate | 362 | 1.55 | 3.83 | 3.97 | [3] | | < 4800 | [25] |
| | Stimulants | caffeine | 194 | 21600 | 10.4 | -0.07 | [49] | 160 | 191 | [29, 39] |
| | | cocaine | 303 | | 8.6 | 2.3 | [50] | | | |
| | β-blocker | atenolol | 266 | 300 | 9.6 | 0.16 | [3] | | 0.8 - 515.7 | [22] |
| | | metoprolol | 342 | 402 | 14.09 | 1.88 | [3] | 5.4 | 9.5 - 335.9 | [39] |
| Personal care products (PCPs) | Antiseptics/Disinfectants | 2-nitrophenol | 139 | 2100 [b] | 7.2 | 1.76 | [51] | | | |
| | | 4-nitrophenol | 139 | 16000 [b] | 7,15 | 1.91 | [51] | | | |
| | | triclosan | 290 | 10 | 7.9 | 4.76 | [49] | 1.5 - 534 | 74.8 | [28, 29] |
| | | triclocarban | 316 | | 11.4 | 4.9 | [13] | 13 | < 5860 | [25, 39] |
| | Preservatives | methylparaben | 152 | | 8.4 | 2 | [52] | < 1062 | < 262 | [53, 54] |
| | | propylparaben | 180 | | 8.2 | 3 | [52] | < 3142 | < 231 | [53, 54] |
| | | benzylparaben | 228 | | 8.2 | 3.6 | [52] | < 3.93 | < 2.9 | [53, 54] |
| | Fragrances | galaxolide | 258 | | | 5.9 | [55] | | | |
| | | tonalide | 258 | | | 5.7 | [55] | | | |
| Other organic pollutants | Disinfection byproducts (DBPs) | dichloroacetic acid (DCAA) | 129 | 1000000 | 1.26 | 0.92 | [48] | < 2.3 | 3.3 - 9.3 | [56] |
| | | trichloroacetic acid (TCAA) | 163 | 44000 | 0.51 | 1.33 | [48] | < 4.2 | 3.4 - 28 | [56] |
| | Organic dyes | methylene blue (MB) | 320 | 43600 [b] | 5.6 | | [57, 58] | | | |
| | | methyl orange (MO) | 327 | 5000 | 3.47 | | [59] | | | |

a. Values for solubility (S) were determined at 20 ℃ unless otherwise stated.
b. The temperature at which S was measured is 25 ℃.
c. [21] and [39]: mean concentrations based on 217 surface water samples across 31 provinces in China; [28]: concentration for surface waters from 7 provinces in China, 25 states in US and 7 countries in EU; [31] and [33]: concentration for surface waters from some East Asian and European countries; [36]: concentrations based on 40 river water samples in Northern Europe; [46]: mean concentrations of surface waters in Asia, North America and Europe; [53]: concentration based on multiple river waters in China; [56]: concentrations based on 51 surface waters from Beijing and Wuhan, China.
d. [22]: concentrations of effluents from 14 WWTPs in China; [24]: mean concentrations of effluents from 50 WWTPs in US; [25], [46] and [54]: concentrations of effluents from some Asian, North American and European countries; [29]: mean concentrations of effluents from 90 WWTPs in EU; [32]: mean concentration of effluents from 15 WWTPs in Europe; [56]: concentrations of effluents based on 5 WWTPs from Beijing and Wuhan, China.

OMPs may originate from both point sources and diffuse sources and they can be emitted into domestic, industrial, agricultural and hospital effluents [13, 60-62]. For example, antibiotics overuse for medical treatments and livestock agriculture especially recently in

China, poses significant threats to ecosystems and human health [63]. OMPs have been detected in surface water [16, 64], groundwater [65], seawater [66], and drinking water [67, 68]. Wastewater treatment plant (WWTP) effluent discharge is the dominant pathway for OMP emission to surface waters and potable-water supplies due to insufficient removal [16, 67, 68].

OMP pollution severity in surface waters can be influenced by effluent volume and effluent concentration (as impacted by regional usage and treatment efficiency) [64]. The fate of some OMPs including many pharmaceuticals, are subject to changes through dilution, partition/adsorption, degradation, biotransformation and photolysis[64]. Other OMPs such as PFCs and PCBs are well-known to be extremely persistent in surface water. Groundwater is usually less impacted by OMP pollution and accordingly has been less researched.

OMPs in groundwater primarily results from landfill and sewer leachates, and the infiltration of OMP-polluted water (e.g., from septic systems) is primarily controlled by both the adsorption/partition to soils as well as soil microbial oxidative processes[16, 65]. OMPs' fate and transfer into subsurface soil and groundwater is also impacted by aquifers' hydraulic conditions, and soil properties [65]. OMPs with low octanol – water partition coefficient ($K_{ow}$) values ($\log K_{ow} < 3$) such as some pharmaceuticals, pesticides, and DBPs likely have high mobility in soils, low affinity to organic sediments, and thus higher probability of occurring in ground water. Adsorption/partition can only retard OMP transport, whereas microbial degradation reduces the concentration of OMPs in

groundwater [69]. The different fates and transport of OMPs through the subsurface have implications for policy makers, environmental regulatory bodies, and water operators to manage recalcitrant OMPs such as phenols in some water sources including drinking water wells.

## 5.4 Conventional membrane-based processes for OMPs removal

### 5.4.1 Advanced membrane processes

Nanofiltration (NF), reverse Osmosis (RO), forward osmosis (FO) and membrane distillation (MD) have shown different success for OMP removal with simple integration, but are limited by fouling propensity and high energy costs. The real-world OMP removal by membrane processes is influenced by membrane selectivity (MWCO), surface properties (hydrophobicity and charge), operating conditions (transmembrane pressure and recovery), feed solution chemistry (pH and ionic strength) and OMP properties ($pK_a$, $K_{ow}$, molecular size, charge, and polarity) [16]. OMP removal by each membrane class is discussed in the context of OMP characteristics and membrane properties.

#### 5.4.1.1 Nanofiltration (NF) and reverse osmosis (RO)

NF and RO processes are high pressure-driven, with low MWCOs and high energy demand. Their reported OMP retentions are commonly above 80% [19]. Generally, loose NF membranes lose their performance due to concentration polarization [13], whereas tight NF and RO membranes more effectively removes OMPs due to smaller pore sizes and denser membrane structure, but at the cost of higher pressure requirements.

Uncharged, non-adsorptive OMPs are predominantly removed by size exclusion (steric hindrance), as affected by OMPs' molecular weight (MW). Košutić et al. [70] found tight NF (NF90) or RO (HR95 and XLE) membranes led to high rejections of uncharged, large MW antibiotics due to greater sieving effect. Uncharged OMPs' polarity (indicated by dipole moment) and hydrophobicity also play a role in some cases when considering membrane adsorption [71]. Interestingly, trace uncharged OMPs can diffuse into dense polymeric phases, affecting RO separation. Yoon et al. [72] concluded that the less polar EDCs and PPCPs were more greatly retained by NF membranes owing to stronger hydrophobic adsorption to NF membranes. Nghiem et al. [71] found that loose NF (NF270) membrane filtration gave lower rejection to sulfamethoxazole (an uncharged OMP with high polarity) than carbamazepine, despite of their similar molecular size. This difference was ascribed to strong interactions between the molecular polar centers and fixed membrane charges. OMP speciation through pH change could cause electrostatic interactions with the charged membrane surfaces, in addition to removal by steric hindrance [71, 73]. Sulfamethoxazole rejection significantly increased with pH rise to above its $pK_a$, due to synergic electrostatic repulsion and size exclusion [71]. Generally, small charged OMPs, such as dyes and some PhACs, are more affected by charge effects than size exclusion [74]. Although RO membranes provide greater OMP removal, they are not an absolute barrier [73]. Even conventional RO membranes struggle to remove low MW uncharged and non-adsorptive OMPs such as some drugs (2-naphthol, phenacetine and primidone) [48].

5.4.1.2 Forward osmosis (FO)

FO process is an emerging separation technique that utilizes the spontaneous water transport by an osmotic pressure difference from the less concentrated feed solution to a highly concentrated draw solution (DS) across a semipermeable membrane, achieving feed water separation from the solutes. FO has advantages of lower energy consumption, low fouling potential, high recovery and simplicity [75], and has thus become increasingly popular for desalination, wastewater reclamation, and concentration of polluted water (*e.g.*, landfill leachate) [75]. FO applications for OMP removal is rare [75-78], and OMP removal efficiency is affected by characteristics of FO membrane and pollutants.

Typically, FO process well rejects charged OMPs, where Hancock et al. [76] obtained different rejections for charged (80 – 98%) and non-charged TOrCs (40 – 90%) at bench scale. The rejection increased with MW due to increased diffusive hindrance [76]. Hydrophobic adsorption governs hydrophobic OMP rejection. Jin et al. [75] found FO rejection for PhACs (diclofenac > ibuprofen > naproxen) increase with pollutants' $K_{ow}$ due to stronger hydrophobic interaction preventing OMP dissolution into the membrane. Foulants on FO membranes can affect interactions with OMPs. Linares et al. [77] found that compared with clean FO membrane, fouled FO membrane showed higher hydrophilicity and negative charge, which increased the removal for hydrophilic charged OMPs (*e.g.*, ibuprofen, naproxen and fenoprofen) due to strong electrostatic repulsion; and increased the removal for hydrophobic neutral OMPs (*e.g.*, BPA and carbamazepine) due to stronger adsorption and reduced mass transport capacity through the membrane. However, the increased MWCO for fouled FO membranes caused membrane swelling,

leading to decreased retention for hydrophilic neutral compounds (*e.g.*, acetaminophen and metronidazole).

For most FO applications, DS recovery and solute leakage prevention are essential at industrial-scale. High total dissolved solids (TDS) DS will achieve high flux and water recovery, but incurs high cost for DS concentrating process. When dewatering OMP-impaired water, future studies should explore new operating conditions (*e.g.*, hybrid FO-RO process [76]) and develop more cost-effective DS solutions (*e.g.*, polyelectrolytes [79]) to improve removal and save energy.

5.4.1.3 Membrane distillation

Membrane distillation (MD) is a thermally driven membrane process in which separation occurs by phase change at the membrane active surface. MD allows water vapor and volatile molecules to pass through a microporous hydrophobic membrane from a hot aqueous solution, in which the driving force is the vapor pressure caused by the temperature differences across the membrane surface from the feed side to the distillate side [80]. MD process renders high rejection performance (for non-volatile solutes) and only requires mild operating temperature (40-80 °C) [81]. MD has some potential for removing OMPs from wastewater [82].

MD separation efficiency is related to solutes' volatility and their hydrophobicity, and the membranes' properties. Wijekoon et al. [80], supported by Plattner et al. [83] concluded that TrOC rejection by direct contact membrane distillation (DCMD) was governed by solutes' volatility rather than hydrophobicity. Non-volatile hydrophilic TrOCs ($pK_H > 9$)

can be effectively rejected in the feed, whereas moderately volatile ($pK_H$ < 9) and hydrophobic compounds can enter the permeate by evaporation or adsorption to the membrane, reducing selectivity. 4-tert-octylphenol, 4-tert-butylphenol and benzophenone for instance with moderate volatility ($pK_H$ < 9) only achieved limited rejection (54, 73 and 66% respectively). Guo et al. [81] found that a negatively charged PVDF membrane led to nearly 100% rejection of 10 negatively charged antibiotics due to electrostatic repulsive. However, removal was lower for the positively charged antibiotics (gentamicin sulfate, 86% and tobramycin, 78%). Some molecules may be susceptible to thermal degradation, leading to the permeation of degradation byproducts [82]. Overall, MD for OMP removal is still an emerging technology demanding further large-scale optimization and commercialization due to membrane wetting and fouling issues [81].

### 5.4.2 Membrane-based hybrid processes

Advanced membrane processes are efficient to remove OMPs, but are energy-intensive and fouling-prone. To benefit from UF membranes' low energy requirements and less pressure demand to achieve greater transmembrane fluxes, hybrid processes in which UF membranes are coupled with adsorption or coagulation have been investigated to remove OMPs.

#### 5.4.2.1 Ultrafiltration with adsorption

Single UF process only removes bacterial, humic acids and colloids and cannot effectively retain OMPs due to loose membrane structure, and hence UF/adsorption hybrid process can be utilized (Figure 2). Permeate post-treatment with adsorption units is an alternative to enhance OMP removal. Gerrity et al. [84] effectively reduced TOrC concentration in a

potable water stream when setting biological activated carbon (BAC) filters post UF and ozone/$H_2O_2$ treatment. Adsorption column can also precede the UF unit to adsorb low MW OMPs and reduce organic loads to mitigate UF membrane fouling. Acero et al. [85] used powered activated carbon (PAC) adsorption as a pretreatment step before cross-flow UF process to remove WWTP OMP-rich effluents. Sbardella et al. [86] investigated BAC – UF hybrid process for PhAC removal through biodegradation and adsorption. Although less adopted, Lowenberg et al. [87] used a mix tank allowing contact between PAC and PhACs, followed by adding $FeCl_3$ coagulant. The treated water underwent a dead-end UF process and obtained 60 – 95% removal for PhACs. Generally, only limited types of OMPs, such as PhACs [85, 87], phenols [88], dyes [89] and pesticides [85] have been investigated using UF/adsorption processes. There is demand to simplify the configuration, better recirculate the sorbents and lessen membrane fouling and pore blockage to minimize cost and operational complexity.

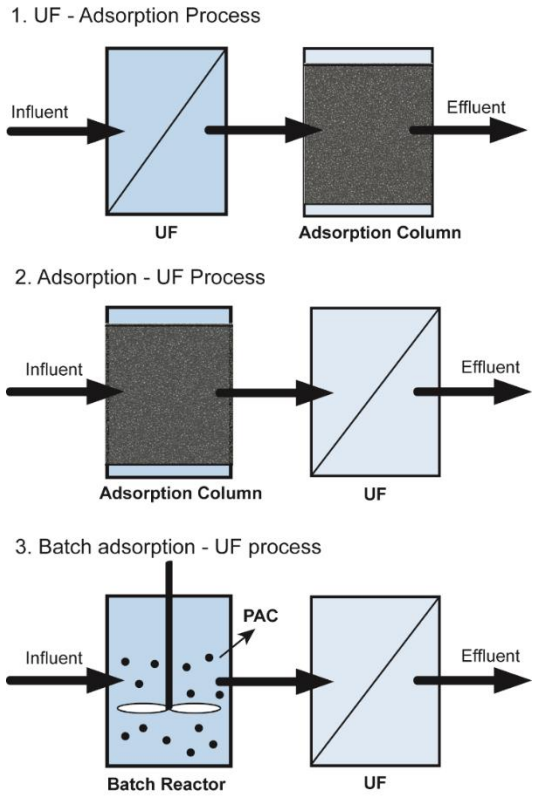


**Fig. 2.** Activated carbon adsorption-ultrafiltration (AC/UF) hybrid system for organic micropollutant removal.

5.4.2.2 Micellar-enhanced ultrafiltration (MEUF)

Micellar-enhanced ultrafiltration (MEUF), introduced in the 1980s [90], combines surfactants in the feed with membrane separation. The added surfactants (e.g., cationic, anionic and nonionic) form micelles above the critical micelle concentration (CMC) in the polluted water. The hydrophobic organic molecules are solubilized in the micelles' interior, whereas the ionic species (*e.g.*, nutrients and heavy metals) or molecules with strong dipoles associate with oppositely charged micellar surfaces through electrostatic interactions [91]. UF membranes retain the micelles with trapped pollutants in the feed side by size exclusion, and only the small-sized unbounded solutes and some surfactant monomers pass to the permeate side. MEUF performance is impacted by membrane type,

operating conditions, solution conditions, surfactant type and target compound characteristics [92]. MEUF has low energy consumption as it operates at low pressure. MEUF for removing aqueous pollutants is pictorially shown in Figure 3.

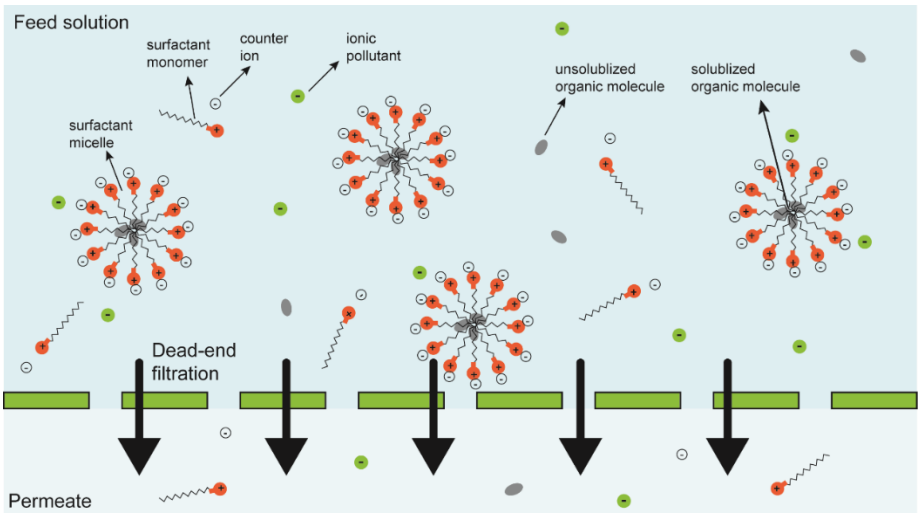


**Fig. 3.** Basic principles for micellar enhanced ultrafiltration (MEUF) for organic micropollutant removal.

MEUF has been traditionally investigated for heavy metal ions and anions removal (oxyanions and nutrients) [93], but OMP removal was also reported, including PhACs [91, 94], phenols [95], dyes [96] and pesticides [97]. Ionic surfactants can remove charged OMPs. Huang et al. [96] solubilized cationic dye methylene blue (MB) by anionic surfactant sodium dodecyl sulfate (SDS) in MEUF, but the high CMC (8 mM) of SDS increased surfactant monomer losses into the permeation. Lowering SDS CMC value by adding salts or other ionic/nonionic surfactants together promoted aggregation which enhanced MB retention in the feed. Cationic surfactants have good commercial availability, large micellar size and low CMC values, and are thus promising for MEUF [91, 93]. Charged sulfonamides and enrofloxacin strongly associated with cationic heads of cetyltremethyl ammonium bromide (CTAB) and cetylpyridinium bromide (CPB) [91], [94].

Nonionic surfactants have low CMCs but cannot form ion-pair complexes with pollutants [92], which remove non-charged OMPs based on hydrophobic solubilization. Doulia et al. [97] reported alachlor removal using nonionic surfactant assisted MEUF. Recently, gemini surfactants have aroused increasing interests due to low CMC and promising organic solubilization effects [95]. MEUF has the potential to remove OMPs, but has not been widely commercialized. Future studies should improve the recovery of surfactants and organic compounds in the permeation [93].

### 5.5 Nanocomposite polymeric membranes for OMPs removal

Nanocomposite polymeric membranes feature significant functional changes through surface or bulk modifications, often providing higher OMP removal than traditional composite and thin film composite (TFC) membranes. Composite membranes can either be surface modified or bulk-modified (nanocomposites), while TFCs can either be modified within the thin film, or below the thin film as shown in Figure 4. OMP separation by nanocomposite polymeric membranes is dictated by fabrication conditions (*e.g.*, modifier type, position and loading), filtration conditions (*e.g.*, applied pressure, flow rate, feed concentration), solution (*e.g.*, pH and coexisting compounds) and pollutant characteristics (*e.g.*, MW, $pK_a$ and $K_{ow}$), which will be discussed below.

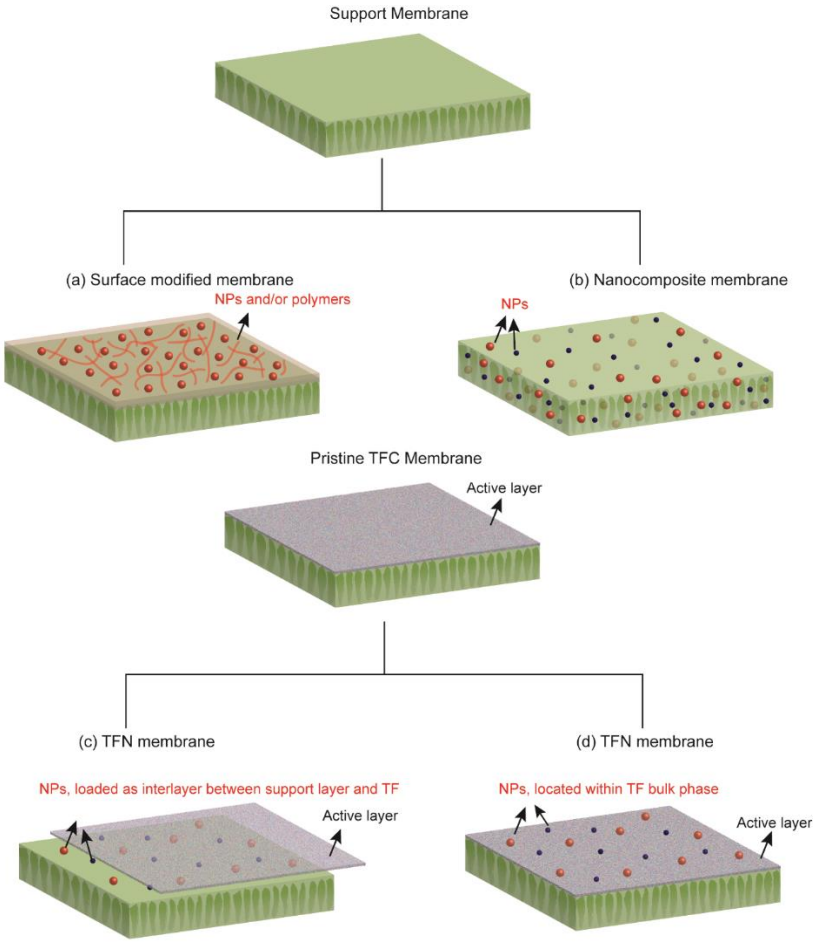


**Fig. 4.** Typical nanocomposite polymeric membranes. Membranes formed either with (a) nanoparticles added to membrane surfaces, or (b) nanoparticles blended into the membrane bulk; and thin film nanocomposites (TFNs) formed either with (c) nanoparticles sandwiched between the support membrane and the thin film (TF) or (d) nanoparticles exposed on the TF surface.

### 5.5.1 Surface modified membranes

#### 5.5.1.1 Fabrication

Surface modified membranes, known as surface located membranes [98], have been rapidly developed for OMP separation over the past decade. Common procedures to modify membrane surface by nanoparticles (NPs) include coating and deposition [47, 99, 100], chemical bonding and grafting [101-103], and layer by layer (LBL) assembly [104]. Pressure deposition or dip coating the membrane in a precursor solution is the easiest

approach to introduce nano-modifiers onto membrane surface. Pressurized filtration has been used to coat carbon-based NPs, including carbon nanotubes (CNTs) [26, 47], carbon nanofibers (CNFs) [105], cellulose nanocrystals (CNCs) [106], graphene oxide (GO) [107] and reduced graphene oxide (rGO) [26, 108]. Of them, two-dimensional (2D) nanomaterials such as GO and rGO have emerged as popular coating materials to make adsorptive membranes due to ultra-thin layer, high surface area and good chemical stability [26, 109]. rGO can also make membrane conductive layers for electrochemical-degradation of various OMPs [104, 110]. Nonetheless, challenges exist as GO-coated membranes show poor stability under cross-flow condition due to GO swelling [111]. Pristine GO or rGO coated membranes have low flux due to short d-spacing of GO and rGO laminates (0.8 nm and 0.35 nm, respectively) [112]. The limited permeation caused by dense membrane structures likely hinder effective OMP removal. Additives have been intercalated to expand the spacing between nanosheets, including organic spacers (*e.g.*, CNTs [26, 109, 110], graphitic carbon nitride (g-$C_3N_4$) [113], covalent organic frameworks (COFs) [114] and chitin nanoycrystals (ChNC) [115]) and inorganic spacers (*e.g.*, metal organic frameworks (MOFs) [116-118], transition metal dichalcogenides (TMDs) [100, 111, 119]), attapulgite nanorods (APTs) [120], halloysite nanotubes (HNTs) [121], MgSi [122], $SiO_2$ [123] and $Fe_3O_4$ [124]). For instance, intercalating CNT [109] and COF material (COF-1) [114] increased GO interlayer spacing to 1.09 nm and 1.03 nm, respectively. These modifications greatly enhanced the water permeation and provided high rejection to water-soluble dyes (> 95%).

Recently, with a deeper understanding of inorganic 2D nanosheets, including MXene [125], hexagonal boron nitride (h-BN) [126] and $MoS_2$ [100, 119], they have been used to modify membrane surfaces. Tong et al. [125] developed MXene and tannic acid (TA)-metal complex surface coated PVDF membranes, giving high selectivity towards hydrophobic OMPs. Hafeez et al. [126] surface modified PVDF membrane with poly(ethylene glycol) (PEG) grafted amine functionalized h-BN ($BN(NH_2)$), leading to superhydrophilicity and subsequently high water flux (> 840 $L \cdot m^{-2} \cdot h^{-1} \cdot bar^{-1}$). Ma et al. [100] intercalated $MoS_2$ into GO nanosheets through van der Waals interactions, which supported the membrane robustness at a wide range of pH conditions (3 -11) while allowing high water flux and strong sieving of dyes.

Stabilizing NPs onto membrane surface during coating is a major challenge, where bio-inspired chemistry has gained much attention to prepare OMP removal membranes. Mussel-inspired protein polydopamine (PDA), prepared by self-polymerization of dopamine (DA), has been widely adopted to stabilize membrane NPs due to strong adhesive force. The reaction is favored in DA-containing Tris - HCl buffer solution at pH = 8.5. PDA-assisted coating has been used to stabilize Au-$TiO_2$ [127], rGO-Cu [99], and MOFs [128] on membranes via dip coating or pressurized filtration onto membrane surface. PDA co-deposition with polyethylenimine (PEI) through interfacial crosslinking is an effective way to improve the surface hydrophilicity and introduce positive charges [103, 129]. Besides, plant polyphenols, such as tannic acid (TA) and gallic acid (GA), are strong adhesives, and cheap cross-linkers to bind thiol and amino groups. Chen et al. [130] investigated dye removal using hydrophilic membranes prepared by crosslinking TA with

PEI via Michael addition or Schiff base reaction, and co-depositing it with HNTs onto PVDF membrane. Further, TA could form coordination complexes with metal ions. Li et al. [131] modified PAN membrane surfaces via doping TA-aminopropyltriethoxysilane (APTES) with $Fe^{3+}$ mediated GO sheets, to remove aqueous OMPs. GO nanosheets can also be cross-linked by other cross-linkers such as ethylenediamine, glutaraldehyde, PEI, dicarboxylic acids and borate [107, 132], which improves the membranes' stability and permeability. These strategies provide new perspectives for obtaining stable, multifunctional, industrially practical membranes for OMP removal.

5.5.1.2 Application for OMP removal

Surface modification by NPs enhance OMP removal, with additional benefits include formation of surfaces that are antifouling, chlorine resistant, and more selective for solutes. Surface modified membranes for OMP removal is summarized in Table 2. Impacts of surface-anchored NPs to OMP removal include increased surface area for adsorption, tuned surface charge and pore size, and provide catalytic properties. Oftentimes, multiple OMP removal mechanisms occur simultaneously. Loose structured MF or UF membranes could greatly enhance the OMP removal through adsorption, as enabled by the introduced NPs. Nano-sorbents are characterized by high surface areas. For example, monolayer GO and single-wall carbon nanotube (SWCNT) have calculated surface areas up to 2400 [133] and 1315 $m^2/g$ [134], respectively. Wang et al. [26] used multi-wall carbon nanotube (MWCNT)/rGO surface modified PVDF microfiltration membranes to treat acetaminophen, caffeine, carbendazim and triclosan, and obtained >76% rejection through adsorption.

Huang et al. [109] found that CNT π-π bonds and hydrophobic interaction enhanced aqueous dye adsorption, when assembled with GO on CA UF membrane surfaces. At only 1 bar transmembrane pressure (TMP), Congo red (CR) and methyl blue reached 98.7 and 94.1% removal, respectively. Wang et al. [47] found that SWCNT coated at PVDF membrane surface favored adsorption of triclosan through π-π donor-acceptor interaction and acetaminophen through hydrogen bonding at neutral pH, respectively. Nanomaterials could alter membrane surface charge to enhance adsorption by electrostatic attraction. Ou et al. [115] established a dopamine modified chitin nanocrystal (D-ChNC)/GO coating on CA membranes, and charged dyes achieved > 98% removal while filtered at 2 bar TMP. Adsorption of cationic dye MB and anionic dye CR were respectively favored by negatively-charged GO and positively-charged ChNC. Electrostatic repulsion may play a role when OMPs and membrane surfaces carry opposite charges. Fang et al. [128] produced a MOF (UiO-66)/PDA thin selective layer atop the GO modified PAN NF membrane. The high electronegativity of UiO-66 and GO and PDA layer's sieving (pore size 2.88 nm) contributed to repulsive exclusion of anionic dye methyl orange (MO) (removal > 94%). Zhang et al. [114] investigated GO/COF-1 nanocomposite coated PAN membrane for dye separation, which led to > 95% removal of anionic dyes. Here negatively-charged GO enhanced membranes' selectivity, whereas the intercalated COF between GO nanosheets had 0.33 nm spacing, much smaller than that of dyes (> 1.5 nm), while allowing water molecules (~ 0.28 nm) to pass through. In both works, low TMP (3 – 4 bar) were needed to reach high removal, much lower than normal NF or RO operating pressures. Further, weakening hydrophobic interactions between solutes and membrane surface can enhance

size exclusion. For example, MXene-TA decreased the PVDF membrane surface hydrophilicity and pore size (1.3 nm), thereby increasing the separation of hydrophobic 4-hydroxybenzoic acid and cinnamic acid at 2 bar TMP [125].

While surface-coated nanomaterials give a more purified permeate through physical interactions, OMPs are concentrated in the retentate or at the membrane surface. Membranes coupling OMP separation and degradation is a novel research area that promises to permanently remove contaminants from solution. Electrically conductive membranes (ECMs) have gained great interest to degrade OMPs at membrane surfaces under an applied voltage. CNT and rGO are the most common conductive coating nanomaterials. Jiang et al. [110] developed an electro-Fenton membrane for PhACs removal. Carboxylic CNT intercalated rGO was used as a membrane cathode, where CNT loaded $Fe^{3+}$ became reduced to $Fe^{2+}$ to serve as catalyst, and $^{\cdot}OH$ was continuously electro-generated with dissolved oxygen (DO). Florfenicol under dead-end filtration exhibited 61.6% removal through size exclusion and electrostatic repulsion, but increased to 95.3% when applied with electro-Fenton oxidation reaction. Sutherland et al. [135] studied the concurrent dead-end filtration and electrochemical reduction of MO using nZVI/CNT surface coated PES membranes at 2.75 bar. Under -2V applied voltage on the membrane cathode, MO removal reached 87.3%, significantly higher than the control test (no voltage, rejection 2.9%). This result was attributed to nZVI's high surface area and strong reductive potential leading to adsorption and electrocatalytic reduction at the membrane surface. As of writing this review, only limited ECMs have been reported to electrocatalytically degrade OMPs. Future studies need to overcome high catalyst cost and operating

complexity. Current modules are restricted to bench-scale, and require optimization for treating realistic wastewaters in industry. For instance, critical research and development work includes improving the bonding stability of the catalytic layer, matching the separation rate with catalytic degradation, and exploring OMP removal with co-existing substances.

Photo-catalytic membranes, based on semiconductor NPs, such as $TiO_2$ [127, 136], ZnO [136] and $Ag_3PO_4$ [137], and other nanomaterials such as $C_3N_4$ [138] and MOFs [139], have also been used to enhance OMP removal via photocatalytic degradation. $TiO_2$ has garnered the most attention due to low cost, excellent photocatalytic activity and chemical stability [127]. Bai et al. [136] used CNT/ZnO/$TiO_2$ coated CA membranes to photo-catalytically degrade acid orange 7, and achieved a > 95% removal through absorption followed by phot-oxidation upon contact under 30 min UV light exposure, which was greater than using CNT alone (~ 80%). Nevertheless, $TiO_2$'s broad energy gap ($E_g$ = 3-3.2 eV) can only be excited under UV light [127]. Recent studies investigated NP-decorated photocatalytic membranes having visible light response. Wang et al. [127] developed an Au-$TiO_2$/PDA surface coated PVDF membrane to remove tetracycline, where Au NPs increased the optical absorption and PDA broadened $TiO_2$'s wavelength response. 120 min visible light irradiation rendered 92% removal, much higher than performed in darkness (28%), and higher than adsorption to pristine PVDF membrane (< 0.5%). $Ag_3PO_4$ and g-$C_3N_4$ have narrow band gaps (Eg = 2.36 eV and 2.7 eV, respectively) [137, 138], enabling visible light response. Zhang et al. [137] examined MB removal at 1 bar TMP by dead-end filtration across a PDA/rGO/ $Ag_3PO_4$ surface modified PVDF membrane under visible

light irradiation. MB removal (up to 99. 1%) increased with surface nanocomposite loading resulting from increased adsorption and photodegradation, much higher than using pristine PVDF membrane (15.2%). Qu et al. [138] deposited O-g-$C_3N_4$/GO/N-CNT onto PC membrane to remove rhodamine 6G in a batch stirring reactor. GO and N-CNT greatly enhanced O-g-$C_3N_4$'s photocatalytic activity, as 360 min of visible light illumination gave 80% removal, and that was only 39% using pure O-g-$C_3N_4$ in the solution. Recently, heterogeneous photo-Fenton reactions on membranes has become a hot topic. Gao et al. [139] intercalated a poly acrylic acid (PAA) modified iron-based MOF ($NH_2$-MIL-88B), in GO nanosheets, and coated it onto a Nylon MF membrane. With the addition of $H_2O_2$, the as-prepared membrane degraded 98.8% of methyl blue during exposure to visible light for 40 min, whereas the pristine Nylon membrane only removed 43.1% MB through adsorption. Such improvement can be attributed to GO's high surface area, which facilitated MB adsorption, as well as its good carrier mobility, which enhanced$NH_2$-MIL-88B's charge separation capabilities for photo-Fenton reactions. Results in this chapter suggest that membrane surface modification by nanomaterials greatly improved the OMP removal between 60 – 100% at low operating pressures (1- 5 bar).

**Table 2** Surface modified membranes using nanomaterials for removing OMPs in water.

| Modifier | Nanomaterial | Substrate | Additive | Pore size/MWCO | Pollutant | Feed concentration (ppm) | Removal (%) | Removal mechanism | Ref. |
|---|---|---|---|---|---|---|---|---|---|
| Organic | GO-Fe [a] | PAN | TA-APTES | 0.56 nm | (1a) naphthalene, 6-methoxytetralin; (1b) pyrene; (1c) bisphenol A, tetracycline hydrochloride; (2) methylene blue; (3) methyl orange | (1a, 2, 3) 10; (1b) 1; (1c) 5 | (1a, 1b, 1c) > 60; (2) 99.5; (3) 90 | (1a, 1b, 1c) size exclusion; (2) adsorption; (3) electrostatic repulsion | [131] |
| | GO/COF-1 | PAN | | 1.5 nm | Congo red, methylene blue, reactive black 5, direct red, chrome black T | 200 | > 98 | size exclusion, electrostatic repulsion | [114] |
| | GO/chitin nanocrystal (ChNC) | CA | PDA | | methylene blue, Congo red | 20 | 99.6, 98.3 | adsorption | [115] |

| | | | | | | | | | |
|---|---|---|---|---|---|---|---|---|---|
| | GO-Fe[b]/rGO | PTFE | | 1000 Da | florfenicol | 1 | 90 | electro-Fenton oxidation | [104] |
| | GO/CNT | CA | | | Congo red, methyl blue | 100 | 98.7, 94.1 | adsorption | [109] |
| | GO/N-CNT/O-g-C3N4 | PC | | | rhodamine 6G | 10 | ~ 80 | photocatalytic degradation | [138] |
| | GO/sodium alginate (SA) | PVDF | | | direct red 80, Congo red, methylene blue | 20 | 99.8 | size exclusion, electrostatic repulsion | [132] |
| | rGO/CNT-Fe[b] | PTFE | | 1.29 nm | (1) amoxicillin, ampicillin, cefalexin, ofloxacin, sulfadiazine, sulfamethoxazole, florfenicol; (2) chloramphenicol, thiamphenicol, atenolol, carbamazepine | 1 | (1) 79 - 100; (2) 71 - 82 | (1) electrostatic repulsion, electro-Fenton oxidation; (2) adsorption, size exclusion, electro-Fenton oxidation | [110] |
| | rGO/MWCNT | PVDF | | | acetaminophen, caffeine, carbendazim, triclosan | 1 | > 76 | adsorption | [26] |
| | rGO/g-$C_3N_4$ | CA | PDA | | rhodamine B | 10 | 98.5 | size exclusion, photocatalytic degradation | [113] |
| | SWCNT | PVDF | | > 10nm | triclosan, ibuprofen, acetaminophen; | 1 | 90, 59, 62 | adsorption | [47] |
| Organic/metallic | GO/$TiO_2$ | PSF | PDA/PEI | 0.87 nm, 978.8 Da | crystal violet, safranine T, eriochome black T, alizarin yellow GG | 100 | 99.99, 96, 99.99, 89.4 | size exclusion, electrostatic repulsion | [103] |
| | GO/$NH_2$-MIL-88B | Nylon | PAA | | (1, 2) methylene blue; (1) Congo red, crystal violet | 20 | (1) > 97; (2) 98.79 | (1) adsorption, size exclusion; (2) adsorption, photo-Fenton degradation | [139] |
| | GO/MIL-88A | PVDF | | | methylene blue, rhodamine B, methyl orange | 10 | > 98 | size exclusion, photo-Fenton degradation | [117] |
| | GO/attapulgite nanorods (APT) | PC | | | rhodamine B | 7.5 | > 99.9 | adsorption, size exclusion | [120] |
| | GO/$SiO_2$ | CA | | | methyl blue | 10 - 40 | > 95 | adsorption, size exclusion | [123] |
| | GO/$MoS_2$ | CA | | | Congo red, direct red 80, methylene blue, rhodamine B | 20 | > 99 | size exclusion | [100] |
| | GO/$MoS_2$ | PVDF | PVA | | Congo red, methylene blue, methyl orange, rhodamine WT | 10 | 99.6, 97.4, 96.3, 94.6 | size exclusion | [119] |
| | GO/$WS_2$ | Nylon | | | rhodamine B, methylene blue | 10 | 97.7, 96.3 | size exclusion | [111] |
| | GO/$NH_2$-$Fe_3O_4$ | PVDF | PDA | | (1) Congo red, methyl orange; (2) methylene blue | 100 | 98, 75, 70 | (1) size exclusion, electrostatic repulsion; (2) adsorption | [124] |
| | rGO/MgSi | PAN | | 1.27 nm, 536 Da | acid brilliant blue, chrome blue-black R, methyl orange | 100 | 98.2, 95.2, 73.4 | size exclusion, electrostatic repulsion | [122] |
| | rGO/Cu | PAN | PDA | 1510 Da | Congo red, direct red 23, reactive blue 2 | 500 | > 98 | size exclusion, electrostatic repulsion | [99] |
| | rGO/UiO-66 | PC | | | rhodamine B | 10 | 95 | size exclusion | [116] |

| | | | | | | | | | |
|---|---|---|---|---|---|---|---|---|---|
| | $rGO/Ag_3PO_4$ | PVDF | PDA | | methylene blue | 30 | 99.1 | adsorption, photocatalytic degradation | [137] |
| | $rGO/SiO_2$ | PVDF | PDA | | methylene blue | 10 | 99.8 | adsorption | [140] |
| | rGO/HKUST-1 | CA | PDA | | methylene blue, Congo red | 40 | 99.8, 89.2 | adsorption, size exclusion | [118] |
| | rGO/HNT | CA | PDA | | methylene blue, Congo red | 100 | > 99 | adsorption, size exclusion | [121] |
| | prGO/UiO-66-$(COOH)_2$ | Nylon | | | Congo red | 10 | > 97.2 | electrostatic repulsion | [141] |
| | CNT/ZnO/$TiO_2$ | CA | | | acid orange 7 | 50 | > 95 | adsorption, photocatalytic degradation | [136] |
| | SWCNT/DWCNT/nZVI | PES | | | methyl orange | 81.8 | 87.3 | adsorption, electrocatalytic reduction | [135] |
| | MWCNT/$TiO_2$ | CA | | | carbamazepine, ibuprofen, acetaminophen | 10 | 80, 45, 24 | adsorption | [142] |
| | MWCNT/nZVI | PTFE | | 41 nm | metoprolol | 2 | 97 | adsorption, electrochemical oxidation | [143] |
| Metallic | Mxene | PVDF | TA-Fe | 1.3 nm | 4-hydroxybenzoic acid, cinnamic acid | 5 | 66, 53 | size exclusion | [125] |
| | h-BN | PVDF | | 1.4 - 3 nm | methylene blue | 5 | 98 | size exclusion | [126] |
| | UiO-66 | GO/PAN | PDA | 2.88 nm | methyl orange, tetracycline hydrochloride | 10 | 94.84 95.5 | size exclusion, electrostatic repulsion | [128] |
| | HNT | PVDF | TA, PEI | 45.2 nm | direct blue 14, direct red 28, direct yellow 4 | 100 | 96, 92.8, 90.7 | adsorption, size exclusion | [130] |
| | $PCu_2W_{11}$ | PVDF | | 200 - 750 nm | tetracycline | 300 | 88.6 | adsorption | [101] |
| | nZVI | PVDF | | | 2-chlorophenol | 10 | 91.63 | adsorption, reductive degradation | [144] |
| | $Au/TiO_2$ | PVDF | PDA | | tetracycline | 10 | 92 | photocatalytic degradation | [127] |
| | $Ag/TiO_2$ | PAN | PDA, PEI | | Congo red, reactive orange 16, reactive black 5 | 200 | 99.6, 96.2, 99.5 | size exclusion, photocatalytic degradation | [129] |
| | ZIF-8 | PAN | PEI | | acid fuschin, methyl orange, methyl blue, Congo red | 100 | 94.4, 81.2, 99.6, 99.2 | adsorption, size exclusion | [102] |

a. $Fe^{3+}$ was introduced to the edge of GO sheets to complex with TA-APTES.
b. $Fe^{2+}$ served as Fenton catalyst and was grafted into the carboxylic CNT or rGO through electrochemical reduction of -$COOFe^{3+}$.

## 5.5.2 Nanocomposite membranes

### 5.5.2.1 Fabrication

Nanocomposite membranes introduce nanofillers into the polymeric matrix, are also classified as mixed matrix membranes. Nanocomposite membranes for OMP removal have

been synthesized with nanospheres, nanosheets and nanotubes, including organic (*e.g.*, CNT [145], CNC [146], GO [147, 148], rGO [149] and carbon dots (CDs) [150]), inorganic (*e.g.*, metals [151], metal oxides [152-154], MOFs [155, 156], $SiO_2$ [157-160], and clays [161-163]) or organic-inorganic hybrids thereof [164-167]. These nano-enabled membranes possess enhanced functionality over commercial UF/NF membranes, such as greater hydrophilicity (thus higher permeability) [147, 150, 168], tuned pore channels [151, 169], increased antifouling property [162, 164, 170] and better mechanical stability [145].

Phase inversion via in situ nanofiller blending has been extensively adopted to fabricate nanocomposite membranes due to low cost and efficiency. This can be achieved by thermally induced phase inversion (TIPS) and non-solvent induced phase inversion (NIPS). The former approach increases the temperature to evaporate the solvents and thereby trigger polymer precipitation, whereas the latter approach immerses the polymer-solvent solution into a non-solvent (typically water) to initiate the demixing process, in which asymmetric membrane structures form during solvent and non-solvent exchanges at the polymer interface. Nanocomposite membranes for OMP removal often employ NIPS during fabrication. NPs are first dispersed into polymer casting solutions before casting. Solvent and polymer selection impacts NP dispersion and the resultant membrane characteristics. The solvent and polymer collectively impact the NP dispersion and the resultant membrane characteristics. DMF [145, 152, 163], DMAc [146, 150, 154], NMP [151, 164, 166] and DMSO [171] have been used as casting solutions. PES and PSF are some of the most frequently investigated base polymers due to good mechanical, structural, and chemical stability [150].

Unlike standard polymeric membranes, nanocomposite membranes' performance sometimes decreases because of NP agglomeration due to their high surface area and strong interactions in the hydrophobic bulk phase, as well as the reduced NP reactivity due to oxidation or hydration reactions (*e.g.*, metallic NPs and MOFs) [154, 164]. Improving NP dispersion and chemical stability becomes vital to maintain efficient OMP removal. Stirring/sonication in the casting step, dosing surfactants to the solvents, and modifying NPs' surfaces with functional groups, grafted oligomers, or non-covalently bound modifiers, can provide better dispersion. Increased inorganic nanofiller-polymer compatibility of several dye separation membranes was achieved through modification with silane coupling agents [160, 162], polymer [157], and carbon-based NPs [164, 165, 168]. These efforts overall improved membrane durability, hydrophilicity and selectivity towards OMPs. Nonetheless, most nanocomposite membranes were studied at bench-scale. NP-modified phase inversion requires optimization so that nanocomposite membranes can be industrially scaled.

5.5.2.2 Application for OMP removal

OMP removal by nanocomposite membranes rely on adsorption by weak forces (van der Waals, dipole, and $\pi - \pi$ interactions) [151, 154, 155, 172], electrostatic repulsion [148, 150, 163], size exclusion [146, 157, 173], catalytic oxidation/reduction [167] and photocatalytic degradation [166, 168, 171]. Nanocomposite membranes for OMP removal is summarized in Table 3. We discuss the effects of three key factors – 1) NP type and loaded mass, 2) operating conditions of pressure and feed concentration, and 3) solution pH– on nanocomposite membranes for removing OMPs.

Firstly, OMP removal by nanocomposite polymeric membranes is dependent on NP type, loading, and how the membrane properties were impacted by NP type and loading. NP inclusion into membranes primarily impacts membrane hydrophilicity, pore size, and porosity, which impacts the membrane's permeability and OMP rejection. Membrane pore formation is affected by NPs during the blending phase inversion step. Thus, evaluating and optimizing NP loading is crucial. Ghaemi et al. [163] studied the effect of organically modified montmorillonite (OMMT) in nanofiltration PES membranes on pesticide removal. Membrane hydrophilicity increased while pore size decreased, when increasing OMMT loading from 0 to 4 wt%. This benefited 3,5-dinitrosalicylic acid and 2,4-dinitrophenol rejection (> 90%). However, adding more OMMT (> 6 wt%) caused a dense skin layer formation and layered silicates aggregation, which decreased the water flux and impeded NF separation. Balcik-Canbolat and Van der Bruggen [146] observed that high content (up to 1 wt%) of CNC in the PES membrane matrix contributed to higher membrane hydrophilicity, pore size, and looser skin layers. This gave higher water flux but sacrificed some direct red 80 removal due to a weakened sieving effect. Despite losing selectivity, all the membranes obtained > 90% rejection. Modi et al. [170] compared the amoxicillin removal efficiencies using PES hollow fiber membranes embedded by carboxylated GO, ZIF-L nanoflakes and their combined nanocomposites, respectively. The latter membrane exhibited the highest hydrophilicity, negative surface charge and largest pore size, while rendering the best water flux and removal to negatively-charged amoxicillin. At 1.5 bar TMP in the cross-flow condition, the removal reached 98.9 %, more than 2 times higher than using bare PES membranes. These studies indicate that the impacts of NP

incorporation are not easily determined, and that NP loading must be experimentally optimized to maximize OMP removal efficiency.

Secondly, operating conditions, OMP concentration, and coexisting species impact nanocomposite membrane performance, as these affect the residence time and interaction between OMPs and the membrane. Nasseri et al. [148] and Goswami et al. [151] investigated the dead-end filtration of BPA using PSF/GO and PES/SWCNT nanocomposite membrane, respectively. Low TMP and high feed concentration gave better separation characteristics because the electrostatic repulsion and adsorption effect dominated the filtration. High TMP was however not favorable for the separation because it increased the solution passage rate, thereby reducing the contact time between the solute and the membrane. This finding aligns well with established adsorption theory that a higher retention time, achieved at lower TMPs, leads to greater adsorption. Mukherjee and De [152] removed catechol using the CA/alumina nanocomposite membranes, and rejection rates significantly dropped in the presence of NaCl electrolytes, which is likely the result of weakening the electrostatic force between OMPs and the membrane due to electrostatic shielding. Additionally, gradual saturation of OMPs on the NPs in the membrane surfaces may impact permeate flux and thus membrane service life, which is a concern. These findings suggest that nanocomposite membranes do not primarily rely on sieving to remove OMPs, unlike traditional NF/RO processes. Rather, their effectiveness for OMP removal is dependent on the adsorptive properties of the OMP with NPs and polymer materials of the membrane and requires a deep understanding of membrane-nanofiller-solute interaction mechanisms.

Thirdly, solution pH critically impacts the nanocomposite membrane performance by affecting membrane surface charge (reflected by zeta potential), nanocomposite stability, dissociation of the charged functional groups from OMPs and solute solubility [155, 172, 174]. Tan et al. [155] developed MIL-68(Al) blended PVDF membrane adsorbers to remove aqueous *p*-nitrophenol ($pK_a$ =7.15). Maximum adsorption (up to 82.7%) of *p*-nitrophenol was obtained at pH values (4-7) below $pK_a$, whereas the adsorption capacities decreased remarkably at pH above $pK_a$, because at higher pH *p*-nitrophenol became anionic and was electrostatically repelled from the negatively charged membrane surface. pH also affects NP stability, where the inherent MOF structure was destroyed at pH < 4, leading to poor OMP removal. Mukherjee and De [152] found maximum catechol adsorption on CAP/alumina nanocomposite membrane surfaces at aqueous pH above the membrane's isoelectric point ($pH_{IEP}$=5.4) and below the $pK_a$ (9.5) of catechol. Under these conditions, the CAP acetate groups were deprotonated such that the membrane surface was negatively charged, which facilitated the protonated catechol transport to the membrane due to their opposite polarity. Niedergall et al. [172] investigated adsorption to remove OMP from water. A sharp decline of BPA adsorption on the polymer NP (P(4-VP-co-TRIM)) mixed PES membrane was observed at high pH above BPA's $pK_a$ (9.6-10.2). This can be explained by BPA deprotonation resulting in electrostatic repulsion against the negatively charged membrane, as well as increased solubility leading to less hydrophobic adsorption. Manipulating solution pH can maximize electrostatic attraction of OMPs to adsorption sites, however, OMP rejection will eventually decrease as adsorption sites are saturated.

**Table 3** Nanocomposite membranes for removing OMPs in water.

| Modifier | Nanomaterial | Substrate | Pore size/MWCO [a] | Pollutant | Feed concentration (ppm) | Removal [a] (%) | Removal mechanism | Ref. |
|---|---|---|---|---|---|---|---|---|
| Organic | PEI | PES | 1.384 nm, 781 Da | reactive red 49, reactive black 5 | 500 | 92, 96 | adsorption, size exclusion | [175] |
| | hollow mesoporous carbon nanospheres (HMCNs) | PES | 3.5 nm, 336 kDa | tetracycline, 17β-estradiol | 0.1, 0.0001 | 97, 94 | adsorption | [176] |
| | GO | PES | 3.8 nm | direct red 16 | 30 | 99 | electrostatic repulsion | [147] |
| | carbon | PSF | 5.93 nm | benzene, toluene, phenol | 50 | 97.7, 82.8, 79.2 | adsorption, size exclusion | [173] |
| | N-doped porous graphene oxide (N-PGO) | PES | 9.14 nm, 1096 Da | reactive red 195 | 100 | 95.6 | electrostatic repulsion | [177] |
| | carbon dots (CDs) | PES | 12 nm | RR 198 | 100 | 98.9 | electrostatic repulsion | [150] |
| | rGO-PDA | PSF | 50.6 nm | direct red 80, methyl blue | 25 | 98.8, 87 | size exclusion, electrostatic repulsion | [149] |
| | GO | PSF | 71.28 nm | bisphenol A | 7.5 | 93 | electrostatic repulsion | [148] |
| | P(4-VP-co-TRIM) | PES | 565 nm | bisphenol A | 0.25 | 87.4 | adsorption | [172] |
| | SWCNT | PES | ~ 80kDa | bisphenol A, 4-nonylphenol | 0.1 | 78, 85 | adsorption | [145] |
| | CNC | PES | | direct red 80 | | 95.8 | size exclusion | [146] |
| Organic/metallic | GO/Cu(tpa) | PES | 3.6 nm for the filler | methylene blue, Congo red, methyl orange | 100 | 65, 92 | size exclusion, electrostatic repulsion | [164] |
| | GO/ZIF-L | PES | ~ 3.1 nm | amoxicillin | 25 | 98.9 | electrostatic repulsion | [170] |
| | GO/CuS | PES | ~ 3.7 nm | oxybenzone, bisphenol A | 25 | 98, 95 | electrostatic repulsion | [165] |
| | g-$C_3N_4$/ZnO | CA | 6.1 nm | lanasol blue 3R | 200 | 93.7 | adsorption | [178] |
| | mpg-$C_3N_4$/$TiO_2$ | PSF | 80 kDa | sulfamethoxazole | 10 | 69 | photocatalytic degradation | [166] |
| | MWCNT/ZnO | PES | | direct red 16 | 30 | 96 | photocatalytic degradation | [168] |
| | HPEI/MWCNT/Fe-Cu | PES | | 2,4,6-trichlorophenol | 0.025 | 99.4 | adsorption, catalytic degradation | [167] |
| Metallic | $SiO_2$-PSS | PES | 0.64 nm, 655 Da | reactive red 49, reactive black 5 | 500 | ~ 90 | size exclusion, electrostatic repulsion | [157] |
| | HNT (sulfonated) | PES | 1.3 nm. 682 Da | reactive red 49, reactive black 5 | 1000 | 90, 94 | size exclusion | [161] |
| | HNT (modified by APTES) | PVDF | 1.922 nm | direct red 28 | 100 | 94.9 | adsorption, electrostatic repulsion | [162] |
| | $Fe_3O_4$@$SiO_2$-$NH_2$ | PES | 9.42 nm | methyl red | 30 | 97 | adsorption | [154] |
| | montmorillonite | PES | 9.59 nm | 3,5-dinitrosalicylic acid, 2,4-dinitrophenol | 22.8, 18.4 | 94, 90 | adsorption, electrostatic repulsion | [163] |
| | alumina | CAP | 22.8 nm, 122 kDa | catechol, p-nitrophenol | 100 | 87, 89 | adsorption | [152] |
| | $CeO_2$ | PES | ~ 23.4 nm | direct red 23, direct red 243, Congo red | 100 | > 99 | size exclusion, electrostatic repulsion | [153] |

| | | | | | | | |
|---|---|---|---|---|---|---|---|
| Pd | PSF | ~ 40 nm | crystal violet | 40.8 | 99 | adsorption | [151] |
| $SiO_2$-DES | PI | > 46.4 nm | phenol | 30 | 96 | adsorption, electrostatic repulsion | [158] |
| $Au_{0.1}Ag_{0.9}/TiO_2$ | CA | 430.12 nm | tetracycline | 5 | 88.7 | photocatalytic degradation | [171] |
| MIL-68(Al) | PVDF | 700 nm | p-nitrophenol, methylene blue | 5 | 82.7, 95 | adsorption | [155] |
| MIL-125(Ti) | PVDF | | rhodamine B | 10 | 99.7 | adsorption, photocatalytic degradation | [156] |
| $SiO_2$ | PES | | bisphenol A | 0.1 | 88 | adsorption | [159] |
| $SiO_2$ (modified by SBMA) | PES | | reactive black 5, reactive green 19 | | 97.9, 99 | electrostatic repulsion | [160] |

a. Data were obtained either from the article contents, or extracted from figures using GetData Graph Digitizer software.

### 5.5.3 Thin film nanocomposite (TFN) membranes

#### 5.5.3.1 Fabrication

Thin film composite (TFC) membranes consist of an ultra-thin barrier layer (commonly polyamide (PA), thickness 50 -300 nm [179]) atop a polymeric membrane support. Compared to integrally-skinned asymmetric membranes, TFC membranes have an independently controlled and optimized top selective layer for enhancing selectivity and pollutant rejection [180, 181]. Interfacial polymerization (IP), first reported by Morgan et al. in the 1960s [179], is the most common route to prepare commercial PA TFC membranes [182]. Typically, the support membrane is impregnated with an aqueous solution of diamine or polyamine, such as PIP [7, 52, 180] and MPD [9, 181], followed by removing excessive solution on the membrane surface. The soaked membrane is then put into contact with a water immiscible organic solution (*e.g.*, hexane) containing acryl chloride monomers, such as TMC [7, 180, 181], to form a PA thin film.

While traditional PA TFC membranes were primarily optimized to make high pressure NF or RO membrane systems for desalination and heavy metal removal, the inherent

permeability-selectivity trade-off, fouling-prone nature and high energy costs limit their application for OMP separation under low pressures. NPs, such as CNT [183]), CNC [180], GO [184, 185], MOFs [52, 181, 186], $SiO_2$ [9], clays [7, 187, 188], and $MoS_2$ [189, 190], have high surface area and high adsorption potential, and hence the exploitation of these NPs into TFC membranes provides thin film nanocomposite (TFN) membranes with great potential for OMP separation. This is due to TFN membranes' improved mechanical and chemical stability, reactive and adsorptive capacities. The porous fillers can be (i) assembled flexibly within the thin film [9, 52, 180, 184], by pre-mixing the NPs in the aqueous solution or the organic solvent before the IP reaction; (ii) formed as an interlayer between the thin film [7, 181, 183, 186], through in-situ growth (*e.g.*, by phase inversion) or pressurized filtration of the NPs, followed by conventional IP reaction. Although less common, nanofillers have been combined with non-PA based thin films to design TFN membranes for OMP separations. For instance, Ghaemi et al. [191] polymerized pyrrole to form hydrophobic polypyrrole (PPy) on the PES membrane, in which nano-zeolite SAPO-34 was blended. Zhang et al. [182] incorporated graphene oxide quantum dots (GOQDs) into a tannic acid (TA) layer during an IP process, which yielded a loose structured NF membrane. Compared with nanocomposite membranes, TFN membranes suffer less NP dissolution, which reduces the potential for secondary contamination caused by toxic and harmful NPs [180].

#### 5.5.3.2 Application for OMP removal

TFN membranes have been increasingly explored for NF [192] and RO [193] processes for OMP separation, and the tailored top layer plays a crucial role for membrane

performance, particularly with respect to membrane flux and selectivity. Here we focus on NF applications, which are much less energy-intensive. The selective layer and the added NPs collectively determine TFN membranes' surface properties, and OMP removal can be attributed to one or more mechanisms, which include size exclusion [180, 190, 194], electrostatic interactions [7, 183, 195], and adsorption/diffusion [9, 52, 186, 196]. TFN membranes for OMP removal is summarized in Table 4. Integrated NPs into conventional TFC membranes produce a highly porous structure, which can reduce the ability of TFCs to remove OMPs by size exclusion but enables control over the TFC pore size. In this section, we discuss how assembly structure and nanofiller loading impact separation performance, as well as the benefits and challenges encountered for OMP removal.

The membrane permeability and OMP separation capacities are greatly impacted by the NP properties and thus their location in the TFN membrane. Basu and Balakrishnan [181], and Dong et al. [7], intercalated ZIF-8 and zeolite, respectively between the PA thin film and the PSF support layer. This approach enhanced the stability of the TFN membrane, because blending these NPs into PA during the IP process can cause micro-sized cavities, reducing separation efficiencies for OMPs. The interlayer set-up preserved the PA's size exclusion effect and enhanced the water permeability by creating nano-pores under the PA which acted as water channels. In this manner, Basu and Balakrishnan [181] obtained 9 % higher rejection for acetaminophen (55 %) and 2 fold permeation increase compared with the unfilled PSF/PA membrane, when tested under dead-end flow conditions at only 4 bar TMP. Dong et al. [7] also observed a similar or higher rejection (> 90 % for most compounds tested) of 21 types of PhACs when using the zeolite-PA blended TFN

membrane in cross-flow condition at only 5 bar TMP compared to the bare PA membrane. In many cases, incorporating NPs into the PA can be challenging, however, some NPs can exhibit high compatibility with PA and high stability during thin film formation by IP. Zhao et al. [186] investigated MOF-PA interaction patterns, and found that MIL-53(Al) can tightly bind with PA post IP. Under either set-up, the obtained TFN membrane achieved 1.3 times higher permeability and significantly higher nalidixic acid and sulfamethoxazole rejections than the TFC control membrane.

Furthermore, NP content in the TFN membranes critically impact the membrane-solute affinity (*e.g.*, through changing membrane hydrophilicity, thin film thickness and available adsorption sites), size exclusion (*e.g.*, through changing pore size) and Donnan exclusion (charge repulsion) (through changing charge density), leading to a change in the dominant OMP removal mechanism. It has been observed that incorporating NPs into TFCs leads to various trade-offs in selectivity and permeability of different OMPs. As such it is has been challenging to remove a wide range of OMPs using a single NP modification to a TFC. For example, Dai et al. [52] incorporated MIL-101(Cr) into PA active layer on the PES membrane, and used the TFN membrane for the removal of EDCs and salts. Increased MIL-101(Cr) content in the PA layer led to moderately higher rejection of hydrophobic methylparaben, propylparaben, benzylparaben, and BPA through stronger hydrophobic adsorption, but greater MIL-101(Cr) content also led to slightly lower rejection of some mono- and divalent salts. Similarly, Wang et al. [184] found a trade-off in incorporating GO into PA thin films. They found that increased GO content in the PA top layer on PSF support provided the TFN membrane with higher negative charge. At moderate GO loading

(0.004 wt%) in the PA layer, the TFN membrane showed 41.85 % removal towards the negatively charged sulfamethoxazole due to charge repulsion, approximately 3 times higher than the control TFC membrane. However, despite the presence of GO, the TFN membrane showed equally poor removal (< 5 %) towards paracetamol as the control TFC membrane, which was a result of its low MW and high hydrophilicity. Gong et al. [183] preloaded PDA modified CNT onto PES membranes, followed by adding a PA top layer. They found that increased PDA-CNT content increased the interlayer thickness and the zeta potential, thus leading to lower MWCO and more negatively charged surface. Having similar MWs, anionic dye methyl violet obtained higher removal than cationic dye MB (99.5 vs 86.4 %) due to the Donnan effect. However, despite high dye removal, the membrane exhibited low rejection towards $Cl^-$, a monovalent ion, due to the disruptions within the PA layer by the CNTs. This suggested promising recovery of aqueous dyes from some saline wastewaters, but without compromising the monovalent ion rejection. To conclude, the engineered TFN membranes have great potential for purification and recovery of different OMPs, but their properties should be tailored to suit the characteristics of the target compounds.

**Table 4** Thin film composite (TFC) membranes for removing OMPs in water.

| Modifier | Nanomaterial | Location | Substrate | Thin film | Pore size/MWCO [a] | Pollutant | Feed concentration (ppm) | Removal [a] (%) | Removal mechanism | Ref. |
|---|---|---|---|---|---|---|---|---|---|---|
| Organic | CNC | within TF | PES | PA | 0.41 nm, 312.06 Da | rose bengal, Congo red, methyl orange, crystal violet, methylene blue | | > 99 | size exclusion | [180] |
| | quaternized carbon quantum dots (QCQDs) | within TF | PVDF | PA | 0.42 nm | sulfamethoxazole, carbamazepine, atenolol, trimethoprim | 1 | 98.2, 98.6, 99.5, 99.7 | size exclusion, electrostatic repulsion | [197] |
| | β-CD-PIM | within TF | PSF | PA | 0.62 nm | erythromycin | 100 | 97 | size exclusion | [198] |
| | GOQDs | within TF | PES | PA | 0.86 nm, 525 Da | orange GII, Congo red | 100 | 95, 99.9 | size exclusion | [194] |
| | GO | within TF | PSF | PA | 1764 Da | new coccine, ponceau S, direct red 80 | 500 | 94,3, 96.2, 99.2 | size exclusion, | [185] |

| | | | | | | | | | | |
|---|---|---|---|---|---|---|---|---|---|---|
| | | | | | | | | | electrostatic repulsion | |
| | GO | within TF | PSF | PA | | norfloxacin, sulfamethoxazole | 1 | 53.32, 41.85 | size exclusion, electrostatic repulsion | [184] |
| | GOQDs | within TF | PAN | TA | | (1) methyl orange, Congo red, methyl blue; (2) methylene blue | 100 | 84, 100, 98, 74 | (1, 2) size exclusion; (1) electrostatic repulsion | [182] |
| | CNT (modified by PDA) | interlayer | PES | PA | 0.878 nm, 365 Da | (1) methylene blue, crystal violet; (2) methyl orange, methyl violet, acid fuchsin, Congo red | 100 | 86.4, 98, 92.5, 99.5, 100, 100 | (1, 2) size exclusion; (2) electrostatic repulsion | [183] |
| | TpPa-1 (modified by PDA) | interlayer | PAN | PA | 16.36 nm | orange GII | 100 | 93 | adsorption, size exclusion | [196] |
| | GO | interlayer | PSF | PA | | safranine T, indigo carmine, coomassie brilliant blue, rose bengal | 100 | > 92 | size exclusion | [199] |
| Metallic | $SiO_2$ (modified by oleic acid) | within TF | PSF | PA | 0.32 nm | atrazine, propazine, prometryn | 10 | > 98 | adsorption, size exclusion | [9] |
| | SAPO-34 | within TF | PVDF/PES | PA | 0.45 nm, 320 Da | raffinose, saccharose, glucose | | 98.6, 95.3, 82.1 | size exclusion | [187] |
| | MIL-101(Cr) | within TF | PES | PA | 0.6 nm | methylparaben, propylparaben, benzylparaben, bisphenol A | 0.2 | 47, 46, 51, 80 | adsorption, size exclusion | [52] |
| | Zn-TCPP | within TF | PSF | PA | 1.54 nm | Congo red, methylene blue, direct red 23 | 200 | > 96 | size exclusion | [200] |
| | SAPo-34 | within TF | PES | PPy | 220 Da | (1) methyl violet 6B; (2) reactive blue 4, acid blue 193 | 50 | 100 | (1) adsorption; (2) size exclusion, electrostatic repulsion | [191] |
| | HNT | within TF | PSF | PA | | setazol red, reactive orange | 100 | 99.7, 99.7 | electrostatic repulsion | [195] |
| | ED-MIL-101(Cr) | within TF | PES | PA | | terbutaline, atenolol, fluoxetine, ketoprofen, diclofenac, bezafibrate | 0.2 | > 82.7 | size exclusion, electrostatic repulsion | [192] |
| | $MoS_2$ (modified by TA-$Fe^{3+}$) | within TF | PSF | PA | | glucose, sucrose, raffinose | 150 | 70, 89, 91 | size exclusion | [190] |
| | h-BN | within TF | PES | PA | | methylene blue | 10 | 73 | size exclusion | [201] |
| | $TiO_2$ | withn TF & interlayer | PES | PA | | Congo red, alcian blue, orange GII | 100 | 98, 96, 85 | size exclusion | [202] |
| | $MoS_2$ | interlayer | PES | PA | 0.53 nm | methylparaben, ethylparaben, propylparaben, benzylparaben | 0.2 | 53.7, 69.1, 79.1, 91.3 | adsorption, size exclusion | [189] |
| | ZIF-8 | interlayer | PSF | PA | | acetaminophen | 100 | 55 | size exclusion | [181] |

| | | | | | | | | |
|---|---|---|---|---|---|---|---|---|
| zeolite | interlayer | PSF | PA | 21 types of PhACs | 0.02 | > 80 | size exclusion, and/or electrostatic repulsion | [7] |
| MIL-53(Al) | interlayer | PSF | PA | phenacetine, nalidixic acid, carbamazepine, sulfamethoxazole, atenolol, sulpiride | 0.05 | 67, 88, 78, 88, 80, 92 | adsorption, size exclusion | [186] |

a. Data were obtained either from the article contents, or extracted from figures using GetData Graph Digitizer software.

## 5.6 Future perspectives

Significant progress on state-of-the-art nanocomposite polymeric membranes has been made over the past 10 years to efficiently remove OMPs in aqueous environmental feeds. Nanomaterial incorporation into traditional polymeric substrates was shown to be promising on selective filtration performance due to customized characteristics and functions to target OMPs. Future research should perform techno-economic analyses to identify the most economically promising nanocomposite materials. In addition, there is no “one size fits all” solution to remove all OMPs; their charge, polarity, molecular weight, and concentration as well as the medium in which OMPs are found all influence removal. As such, standard OMPs should be used to reveal different nanocomposite polymeric membrane – OMP interaction mechanisms to help select the best membrane properties and operating conditions. Developing durable membranes with longer operation life that can achieve high throughput and removal efficiency is an urgent need. Furthermore, more realistic complex pilot-scale operations have rarely been investigated and should be the continued focus of future research. Challenges, such as scalability, agglomeration, permeability and selectivity, need to be addressed for the membrane types that have been developed so far.

NP agglomeration, especially at high loading content, on membrane surface or with the matrices can result in defective membranes with poor OMP removal efficiency. The translocation and depletion of NPs in the membrane during filtration over time would likely destroy the original structures, reduce the membrane life span, and eventually become a secondary nanomaterial-laden pollutant stream. Future works should develop better chemistries to stabilize or covalently bind the NPs to the membranes, and study the retention and leaching of NPs in the nanocomposites. For instance, many exciting research in bio-inspired membranes employs biological molecules including mussel proteins to adhere NPs to the skin layer or within the support. Another emerging tool is the use of atomic layer deposition (ALD), which allows deposition of various metallic or organic materials to be layered onto porous membranes to produce nano-scaled ultrathin films, which have good conformity, high layer thickness precision and control, and even regulated pore sizes [203]. These membrane types have not been given much attention – likely because ALD has not been used at scale for membrane production – but, these membranes have high potential for OMP separation. The robustness of the nanocomposite membranes for long-term OMP treatment under realistic working conditions (*e.g.*, WWTPs) should also be investigated.

PA TFC membranes have wide applicability in industry, but are prone to swell in contact with organic solvents [204]. PA layers also have the drawbacks of low cross-linking degree and non-uniform functional groups, which make the thin films heterogeneous with respect to their hydrophilicity and polarity [8]. A high priority is the development of TFN membranes aimed to address the limitations of low flux, swelling by solvents,

heterogeneous surface properties (hydrophilicity and polarity), and sensitivity to foulants and chlorine. PA TFN membranes have potential to overcome current permeability – selectivity trade-offs, which would enable them to remove OMPs at much lower TMPs. Nonetheless, NP agglomeration and leaching may cause defective PA structures and thereby reduce the NP effective surface area. Future studies should seek proper surface modifications of NPs to increase the compatibility with the organic phase and employ new chemistries or adopt novel monomers for constructing the thin film. Finally, more effort should be paid to develop loose TFN membranes for low pressure operations (UF and NF processes), without sacrificing the rejection rates of OMPs and salts.

## 5.7 Conclusion

OMP presence in water bodies used for the potable water supply has raised public concern about the long-term drinking water safety and quality. Natural ecological and physicochemical processes and conventional water treatment technologies cannot sufficiently degrade or remove these pollutants. In the absence of broad regulation or societal change in behaviors and consumption, new technologies are needed to address the growing environmental issue. Pressure-driven membrane-based technologies are proven and widely adopted, and can be easily upgraded to treat various water types. However, most membrane technologies require enhancements to efficiently remove OMPs from feed waters. Nanocomposite polymeric membranes are one such technological improvement.

The reported OMP removal performance of nanocomposite polymeric membranes depends on membrane characteristics, operating conditions, and OMP physicochemical properties.

Among MF, UF and NF membranes, NF membranes have the lowest MWCO, and can achieve a high rejection towards small-sized OMPs based on size exclusion. However, NF membranes require high pressures, and suffer from severe fouling issues in drinking water treatment. Traditional UF or MF membranes demand lower operational pressures, but can only partially remove large molecule OMPs due to these membranes' larger pore size and higher MWCO. Recent studies have demonstrated UF or MF membranes with modification to their surface charge and hydrophilicity can enhance OMP rejection. The physicochemical properties of these loose membranes could be further improved through surface or matrix modification with nano-modifiers. In this regard, rejection rates for OMPs could be greatly improved, depending on their charge and polarity. Furthermore, there is an exciting possibility to reduce the membrane operating pressures if these membranes are combined with means of OMP degradation and removal, achieved either through photocatalysis, electrochemical redox reactions, or enhanced adsorption. Should the researchers continue to optimize membrane material costs, long-term stability, scalability and separation characteristics, we expect that nanocomposite polymeric membranes will be the dominant method to treat emerging pollutants, such as PhACs and EDCs, in complex aquatic environments.

## 5.8 References

[1] T.L. Zearley, R.S. Summers, Removal of Trace Organic Micropollutants by Drinking Water Biological Filters, Environmental Science & Technology, 46 (2012) 9412-9419.
[2] A. Verliefde, E. Cornelissen, G. Amy, B. Van der Bruggen, H. van Dijk, Priority organic micropollutants in water sources in Flanders and the Netherlands and assessment of removal possibilities with nanofiltration, Environmental Pollution, 146 (2007) 281-289.
[3] S. Das, N.M. Ray, J. Wan, A. Khan, T. Chakraborty, M.B. Ray, Micropollutants in wastewater: fate and removal processes, Physico-Chemical Wastewater Treatment and Resource Recovery, (2017) 75-117.

[4] USEPA, Drinking water contaminant candidate list 4 - Final, in: Federal Register, 2016, pp. 81099-81114.
[5] C.E.P. Act, Priority substances list assessment report: Nonylphenol and its Ethoxylates, in, Ottawa: Environment Canada, Gatineau, and Health Canada, 1999.
[6] E. Eur, Commission Implementing Decision (EU) 2020/1161 of 4 August 2020 Establishing a watch list of substances for union-wide monitoring in the field of water policy pursuant to directive 2008/105/EC of the European Parliament and of the council, Off. J. Eur. Union., 257 (2020) 32-35.
[7] L.-x. Dong, X.-c. Huang, Z. Wang, Z. Yang, X.-m. Wang, C.Y. Tang, A thin-film nanocomposite nanofiltration membrane prepared on a support with in situ embedded zeolite nanoparticles, Separation and Purification Technology, 166 (2016) 230-239.
[8] H. Guo, L.E. Peng, Z. Yao, Z. Yang, X. Ma, C.Y. Tang, Non-polyamide based nanofiltration membranes using green metal–organic coordination complexes: implications for the removal of trace organic contaminants, Environmental science & technology, 53 (2019) 2688-2694.
[9] N. Rakhshan, M. Pakizeh, Removal of triazines from water using a novel OA modified SiO2/PA/PSf nanocomposite membrane, Separation and Purification Technology, 147 (2015) 245-256.
[10] V. Albergamo, B. Blankert, W. van der Meer, P. de Voogt, E. Cornelissen, Removal of polar organic micropollutants by mixed-matrix reverse osmosis membranes, Desalination, 479 (2020) 114337.
[11] R.M. Rajendran, S. Garg, S. Bajpai, Study of transport models for arsenic removal using nanofiltration process: recent perspectives, Emerging Technologies in Environmental Bioremediation, (2020) 391.
[12] S.G. Arhin, N. Banadda, A.J. Komakech, I. Kabenge, J. Wanyama, Membrane fouling control in low pressure membranes: A review on pretreatment techniques for fouling abatement, Environmental Engineering Research, 21 (2016) 109-120.
[13] N.K. Khanzada, M.U. Farid, J.A. Kharraz, J. Choi, C.Y. Tang, L.D. Nghiem, A. Jang, A.K. An, Removal of organic micropollutants using advanced membrane-based water and wastewater treatment: A review, Journal of Membrane Science, 598 (2020) 117672.
[14] A.R. Lado Ribeiro, N.F.F. Moreira, G. Li Puma, A.M.T. Silva, Impact of water matrix on the removal of micropollutants by advanced oxidation technologies, Chemical Engineering Journal, 363 (2019) 155-173.
[15] C. Grandclément, I. Seyssiecq, A. Piram, P. Wong-Wah-Chung, G. Vanot, N. Tiliacos, N. Roche, P. Doumenq, From the conventional biological wastewater treatment to hybrid processes, the evaluation of organic micropollutant removal: A review, Water Research, 111 (2017) 297-317.
[16] Y. Luo, W. Guo, H.H. Ngo, L.D. Nghiem, F.I. Hai, J. Zhang, S. Liang, X.C. Wang, A review on the occurrence of micropollutants in the aquatic environment and their fate and removal during wastewater treatment, Science of The Total Environment, 473-474 (2014) 619-641.
[17] S. Kim, K.H. Chu, Y.A.J. Al-Hamadani, C.M. Park, M. Jang, D.-H. Kim, M. Yu, J. Heo, Y. Yoon, Removal of contaminants of emerging concern by membranes in water and wastewater: A review, Chemical Engineering Journal, 335 (2018) 896-914.
[18] S.P. Dharupaneedi, S.K. Nataraj, M. Nadagouda, K.R. Reddy, S.S. Shukla, T.M. Aminabhavi, Membrane-based separation of potential emerging pollutants, Separation and Purification Technology, 210 (2019) 850-866.
[19] O. Ojajuni, D. Saroj, G. Cavalli, Removal of organic micropollutants using membrane-assisted processes: a review of recent progress, Environmental Technology Reviews, 4 (2015) 17-37.
[20] K. Sornalingam, A. McDonagh, J.L. Zhou, Photodegradation of estrogenic endocrine disrupting steroidal hormones in aqueous systems: Progress and future challenges, Science of The Total Environment, 550 (2016) 209-224.

[21] B. Yao, R. Li, S. Yan, S.-A. Chan, W. Song, Occurrence and estrogenic activity of steroid hormones in Chinese streams: A nationwide study based on a combination of chemical and biological tools, Environment international, 118 (2018) 1-8.
[22] W. Ben, B. Zhu, X. Yuan, Y. Zhang, M. Yang, Z. Qiang, Occurrence, removal and risk of organic micropollutants in wastewater treatment plants across China: Comparison of wastewater treatment processes, Water research, 130 (2018) 38-46.
[23] I. Koyuncu, O.A. Arikan, M.R. Wiesner, C. Rice, Removal of hormones and antibiotics by nanofiltration membranes, Journal of membrane science, 309 (2008) 94-101.
[24] M.S. Kostich, A.L. Batt, J.M. Lazorchak, Concentrations of prioritized pharmaceuticals in effluents from 50 large wastewater treatment plants in the US and implications for risk estimation, Environmental Pollution, 184 (2014) 354-359.
[25] N.H. Tran, M. Reinhard, K.Y.-H. Gin, Occurrence and fate of emerging contaminants in municipal wastewater treatment plants from different geographical regions-a review, Water research, 133 (2018) 182-207.
[26] Y. Wang, Y. Liu, Y. Yu, H. Huang, Influence of CNT-rGO composite structures on their permeability and selectivity for membrane water treatment, Journal of Membrane Science, 551 (2018) 326-332.
[27] I. Ibrahim, A. Togola, C. Gonzalez, Polar organic chemical integrative sampler (POCIS) uptake rates for 17 polar pesticides and degradation products: laboratory calibration, Environmental Science and Pollution Research, 20 (2013) 3679-3687.
[28] W. Fang, Y. Peng, D. Muir, J. Lin, X. Zhang, A critical review of synthetic chemicals in surface waters of the US, the EU and China, Environment international, 131 (2019) 104994.
[29] R. Loos, R. Carvalho, D.C. António, S. Comero, G. Locoro, S. Tavazzi, B. Paracchini, M. Ghiani, T. Lettieri, L. Blaha, EU-wide monitoring survey on emerging polar organic contaminants in wastewater treatment plant effluents, Water research, 47 (2013) 6475-6487.
[30] D. Błędzka, D. Gryglik, J.S. Miller, Photolytic degradation of 4-tert-octylphenol in aqueous solution, Environment Protection Engineering, 35 (2009) 235-247.
[31] Y.-H. Liu, S.-H. Zhang, G.-X. Ji, S.-M. Wu, R.-X. Guo, J. Cheng, Z.-Y. Yan, J.-Q. Chen, Occurrence, distribution and risk assessment of suspected endocrine-disrupting chemicals in surface water and suspended particulate matter of Yangtze River (Nanjing section), Ecotoxicology and environmental safety, 135 (2017) 90-97.
[32] M. Clara, G. Windhofer, W. Hartl, K. Braun, M. Simon, O. Gans, C. Scheffknecht, A. Chovanec, Occurrence of phthalates in surface runoff, untreated and treated wastewater and fate during wastewater treatment, Chemosphere, 78 (2010) 1078-1084.
[33] K.M. Gani, V.K. Tyagi, A.A. Kazmi, Occurrence of phthalates in aquatic environment and their removal during wastewater treatment processes: a review, Environmental Science and Pollution Research, 24 (2017) 17267-17284.
[34] F.-L. Zhang, X.-J. Yang, X.-L. Xue, X.-Q. Tao, G.-N. Lu, Z. Dang, Estimation of n-octanol/water partition coefficients (log) of polychlorinated biphenyls by using quantum chemical descriptors and partial least squares, Journal of Chemistry, 2013 (2013).
[35] R. Rattanaoudom, C. Visvanathan, Removal of PFOA by hybrid membrane filtration using PAC and hydrotalcite, Desalination and Water Treatment, 32 (2011) 262-270.
[36] M.A. Nguyen, K. Wiberg, E. Ribeli, S. Josefsson, M. Futter, J. Gustavsson, L. Ahrens, Spatial distribution and source tracing of per-and polyfluoroalkyl substances (PFASs) in surface water in Northern Europe, Environmental Pollution, 220 (2017) 1438-1446.
[37] S. Deng, Y. Bei, X. Lu, Z. Du, B. Wang, Y. Wang, J. Huang, G. Yu, Effect of co-existing organic compounds on adsorption of perfluorinated compounds onto carbon nanotubes, Frontiers of Environmental Science & Engineering, 9 (2015) 784-792.

[38] Y. Zhang, D. Tan, Y. Geng, L. Wang, Y. Peng, Z. He, Y. Xu, X. Liu, Perfluorinated compounds in greenhouse and open agricultural producing areas of three provinces of China: Levels, sources and risk assessment, International journal of environmental research and public health, 13 (2016) 1224.
[39] B. Yao, S. Yan, L. Lian, X. Yang, C. Wan, H. Dong, W. Song, Occurrence and indicators of pharmaceuticals in Chinese streams: a nationwide study, Environmental Pollution, 236 (2018) 889-898.
[40] D. Rana, R.M. Narbaitz, A.-M. Garand-Sheridan, A. Westgate, T. Matsuura, S. Tabe, S.Y. Jasim, Development of novel charged surface modifying macromolecule blended PES membranes to remove EDCs and PPCPs from drinking water sources, Journal of Materials Chemistry A, 2 (2014) 10059-10072.
[41] V. Sharma, R.V. Kumar, K. Pakshirajan, G. Pugazhenthi, Integrated adsorption-membrane filtration process for antibiotic removal from aqueous solution, Powder Technology, 321 (2017) 259-269.
[42] L. Jank, R.B. Hoff, F.J.d. Costa, T.M. Pizzolato, Simultaneous determination of eight antibiotics from distinct classes in surface and wastewater samples by solid-phase extraction and high-performance liquid chromatography–electrospray ionisation mass spectrometry, International Journal of Environmental Analytical Chemistry, 94 (2014) 1013-1037.
[43] S.P. Sun, T.A. Hatton, T.-S. Chung, Hyperbranched polyethyleneimine induced cross-linking of polyamide− imide nanofiltration hollow fiber membranes for effective removal of ciprofloxacin, Environmental science & technology, 45 (2011) 4003-4009.
[44] S. Zhao, C. Ba, Y. Yao, W. Zheng, J. Economy, P. Wang, Removal of antibiotics using polyethylenimine cross-linked nanofiltration membranes: Relating membrane performance to surface charge characteristics, Chemical Engineering Journal, 335 (2018) 101-109.
[45] F.M. Bojnourd, M. Pakizeh, Preparation and characterization of a PVA/PSf thin film composite membrane after incorporation of PSSMA into a selective layer and its application for pharmaceutical removal, Separation and Purification Technology, 192 (2018) 5-14.
[46] P. Kovalakova, L. Cizmas, T.J. McDonald, B. Marsalek, M. Feng, V.K. Sharma, Occurrence and toxicity of antibiotics in the aquatic environment: A review, Chemosphere, 251 (2020) 126351.
[47] Y. Wang, J. Zhu, H. Huang, H.-H. Cho, Carbon nanotube composite membranes for microfiltration of pharmaceuticals and personal care products: Capabilities and potential mechanisms, Journal of membrane science, 479 (2015) 165-174.
[48] K. Kimura, G. Amy, J.E. Drewes, T. Heberer, T.-U. Kim, Y. Watanabe, Rejection of organic micropollutants (disinfection by-products, endocrine disrupting compounds, and pharmaceutically active compounds) by NF/RO membranes, Journal of membrane science, 227 (2003) 113-121.
[49] A. Karnjanapiboonwong, A.N. Morse, J.D. Maul, T.A. Anderson, Sorption of estrogens, triclosan, and caffeine in a sandy loam and a silt loam soil, Journal of Soils and Sediments, 10 (2010) 1300-1307.
[50] S. Vigneswaran, Waste Water Treatment Technologies-Volume I, EOLSS Publications, 2009.
[51] P. Kjeldsen, J. Kjølholt, B. Schultz, T.H. Christensen, J.C. Tjell, Sorption and degradation of chlorophenols, nitrophenols and organophosphorus pesticides in the subsoil under landfills—laboratory studies, Journal of contaminant hydrology, 6 (1990) 165-184.
[52] R. Dai, H. Guo, C.Y. Tang, M. Chen, J. Li, Z. Wang, Hydrophilic Selective Nanochannels Created by Metal Organic Frameworks in Nanofiltration Membranes Enhance Rejection of Hydrophobic Endocrine-Disrupting Compounds, Environmental science & technology, 53 (2019) 13776-13783.

[53] X. Ma, Y. Wan, M. Wu, Y. Xu, Q. Xu, Z. He, W. Xia, Occurrence of benzophenones, parabens and triclosan in the Yangtze River of China, and the implications for human exposure, Chemosphere, 213 (2018) 517-525.
[54] W.-L. Ma, X. Zhao, Z.-F. Zhang, T.-F. Xu, F.-J. Zhu, Y.-F. Li, Concentrations and fate of parabens and their metabolites in two typical wastewater treatment plants in northeastern China, Science of the total environment, 644 (2018) 754-761.
[55] I. Muñoz, M.J. Gómez-Ramos, A. Agüera, A.R. Fernández-Alba, J.F. García-Reyes, A. Molina-Díaz, Chemical evaluation of contaminants in wastewater effluents and the environmental risk of reusing effluents in agriculture, TrAC Trends in Analytical Chemistry, 28 (2009) 676-694.
[56] Z. Li, G. Song, Y. Bi, W. Gao, A. He, Y. Lu, Y. Wang, G. Jiang, Occurrence and Distribution of Disinfection Byproducts in Domestic Wastewater Effluent, Tap Water, and Surface Water during the SARS-CoV-2 Pandemic in China, Environmental Science & Technology, (2021).
[57] D.S. Franco, E.H. Tanabe, D.A. Bertuol, G.S. dos Reis, É.C. Lima, G.L. Dotto, Alternative treatments to improve the potential of rice husk as adsorbent for methylene blue, Water Science and Technology, 75 (2017) 296-305.
[58] G. Dotto, J. Santos, I. Rodrigues, R. Rosa, F. Pavan, E. Lima, Adsorption of methylene blue by ultrasonic surface modified chitin, Journal of colloid and interface science, 446 (2015) 133-140.
[59] C. Tizaoui, H. Mohammad-Salim, J. Suhartono, Multiwalled carbon nanotubes for heterogeneous nanocatalytic ozonation, Ozone: Science & Engineering, 37 (2015) 269-278.
[60] C. Miège, J.M. Choubert, L. Ribeiro, M. Eusèbe, M. Coquery, Fate of pharmaceuticals and personal care products in wastewater treatment plants – Conception of a database and first results, Environmental Pollution, 157 (2009) 1721-1726.
[61] T. Deblonde, C. Cossu-Leguille, P. Hartemann, Emerging pollutants in wastewater: A review of the literature, International Journal of Hygiene and Environmental Health, 214 (2011) 442-448.
[62] E.N. Evgenidou, I.K. Konstantinou, D.A. Lambropoulou, Occurrence and removal of transformation products of PPCPs and illicit drugs in wastewaters: A review, Science of The Total Environment, 505 (2015) 905-926.
[63] J.-L. Liu, M.-H. Wong, Pharmaceuticals and personal care products (PPCPs): a review on environmental contamination in China, Environment international, 59 (2013) 208-224.
[64] A. Pal, K.Y.-H. Gin, A.Y.-C. Lin, M. Reinhard, Impacts of emerging organic contaminants on freshwater resources: Review of recent occurrences, sources, fate and effects, Science of The Total Environment, 408 (2010) 6062-6069.
[65] Q. Sui, X. Cao, S. Lu, W. Zhao, Z. Qiu, G. Yu, Occurrence, sources and fate of pharmaceuticals and personal care products in the groundwater: A review, Emerging Contaminants, 1 (2015) 14-24.
[66] L. Arpin-Pont, M.J.M. Bueno, E. Gomez, H. Fenet, Occurrence of PPCPs in the marine environment: a review, Environmental Science and Pollution Research, 23 (2016) 4978-4991.
[67] E. Vulliet, C. Cren-Olivé, M.-F. Grenier-Loustalot, Occurrence of pharmaceuticals and hormones in drinking water treated from surface waters, Environmental Chemistry Letters, 9 (2011) 103-114.
[68] M.J. Benotti, R.A. Trenholm, B.J. Vanderford, J.C. Holady, B.D. Stanford, S.A. Snyder, Pharmaceuticals and Endocrine Disrupting Compounds in U.S. Drinking Water, Environmental Science & Technology, 43 (2009) 597-603.
[69] J. Greskowiak, E. Hamann, V. Burke, G. Massmann, The uncertainty of biodegradation rate constants of emerging organic compounds in soil and groundwater – A compilation of literature values for 82 substances, Water Research, 126 (2017) 122-133.
[70] K. Košutić, D. Dolar, D. Ašperger, B. Kunst, Removal of antibiotics from a model wastewater by RO/NF membranes, Separation and purification technology, 53 (2007) 244-249.

[71] L.D. Nghiem, A.I. Schäfer, M. Elimelech, Pharmaceutical retention mechanisms by nanofiltration membranes, Environmental science & technology, 39 (2005) 7698-7705.
[72] Y. Yoon, P. Westerhoff, S.A. Snyder, E.C. Wert, Nanofiltration and ultrafiltration of endocrine disrupting compounds, pharmaceuticals and personal care products, Journal of Membrane Science, 270 (2006) 88-100.
[73] V. Yangali-Quintanilla, A. Sadmani, M. McConville, M. Kennedy, G. Amy, Rejection of pharmaceutically active compounds and endocrine disrupting compounds by clean and fouled nanofiltration membranes, Water Research, 43 (2009) 2349-2362.
[74] B. Van der Bruggen, J. Schaep, D. Wilms, C. Vandecasteele, Influence of molecular size, polarity and charge on the retention of organic molecules by nanofiltration, Journal of Membrane Science, 156 (1999) 29-41.
[75] X. Jin, J. Shan, C. Wang, J. Wei, C.Y. Tang, Rejection of pharmaceuticals by forward osmosis membranes, Journal of hazardous materials, 227 (2012) 55-61.
[76] N.T. Hancock, P. Xu, D.M. Heil, C. Bellona, T.Y. Cath, Comprehensive bench-and pilot-scale investigation of trace organic compounds rejection by forward osmosis, Environmental science & technology, 45 (2011) 8483-8490.
[77] R.V. Linares, V. Yangali-Quintanilla, Z. Li, G. Amy, Rejection of micropollutants by clean and fouled forward osmosis membrane, Water research, 45 (2011) 6737-6744.
[78] J. Xu, T.N. Tran, H. Lin, N. Dai, Removal of disinfection byproducts in forward osmosis for wastewater recycling, Journal of Membrane Science, 564 (2018) 352-360.
[79] P. Zhao, B. Gao, S. Xu, J. Kong, D. Ma, H.K. Shon, Q. Yue, P. Liu, Polyelectrolyte-promoted forward osmosis process for dye wastewater treatment–exploring the feasibility of using polyacrylamide as draw solute, Chemical Engineering Journal, 264 (2015) 32-38.
[80] K.C. Wijekoon, F.I. Hai, J. Kang, W.E. Price, T.Y. Cath, L.D. Nghiem, Rejection and fate of trace organic compounds (TrOCs) during membrane distillation, Journal of Membrane Science, 453 (2014) 636-642.
[81] J. Guo, M.U. Farid, E.-J. Lee, D.Y.-S. Yan, S. Jeong, A.K. An, Fouling behavior of negatively charged PVDF membrane in membrane distillation for removal of antibiotics from wastewater, Journal of Membrane Science, 551 (2018) 12-19.
[82] T.L. Silva, S. Morales-Torres, C.M. Esteves, A.R. Ribeiro, O.C. Nunes, J.L. Figueiredo, A.M. Silva, Desalination and removal of organic micropollutants and microorganisms by membrane distillation, Desalination, 437 (2018) 121-132.
[83] J. Plattner, C. Kazner, G. Naidu, T. Wintgens, S. Vigneswaran, Removal of selected pesticides from groundwater by membrane distillation, Environmental Science and Pollution Research, 25 (2018) 20336-20347.
[84] D. Gerrity, S. Gamage, J.C. Holady, D.B. Mawhinney, O. Quiñones, R.A. Trenholm, S.A. Snyder, Pilot-scale evaluation of ozone and biological activated carbon for trace organic contaminant mitigation and disinfection, Water research, 45 (2011) 2155-2165.
[85] J.L. Acero, F.J. Benitez, F.J. Real, F. Teva, Coupling of adsorption, coagulation, and ultrafiltration processes for the removal of emerging contaminants in a secondary effluent, Chemical Engineering Journal, 210 (2012) 1-8.
[86] L. Sbardella, J. Comas, A. Fenu, I. Rodriguez-Roda, M. Weemaes, Advanced biological activated carbon filter for removing pharmaceutically active compounds from treated wastewater, Science of the Total Environment, 636 (2018) 519-529.
[87] J. Löwenberg, A. Zenker, M. Baggenstos, G. Koch, C. Kazner, T. Wintgens, Comparison of two PAC/UF processes for the removal of micropollutants from wastewater treatment plant effluent: process performance and removal efficiency, Water Research, 56 (2014) 26-36.

[88] İ.Y. İpek, N. Kabay, M. Yüksel, D. Yapıcı, Ü. Yüksel, Application of adsorption–ultrafiltration hybrid method for removal of phenol from water by hypercrosslinked polymer adsorbents, Desalination, 306 (2012) 24-28.
[89] F. Banat, N. Al-Bastaki, Treating dye wastewater by an integrated process of adsorption using activated carbon and ultrafiltration, Desalination, 170 (2004) 69-75.
[90] R.O. Dunn Jr, J.F. Scamehorn, S.D. Christian, Use of micellar-enhanced ultrafiltration to remove dissolved organics from aqueous streams, Separation science and technology, 20 (1985) 257-284.
[91] K. Exall, V.K. Balakrishnan, J. Toito, R. McFadyen, Impact of selected wastewater constituents on the removal of sulfonamide antibiotics via ultrafiltration and micellar enhanced ultrafiltration, Science of the total environment, 461 (2013) 371-376.
[92] M. Schwarze, Micellar-enhanced ultrafiltration (MEUF)–state of the art, Environmental Science: Water Research & Technology, 3 (2017) 598-624.
[93] M. Chen, C.T. Jafvert, Y. Wu, X. Cao, N.P. Hankins, Inorganic anion removal using micellar enhanced ultrafiltration (MEUF), modeling anion distribution and suggested improvements of MEUF: A review, Chemical Engineering Journal, (2020) 125413.
[94] S. Chowdhury, G. Halder, T. Mandal, J. Sikder, Cetylpyridinium bromide assisted micellar-enhanced ultrafiltration for treating enrofloxacin-laden water, Science of the total environment, 687 (2019) 10-23.
[95] W. Zhang, G. Huang, J. Wei, H. Li, R. Zheng, Y. Zhou, Removal of phenol from synthetic waste water using Gemini micellar-enhanced ultrafiltration (GMEUF), Journal of hazardous materials, 235 (2012) 128-137.
[96] J.-H. Huang, C.-F. Zhou, G.-M. Zeng, X. Li, H.-J. Huang, J. Niu, F. Li, L.-J. Shi, S.-B. He, Studies on the solubilization of aqueous methylene blue in surfactant using MEUF, Separation and purification technology, 98 (2012) 497-502.
[97] D. Doulia, I. Xiarchos, Ultrafiltration of micellar solutions of nonionic surfactants with or without alachlor pesticide, Journal of membrane science, 296 (2007) 58-64.
[98] J. Yin, B. Deng, Polymer-matrix nanocomposite membranes for water treatment, Journal of membrane science, 479 (2015) 256-275.
[99] J. Zhu, J. Wang, A.A. Uliana, M. Tian, Y. Zhang, Y. Zhang, A. Volodin, K. Simoens, S. Yuan, J. Li, Mussel-inspired architecture of high-flux loose nanofiltration membrane functionalized with antibacterial reduced graphene oxide–copper nanocomposites, ACS applied materials & interfaces, 9 (2017) 28990-29001.
[100] J. Ma, X. Tang, Y. He, Y. Fan, J. Chen, Robust stable MoS2/GO filtration membrane for effective removal of dyes and salts from water with enhanced permeability, Desalination, 480 (2020) 114328.
[101] T. Lu, X. Xu, X. Liu, T. Sun, Super hydrophilic PVDF based composite membrane for efficient separation of tetracycline, Chemical Engineering Journal, 308 (2017) 151-159.
[102] L. Yang, Z. Wang, J. Zhang, Zeolite imidazolate framework hybrid nanofiltration (NF) membranes with enhanced permselectivity for dye removal, Journal of membrane science, 532 (2017) 76-86.
[103] Y. Xu, G. Peng, J. Liao, J. Shen, C. Gao, Preparation of molecular selective GO/DTiO2-PDA-PEI composite nanofiltration membrane for highly pure dye separation, Journal of Membrane Science, 601 (2020) 117727.
[104] W.-L. Jiang, X. Xia, J.-L. Han, Y.-C. Ding, M.R. Haider, A.-J. Wang, Graphene modified electro-Fenton catalytic membrane for in situ degradation of antibiotic florfenicol, Environmental science & technology, 52 (2018) 9972-9982.

[105] T. Liu, H. Zhou, N. Graham, Y. Lian, W. Yu, K. Sun, The antifouling performance of an ultrafiltration membrane with pre-deposited carbon nanofiber layers for water treatment, Journal of Membrane Science, 557 (2018) 87-95.
[106] L. Bai, Y. Liu, A. Ding, N. Ren, G. Li, H. Liang, Surface coating of UF membranes to improve antifouling properties: A comparison study between cellulose nanocrystals (CNCs) and cellulose nanofibrils (CNFs), Chemosphere, 217 (2019) 76-84.
[107] F.-x. Kong, Q. Liu, L.-q. Dong, T. Zhang, Y.-b. Wei, J.-f. Chen, Y. Wang, C.-m. Guo, Rejection of pharmaceuticals by graphene oxide membranes: Role of crosslinker and rejection mechanism, Journal of Membrane Science, 612 (2020) 118338.
[108] X. Fan, C. Cai, J. Gao, X. Han, J. Li, Hydrothermal reduced graphene oxide membranes for dyes removing, Separation and Purification Technology, 241 (2020) 116730.
[109] L. Huang, Z. Li, Y. Luo, N. Zhang, W. Qi, E. Jiang, J. Bao, X. Zhang, W. Zheng, B. An, Low-pressure loose GO composite membrane intercalated by CNT for effective dye/salt separation, Separation and Purification Technology, 256 (2021) 117839.
[110] W.-L. Jiang, M.R. Haider, J.-L. Han, Y.-C. Ding, X.-Q. Li, H.-C. Wang, H.M.A. Sharif, A.-J. Wang, N.-Q. Ren, Carbon nanotubes intercalated RGO electro-Fenton membrane for coenhanced permeability, rejection and catalytic oxidation of organic micropollutants, Journal of Membrane Science, (2021) 119069.
[111] P. Cheng, Y. Chen, Y.-H. Gu, X. Yan, W.-Z. Lang, Hybrid 2D WS2/GO nanofiltration membranes for finely molecular sieving, Journal of Membrane Science, 591 (2019) 117308.
[112] J. Lyu, X. Wen, U. Kumar, Y. You, V. Chen, R. Joshi, Separation and purification using GO and r-GO membranes, RSC advances, 8 (2018) 23130-23151.
[113] Y. Wei, Y. Zhu, Y. Jiang, Photocatalytic self-cleaning carbon nitride nanotube intercalated reduced graphene oxide membranes for enhanced water purification, Chemical Engineering Journal, 356 (2019) 915-925.
[114] X. Zhang, H. Li, J. Wang, D. Peng, J. Liu, Y. Zhang, In-situ grown covalent organic framework nanosheets on graphene for membrane-based dye/salt separation, Journal of Membrane Science, 581 (2019) 321-330.
[115] X. Ou, X. Yang, J. Zheng, M. Liu, Free-Standing Graphene Oxide–Chitin Nanocrystal Composite Membrane for Dye Adsorption and Oil/Water Separation, ACS Sustainable Chemistry & Engineering, 7 (2019) 13379-13390.
[116] K. Guan, D. Zhao, M. Zhang, J. Shen, G. Zhou, G. Liu, W. Jin, 3D nanoporous crystals enabled 2D channels in graphene membrane with enhanced water purification performance, Journal of Membrane Science, 542 (2017) 41-51.
[117] A. Xie, J. Cui, J. Yang, Y. Chen, J. Lang, C. Li, Y. Yan, J. Dai, Graphene oxide/Fe (III)-based metal-organic framework membrane for enhanced water purification based on synergistic separation and photo-Fenton processes, Applied Catalysis B: Environmental, 264 (2020) 118548.
[118] Y. Liu, M. Zhu, M. Chen, L. Ma, B. Yang, L. Li, W. Tu, A polydopamine-modified reduced graphene oxide (RGO)/MOFs nanocomposite with fast rejection capacity for organic dye, Chemical Engineering Journal, 359 (2019) 47-57.
[119] P. Zhang, J.-L. Gong, G.-M. Zeng, B. Song, W. Cao, H.-Y. Liu, S.-Y. Huan, P. Peng, Novel "loose" GO/MoS2 composites membranes with enhanced permeability for effective salts and dyes rejection at low pressure, Journal of Membrane Science, 574 (2019) 112-123.
[120] C.-Y. Wang, W.-J. Zeng, T.-T. Jiang, X. Chen, X.-L. Zhang, Incorporating attapulgite nanorods into graphene oxide nanofiltration membranes for efficient dyes wastewater treatment, Separation and Purification Technology, 214 (2019) 21-30.

[121] Y. Liu, W. Tu, M. Chen, L. Ma, B. Yang, Q. Liang, Y. Chen, A mussel-induced method to fabricate reduced graphene oxide/halloysite nanotubes membranes for multifunctional applications in water purification and oil/water separation, Chemical Engineering Journal, 336 (2018) 263-277.
[122] B. Liang, P. Zhang, J. Wang, J. Qu, L. Wang, X. Wang, C. Guan, K. Pan, Membranes with selective laminar nanochannels of modified reduced graphene oxide for water purification, Carbon, 103 (2016) 94-100.
[123] Y. Liu, F. Zhang, W. Zhu, D. Su, Z. Sang, X. Yan, S. Li, J. Liang, S.X. Dou, A multifunctional hierarchical porous SiO2/GO membrane for high efficiency oil/water separation and dye removal, Carbon, 160 (2020) 88-97.
[124] L. Dong, M. Li, S. Zhang, X. Si, Y. Bai, C. Zhang, NH2-Fe3O4-regulated graphene oxide membranes with well-defined laminar nanochannels for desalination of dye solutions, Desalination, 476 (2020) 114227.
[125] X. Tong, S. Liu, D. Qu, H. Gao, L. Yan, Y. Chen, J. Crittenden, Tannic acid-metal complex modified MXene membrane for contaminants removal from water, Journal of Membrane Science, 622 (2021) 119042.
[126] A. Hafeez, Z.A. Karim, A.F. Ismail, A. Samavati, K.A.M. Said, S. Selambakkannu, Functionalized boron nitride composite ultrafiltration membrane for dye removal from aqueous solution, Journal of Membrane Science, 612 (2020) 118473.
[127] C. Wang, Y. Wu, J. Lu, J. Zhao, J. Cui, X. Wu, Y. Yan, P. Huo, Bioinspired synthesis of photocatalytic nanocomposite membranes based on synergy of Au-TiO2 and polydopamine for degradation of tetracycline under visible light, ACS applied materials & interfaces, 9 (2017) 23687-23697.
[128] S.-Y. Fang, P. Zhang, J.-L. Gong, L. Tang, G.-M. Zeng, B. Song, W.-C. Cao, J. Li, J. Ye, Construction of highly water-stable metal-organic framework UiO-66 thin-film composite membrane for dyes and antibiotics separation, Chemical Engineering Journal, 385 (2020) 123400.
[129] J. Li, S. Yuan, J. Zhu, B. Van der Bruggen, High-flux, antibacterial composite membranes via polydopamine-assisted PEI-TiO2/Ag modification for dye removal, Chemical Engineering Journal, 373 (2019) 275-284.
[130] X. Chen, Y. He, Y. Fan, G. Zeng, L. Zhang, Nature-inspired polyphenol chemistry to fabricate halloysite nanotubes decorated PVDF membrane for the removal of wastewater, Separation and Purification Technology, 212 (2019) 326-336.
[131] S. Li, Y. Wan, S. Guo, J. Luo, Ferric ions mediated defects narrowing of graphene oxide nanofiltration membrane for robust removal of organic micropollutants, Chemical Engineering Journal, (2021) 128587.
[132] J. Yu, Y. Wang, Y. He, Y. Gao, R. Hou, J. Ma, L. Zhang, X. Guo, L. Chen, Calcium ion-sodium alginate double cross-linked graphene oxide nanofiltration membrane with enhanced stability for efficient separation of dyes, Separation and Purification Technology, 276 (2021) 119348.
[133] S. Zhang, H. Wang, J. Liu, C. Bao, Measuring the specific surface area of monolayer graphene oxide in water, Materials Letters, 261 (2020) 127098.
[134] A. Peigney, C. Laurent, E. Flahaut, R. Bacsa, A. Rousset, Specific surface area of carbon nanotubes and bundles of carbon nanotubes, Carbon, 39 (2001) 507-514.
[135] A.J. Sutherland, M.-X. Ruiz-Caldas, C.-F. de Lannoy, Electro-catalytic microfiltration membranes electrochemically degrade azo dyes in solution, Journal of Membrane Science, 611 (2020) 118335.
[136] H. Bai, X. Zan, L. Zhang, D.D. Sun, Multi-functional CNT/ZnO/TiO2 nanocomposite membrane for concurrent filtration and photocatalytic degradation, Separation and Purification Technology, 156 (2015) 922-930.

[137] R. Zhang, Y. Cai, X. Zhu, Q. Han, T. Zhang, Y. Liu, Y. Li, A. Wang, A novel photocatalytic membrane decorated with PDA/RGO/Ag3PO4 for catalytic dye decomposition, Colloids and Surfaces A: Physicochemical and Engineering Aspects, 563 (2019) 68-76.
[138] L. Qu, G. Zhu, J. Ji, T. Yadav, Y. Chen, G. Yang, H. Xu, H. Li, Recyclable visible light-driven Og-C3N4/graphene oxide/N-carbon nanotube membrane for efficient removal of organic pollutants, ACS applied materials & interfaces, 10 (2018) 42427-42435.
[139] Y. Gao, S. Yan, Y. He, Y. Fan, L. Zhang, J. Ma, R. Hou, L. Chen, J. Chen, A photo-Fenton self-cleaning membrane based on NH2-MIL-88B (Fe) and graphene oxide to improve dye removal performance, Journal of Membrane Science, 626 (2021) 119192.
[140] Y. Peng, Z. Yu, F. Li, Q. Chen, D. Yin, X. Min, A novel reduced graphene oxide-based composite membrane prepared via a facile deposition method for multifunctional applications: oil/water separation and cationic dyes removal, Separation and Purification Technology, 200 (2018) 130-140.
[141] P. Zhang, J.-L. Gong, G.-M. Zeng, B. Song, H.-Y. Liu, S.-Y. Huan, J. Li, Ultrathin reduced graphene oxide/MOF nanofiltration membrane with improved purification performance at low pressure, Chemosphere, 204 (2018) 378-389.
[142] Q. Zaib, B. Mansoor, F. Ahmad, Photo-regenerable multi-walled carbon nanotube membranes for the removal of pharmaceutical micropollutants from water, Environmental Science: Processes & Impacts, 15 (2013) 1582-1589.
[143] J.E. Yanez H, Z. Wang, S. Lege, M. Obst, S. Roehler, C.J. Burkhardt, C. Zwiener, Application and characterization of electroactive membranes based on carbon nanotubes and zerovalent iron nanoparticles, Water Research, 108 (2017) 78-85.
[144] N. Li, H.-d. Chen, Y.-z. Lu, M.-c. Zhu, Z.-x. Hu, S.-w. Chen, R.J. Zeng, Nanoscale zero-valent iron-modified PVDF membrane prepared by a simple filter-press coating method can robustly remove 2-chlorophenol from wastewater, Chemical Engineering Journal, (2020) 127701.
[145] G. Kaminska, J. Bohdziewicz, J. Calvo, P. Prádanos, L. Palacio, A. Hernández, Fabrication and characterization of polyethersulfone nanocomposite membranes for the removal of endocrine disrupting micropollutants from wastewater. Mechanisms and performance, Journal of Membrane Science, 493 (2015) 66-79.
[146] C. Balcik-Canbolat, B. Van der Bruggen, Efficient removal of dyes from aqueous solution: the potential of cellulose nanocrystals to enhance PES nanocomposite membranes, Cellulose, 27 (2020) 5255-5266.
[147] S. Zinadini, A.A. Zinatizadeh, M. Rahimi, V. Vatanpour, H. Zangeneh, Preparation of a novel antifouling mixed matrix PES membrane by embedding graphene oxide nanoplates, Journal of Membrane Science, 453 (2014) 292-301.
[148] S. Nasseri, S. Ebrahimi, M. Abtahi, R. Saeedi, Synthesis and characterization of polysulfone/graphene oxide nano-composite membranes for removal of bisphenol A from water, Journal of environmental management, 205 (2018) 174-182.
[149] A. Alkhouzaam, H. Qiblawey, Novel polysulfone ultrafiltration membranes incorporating polydopamine functionalized graphene oxide with enhanced flux and fouling resistance, Journal of Membrane Science, 620 (2021) 118900.
[150] H. Koulivand, A. Shahbazi, V. Vatanpour, M. Rahmandoust, Development of carbon dot-modified polyethersulfone membranes for enhancement of nanofiltration, permeation and antifouling performance, Separation and Purification Technology, 230 (2020) 115895.
[151] R. Goswami, M. Gogoi, H.J. Borah, P.G. Ingole, S. Hazarika, Biogenic synthesized Pd-nanoparticle incorporated antifouling polymeric membrane for removal of crystal violet dye, Journal of environmental chemical engineering, 6 (2018) 6139-6146.

[152] R. Mukherjee, S. De, Adsorptive removal of phenolic compounds using cellulose acetate phthalate–alumina nanoparticle mixed matrix membrane, Journal of hazardous materials, 265 (2014) 8-19.
[153] T. Tavangar, M. Karimi, M. Rezakazemi, K.R. Reddy, T.M. Aminabhavi, Textile waste, dyes/inorganic salts separation of cerium oxide-loaded loose nanofiltration polyethersulfone membranes, Chemical Engineering Journal, 385 (2020) 123787.
[154] S. Kamari, A. Shahbazi, Biocompatible Fe3O4@ SiO2-NH2 nanocomposite as a green nanofiller embedded in PES–nanofiltration membrane matrix for salts, heavy metal ion and dye removal: Long–term operation and reusability tests, Chemosphere, 243 (2020) 125282.
[155] Y. Tan, Z. Sun, H. Meng, Y. Han, J. Wu, J. Xu, Y. Xu, X. Zhang, A new MOFs/polymer hybrid membrane: MIL-68 (Al)/PVDF, fabrication and application in high-efficient removal of p-nitrophenol and methylene blue, Separation and Purification Technology, 215 (2019) 217-226.
[156] S. Zhou, J. Gao, J. Zhu, D. Peng, Y. Zhang, Y. Zhang, Self-cleaning, antibacterial mixed matrix membranes enabled by photocatalyst Ti-MOFs for efficient dye removal, Journal of Membrane Science, 610 (2020) 118219.
[157] L. Xing, N. Guo, Y. Zhang, H. Zhang, J. Liu, A negatively charged loose nanofiltration membrane by blending with poly (sodium 4-styrene sulfonate) grafted SiO2 via SI-ATRP for dye purification, Separation and Purification Technology, 146 (2015) 50-59.
[158] J.K. Ali, C.M. Chabib, M. Abi Jaoude, E. Alhseinat, S. Teotia, S. Patole, D.H. Anjum, I. Qattan, Enhanced removal of aqueous phenol with polyimide ultrafiltration membranes embedded with deep eutectic solvent-coated nanosilica, Chemical Engineering Journal, 408 (2021) 128017.
[159] M.S. Muhamad, M.R. Salim, W.J. Lau, T. Hadibarata, Z. Yusop, Removal of bisphenol A by adsorption mechanism using PES–SiO2 composite membranes, Environmental technology, 37 (2016) 1959-1969.
[160] Y. Zhang, Q. Song, X. Liang, J. Wang, Y. Jiang, J. Liu, High-flux, high-selectivity loose nanofiltration membrane mixed with zwitterionic functionalized silica for dye/salt separation, Applied Surface Science, 515 (2020) 146005.
[161] Y. Wang, J. Zhu, G. Dong, Y. Zhang, N. Guo, J. Liu, Sulfonated halloysite nanotubes/polyethersulfone nanocomposite membrane for efficient dye purification, Separation and Purification Technology, 150 (2015) 243-251.
[162] G. Zeng, Y. He, Y. Zhan, L. Zhang, Y. Pan, C. Zhang, Z. Yu, Novel polyvinylidene fluoride nanofiltration membrane blended with functionalized halloysite nanotubes for dye and heavy metal ions removal, Journal of Hazardous Materials, 317 (2016) 60-72.
[163] N. Ghaemi, S.S. Madaeni, A. Alizadeh, H. Rajabi, P. Daraei, Preparation, characterization and performance of polyethersulfone/organically modified montmorillonite nanocomposite membranes in removal of pesticides, Journal of Membrane Science, 382 (2011) 135-147.
[164] T. Makhetha, R. Moutloali, Antifouling properties of Cu (tpa)@ GO/PES composite membranes and selective dye rejection, Journal of Membrane Science, 554 (2018) 195-210.
[165] A. Modi, J. Bellare, Copper sulfide nanoparticles/carboxylated graphene oxide nanosheets blended polyethersulfone hollow fiber membranes: Development and characterization for efficient separation of oxybenzone and bisphenol A from water, Polymer, 163 (2019) 57-67.
[166] S. Yu, Y. Wang, F. Sun, R. Wang, Y. Zhou, Novel mpg-C3N4/TiO2 nanocomposite photocatalytic membrane reactor for sulfamethoxazole photodegradation, Chemical Engineering Journal, 337 (2018) 183-192.
[167] S. Dube, R. Moutloali, S. Malinga, Hyperbranched polyethyleneimine/multi-walled carbon nanotubes polyethersulfone membrane incorporated with Fe-Cu bimetallic nanoparticles for water treatment, Journal of Environmental Chemical Engineering, 8 (2020) 103962.

[168] S. Zinadini, S. Rostami, V. Vatanpour, E. Jalilian, Preparation of antibiofouling polyethersulfone mixed matrix NF membrane using photocatalytic activity of ZnO/MWCNTs nanocomposite, Journal of Membrane Science, 529 (2017) 133-141.
[169] Y. Ren, T. Li, W. Zhang, S. Wang, M. Shi, C. Shan, W. Zhang, X. Guan, L. Lv, M. Hua, MIL-PVDF blend ultrafiltration membranes with ultrahigh MOF loading for simultaneous adsorption and catalytic oxidation of methylene blue, Journal of hazardous materials, 365 (2019) 312-321.
[170] A. Modi, J. Bellare, Amoxicillin removal using polyethersulfone hollow fiber membranes blended with ZIF-L nanoflakes and cGO nanosheets: Improved flux and fouling-resistance, Journal of Environmental Chemical Engineering, 8 (2020) 103973.
[171] W. Li, B. Li, M. Meng, Y. Cui, Y. Wu, Y. Zhang, H. Dong, Y. Feng, Bimetallic Au/Ag decorated TiO2 nanocomposite membrane for enhanced photocatalytic degradation of tetracycline and bactericidal efficiency, Applied Surface Science, 487 (2019) 1008-1017.
[172] K. Niedergall, M. Bach, T. Hirth, G.E. Tovar, T. Schiestel, Removal of micropollutants from water by nanocomposite membrane adsorbers, Separation and Purification Technology, 131 (2014) 60-68.
[173] R. Mukherjee, S. De, Novel carbon-nanoparticle polysulfone hollow fiber mixed matrix ultrafiltration membrane: adsorptive removal of benzene, phenol and toluene from aqueous solution, Separation and Purification Technology, 157 (2016) 229-240.
[174] S.A. Hosseini, M. Vossoughi, N.M. Mahmoodi, M. Sadrzadeh, Efficient dye removal from aqueous solution by high-performance electrospun nanofibrous membranes through incorporation of SiO2 nanoparticles, Journal of Cleaner Production, 183 (2018) 1197-1206.
[175] J. Zhu, Y. Zhang, M. Tian, J. Liu, Fabrication of a mixed matrix membrane with in situ synthesized quaternized polyethylenimine nanoparticles for dye purification and reuse, ACS Sustainable Chemistry & Engineering, 3 (2015) 690-701.
[176] Z. Liao, M.N. Nguyen, G. Wan, J. Xie, L. Ni, J. Qi, J. Li, A.I. Schäfer, Low pressure operated ultrafiltration membrane with integration of hollow mesoporous carbon nanospheres for effective removal of micropollutants, Journal of hazardous materials, 397 (2020) 122779.
[177] V. Vatanpour, S.S.M. Khadem, A. Dehqan, M.A. Al-Naqshabandi, M.R. Ganjali, S.S. Hassani, M.R. Rashid, M.R. Saeb, N. Dizge, Efficient removal of dyes and proteins by nitrogen-doped porous graphene blended polyethersulfone nanocomposite membranes, Chemosphere, 263 (2021) 127892.
[178] V. Vatanpour, S. Faghani, R. Keyikoglu, A. Khataee, Enhancing the permeability and antifouling properties of cellulose acetate ultrafiltration membrane by incorporation of ZnO@ graphitic carbon nitride nanocomposite, Carbohydrate Polymers, 256 (2021) 117413.
[179] W. Lau, A. Ismail, N. Misdan, M. Kassim, A recent progress in thin film composite membrane: a review, Desalination, 287 (2012) 190-199.
[180] L. Bai, Y. Liu, A. Ding, N. Ren, G. Li, H. Liang, Fabrication and characterization of thin-film composite (TFC) nanofiltration membranes incorporated with cellulose nanocrystals (CNCs) for enhanced desalination performance and dye removal, Chemical Engineering Journal, 358 (2019) 1519-1528.
[181] S. Basu, M. Balakrishnan, Polyamide thin film composite membranes containing ZIF-8 for the separation of pharmaceutical compounds from aqueous streams, Separation and Purification Technology, 179 (2017) 118-125.
[182] C. Zhang, K. Wei, W. Zhang, Y. Bai, Y. Sun, J. Gu, Graphene oxide quantum dots incorporated into a thin film nanocomposite membrane with high flux and antifouling properties for low-pressure nanofiltration, ACS applied materials & interfaces, 9 (2017) 11082-11094.

[183] G. Gong, P. Wang, Z. Zhou, Y. Hu, New insights into the role of an interlayer for the fabrication of highly selective and permeable thin-film composite nanofiltration membrane, ACS applied materials & interfaces, 11 (2019) 7349-7356.
[184] J. Wang, N. Lia, Y. Zhaoa, S. Xiaa, Graphene oxide modified semi-aromatic polyamide thin film composite membranes for PPCPs removal, DESALINATION AND WATER TREATMENT, 66 (2017) 166-175.
[185] H. Zhang, B. Li, J. Pan, Y. Qi, J. Shen, C. Gao, B. Van der Bruggen, Carboxyl-functionalized graphene oxide polyamide nanofiltration membrane for desalination of dye solutions containing monovalent salt, Journal of Membrane Science, 539 (2017) 128-137.
[186] Y.-y. Zhao, Y.-l. Liu, X.-m. Wang, X. Huang, Y.F. Xie, Impacts of Metal–Organic Frameworks on Structure and Performance of Polyamide Thin-Film Nanocomposite Membranes, ACS applied materials & interfaces, 11 (2019) 13724-13734.
[187] T.-Y. Liu, Z.-H. Liu, R.-X. Zhang, Y. Wang, B. Van der Bruggen, X.-L. Wang, Fabrication of a thin film nanocomposite hollow fiber nanofiltration membrane for wastewater treatment, Journal of membrane science, 488 (2015) 92-102.
[188] P. Daraei, S.S. Madaeni, E. Salehi, N. Ghaemi, H.S. Ghari, M.A. Khadivi, E. Rostami, Novel thin film composite membrane fabricated by mixed matrix nanoclay/chitosan on PVDF microfiltration support: Preparation, characterization and performance in dye removal, Journal of membrane science, 436 (2013) 97-108.
[189] R. Dai, H. Han, T. Wang, X. Li, Z. Wang, Enhanced removal of hydrophobic endocrine disrupting compounds from wastewater by nanofiltration membranes intercalated with hydrophilic MoS2 nanosheets: Role of surface properties and internal nanochannels, Journal of Membrane Science, (2021) 119267.
[190] H. Zhang, X.-Y. Gong, W.-X. Li, X.-H. Ma, C.Y. Tang, Z.-L. Xu, Thin-film nanocomposite membranes containing tannic acid-Fe3+ modified MoS2 nanosheets with enhanced nanofiltration performance, Journal of Membrane Science, 616 (2020) 118605.
[191] N. Ghaemi, P. Safari, Nano-porous SAPO-34 enhanced thin-film nanocomposite polymeric membrane: simultaneously high water permeation and complete removal of cationic/anionic dyes from water, Journal of hazardous materials, 358 (2018) 376-388.
[192] R. Dai, X. Wang, C.Y. Tang, Z. Wang, Dually charged MOF-based thin-film nanocomposite nanofiltration membrane for enhanced removal of charged pharmaceutically active compounds, Environmental Science & Technology, 54 (2020) 7619-7628.
[193] Z. Yang, H. Guo, Z.-k. Yao, Y. Mei, C.Y. Tang, Hydrophilic silver nanoparticles induce selective nanochannels in thin film nanocomposite polyamide membranes, Environmental science & technology, 53 (2019) 5301-5308.
[194] R. Bi, Q. Zhang, R. Zhang, Y. Su, Z. Jiang, Thin film nanocomposite membranes incorporated with graphene quantum dots for high flux and antifouling property, Journal of Membrane Science, 553 (2018) 17-24.
[195] T. Ormanci-Acar, F. Celebi, B. Keskin, O. Mutlu-Salmanlı, M. Agtas, T. Turken, A. Tufani, D.Y. Imer, G.O. Ince, T.U. Demir, Fabrication and characterization of temperature and pH resistant thin film nanocomposite membranes embedded with halloysite nanotubes for dye rejection, Desalination, 429 (2018) 20-32.
[196] M. Wu, J. Yuan, H. Wu, Y. Su, H. Yang, X. You, R. Zhang, X. He, N.A. Khan, R. Kasher, Ultrathin nanofiltration membrane with polydopamine-covalent organic framework interlayer for enhanced permeability and structural stability, Journal of Membrane Science, 576 (2019) 131-141.
[197] Y. Song, Y. Wang, N. Zhang, X. Li, X. Bai, T. Li, Quaternized carbon-based nanoparticles embedded positively charged composite membranes towards efficient removal of cationic small-sized contaminants, Journal of Membrane Science, 630 (2021) 119332.

[198] Z. Wang, S. Guo, B. Zhang, L. Zhu, Hydrophilic polymers of intrinsic microporosity as water transport nanochannels of highly permeable thin-film nanocomposite membranes used for antibiotic desalination, Journal of Membrane Science, 592 (2019) 117375.
[199] L. Tian, Y. Jiang, S. Li, L. Han, B. Su, Graphene oxide interlayered thin-film nanocomposite hollow fiber nanofiltration membranes with enhanced aqueous electrolyte separation performance, Separation and Purification Technology, 248 (2020) 117153.
[200] M. Xu, X. Feng, X. Han, J. Zhu, J. Wang, B. Van der Bruggen, Y. Zhang, MOF laminates functionalized polyamide self-cleaning membrane for advanced loose nanofiltration, Separation and Purification Technology, (2021) 119150.
[201] S. Casanova, T.-Y. Liu, Y.-M.J. Chew, A. Livingston, D. Mattia, High flux thin-film nanocomposites with embedded boron nitride nanotubes for nanofiltration, Journal of Membrane Science, 597 (2020) 117749.
[202] Q. Zhang, L. Fan, Z. Yang, R. Zhang, Y.-n. Liu, M. He, Y. Su, Z. Jiang, Loose nanofiltration membrane for dye/salt separation through interfacial polymerization with in-situ generated TiO2 nanoparticles, Applied Surface Science, 410 (2017) 494-504.
[203] H.-C. Yang, R.Z. Waldman, Z. Chen, S.B. Darling, Atomic layer deposition for membrane interface engineering, Nanoscale, 10 (2018) 20505-20513.
[204] W. Mu, J. Liu, J. Wang, H. Mao, X. Wu, Z. Li, Y. Li, Bioadhesion-inspired fabrication of robust thin-film composite membranes with tunable solvent permeation properties, RSC advances, 6 (2016) 103981-103992.

# Chapter 6

## Bioinspired hyperbranched polyethylenimine (HPEI) cross-linked iron doped reduced graphene oxide (rGO) membrane for ultrafiltration of phenols and azo dyes from water

## 6.1 Abstract

Organic micropollutant contamination of potable waters and wastewaters is a global concern exacerbated by industrial growth. Graphene-based two-dimensional nanomaterials including reduced graphene oxide (rGO) have been shown to enhance the separation performance of membranes for a range of organic contaminants when incorporated into membrane surfaces by increasing adsorption and altering membrane pore size. However, rGO surface-modified membranes demonstrate very low water fluxes and poor stability due to the high rGO interlayer packing density and swelling of rGO nanosheets. In this study, we report the synthesis of a novel, crosslinked rGO nanocomposite membrane, exhibiting high water permeance and greatly improved dimensional stability. These membranes were formed by a layer of iron doped rGO (rGO – Fe) cross-linked with hyperbranched polyethylenimine (HPEI) vacuum deposited onto a polydopamine (PDA) surface-modified polyethersulfone (PES) ultrafiltration membrane. The HPEI cross-linking of iron-doped rGO was accomplished by 1) activating the carbonyl groups of the iron nanoparticles anchored on graphene oxide (GO – Fe) by N-(3-Dimethylaminopropyl)-N′-ethylcarbodiimide hydrochloride (EDC hydrochloride) and N-Hydroxysuccinimide (NHS) reaction chemistry, 2) cross-linking GO – Fe through the primary amines of HPEI, and 3) thermal reduction of crosslinked GO – Fe by $NaBH_4$. The resulting rGO nanocomposite membrane was stable in water of different pH for over 20 days. HPEI crosslinking and *in-situ* growth of nano-sized Fe on rGO nanosheets expanded the rGO interlayer spacing allowing higher water permeance. The optimized membrane achieved a water permeance of 39.8 $L \cdot m^{-2} \cdot h^{-1} \cdot bar^{-1}$, which was 2-fold greater than most reported

GO or rGO-based membranes. Adsorption, size exclusion, and pH-dependent electrostatic interactions controlled the separation of charged solutes, resulting in removals above 75.8%, 81.6% and 95.7% respectively for *p*-nitrophenol (PNP, 6.5 mg/L) and methyl orange (MO, 20 mg/L) and methylene blue (MB, 20 mg/L) during dead-end ultrafiltration. This study provides an enhanced material framework for rGO nanocomposite membranes for low-pressure micropollutant removal.

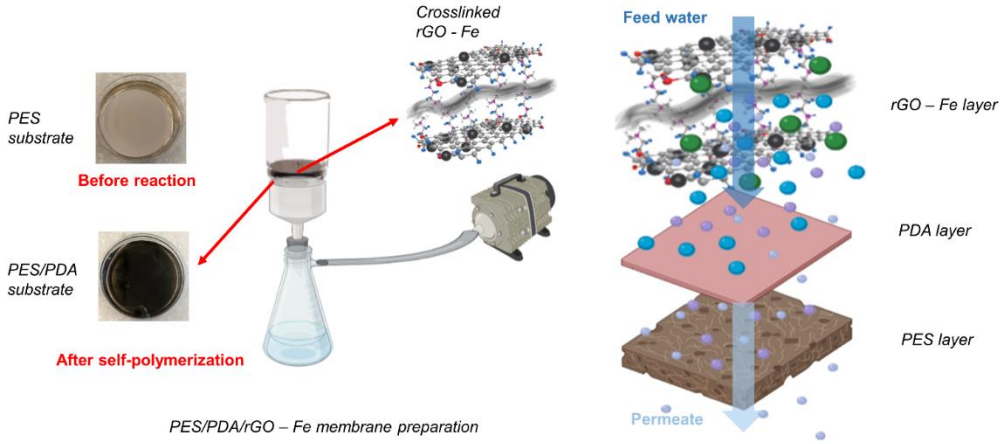


## 6.2 Introduction

Potable water and wastewater treatment, and resource recovery are critical to address global water scarcity and security, especially considering the increased organic micropollutant discharge from municipal and industrial sources. Many methods have been developed for achieving water sustainability, such as coagulation [1], adsorption [2], advanced oxidation processes (AOPs) (*e.g.*, Fenton oxidation [3], electrochemical degradation [4], photocatalytic degradation [5], and ozonation [6]), biological treatment (*e.g.*, activated sludge process) [7] and membrane separation [8]. Membranes have distinct advantages in organic micropollutant treatment over other methods including simple

operation, small footprints, modular design, the potential to achieve high permeate purity, consistent and reliable operation, as well as sometimes achieving synergic desalination. Nanofiltration (NF) and reverse osmosis (RO) membrane processes are accepted membrane methods for removing organics from wastewaters. However, the dense-structure of NF and RO membranes (with molecular weight cut-off (MWCO) range of 200 -1000 Da and < 50 Da, respectively) requires they be operated at high feed pressures (6 – 10 bar and 14 – 70 bar, respectively), resulting in high energy consumption, and thus high operational costs, as well as high fouling potential. Ultrafiltration (UF) and microfiltration (MF) membranes have loose structures and thus can achieve similar water fluxes at far lower pressures (2 – 5 bar, and 0.1 – 2 bar, respectively) [9, 10], however they lack rejection of small-sized organic solutes due to their large pore size (0.001 – 0.1 μm) [9], as these membranes rely predominantly on size exclusion for solutes rejection. Therefore, greater rejection of small organic solutes using UF membranes can only be achieved with additional removal mechanisms.

Recently, graphene-based two-dimensional (2D) nanomaterials such as reduced graphene oxide (rGO) have received substantial attention as they can greatly increase the available surface area of membranes to enhance their adsorption of small organic solutes. Many of these 2D nanomaterials also exhibit good mechanical stability, inherent molecular sieving characteristics, and the promise of making atomically thin membrane active layers with tunable pore sizes [11]. However, simply depositing these materials onto membranes fails to achieve this promise. For example, unmodified rGO aggregates into dense multi-layered structures in many solvents and depositing these stacks onto membranes creates dense rGO

layers (interlayer spacing ~ 0.35 nm) leading to extremely low trans-membrane flux [12]. Further, while rGO is more stable than the water dispersible GO, rGO layers have low structural stability especially when they are deposited onto more hydrophilic membrane surfaces[13].. To enhance permeability researchers have intercalated organic or inorganic spacers between rGO layers to increase the laminate spacing. Carbon nanotubes (CNTs) [14], graphitic carbon nitride (g-$C_3N_4$) [15], and halloysite nanotubes (HNTs) [16] have been demonstrated promise in preliminary studies, but further enhancement on membrane dimensional stability and interlaying spacing is needed. Alternatively, covalently cross-linking graphene nanosheets has been proposed as a strategy to prepare more structurally stable nanocomposite membranes. Studies on crosslinked rGO membranes are scarce, and to date GO layers have been crosslinked by small molecules (*e.g.*, ethylenediamine (EDA) [17] and cysteamine [18]), metal cations (*e.g.*, $Mg^{2+}$, $Ca^{2+}$, $Fe^{3+}$ and $Al^{3+}$) [13], and polyelectrolytes (*e.g.*, polyethyleneimine (PEI)) for use in membranes [19]. Despite successful cross-linking induced stability, the resulting membranes typically showed low water flux.

Developing crosslinked rGO membranes with permeability near to that of MF or UF membranes and greater small organic molecule separation efficiency would be a cost-effective alternative to many dense, energy-intensive composite membranes for low-pressure organic micropollutant removal. We have proposed a unique synthesis route that has not been attempted by previous researchers to realize these goals. For the first time, nano-sized iron (Fe) was grafted to GO to expand their interlayer distance and increase the overall surface area for adsorption, then crosslinked with hyperbranched polyethylenimine

(HPEI) to enable GO structural stability. Finally, the cross-linked GO – Fe was chemically reduced to obtain rGO – Fe nanocomposites, which were deposited onto a polyethersulfone (PES) membrane modified with polydopamine (PDA) to obtain strong physical adhesion. Physicochemical properties of the fabricated membranes were characterized, and their separation towards hazardous phenolic micropollutants and azo dye model contaminants were investigated at different solute conditions under typical ultrafiltration pressures.

## 6.3 Experimental

### 6.3.1 Materials and reagents

Polyethersulfone flat sheet membranes (PES, pore size 0.1 μm, dia. 47 mm) were purchased from Sterlitech, USA. GO water dispersion (particle size < 10 μm, 0.4 wt %) was purchased from Graphenea, USA. Dopamine hydrochloride, tris(hydroxymethyl)aminomethane hydrochloride (Tris HCl, ≥ 99 %), hyperbranched polyethylenimine (HPEI, $M_w$ = ~ 800 by LS), N-(3-Dimethylaminopropyl)-N′-ethylcarbodiimide hydrochloride (EDC hydrochloride), N-Hydroxysuccinimide (NHS, 98 %), iron(II) sulfate heptahydrate ($FeSO_4 \cdot 7H_2O$), sodium borohydride ($NaBH_4$, ≥ 98 %), *p*-nitrophenol (PNP, ≥ 99%), methyl orange (MO) and methylene blue (MB) obtained from Sigma Aldrich.

### 6.3.2 Synthesis of iron doped reduced graphene oxide (rGO – Fe) nanocomposites

20 mL, 0.4 wt% GO water dispersion was diluted to 2 mg/mL with DI water, and 80 mg $FeSO_4 \cdot 7H_2O$ (equivalents to 16 mg Fe) was subsequently added under stirring and $N_2$ flow for 10 min. $NaBH_4$ ($n(BH_4^-) : n(Fe^{2+}) = 2.4:1$) was added into the suspension and

stirred under $N_2$ flow for another 30 min to allow complete reduction of $Fe^{2+}$ to $Fe^0$. GO carboxyl group content (0.0018 mmol/mg GO) was pre-determined through conductometric titration (Fig. S1) method by an auto-titrator. An excess amount of EDC hydrochloride and NHS (40 mg and 24 mg, equivalent to 0.0026 mmol/mg GO, respectively) was added into the suspension and stirred for 15 min to allow sufficient activation of GO carboxyl group, considering the possible hydrolysis of the amine-reactive ester intermediates. After changing the suspension pH to 8 by 1 N NaOH, 4 mL 200 mg/mL HPEI solution was dropwise added into the suspension and stirred for 15 min to perform the crosslinking reaction to obtain GO – Fe nanocomposites. The rGO – Fe nanocomposites (rGO : Fe mass ratio was approximately 5 : 1) were prepared by $NaBH_4$ (300 mM) reduction of GO at 80 ℃ in an oil bath for 24 hr. The as-prepared suspension was diluted to 400 mL and probe-sonicated (Qsonica Q500, 500 Watts, 20 kHz) for 15 min effective time (interspersed by 2 s pulses) to yield a homogeneous mixture.

### 6.3.3 Preparation of PES/PDA/rGO – Fe nanocomposite membranes

Inspired by biological mussel chemistry, dopamine can undergo self-polymerization to form adhesive polydopamine (PDA) onto PES membranes that strengthens the interaction between the support membrane and the rGO – Fe nanocomposite. Membrane modification by PDA was achieved through dip coating following established methods with slight modification [15]. Briefly, 240 mL Tris HCl solution (0.013 M) was prepared, followed by pH adjustment to 8.5 using 1N NaOH. Dopamine hydrochloride (2.6 mg/mL) was added under stirring until complete dissolution. 15 mL solution was immediately transferred to submerge the PES membrane in a petri dish (dia. 50 mm, ht. 11 mm). The reaction was

performed at room temperature for 24 hr. The PDA surface-functionalized (PES/PDA) membranes were thoroughly washed with DI water. Different amounts of rGO – Fe (rGO content equivalents to 1, 2, 4 and 6 mg) were vacuum-filtered onto PES/PDA membranes (effective area 10.7 $cm^2$), yielding a surface loading of 934.6, 1869.2, 3738.3 and 5607.5 $mg/m^2$, respectively. A schematic diagram of the detailed synthesis steps is shown in Figure 1.

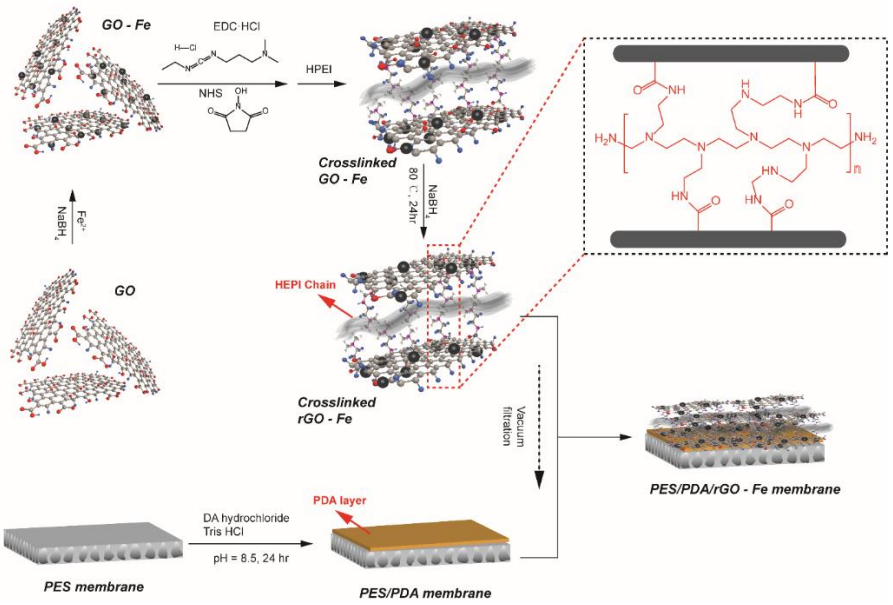


**Fig. 1.** Preparation steps for PES/PDA/rGO – Fe nanocomposite membrane.

6.3.4 Characterization

Raman spectra were collected at room temperature with a Renishaw InVia Laser Raman spectrometer, using a 300 mW Renishaw laser (785 nm, 1200 L/mm grating). Spectra were collected once in the 3200 – 100 $cm^{-1}$ range over a 58 s exposure time. Infrared spectra were identified by a Nicolet 6700 FT-IR spectrometer, within the mid-infrared range from 4000 – 525 $cm^{-1}$ with a resolution of 4 $cm^{-1}$ based on 32 scans. X-ray photoelectron spectroscopy (XPS) was performed using a scanning XPS microprobe (PHI Quantera II).

X-ray beam was set at 12.5 W and 15 kV. Beam size was 100 μm. The photoelectron take-off angle was 45°. The pass energies for the survey scan, C1s scan and O1s high resolution scan are 224 eV, 26 eV and 55 eV, respectively. X-ray powder diffraction (XRD) patterns were taken on a Bruker D8 Discover analyzer with DAVINCI.DESIGN diffractometer operating at 35 kV and 45 mA. The approximate interlayer spacing of nanocomposites were calculated by Bragg equation: $\lambda = 2d\sin\theta$, where d represents the interlayer spacing (d-spacing) of nanocomposites; $\theta$ is the diffraction angle; $\lambda$ is the wavelength of the cobalt sealed tube source (0.179 nm).

Membrane surface and cross-sectional morphologies were examined by a JEOL JSM-7000 F SEM equipment, with elemental distributions examined by energy dispersive X-ray spectroscopy (EDS). Cross sections were obtained by freeze fracturing membranes in liquid nitrogen for 10 s. Samples were coated with either 7 nm gold (Au) for SEM or 10 nm carbon for EDS using a sputter coater. rGO layer structure, distribution and size of doped Fe were examined by transmission electron microscopy (TEM). rGO – Fe nanocomposites were dispersed in anhydrous ethanol and drop-cast onto lacey carbon TEM grids (SPI), and then characterized by a FEI Titan LB80-300 TEM equipment. PES/PDA/rGO – Fe membrane samples were also cut into strips and placed into flat embedding molds filled with Spurr resin, and polymerized at 60℃ overnight in an oven. The thin sections were microtomed with a diamond knife and then characterized by a FEI Talos 200X 80-200 TEM equipment.

Brunauer-Emmett-Teller (BET) surface area was characterized by $N_2$ adsorption-desorption isotherms using a gas sorption analyzer (Autosorb iQ, Quantachrome

Instruments). Samples were degassed at 105℃ for 24 hr prior to analyses. rGO – Fe nanocomposites zeta potentials were determined by a Malvern Zetasizer device. Streaming potentials were measured using a Surpass 3 instrument (Anton Paar). Contact angle measurement was conducted by sessile drop method using an optical contact angle device (OCA 35). 5 – 10 μL Milli-Q water droplet was dispersed onto the membrane surface, and upon contact the initial contact angle was recorded. Each membrane was tested at 5 different locations to obtain an average value.

6.3.5 Filtration performance

Pure water permeance of the prepared membranes was determined by a bench-scale dead-end filtration unit (Sterlitech HP4750, USA), with effective membrane surface areas of 10.75 $cm^2$. All the membranes were pre-pressed with DI water under 4.14 bar for 20 min until steady-state flow was achieved prior to further tests. Pure water flux was measured under applied pressures of 0.69, 1.38, 2.76 and 4.14 bar. At each pressure, permeate weight was measured every certain interval for a total of 6 measurements and an average value was recorded. All tests were done in triplicate, and permeance ($L/(m^2 \cdot hr \cdot bar)$) was calculated using Eq. (1).

$$Permeance = \frac{\Delta M}{\rho_{water} \cdot A_{eff} \cdot P \cdot \Delta t} \quad (1)$$

Where $\Delta M$ ($g$) is the permeate weight at time interval $\Delta t$ (recorded in $s$, converted to $hr$); $\rho_{water}$ ($g/L$) is the water density at 25 ℃ (997 $g/L$); $A_{eff}$ ($m^2$) is the effective membrane surface area and P ($bar$) is the transmembrane pressure.

Membrane pollutant separation performance of the PES/PDA/rGO – Fe nanocomposite membranes was evaluated by dead-end filtration at 4.14 bar for different feed solutions including phenolic micropollutant (PNP, 6.5 – 50 mg/L) and azo dyes (MO and MB, 20 mg/L). Feed solutions were prepared at different phosphate buffer conditions (molarity = 5 mM at pH = 5.4, 7.2 or 8.6) to mimic different wastewater conditions. Permeate concentrations of PNP, MO and MB were determined by a UV-vis spectrophotometer (Tecan Spark 10M) at given wavelengths (PNP at 398 nm for pH = 7.2 and 8.6, and 316 nm for pH = 5.4; MO and MB at 464 nm and 664 nm for pH = 7.2, respectively), after establishing corresponding calibration curves. Up to 75 mL feed solution was filtered through the membrane in the dead-end configuration under 4.14 bar, and every 5 mL permeate was taken to measure the segment pollutant concentration. The total removal (%) can be calculated using Eq. (2).

$$\mathrm{Re}\,moval(\%) = \frac{\sum_{i=1}^{j} C_{segment} \cdot V_{segment}}{C_0 \cdot V_{tot}} \times 100\% \qquad (2)$$

Where $C_{segment}\,(mg/L)$ and $C_0\,(mg/L)$ are the average concentration of 5 mL segment permeate and the feed concentration, respectively; $V_{segment}\,(mL)$ and $V_{tot}\,(mL)$ are the segment volume (5 mL) and the total filtrate volume (75 mL), respectively; j represents segment numbers (segments #5, #10, and #15) which were measured after 25, 50, and 75 mL were filtered, respectively.

Average water flux ($L/(m^2 \cdot hr)$) of PNP solution was calculated by Eq. (3).

$$J = \frac{V_{tot}}{A_{eff} \cdot \Delta t} \quad (3)$$

Where $J$ $L/(m^2 \cdot hr)$ is permeate flux; $V_{tot}$ ($L$) is the total filtrate volume (0.075 L); $A_{eff}$ ($m^2$) is the effective membrane surface area; and $\Delta t$ ($hr$) is the filtration time.

## 6.4 Results and discussion

### 6.4.1 Characterization of membranes

#### 6.4.1.1 Material chemistry

Samples' chemical structures, molecular bond vibrations and the extent to which chemical reactions achieved completion were identified by Raman spectra (Figure 2a). Compared to pure PES membranes, two distinct peaks appeared at around 1375 $cm^{-1}$ and 1580 $cm^{-1}$, which supported the presence of catechol groups and quinone structures from PDA, respectively [20]. These peaks can be clearly identified despite PES/PDA membranes showing a higher background interference signal. Pristine GO, GO – Fe and rGO – Fe thin films exhibited two characteristic peaks near 1580 $cm^{-1}$ (G band) and 1310 $cm^{-1}$ (D band), which were ascribed to $sp^2$ stretching of hybridized graphene's graphitic structure and lattice defects within that structure and distortion of graphitic structures associated with the breathing mode, respectively [21]. The intensity ratio of D band and G band ($I_D/I_G$) increased with increased reduction extent of GO (pristine GO: 1.24, GO – Fe: 1.38, rGO – Fe: 1.73), suggesting an increase in structural defects and a decline of average lattice size of the $sp^2$ domain, despite reduction of the oxygen bonds within the graphene. These changes are indicative of successful crosslinking/reduction of GO, where HPEI grafting

introduced C—N bonds at GO surfaces and edges to replace some $sp^2$ carbon sites and increased the $sp^3$ character [22], and the subsequent $NaBH_4$ reduction decreased the nanosheet size through fragmentation to form more smaller-sized rGO domains with increased defective edges [21].

Samples' functional group types were probed by FTIR (Figure 2b). Pure PES membranes demonstrated the following characteristic peaks: C=C stretching of aryl rings at 1577 $cm^{-1}$, asymmetric stretching of $CSO_2C$ at 1321 $cm^{-1}$, and S=O stretching at 1297 $cm^{-1}$ and 1148 $cm^{-1}$ [23]. PES/PDA membrane exhibited two new peaks at 3381 $cm^{-1}$ and 1634 $cm^{-1}$, which corresponded to the N—H/O—H stretching and C=O stretching from PDA [20], respectively. Prior to reactions, GO had abundant oxygen groups such as hydroxyl groups, carboxylic groups and epoxy groups, which were confirmed by the existence of O—H, C=O, C—OH and C—O stretching at 3130, 1722, 1224 and 1054 $cm^{-1}$, respectively; whereas the C=C stretching at 1617 $cm^{-1}$ was from the skeletal GO nanosheet [24, 25]. GO – Fe showed an additional peak at 3242 $cm^{-1}$, which was caused by hydrogen bonding including O-H and N-H stretching [25].The new bonds at 1634 $cm^{-1}$ and 1558 $cm^{-1}$ can be explained by graphene aromatic C=C stretching and C=O—NH stretching, and amide C—N stretching, respectively [26, 27]. These peaks shifted to 1654 $cm^{-1}$ and 1560 $cm^{-1}$ for rGO – Fe, while the peaks for the oxygen groups were eliminated. These results confirmed the successful covalent bonding between HPEI and GO (given HPEI had no amide group), as well as the reduction of GO to rGO.

Element composition and chemical states of materials were examined by XPS (Figure S2 and Figure 2c). XPS survey spectra confirmed the elements of the PES membrane (Figure

S2a, C, O and S), PES/PDA membrane (Figure S2d, C, N, O, S and Na) and PES/PDA/rGO – Fe membrane (Figure 2c, C, N, O, S, Na and Fe), as expected. C1s spectra of PES and PES/PDA membranes (Figure 2c) were deconvoluted into two peaks assigned to C—C/C=C (284.8 eV and 284.7 eV) and C-O (286.2 eV) [28]. O1s spectra of the PES membrane (Figure S2c) showed two peaks representing O=S (531.6 eV) and O—C (533.3 eV) [29], which were from the sulpone bonds within the polymer backbone. O1s signals for the PES/PDA membrane (Figure S2f) were similar (531.5 eV and 533.3 eV), but the peak at 531.5 eV was caused by overlapping O=S and O=C bond peaks[29]. PES/PDA/rGO – Fe membranes exhibited four C1s peaks (Figure 2c): C—C/C=C (284.7 eV), C—O/ C—N (285.7 eV), C—O—C (286.8 eV) and C=O (288.3 eV), which correspond to oxygen-containing functional groups from rGO nanosheets, amine groups from HPEI, and amide groups from the crosslinked rGO – Fe [28]. Worth noting, the contribution of amide groups to the C—N bond detected by XPS was also supported by FTIR C=O—NH stretching (Figure 2b). O1s spectra could be fit into three peaks (Figure 2c): lattice $O^{2-}$ from O—Fe (530.4 eV), O=C (531.8 eV) and O—C (533.5 eV) [29, 30]. As shown in Figure 2c, Fe 2p3/2 (main peak, 711.9 eV) and Fe 2p1/2 (719.2 eV) are characteristic peaks for $Fe^{3+}$, whereas the peak at 710.3 eV and Fe satellite peak (714.0 eV) was attributed to $Fe^{2+}$ [29, 30]. These results suggested that the main oxide state of Fe is $Fe_2O_3$ and FeO, which likely formed an oxide shell over the Fe particle surface due to oxidation.

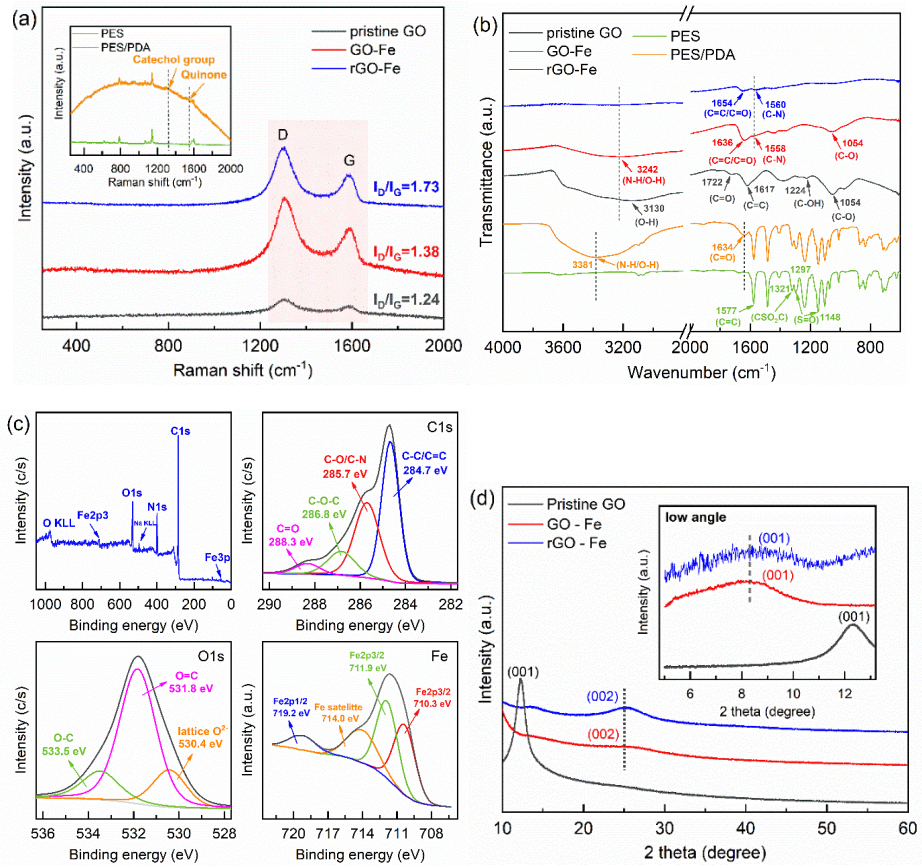


**Fig. 2.** (a) Raman and (b) FTIR spectra of PES membrane, PES/PDA membrane, pristine GO, GO – Fe and rGO – Fe; (c) XPS survey spectra, C1s, O1s and Fe spectra of PES/PDA/rGO – Fe membrane; (d) XRD spectra of pristine GO, GO – Fe and rGO – Fe free-standing thin films.

6.4.1.2 Structure and morphology

Crystalline structures, reduction degree, and structure defects of control membranes (Figure S3) and pristine GO, GO – Fe and rGO – Fe thin films were characterized by XRD patterns (Figure 2d). PES and PES/PDA membranes showed one broad peak at around $2\theta = 20.84°$, suggesting the amorphous nature of the polymers[31]. Pristine GO exhibited a pronounced single diffraction peak (001 plane) at $2\theta = 12.35°$ (with a d-spacing of 8.3 Å) resulting from oxygen-containing functional groups at the GO surface, whereas GO – Fe and rGO – Fe showed two different stacking pattern structures, at $2\theta = 7.87°$ (001 plane)

and $2\theta = 25.32°$ (002 plane) corresponding to d-spacing values of 13 Å and 4.1 Å respectively. The larger d-spacing was attributed to the crosslinked GO or rGO layers that were expanded by the cross-linking HPEI polymers, and the smaller d-spacing was attributed to densely stacked GO or rGO layers that did not undergo cross-linking. The smaller spacing, however confirmed the reduction of GO due reduction reactions which allowed closer stacking of the sheets. [32].

Surface morphology of as-prepared membranes were characterized by SEM. PDA modification of PES membranes showed minimal change on membrane surface morphology (Figure S4). However, PES/PDA/rGO – Fe membranes revealed a rough surface with a distinctive wrinkled structure (Figure 3a-1, 3b-1, 3c-1 and 3d-1). Cross section images (Figure 3a-2, 3b-2, 3c-2 and 3d-2) exhibited two distinct layers, where the nanocomposite layer thickness varies from 1.5 to 8.37 μm. Another study led by Wang et al. [31] reported unmodified GO nanosheet thicknesses up to 70 nm when depositing 75.2 $mg/m^2$on PES/PDA membranes . Extrapolating this surface density to our system would be equivalent to a thickness of 0.87 μm (assuming GO and rGO had the same density, rGO mass 1 mg). The thickness obtained in our study (1.5 μm) was markedly higher. We hypothesize that the thicker deposited layer could be explained by two aspects, supported by XRD (Figure 2d): (1) High surface density of coated rGO, *i.e.*, 934.6 – 5607.5 $mg/m^2$; (2) Grafted HPEI polymer and Fe nanoparticles expanded the 3D nanochannels within nanocomposite.

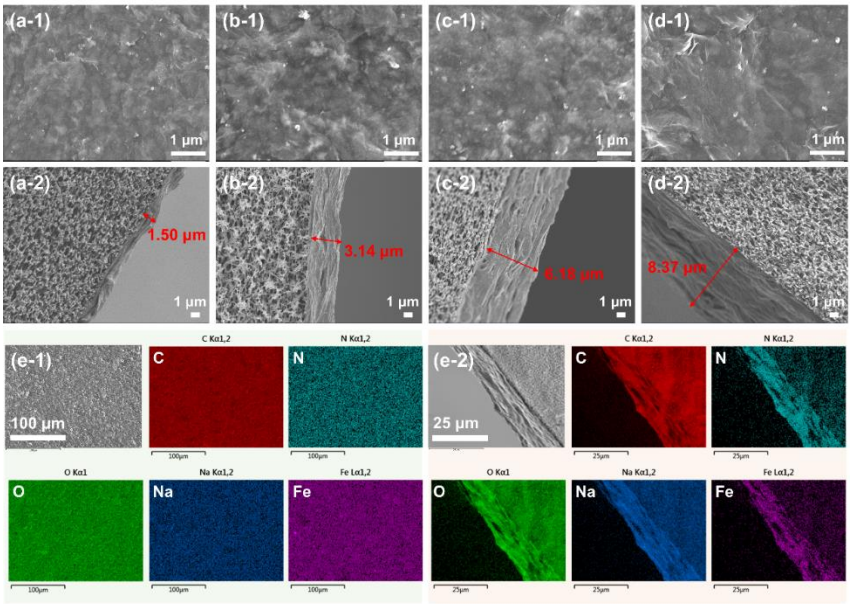


**Fig. 3.** SEM/EDS images of PES/PDA/rGO – Fe membranes. rGO content equivalents to 1 mg (a-1 and a-2), 2 mg (b-1 and b-2), 4 mg (c-1 and c-2) and 6 mg (d-1, d-2, e-1 and e-2). n-1 indicates membrane top views, and n-2 indicates membrane cross sections, where n corresponds to a, b, c, d or e.

At the microstructure level, EDS pictorially reflected the elemental distribution of as-prepared membranes, which served as a useful supplement to XPS analyses. Both PES and PES/PDA membranes (Figure S5) showed uniform elemental distributions across their surface and throughout their cross section, including the distribution of N on PES/PDA membranes throughout the top layer, showing successful adhesion and distribution of the PDA layer. Likewise, Fe and N were found to exist uniformly within rGO – Fe nanocomposites across the surface and cross-section for the PES/PDA/rGO – Fe membranes (Figure 3e-1 and 3e-2), suggesting an evenly dispersed rGO – HPEI – Fe network after crosslinking. This conclusion was further strengthened by high resolution TEM imaging (Figure 4a and Figure 4b), in which it can be clearly observed that Fe (surface oxidized to Fe (II, III) oxides) nanoparticles were widely dispersed on rGO

nanosheets. TEM images of the microtomed cross sections of rGO – Fe (Figure 4c and Figure 4d) also showed that the iron nanoparticles grew between the rGO sheets and did not aggregate, with average particle sizes of approximately 8 nm. The introduction of Fe nanoparticles potentially increased the adsorption sites for micropollutants removal.

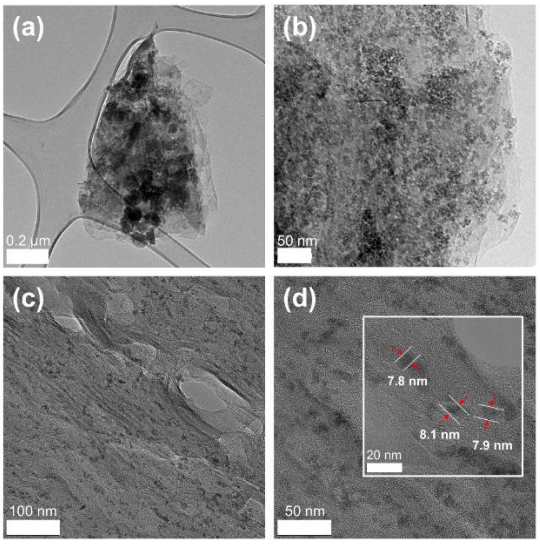


**Fig. 4.** TEM images of (a and b) rGO – Fe nanocomposites and (c and d) cross-section of rGO – Fe thin film from the microtomed PES/PDA/rGO – Fe membrane.

6.4.1.3 Water permeance, surface properties, and stability

As shown in Figure 5a, pure water permeance was measured under pressures ranging from 0.69 to 4.14 bar for PES/PDA/rGO – Fe nanocomposite membranes containing varying amounts of rGO from 1 mg – 6 mg. PES/PDA/rGO-Fe nanocomposite membranes demonstrated pure water permeance decreased from 356.3 to 39.8 $L \cdot m^{-2} \cdot h^{-1} \cdot bar^{-1}$ accompanied by a slight increase in surface hydrophobicity ($58.5°C$ to $66.1°C$) with increasing mass content of rGO from 1 to 6 mg. Note that the grafted HPEI introduced hydrophilic amine groups to rGO significantly increased the hydrophilicity, which can promote a membrane's affinity to hydrophilic solutes. The permeance obtained in this

study was an order of magnitude higher than many other GO or rGO-coated membranes (< 15 $L \cdot m^{-2} \cdot h^{-1} \cdot bar^{-1}$) [28, 33, 34], possibly because the embedded HPEI chain and the anchored Fe nanoparticles effectively expanded the rGO interlayer spacing (13 Å) reducing the membrane fluid resistance (Figure 1).

Membrane surface charge at different pH (5.4, 7.2, 8.6) was evaluated by streaming potential (Figure 5b), which impacts the electrostatic interaction with charged molecules. Unmodified PES membranes exhibited a negative zeta potential over the entire pH ranges (above its isoelectric point at 3.6) suggesting a negatively-charged surface [35]. After PDA modification, membrane surfaces carried a positive charge at acidic pH due to the protonation of PDA amine groups, but became more negatively-charged compared to neat PES membranes at both neutral and basic pH 7.2 and 8.6 due to deprotonation of PDA phenolic groups [36]. Crosslinked rGO – Fe showed a positive charge at acidic and neutral pH 5.4 and 7.2 as attributed to the protonated amine groups from HPEI chains, while increasing pH to 8.6 resulted in a negative surface charge, caused by $OH^-$ neutralization of cationic charges on HPEI chains as well as ionization of the remaining non-crosslinked carboxylic groups from rGO to form carboxylate anion. BET analyses (Figure 5c) suggested that control PES membranes had relatively low surface area and pore sizes at the low mesopore ranges (2 – 10 nm), and that rGO – Fe surface coating increased available adsorption sites (BET surface area reached 110.6 $m^2/g$) and slightly decreased the average pore size from 2.8 to 2.6 nm, which may have enhanced the exclusion of small solutes.

Stability of PES/PDA/rGO – Fe membranes was examined by immersing membranes in phosphate buffer solutions (molarity = 5 mM) at acidic, near neutral, and basic pH for up

to 20 days (Figure 5d), and comparing these with the stability of non-crosslinked rGO – Fe coated membranes. These control membranes did not include rGO carboxyl group activation by EDC hydrochloride and NHS, and the subsequent HPEI crosslinking. From the images, it can be clearly observed that crosslinked rGO – Fe membranes remain stable in water without observed loss in nanocomposite structural integrity across all pH values measured for 20 days. Non-crosslinked rGO – Fe membranes in comparison disintegrated, with graphene exfoliating from the membranes within a few days. This evidence demonstrated the hydration stability of the crosslinked rGO – Fe membranes, which is critical for maintaining robust long-term separation performance.

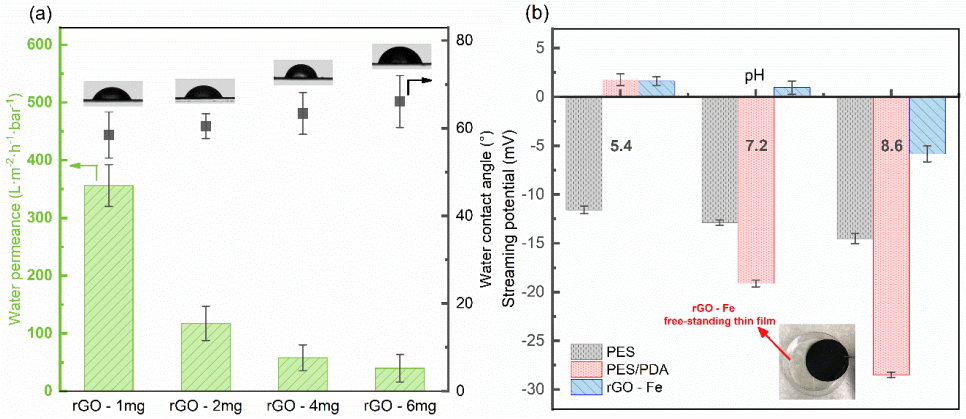

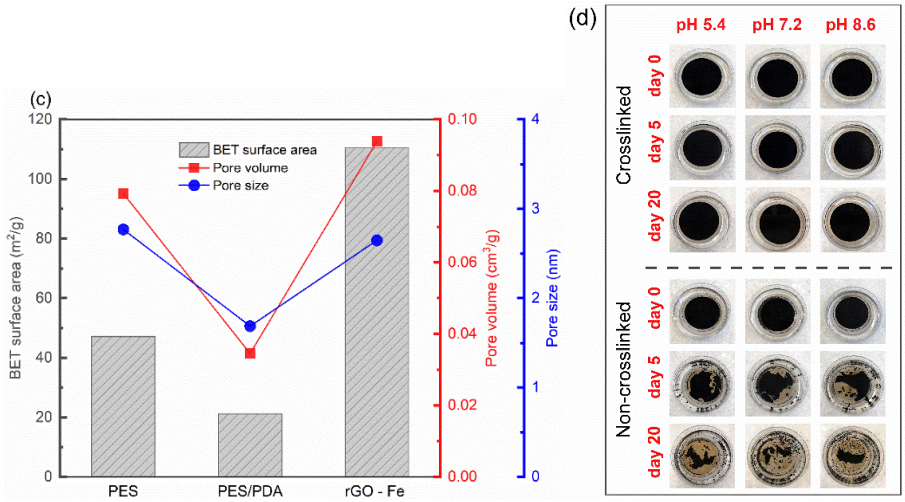


**Fig. 5.** (a) Water permeance and contact angle of PES/PDA/rGO – Fe membranes with different surface coating mass; (b) Streaming potential and (c) BET analyses of PES membrane, PES/PDA membrane and rGO – Fe thin film (rGO mass equals to 6 mg), pore size and pore volume were calculated based on DFT method; (d) stability comparison between crosslinked and non-crosslinked PES/PDA/rGO – Fe membranes at different pH.

### 6.4.2 Performance evaluation

#### 6.4.2.1 Removal of PNP micropollutant

*p*-nitrophenol (PNP) is representative of recalcitrant nitroaromatic micropollutants of prime importance in effluents across various industries such as pharmaceuticals, textiles, oil refining and coal conversion [37], and thus was selected as a model micropollutant for membrane separation. We investigated the effect of pH and PNP concentration on PNP removal using PES/PDA/rGO-Fe membranes (Figure 6a and Figure S6). Removal of PNP was monitored over time, with PNP concentrations in the permeate measured for 25, 50 and 75 mL of feed filtered through the membrane. High PNP removal (PNP concentration: 6.5 mg/L) was obtained for the first 25 mL permeate at all pH, reaching 98.8% at pH 7.2, 93.4% at pH 8.6 and 88.9% at pH 5.4. The removal efficiency decreased to 75% for the 50 mL treatment of permeate, and further decreased to 36.5% at pH 8.6 and 27.8% at pH 5.4,

while remained above 75% (75.8%) at pH 7.2 for the total 75 mL permeate (Figure 6a and Figure S6a). This overall removal efficiency was much higher than that achieved with control PES membranes (< 15%, data not shown). PNP removal was greater for lower concentrations as compared with higher concentrations at pH 7.2 (6.5 mg/L: 98.8 – 75.8%, 20 mg/L: 80.0 – 52.2% and 50 mg/L: 42.7 – 36.1%).

We hypothesize the PNP removal mechanisms to include the synergistic effect of adsorption, size exclusion and electrostatic interactions (Figure 7). It is well establish that rGO surfaces enable adsorption and π-π interactions of organic molecules, and these rGO-Fe nanocomposites with expanded interlayer structures and high surface area (110.6 $m^2/g$) demonstrate enhanced PNP enrichment on rGO aromatic moieties [2]. The gradual saturation of available adsorptive sites led to decreased removal of PNP with increasing feed volume. The DFT pore size (2.65 nm) of rGO – Fe nanocomposites was within the micropore range (0 – 2 nm) which is ideal for adsorbing small PNP molecules(0.66 × 0.43 nm) [2], while continued filtration led to pore occlusion and homo-adsorption of PNP. The influence of pH on PNP removal can be partly explained by the electrostatic changes on the membranes and solutes under different pH. Hydroxyl groups on PNP became protonated/deprotonated at acidic/basic aqueous solutions. At pH 5.4 or 8.6, electrostatic repulsion impeded membrane adsorption of PNP due to like charges of rGO – Fe and PNP (negative charge at pH 5.4 and positive charge at pH 8.6). At pH 7.2, rGO – Fe carried positive charges from protonated HPEI amine groups, whereas PNP was neutral or partially ionized to *p*-nitrophenolate as indicatd by its $pK_a$ (7.15). Therefore, weak electrostatic attraction enhanced the adsorptive removal of PNP at neutral pH.

PNP permeation flux was also impacted by aqueous pH and PNP concentration. At different pH (PNP concentration: 6.5 mg/L), the average flux was impacted by electrostatic interactions enhancing or impeding solute transport across the membranes. The flux was greatest at neutral pH, following the order of $J_{pH7.2} = 180.0\ L/(m^2 \cdot hr) > J_{pH5.4} = 117.7\ L/(m^2 \cdot hr) > J_{pH8.6} = 76.3\ L/(m^2 \cdot hr)$. Although a higher permeation flux at pH 7.2 slightly reduced the contact time of PNP to the rGO-Fe membranes during filtration, this shortened residence time did not seem to reduce the PNP removal rate. This suggested a rapid adsorption/partition of PNP to the nanocomposite membrane, which was likely caused by a high affinity of PNP to the rGO – Fe nanocomposite (and the PDA adhesive layer) due to abundant active sites for adsorption and strong membrane – solute hydrophilic interactions (PNP log $K_{ow}$ = 1.91 [38], membrane contact angle $66.1^{\circ}$). By contrast, an increase of PNP feed concentration at pH 7.2 significantly decreased the transmembrane flux ($J_{6.5mg/L} = 180.0\ L/(m^2 \cdot hr) > J_{20mg/L} = 132.6\ L/(m^2 \cdot hr) > J_{50mg/L} = 39.7\ L/(m^2 \cdot hr)$) due to concentration polarization, which impeded filtration. At 6.5 and 20 mg/L PNP feed concentration, removal efficiencies decreased slowly with filtrate volume due to gradual adsorption saturation within the nanocomposite (Figure S6b). Removal efficiency decreased sharply after filtrating the first 10 mL of the 50 mg/L PNP feed solution, providing a stable but low removal rate for subsequent filtrates (Figure S6b). Greatly reduced removal efficiencies were likely due to early nanocomposite saturation by PNP and subsequent PNP breakthrough.

6.4.2.2 Removal of azo dyes

Separation performance of azo dyes (methyl orange (MO) and methylene blue (MB), concentration: 20 mg/L) through different PES/PDA/rGO – Fe membranes simulated the removal of charged hazardous small organic pollutants with opposite charges. As shown in Figure 6b, increasing the rGO content from 1 to 6 mg greatly improved their removal, from 34.5 to 95.7% for MO and 23.9 to 81.6% for MB in 75 mL of treated permeate. Removal rates decreased for both MO and MB with increased treated volume for all membranes due to adsorption saturation of the rGO – Fe nanocomposites (Figure 6b and Figure S7). Nevertheless, the 6 mg rGO equivalent mass coated PES/PDA/rGO – Fe membrane possessed a sufficient number of active sites for dye adsorption, achieving relatively high removals without significantly decreasing the removal rates for up to 75 mL treated volume, reaching 95.7% for MO, and 81.6% for MB, respectively.

Furthermore, despite MO and MB having similar sizes, the removal to MO was up to 14% higher. This is because at pH 7.2, MO is negatively charged, which increased its adsorption through electrostatic attraction, whereas MB is positively charged thus impeding its adsorption through electrostatic repulsion to rGO – Fe nanocomposites (Figure 7). Additionally, the MO molecule can rotate about its two central C—N bonds [28], which can facilitate its diffusion between the laminated rGO – Fe nanochannels. The removal rates for MO (97.7 – 95.7%) and MB (92.5 – 81.6%) are both higher than PNP (80.0 – 52.2%) at the same operating condition (20 mg/L, 6 mg rGO equivalent mass coating, aqueous pH 7.2, up to 75 mL filtrates), which could be explained by greater size exclusion

of the higher molecular weight MO (327.3) and MB (319.8) as compared to the lower molecular weight PNP (139.1).

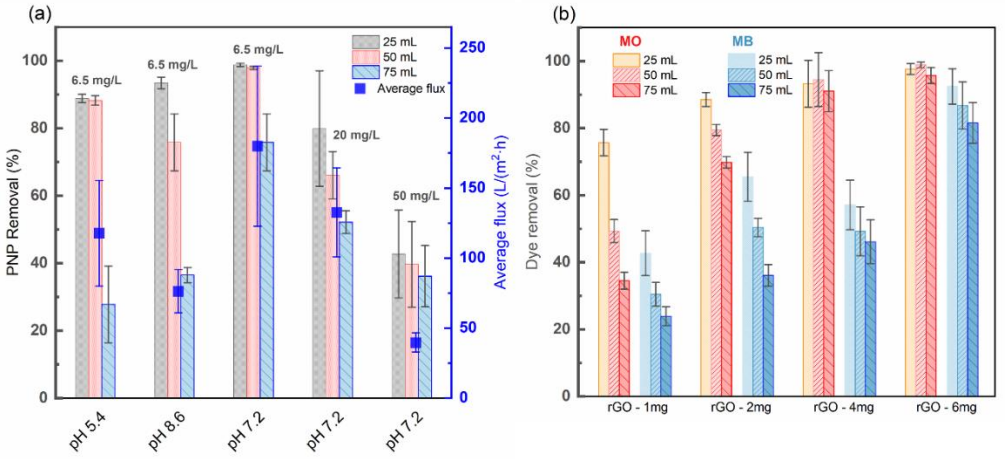


**Fig. 6.** Separation performance of (a) PNP by PES/PDA/rGO – Fe membrane (rGO mass equals to 6 mg) at different pH and PNP concentration; (b) MO and MB by PES/PDA/rGO – Fe membranes (rGO mass equals to 1, 2, 4 or 6 mg) at pH 7.2. Operating pressure 4.14 bar. Error bars represent standard deviations of triplicate measurements for PNP and azo dye removal, and duplicate measurements for PNP average flux.

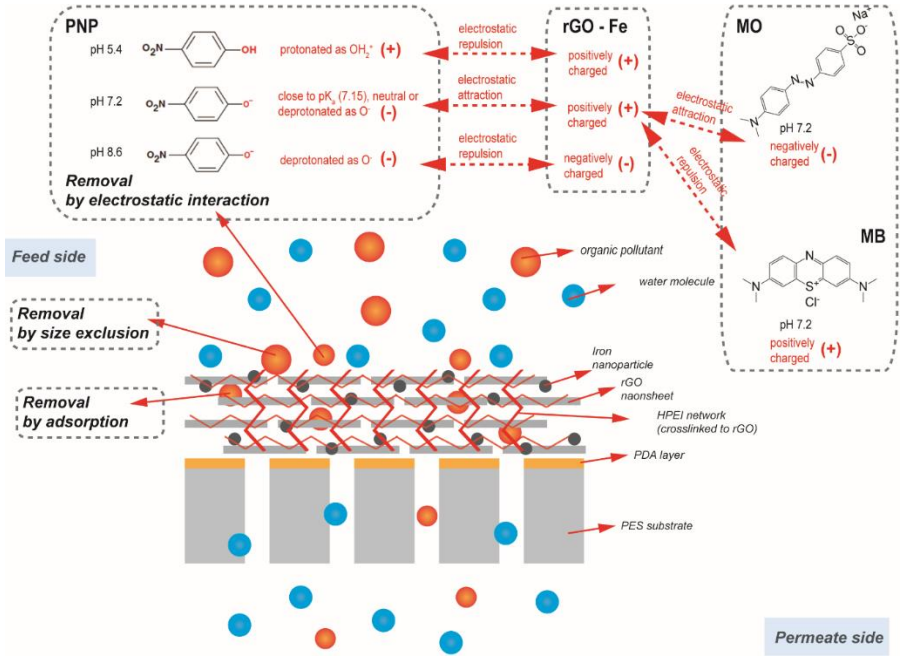


**Fig. 7.** Mechanisms of PNP and azo dye removal by PES/PDA/rGO – Fe nanocomposite membrane.

6.4.2.3 Future perspectives for water treatment practices

The rGO membrane designed in this study demonstrated the ability to remove various small organic molecules typical of wastewaters at low operating pressure and provided a useful basis for developing other process-intensified advanced membranes to address small organic micropollutants. Membrane surface-loaded rGO could serve as an electron transfer interface to catalyze the formation of reactive oxygen species (ROS) and/or to produce radical species such as $-OH$ and $SO_4^{2-}$ upon contact with other oxidants (*e.g.*, $H_2O_2$ or persulfate precursors) in the feed solution. rGO membrane-generated oxidants can be used for selective degradation of refractory organic micropollutants during ultrafiltration [39]. The crosslinked nanostructured rGO – Fe prepared in this study had sufficient surface area to provide reactive sites and successfully prevented catalytic Fe nanoparticle aggregation thereby potentially overcoming catalyst attrition through aggregation; an advantage that is worth further investigation.

In addition, rGO catalytic membranes could be used for reductive removal of micropollutants. Nano zero-valent iron (nZVI) has gained great interest for adsorption and reduction of certain contaminants. However, nZVI quickly oxidize, which was also observed in this study in which the 8 nm Fe nanoparticles were covered by $Fe_2O_3$ and FeO (Figure 2c), leading to reactivity loss. Given the conductive property of rGO-based membranes, a negative electrical potential can be applied to the PES/PDA/rGO – Fe membrane surface to help regenerate the oxidized Fe nanoparticles at the rGO nanosheet to realize continuous electrically catalytic reduction of many micropollutants such as nitroaromatics [40]. However, chemically-obtained rGO often has inadequate conductivity

due to structural defects and the presence of various functional groups during chemical reduction [41], which limits the application for electrochemical water treatment. Future research in this direction should investigate new synthesis approach (such as laser irradiation [42]) to produce more conductive rGO materials and to investigate the rGO : Fe ratio to optimized adsorption and permeance for micropollutant removal and degradation rates during filtration.

Finally, since scaled water treatment units employ cross-flow systems for contaminant separation, there is a need to further improve the cross-flow stability of PES/PDA/rGO – Fe membrane through covalently tethering the nanocomposites with the underlying polymer membrane substrate. For instance, Zhang et al. [43] used click chemistry to connect alkyne-terminated GO with azido-functionalized polypropylene (PP) membrane surface. Meng et al. [17] crosslinked GO nanosheets with brominated poly (phenylene oxide) membrane substrate using EDA as crosslinker. Future efforts should continue to explore alternative chemistries to functionalize rGO nanocomposites and polymeric membrane substrate, and identify crosslinkers that will provide sufficient membrane stability, permeance and selectivity. Moreover, similar reactions could be adopted for other carbon-nanomaterial-based thin films including various carbon nanotube (CNT) surface-modified membranes.

### 6.5 Conclusions

In this work, a novel, moderately stable crosslinked layer-structured rGO nanocomposite membrane was prepared by vacuum filtration of HPEI crosslinked Fe doped rGO onto

PDA surface-modified PES membrane substrate using mostly environmentally-benign solvents and chemical constituents. The crosslinking bond between HPEI and rGO was confirmed by FTIR and XPS. The deposited HPEI crosslinked rGO – Fe nanocomposites showed structural stability and durability in different pH aqueous solutions without any exfoliation or delamination after 20 days. The optimum PES/PDA/rGO – Fe membrane showed promising removal to PNP micropollutant (up to 98.8%), MO (up to 97.7%) and MB (up to 92.5%) under low-pressure ultrafiltration conditions. Removal occurred through membrane adsorption, size exclusion, and pH-dependent electrostatic interactions. The insertion of HPEI and *in-situ* growth of Fe nanoparticles on rGO layers expanded the interlayer nanochannels, which improved the permeance of the resultant PES/PDA/rGO – Fe membrane (39.8 $L \cdot m^{-2} \cdot h^{-1} \cdot bar^{-1}$), achieving 2-fold greater permeance than many reported GO or rGO-based membranes. The results of this study provide a novel perspective for guiding the synthesis of next-generation rGO nanocomposite membranes for practical water treatment.

### 6.6 Acknowledgements

This work was supported by Canada First Research Excellence Foundation Global Water Futures (GWF) grant. SEM and TEM were performed at the Canadian Centre for Electron Microscopy (CCEM). We acknowledge Matthew McClure for assistance in streaming potential measurement.

## 6.7 References

[1] S. Chen, Z. Yuan, D. Hanigan, P. Westerhoff, H. Zhao, J. Ni, Coagulation behaviors of new covalently bound hybrid coagulants (CBHyC) in surface water treatment, Separation and Purification Technology, 192 (2018) 322-328.
[2] Y. Wu, N. Zhang, C.-F. de Lannoy, Upcycling wildfire-impacted boreal peats into porous carbons that efficiently remove phenolic micropollutants, Journal of Environmental Chemical Engineering, 9 (2021) 105305.
[3] G. Vilardi, L. Di Palma, N. Verdone, On the critical use of zero valent iron nanoparticles and Fenton processes for the treatment of tannery wastewater, Journal of Water Process Engineering, 22 (2018) 109-122.
[4] G.O. Santos, A.R. Dória, V.M. Vasconcelos, C. Sáez, M.A. Rodrigo, K.I. Eguiluz, G.R. Salazar-Banda, Enhancement of wastewater treatment using novel laser-made Ti/SnO2–Sb anodes with improved electrocatalytic properties, Chemosphere, 259 (2020) 127475.
[5] P. Raizada, A. Sudhaik, P. Singh, A. Hosseini-Bandegharaei, P. Thakur, Converting type II AgBr/VO into ternary Z scheme photocatalyst via coupling with phosphorus doped g-C3N4 for enhanced photocatalytic activity, Separation and Purification Technology, 227 (2019) 115692.
[6] Q. Cao, L. Sang, J. Tu, Y. Xiao, N. Liu, L. Wu, J. Zhang, Rapid degradation of refractory organic pollutants by continuous ozonation in a micro-packed bed reactor, Chemosphere, 270 (2021) 128621.
[7] M. Kamali, T.M. Aminabhavi, L. Tarelho, R. Hellemans, J. Cuypers, I. Capela, M.E.V. Costa, R. Dewil, L. Appels, Acclimatized Activated Sludge for Enhanced Phenolic Wastewater Treatment Using Pinewood Biochar, Chemical Engineering Journal, (2021) 131708.
[8] J. Heo, S. Kim, N. Her, C.M. Park, M. Yu, Y. Yoon, Removal of contaminants of emerging concern by FO, RO, and UF membranes in water and wastewater, Contaminants of Emerging Concern in Water and Wastewater, (2020) 139-176.
[9] R.W. Baker, Membrane technology and applications, John Wiley & Sons, 2012.
[10] R.M. Rajendran, S. Garg, S. Bajpai, Study of transport models for arsenic removal using nanofiltration process: recent perspectives, in: Emerging Technologies in Environmental Bioremediation, Elsevier, 2020, pp. 391-405.
[11] S. Dervin, D.D. Dionysiou, S.C. Pillai, 2D nanostructures for water purification: graphene and beyond, Nanoscale, 8 (2016) 15115-15131.
[12] J. Lyu, X. Wen, U. Kumar, Y. You, V. Chen, R. Joshi, Separation and purification using GO and r-GO membranes, RSC advances, 8 (2018) 23130-23151.
[13] Z. Wang, F. He, J. Guo, S. Peng, X.Q. Cheng, Y. Zhang, E. Drioli, A. Figoli, Y. Li, L. Shao, The stability of a graphene oxide (GO) nanofiltration (NF) membrane in an aqueous environment: progress and challenges, Materials Advances, 1 (2020) 554-568.
[14] W.-L. Jiang, M.R. Haider, J.-L. Han, Y.-C. Ding, X.-Q. Li, H.-C. Wang, H.M.A. Sharif, A.-J. Wang, N.-Q. Ren, Carbon nanotubes intercalated RGO electro-Fenton membrane for coenhanced permeability, rejection and catalytic oxidation of organic micropollutants, Journal of Membrane Science, 623 (2021) 119069.
[15] Y. Wei, Y. Zhu, Y. Jiang, Photocatalytic self-cleaning carbon nitride nanotube intercalated reduced graphene oxide membranes for enhanced water purification, Chemical Engineering Journal, 356 (2019) 915-925.
[16] Y. Liu, W. Tu, M. Chen, L. Ma, B. Yang, Q. Liang, Y. Chen, A mussel-induced method to fabricate reduced graphene oxide/halloysite nanotubes membranes for multifunctional applications in water purification and oil/water separation, Chemical Engineering Journal, 336 (2018) 263-277.

[17] N. Meng, W. Zhao, E. Shamsaei, G. Wang, X. Zeng, X. Lin, T. Xu, H. Wang, X. Zhang, A low-pressure GO nanofiltration membrane crosslinked via ethylenediamine, Journal of Membrane Science, 548 (2018) 363-371.
[18] L. Cheng, K. Guan, G. Liu, W. Jin, Cysteamine-crosslinked graphene oxide membrane with enhanced hydrogen separation property, Journal of Membrane Science, 595 (2020) 117568.
[19] P.S. Parsamehr, M. Zahed, M.A. Tofighy, T. Mohammadi, M. Rezakazemi, Preparation of novel cross-linked graphene oxide membrane for desalination applications using (EDC and NHS)-activated graphene oxide and PEI, Desalination, 468 (2019) 114079.
[20] J. Xing, Q. Wang, T. He, Z. Zhou, D. Chen, X. Yi, Z. Wang, R. Wang, G. Tan, P. Yu, Polydopamine-assisted immobilization of copper ions onto hemodialysis membranes for antimicrobial, ACS Applied Bio Materials, 1 (2018) 1236-1243.
[21] J. Shen, T. Li, M. Shi, N. Li, M. Ye, Polyelectrolyte-assisted one-step hydrothermal synthesis of Ag-reduced graphene oxide composite and its antibacterial properties, Materials Science and Engineering: C, 32 (2012) 2042-2047.
[22] A.K. Swain, D. Bahadur, Enhanced stability of reduced graphene oxide colloid using cross-linking polymers, The Journal of Physical Chemistry C, 118 (2014) 9450-9457.
[23] G. Moradi, S. Zinadini, L. Rajabi, Development of the tetrathioterephthalate filler incorporated PES nanofiltration membrane with efficient heavy metal ions rejection and superior antifouling properties, Journal of Environmental Chemical Engineering, 8 (2020) 104431.
[24] A. Alkhouzaam, H. Qiblawey, Novel polysulfone ultrafiltration membranes incorporating polydopamine functionalized graphene oxide with enhanced flux and fouling resistance, Journal of Membrane Science, 620 (2021) 118900.
[25] S.-Y. Fang, P. Zhang, J.-L. Gong, L. Tang, G.-M. Zeng, B. Song, W.-C. Cao, J. Li, J. Ye, Construction of highly water-stable metal-organic framework UiO-66 thin-film composite membrane for dyes and antibiotics separation, Chemical Engineering Journal, 385 (2020) 123400.
[26] Z.C. Ng, W.J. Lau, K.C. Wong, M.A. Al-Ghouti, A.F. Ismail, Improving properties of thin film nanocomposite membrane through polyethyleneimine intermediate layer: A parametric study, Separation and Purification Technology, 274 (2021) 119035.
[27] J. Yin, G. Zhu, B. Deng, Graphene oxide (GO) enhanced polyamide (PA) thin-film nanocomposite (TFN) membrane for water purification, Desalination, 379 (2016) 93-101.
[28] N. Zhang, W. Qi, L. Huang, E. Jiang, Z. Li, Y. Luo, X. Zhang, J. Bao, W. Zheng, G. He, A composite membrane of cross-linked GO network semi-interpenetrating in polysulfone substrate for dye removal from water, Journal of Membrane Science, 613 (2020) 118456.
[29] R. Wang, X. Zhao, Y. Lan, L. Liu, C. Gao, In situ metal-polyphenol interfacial assembly tailored superwetting PES/SPES/MPN membranes for oil-in-water emulsion separation, Journal of Membrane Science, 615 (2020) 118566.
[30] C. Hu, Z. Chen, C. Wei, X. Wan, W. Li, Q. Lin, Au Nanoparticles Supported on Iron-Based Oxides for Soot Oxidation: Physicochemical Properties Before and After the Reaction, ACS omega, 6 (2021) 11510-11518.
[31] C. Wang, Z. Li, J. Chen, Y. Yin, H. Wu, Structurally stable graphene oxide-based nanofiltration membranes with bioadhesive polydopamine coating, Applied Surface Science, 427 (2018) 1092-1098.
[32] H. Lin, R. Liu, S. Dangwal, S.-J. Kim, N. Mehra, Y. Li, J. Zhu, Permselective H2/CO2 separation and desalination of hybrid GO/rGO membranes with controlled pre-cross-linking, ACS applied materials & interfaces, 10 (2018) 28166-28175.
[33] Y. Li, S. Yuan, Y. Xia, W. Zhao, C.D. Easton, C. Selomulya, X. Zhang, Mild annealing reduced graphene oxide membrane for nanofiltration, Journal of Membrane Science, 601 (2020) 117900.

[34] S. Li, Y. Wan, S. Guo, J. Luo, Ferric ions mediated defects narrowing of graphene oxide nanofiltration membrane for robust removal of organic micropollutants, Chemical Engineering Journal, 411 (2021) 128587.
[35] M. Peydayesh, T. Mohammadi, S.K. Nikouzad, A positively charged composite loose nanofiltration membrane for water purification from heavy metals, Journal of Membrane Science, 611 (2020) 118205.
[36] Q. Liu, B. Yu, W. Ye, F. Zhou, Highly selective uptake and release of charged molecules by pH-responsive polydopamine microcapsules, Macromolecular bioscience, 11 (2011) 1227-1234.
[37] W.W. Anku, M.A. Mamo, P.P. Govender, Phenolic compounds in water: sources, reactivity, toxicity and treatment methods, Phenolic compounds-natural sources, importance and applications, (2017) 419-443.
[38] L. Pan, Y. Nishimura, H. Takaesu, Y. Matsui, T. Matsushita, N. Shirasaki, Effects of decreasing activated carbon particle diameter from 30 μm to 140 nm on equilibrium adsorption capacity, Water research, 124 (2017) 425-434.
[39] M. Pedrosa, G. Drazic, P.B. Tavares, J.L. Figueiredo, A.M. Silva, Metal-free graphene-based catalytic membrane for degradation of organic contaminants by persulfate activation, Chemical Engineering Journal, 369 (2019) 223-232.
[40] A.J. Sutherland, M.-X. Ruiz-Caldas, C.-F. de Lannoy, Electro-catalytic microfiltration membranes electrochemically degrade azo dyes in solution, Journal of Membrane Science, 611 (2020) 118335.
[41] H.J. Shin, K.K. Kim, A. Benayad, S.M. Yoon, H.K. Park, I.S. Jung, M.H. Jin, H.K. Jeong, J.M. Kim, J.Y. Choi, Efficient reduction of graphite oxide by sodium borohydride and its effect on electrical conductance, Advanced Functional Materials, 19 (2009) 1987-1992.
[42] A.P. Straub, D.S. Bergsman, B.A. Getachew, L.M. Leahy, J.J. Patil, N. Ferralis, J.C. Grossman, Highly Conductive and Permeable Nanocomposite Ultrafiltration Membranes Using Laser-Reduced Graphene Oxide, Nano Letters, 21 (2021) 2429-2435.
[43] Z.-B. Zhang, J.-J. Wu, Y. Su, J. Zhou, Y. Gao, H.-Y. Yu, J.-S. Gu, Layer-by-layer assembly of graphene oxide on polypropylene macroporous membranes via click chemistry to improve antibacterial and antifouling performance, Applied Surface Science, 332 (2015) 300-307.

# Chapter 7

# Contributions and future perspectives

## 7.1 Contributions

This thesis highlighted the scientific importance of addressing water quality problems in freshwater systems associated with industrial and natural chemical micropollutants, particularly when these waters are sourced for potable use. The need to protect drinking water sources is of acute concern considering increased water pollution and the impending impacts of climate change which will exacerbate water quantity and quality through frequent natural disasters such as floods, droughts and wildfires.

Chapter 2 and chapter 3 investigated the environmental chemistry of soils and waters typical of a wetland system (boreal peatland) impacted by wildfires. Through lab-designed low-temperature peat heating (250 – 300 ℃) and contaminant leaching studies, we elucidated the main mechanisms and environmental implications for fire-induced peat soil hydrophobicity, organic matter chemical transformations, and associated peat pollutant leaching. Moisture-induced organic molecular arrangements within peat particles, heat-induced degradation/transformation/volatilization of peat organic molecules, coupled with different fire temperature/duration, collectively impact peat soil hydrophobicity. At low-temperature heating (250 – 300 ℃), moist peats first undergo water vaporization in the first few minutes, and then chemical changes occur to the organic substances. Particularly, changes in hydrophobic fatty acids and polycyclic compounds, and hydrophilic sugars within peats play key roles for post-fire peat soil hydrophobicity, which subsequently decide the types and concentrations of leachable peat-derived pollutants as they leach out through partition/dissolution during large flow events. Lab results suggest that peat-derived pollutant leaching was temperature-dependent, whereas 250 ℃ enhanced the leaching of

carbon-based pollutants and 300 ℃ increased the leaching of nutrients. Phenolic micropollutants were also increasingly observed in leachates from post-heated peat soils, which is a concern for potable water treatment. Results from these studies provide theoretical basis for better managing soil and water pollution from fire and drainage impacted boreal peatlands.

Chapter 4 explored cost-effective peatland remediation strategy via environmental utilization of wildfire-damaged boreal peats to minimize peatland critical pollutants, which not only removed the hydrophobic surface peats that cause flooding and impede forest regrowth, but also produced high surface area bio-sorbents for sustainable water treatment. Effect of synthesis condition (*i.e.*, pyrolysis temperature (400 and 600 ℃) and peat type (*feather moss* and *sphagnum*)) on the product porosity and adsorptive characteristics towards phenolic micropollutants were investigated, and the sorbent-solute interacting mechanisms were sufficiently discussed. A simple, one-step chemical activation approach using $ZnCl_2$ for activation of carbon-based precursors under inert $N_2$ condition at moderately high temperatures (400 or 600 ℃) was developed to make highly porous, high surface area bio-based sorbents. 300 ℃ post-heated peats derived porous carbons exhibited microporous characteristics, whereas pristine peats derived porous carbons exhibited mesoporous characteristics. Peat-based porous carbons exhibited higher surface areas (> 1377 $m^2/g$) than routinely used CACs such as Norit GSX. The high *p*-nitrophenol adsorption capacities (> 527 mg/g) on all the peat-derived porous carbons were attributed to electron donor-acceptor mechanism, π-π interactions, and steric effects. Results provided a viable solution to utilize drought- and fire-damaged boreal peats to make

economic and sustainable sorbents for environmental applications. These efforts to remove the peatland surface hydrophobic, damaged peats potentially also help to promote peatland forestry recovery, and mitigate flooding and wildfire events.

Chapter 5 critically reviewed the state-of-the-art advancements and provided a first organized perspectives in synthesis and application of nanocomposite polymeric membranes for OMP removal, which aimed to inspire relevant researchers to better develop next generation of nano-enabled composite membranes to address emerging pollutants in aquatic environment. First, this review paper gives a comprehensive summary of concentrations of typical OMPs in surface waters and treated wastewaters, these OMPs' physical and chemical properties, and their transport pathways into aquatic environment. Then, previous membrane-assisted processes for OMP removal were briefly discussed in terms of their performance and limitations. Next, this review discussed the ways for fabricating nanocomposite membranes and how they can be applied to treat OMPs in water. Based on the location of the nanofillers, these membranes were categorized these membranes into surface-modified membranes, bulk-modified membranes and thin film nanocomposite membranes. Correlations between OMP properties (*e.g.*, size, charge, polarity and hydrophobicity) and membrane properties (*e.g.*, pore size, pore morphology and nanofiller characteristics) were identified. Performance for OMP removal was linked to different removal mechanisms including size exclusion, charge interaction, adsorption, and catalytic degradation. Current limitations and suggestions for future improvements were also discussed.

Chapter 6 reported a simple, novel approach for making cross-linked rGO surface-located, layer-structured nanocomposite membranes for aqueous micropollutant and azo dye removal in low pressure dead-end filtration. The novelty was shown in several aspects. Firstly, iron nanoparticles were doped in-situ on rGO nanosheets, which increased the available adsorption sites for pollutants. Secondly, HPEI cross-linker was used to bond with rGO nanosheets, where the HPEI's amine groups were linked with rGO's carboxyl groups. This polymer expanded the rGO interlayer spacing and led to more stable rGO nanosheets that do not fall apart in water. Thirdly, HPEI cross-linked rGO nanocomposites carry pH-dependent charges that show charge attraction/repulsion to charged solutes at different pH, suggesting an exciting opportunity to enhance a variety of OMP removal when utilizing these interactions through modulating aqueous pH during filtration. Compared with previously reported graphene-based membranes, the as-prepared membranes exhibited higher hydration stability and higher water fluxes. Removals for PNP ($C_0$ =6.5 mg/L), MO ($C_0$ =20 mg/L) and MB ($C_0$ =20 mg/L) reached 75.8%, 81.6% and 95.7% in the lab-based dead-end filtration system through combined mechanisms of adsorption, size exclusion and electrical charge interaction. Results from this work proposed an enhanced rGO framework for polymeric membrane modification, and provided useful reference for the future development of more robust rGO membranes to suit industrial-scale water treatment demands.

### 7.2 Future perspectives

This thesis recommends that future researchers should investigate the following aspects.

**1.** Environmental chemistry of peat soils and their leachates were characterized in the laboratory setting, which represented a simplified scenario, neglecting variables such as heterogeneity of wildfires, hydrologic connectivity, and surface vegetations. Therefore, it is recommended to perform prescribed field burnings of different intensity and duration scale on peatland regions, and to collect post-fire peat soil and water samples for data validation and correction.

**2.** Porous carbon bio-sorbents developed from fire-damaged boreal peats exhibited high adsorptive capacities for PNP micropollutant. It is worth to investigate the adsorptive behaviors to other recalcitrant OMPs, such as pharmaceutical compounds and pesticides, as well as heavy metal species such as mercury (Hg). Future studies should also consider testing its use in combination with other water treatment units, such as NF or RO process, for further enhancing the OMP treatment efficiencies.

**3.** rGO nanocomposite membranes developed in this study still has room for improvement. For instance, researchers should investigate the regeneration of rGO nanocomposite membranes after saturation with OMPs, and assess long-term the nanoparticle leaching potential throughout adsorption operation. Furthermore, efforts should be made to make rGO membranes more robust, by developing novel chemistries to covalently bond rGO nanosheets with polymeric membrane substrates to improve the membrane stability under cross-flow conditions. Finally, rGO is known to be electrically conductive, but its full potential has not been realized in membrane applications. The conductivity of rGO should be explored to achieve antifouling and redox reactive electrically conductive membranes for water treatment. To this end, synthesis approaches (*e.g.*, chemical and thermal reduction

of GO, and/or heteroatom and conductive polymer doping) should be optimized to provide more conductive rGO nanosheets [1, 2].

## 7.3 References

[1] E.L. Subtil, J. Goncalves, H.G. Lemos, E.C. Venancio, J.C. Mierzwa, J.d.S. de Souza, W. Alves, P. Le-Clech, Preparation and characterization of a new composite conductive polyethersulfone membrane using polyaniline (PANI) and reduced graphene oxide (rGO), Chemical Engineering Journal, 390 (2020) 124612.
[2] R. Wang, Y. Wang, C. Xu, J. Sun, L. Gao, Facile one-step hydrazine-assisted solvothermal synthesis of nitrogen-doped reduced graphene oxide: reduction effect and mechanisms, RSC advances, 3 (2013) 1194-1200.

# Appendix A. Supplementary Material

## Chapter 2 Supplementary Information

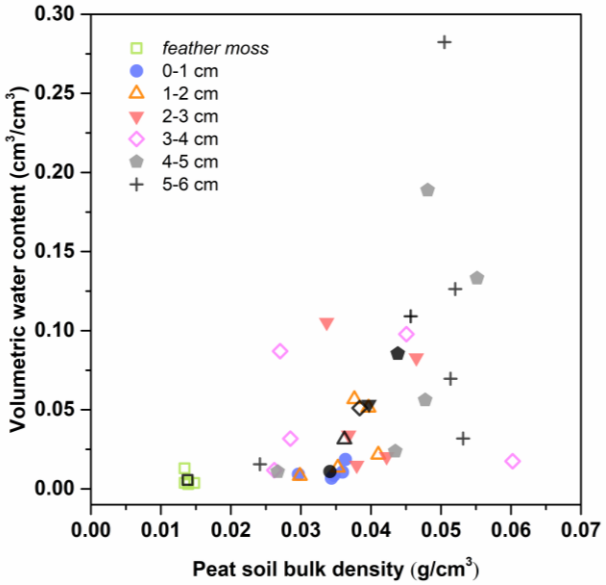


**Fig. S1.** Distribution of moss and peat soil field volumetric water content and bulk density from the study site. Data points represent various raw peat soil samples that were not modified in any way. The black dots demonstrate the depth averaged data.

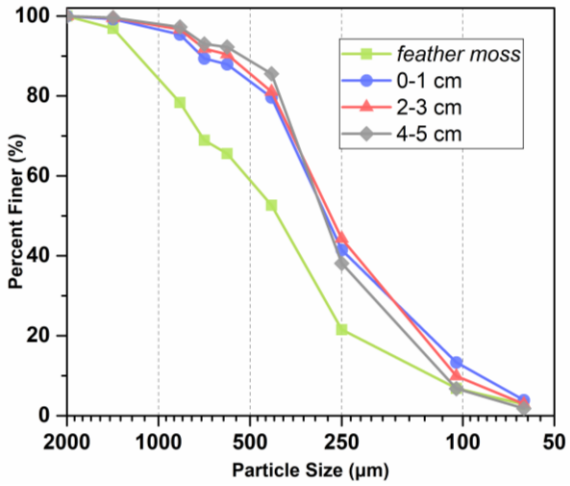


**Fig. S2.** The percentage of particles that are finer than a sieve of the corresponding size at various depths, indicating the cumulative size distribution of particles.

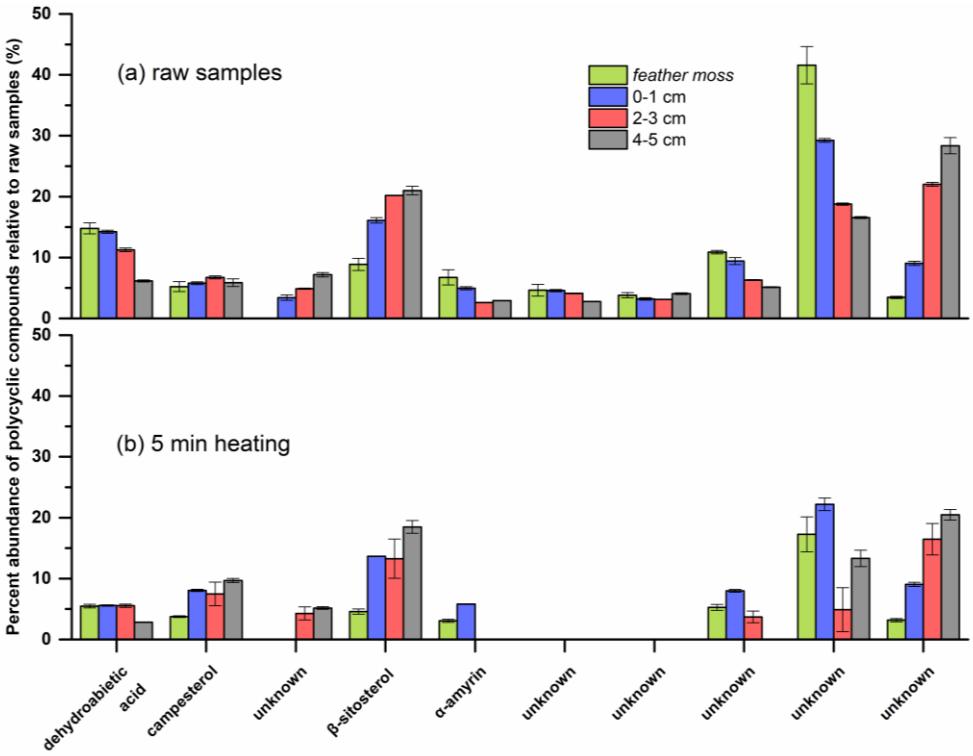


**Fig. S3.** Changes in percent abundance of polycyclic compounds relative to raw samples under 300 °C laboratory heating for peat soils from different depth (Graph for 20 min heating was not shown because no compounds were detected). All runs were measured in triplicates.

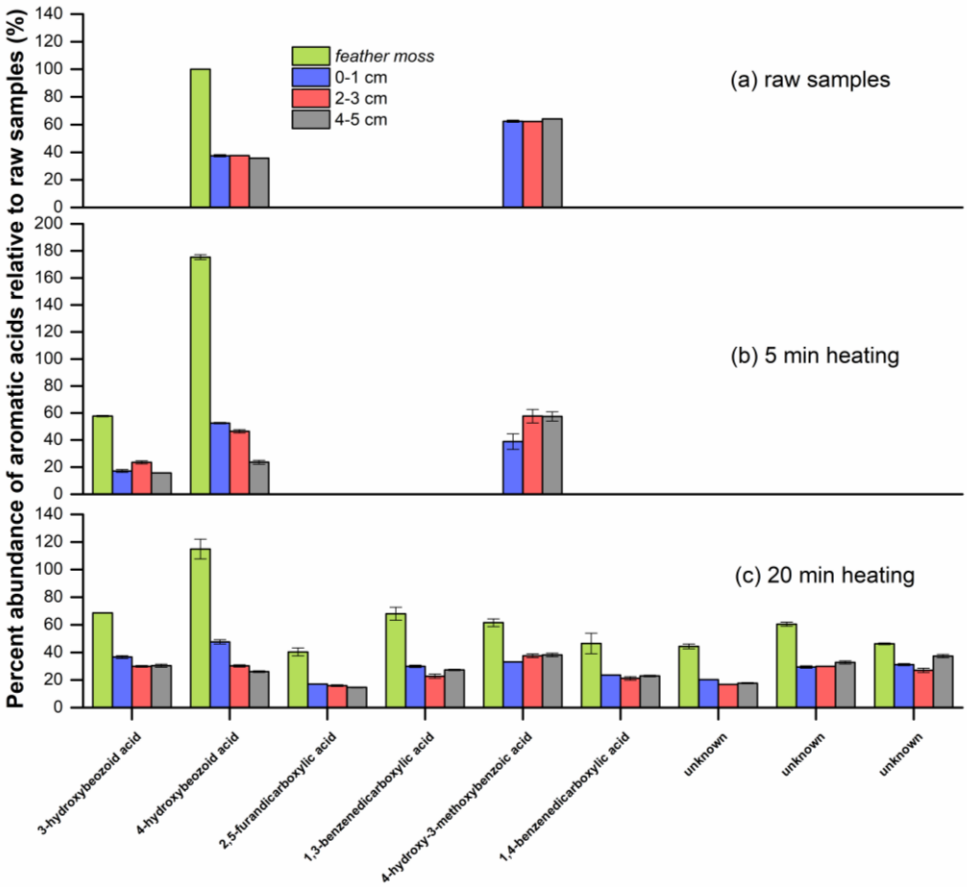


**Fig. S4.** Changes in percent abundance of aromatic acids relative to raw samples under 300 °C laboratory heating for peat soils from different depth. All runs were measured in triplicates.

**Table S1** Main characteristics of the sampling points from the study site.

| Soil No. | Vegetation | Treatment | Microtopography |
|---|---|---|---|
| 1 | *feather moss* | hand-thinned | hummock |
| 2 | *feather moss* | hand-thinned | on side of hummock |
| 3 | *feather moss* | hand-thinned | lawn |
| 4 | *feather moss* | control | hummock |
| 5 | *feather moss* | control | lawn |

## Chapter 3 Supplementary Information

### Analytical methodologies

Chemical oxygen demand (COD), total organic nitrogen (TN), nitrate (shown as $NO_3^-$-N), ammonia ($NH_3$-N), total phosphorus (TP, measured as orthophosphate, $PO_4^{3-}$), reactive phosphorus (RP, measured as $PO_4^{3-}$), and phenols were analyzed using standard Hach testing kits based on Hach methods. COD (USEPA reactor digestion method, Hach method 8000) was measured through heating samples for 2 hrs with a strong oxidizing agent potassium dichromate, in which the oxidizable organic compounds reacted and reduced the dichromate ion to green chromic ion. TN (Persulfate digestion method, Hach Method 10208) was analyzed through oxidizing inorganically and organically bonded nitrogen to nitrate by peroxodisulphate digestion, where the formed nitrates reacted with 2.6-dimethylphenol in sulphuric and phosphoric acid solution to form a nitrophenol. Nitrate (shown as $NO_3^-$-N) (Chromotropic acid method, Hach method 10020) was measured through reacting sample nitrates with chromotropic acid under strongly acidic conditions to yield a yellow product with a maximum absorbance at 410 nm. Ammonia ($NH_3$-N) (Salicylate method, Hach method 10205) was analyzed through reacting sample ammonium ions with hypochlorite ions and salicylate ions at pH 12.6 using sodium nitroprusside catalyst to form indophenol. The amount of color formed was proportional to the ammonia nitrogen present in the sample, and the measurement was performed at 690 nm. TP (measured as orthophosphate, $PO_4^{3-}$) (USEPA PhosVer 3 with acid persulfate digestion method) was measured in several steps. First, condensed inorganic phosphates (meta-, pyro- or other polyphosphates) and organic phosphates were converted to reactive

orthophosphates by heating with acid and persulfate. Then, the formed reactive orthophosphates were reacted with molybdate in acidic condition to produce a mixed phosphate/molybdate complex. Next, ascorbic acid reduced the complex and gave an intense molybdenum blue color, with an absorbance at 880 nm. RP (measured as $PO_4^{3-}$) (USEPA PhosVer 3 (Ascorbic acid) method, Hach method 8048) was measured using the same approach as described for TP, but without the hydrolysis pretreatment step. Phenols (USEPA 4-aminoantipyrine method, Hach method 10266) was measured by reacting ortho- and meta-substituted phenolic materials with 4-aminoantipyrine in the presence of an oxidizing agent to form colored complexes. The measurement wavelength was 510 nm.

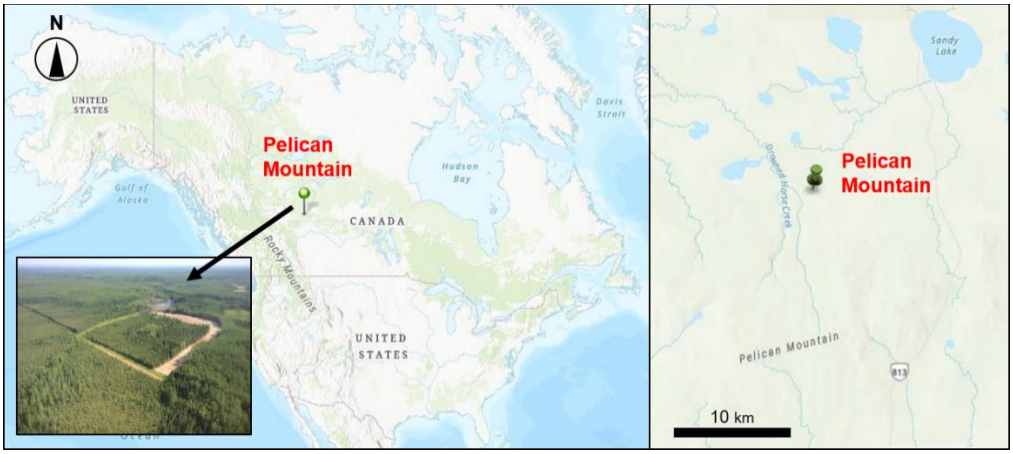


**Fig. S1.** Location of the Pelican Mountain FireSmart Fuel Management Research Site, where the peat cores were collected from.

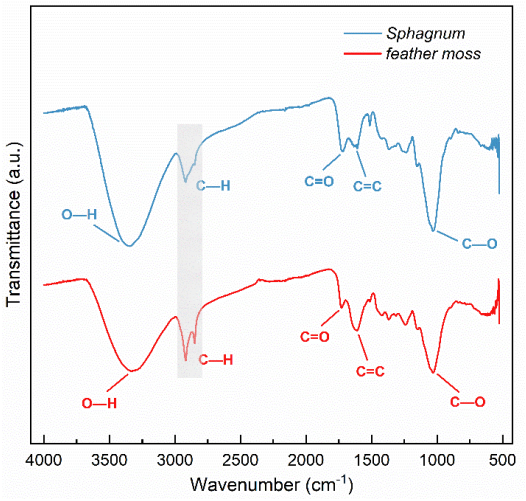


**Fig. S2.** FTIR spectra of *Sphagnum* and *feather moss* peats.

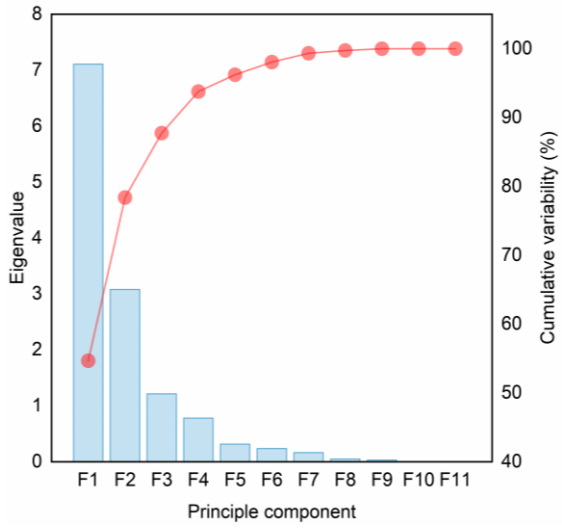


**Fig. S3.** Principal component analysis (PCA) eigenvalue and cumulative variability of peat leachate water chemistry parameters.

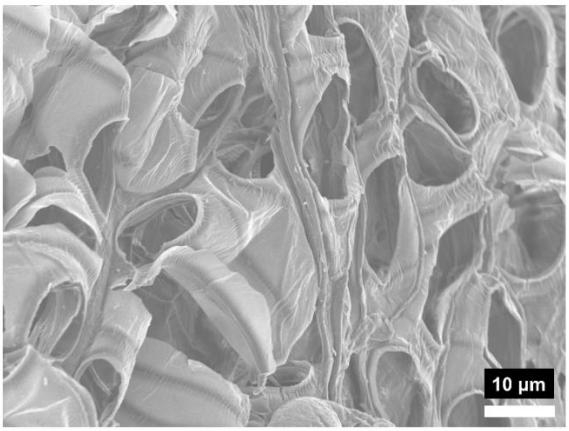


**Fig. S4.** SEM image of *Sphagnum* peat.

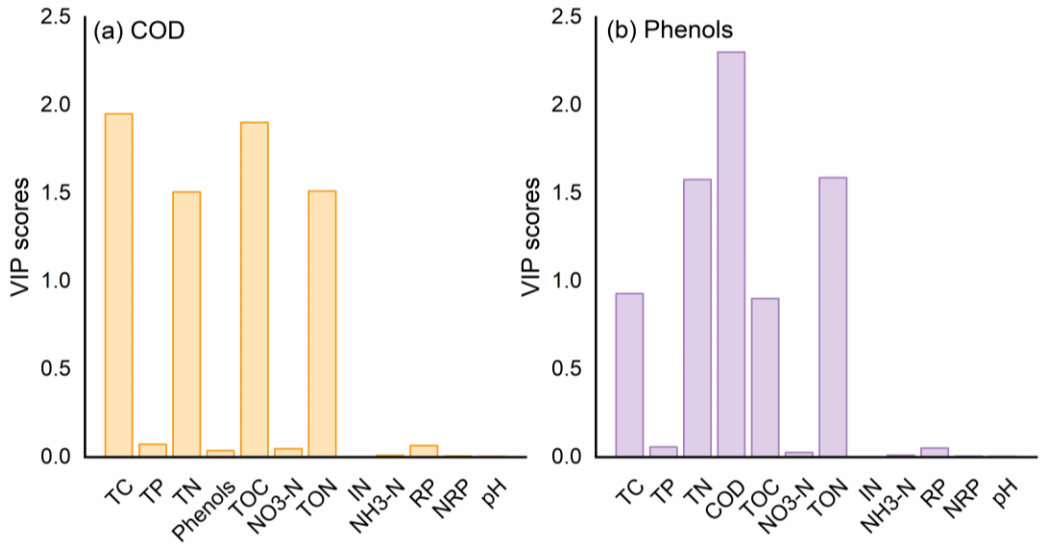


**Fig. S5.** PLS variable importance in the projection (VIP) scores of various predictors for (a) COD; and (b) Phenols prediction.

**Table S1** Elemental compositions (%) of pristine *Sphagnum* and *feather moss* peats.

| Peat moss | Elemental composition [a] (%) | | | | |
|---|---|---|---|---|---|
| | C | H | O [b] | N | S |
| ***sphagnum*** | 48.99 | 5.88 | 44.18 | 0.79 | 0.16 |
| ***feather moss*** | 47.93 | 5.84 | 45.12 | 0.92 | 0.19 |

a. Elemental contents reflect the mean value of triplicate samples.
b. Oxygen content was determined by the weight difference of mean values, normalized by the 5 elements analyzed.

**Table S2** Summary of statistical factors from ANOVA Duncan analyses.

| Parameter | Source | Standardized difference | Critical value | Pr > Diff | alpha (Modified) | Significant | F | Pr > F |
|---|---|---|---|---|---|---|---|---|
| COD | Model | | | | | | 5.894 | **0.016** |
| | B250 vs R | 3.283 | 2.281 | 0.017 | 0.098 | Yes | | |
| | B250 vs B300 | 2.512 | 2.179 | 0.027 | 0.050 | Yes | | |
| | B300 vs R | 0.771 | 2.179 | 0.456 | 0.050 | No | | |
| TC | Model | | | | | | 5.673 | **0.018** |
| | B250 vs R | 3.276 | 2.281 | **0.017** | 0.098 | Yes | | |
| | B250 vs B300 | 2.316 | 2.179 | **0.039** | 0.050 | Yes | | |
| | B300 vs R | 0.960 | 2.179 | 0.356 | 0.050 | No | | |
| TN | Model | | | | | | 16.522 | **0.000** |
| | B250 vs R | 2.650 | 2.179 | **0.021** | 0.050 | Yes | | |
| | B250 vs B300 | 3.093 | 2.179 | **0.009** | 0.050 | Yes | | |
| | B300 vs R | 5.743 | 2.281 | **0.000** | 0.098 | Yes | | |
| TP | Model | | | | | | 12.476 | **0.001** |
| | B250 vs R | 1.673 | 2.179 | 0.120 | 0.050 | No | | |
| | B250 vs B300 | 3.240 | 2.179 | **0.007** | 0.050 | Yes | | |
| | B300 vs R | 4.913 | 2.281 | **0.001** | 0.098 | Yes | | |
| Phenols | Model | | | | | | 19.971 | **0.000** |
| | B250 vs R | 5.465 | 2.179 | **0.000** | 0.050 | Yes | | |
| | B250 vs B300 | 0.016 | 2.179 | 0.988 | 0.050 | No | | |
| | B300 vs R | 5.481 | 2.281 | **0.000** | 0.098 | Yes | | |

**Table S3** Surface water and wastewater discharge guidelines for certain pollutants from USA, EU and Canada.

| Substance | United States (mg/L) | European Union [e] (mg/L) | Canada [f] (mg/L) | | |
|---|---|---|---|---|---|
| | | | Ottawa | Toronto | Hamilton |
| COD | 5 - 90 [a] | 125 | | | |
| Total Phosphorus | 0.025 - 0.05 [b] | 2 (10000 - 100000 p.e.), 1 (> 100000 p.e.) | 10 (0.4) | 10 (0.4) | 10 |
| Total Nitrogen | 2 - 10 [c] | 15 (10000 - 100000 p.e.), 10 (> 100000 p.e.) | | | |
| Total Kjeldahl Nitrogen | | | 100 | 100 | 100 |

| | | | | |
|---|---|---|---|---|
| Phenols | 0.005 [d] | 1 (0.008) | 1 (0.008) | 1 (0.02) |

a. site-specific values of water quality objectives for inland surface streams, Santa Ana, California.
b. site-specific values of water quality objectives for inland surface waters, San Diego, California.
c. site-specific values of water quality objectives for inland surface waters, Los Angeles, California.
d. ambient water quality standard guidance value for phenols, total unchlorinated, New York.
e. EU limits for urban waste water treatment plants discharge to sensitive areas.
f. Canadian local by-law limits for sanitary and combined sewers discharge, and limits for storm sewer discharge (shown in brackets).

**Table S4** Surface water and wastewater discharge guidelines for certain pollutants from USA, EU and Canada.

| Variables | TC | TP | TN | COD | Phenol | TOC | IC | TON | IN | $NH_3$-N | RP | NRP | pH |
|---|---|---|---|---|---|---|---|---|---|---|---|---|---|
| TC | **1** | 0.134 | 0.265 | **0.996** | **0.774** | **0.999** | **0.670** | 0.266 | **0.559** | -0.497 | 0.128 | 0.104 | **0.610** |
| TP | 0.134 | **1** | **0.882** | 0.089 | **0.563** | 0.120 | 0.391 | **0.882** | 0.118 | **-0.585** | **0.994** | 0.419 | **0.679** |
| TN | 0.265 | **0.882** | **1** | 0.226 | **0.676** | 0.254 | 0.413 | **1.000** | 0.127 | **-0.683** | **0.862** | 0.502 | **0.700** |
| COD | **0.996** | 0.089 | 0.226 | **1** | **0.746** | **0.998** | **0.625** | 0.227 | **0.556** | -0.477 | 0.082 | 0.092 | **0.566** |
| Phenol | **0.774** | **0.563** | **0.676** | **0.746** | **1** | **0.766** | **0.660** | **0.678** | 0.339 | **-0.846** | **0.547** | 0.345 | **0.840** |
| TOC | **0.999** | 0.120 | 0.254 | **0.998** | **0.766** | **1** | **0.643** | 0.255 | **0.562** | -0.499 | 0.111 | 0.116 | **0.592** |
| IC | **0.670** | 0.391 | 0.413 | **0.625** | **0.660** | **0.643** | **1** | 0.413 | 0.317 | -0.269 | 0.428 | -0.175 | **0.777** |
| TON | 0.266 | **0.882** | **1.000** | 0.227 | **0.678** | 0.255 | 0.413 | **1** | 0.127 | **-0.685** | **0.862** | 0.503 | **0.700** |
| IN | **0.559** | 0.118 | 0.127 | **0.556** | 0.339 | **0.562** | 0.317 | 0.127 | **1** | -0.135 | 0.109 | 0.126 | 0.234 |
| $NH_3$-N | -0.497 | **-0.585** | **-0.683** | -0.477 | **-0.846** | -0.499 | -0.269 | **-0.685** | -0.135 | **1** | **-0.540** | **-0.612** | **-0.679** |
| RP | 0.128 | **0.994** | **0.862** | 0.082 | **0.547** | 0.111 | 0.428 | **0.862** | 0.109 | **-0.540** | **1** | 0.322 | **0.669** |
| NRP | 0.104 | 0.419 | 0.502 | 0.092 | 0.345 | 0.116 | -0.175 | 0.503 | 0.126 | **-0.612** | 0.322 | **1** | 0.340 |
| pH | **0.610** | **0.679** | **0.700** | **0.566** | **0.840** | **0.592** | **0.777** | **0.700** | 0.234 | **-0.679** | **0.669** | 0.340 | **1** |

Note: Values in bold indicate correlated parameters that are different from 0 with a significance level alpha=0.05.

**Table S5** Average COD and TOC concentrations in the pre- and post-heat peat leachates (n=5 per treatment) contributed by dissolvable substances and leached particulates (< 1.6 μm) and leachate pH ranges.

| | **COD (mg/L)** | | **TOC (mg/L)** | | **pH** |
|---|---|---|---|---|---|
| | Dissolvable | Particulate | Dissolvable | Particulate | |
| **R** | 49.7 | 78.2 | 19.0 | 23.4 | 5.41 - 6.33 |
| **B250** | 261.8 | 135.3 | 93.2 | 54.0 | 6.25 - 7.10 |
| **B300** | 81.0 | 110.1 | 30.7 | 40.4 | 6.35 - 7.13 |

Note: Vacuum filtration of leachates through 1.6 μm glass microfiber membrane yielded permeates containing both dissolvable compounds and particulates. Permeates from subsequent vacuum-filtering of the collected leachates by 0.45 μm PES membranes could be assumed to contain only dissolvable compounds.

## Chapter 4 Supplementary Information

The sorbed amount of *p*-nitrophenol onto the ACs can be calculated based on the following equation.

$$q_t = \frac{V(C_0 - C_t)}{m} \quad (1)$$

Where $q_t$ is the sorbed amount per mass sorbent at time $t$ ($mg/g$); $C_0$ and $C_t$ represent the aqueous concentration at initial and a certain time $t$, respectively; $V$ is the volume of the solution ($L$); m is the weight of the sorbent ($g$). At time t when where the adsorption equilibrium reaches, $C_t$ becomes the equilibrium concentration $C_e$ and $q_t$ becomes the equilibrium adsorption capacity $q_e$ ($mg/g$).

### Freundlich isotherm

Freundlich isotherm is applicable for multi-layer adsorption, and empirically assumes that the heterogeneous adsorptive energies are independent of surface coverage, and can be written as,

$$q_e = k_F C_e^{1/n} \quad (2)$$

Where $k_F$ ($(mg/g)\cdot(L/mg)^{1/n}$) is the Freundlich constant characterizing adsorption capacity; $1/n$ is an empirical constant describing the adsorption intensity, and a value of higher $1/n$ reflects higher adsorption intensity, i.e. the higher the adsorption capacity for the sorbent; $q_e$ ($mg/g$) is the equilibrium adsorption capacity; $C_e$ ($mg/L$) is the equilibrium *p*-nitrophenol concentration.

**Langmuir isotherm**

Langmuir isotherm, on the other hand, is based on monolayer adsorption on homogeneous surfaces with identical sites, which can be written as,

$$q_e = \frac{q_m k_L C_e}{1 + k_L C_e} \tag{3}$$

Where $k_L$ (L/$mg$) is the Langmuir constant related to free energy of adsorption; $C_e$ ($mg / L$) is the equilibrium *p*-nitrophenol concentration; $q_e$ ($mg / g$) and $q_m$ ($mg / g$) are the equilibrium adsorption capacity and maximum adsorption capacity, respectively.

The essential characteristics of this model can be characterized by a dimensionless constant, $R_L$, known as the separation factor, where $R_L = \frac{1}{1 + k_L C_0}$. The adsorption is considered to be irreversible ($R_L = 0$), favorable ($0 < R_L < 1$), linear ($R_L = 1$), or unfavorable ($R_L > 1$). Where $k_L$ ($mg / g$) is the Langmuir constant; $C_0$ ($mg / L$) is the highest initial solute concentration of the study.

**Redlich-Peterson isotherm**

Redlich-Peterson isotherm is an empirical model compromised between the Freundlich and Langmuir models incorporating three parameters, and is defined as the following equation.

$$q_e = \frac{k_{RP} C_e}{1 + \alpha_R C_e^{\beta}} \tag{4}$$

Where $k_{RP}$ (L/g) is the Redlich-Peterson constant; $C_e$ ($mg / L$) and $q_e$ ($mg / g$) are the equilibrium *p*-nitrophenol concentration and the equilibrium adsorption capacity

respectively; $\alpha_R$ and $\beta$ are constants. The model becomes Langmuir type if $\beta = 1$, whereas becomes Freundlich type if $\alpha_R C_e^{\beta} \gg 1$. The value of $k_{RP} / \alpha_R$ reflects the adsorption capacity.

**Pseudo-first-order reaction**

$$\ln(q_e - q_t) = \ln q_e - k_1 t \quad (5)$$

Where $q_e$ ($mg / g$) and $q_t$ ($mg / g$) are the adsorption capacity at equilibrium and at time $t$ (min); $k_1$ ($\min^{-1}$) is the pseudo-first-order rate constant.

**Pseudo-second-order reaction**

$$\frac{\mathrm{t}}{q_t} = \frac{1}{k_2 q_e^2} + \frac{t}{q_e} \quad (6)$$

Where $q_e$ ($mg / g$) and $q_t$ ($mg / g$) are the adsorption capacity at equilibrium and at time $t$ (min); $k_2$ ($g \cdot mg^{-1} \cdot \min^{-1}$) is the pseudo-second-order rate constant. Pseudo-first-order model implies that *p*-nitrophenol concentration decides the adsorption kinetics. Pseudo-second-order model indicates that *p*-nitrophenol adsorption is controlled by both sorbate concentration and availability of adsorptive sites.

**Intra-particle diffusion model**

$$\mathrm{q}_t = k_d t^{1/2} + C \quad (7)$$

Where $q_t$ ($mg/g$) is the adsorption capacity at time $t$ (min); $k_d$ ($mg/g \cdot \min^{0.5}$) is the intra-particle diffusion rate constant; C is a constant. Intra-particle diffusion model describes the mass transfer and diffusion process as rate limiting steps.

**Table S1** Yield and elemental compositions (wt %) of feedstocks and the sorbents. Fm (*Feather moss*), Sph (*Sphagnum*), CS (corn starch), CL (cellulose), B- prefix indicates burned samples, ZC postscript indicated activation with zinc chloride, -300 is the temperature at which the samples were burned, -400, -600 indicates the temperature at which the samples were activated.

| | Material | Yield[a] (%) | $pH_{ZPC}$ | Elemental composition[b] | | | | | | |
|---|---|---|---|---|---|---|---|---|---|---|
| | | | | C(%) | H(%) | O[c](%) | N(%) | S(%) | H/C (moles) | O/C (moles) |
| Feedstocks | Fm | — | — | 47.93 | 5.84 | 45.13 | 0.92 | 0.19 | 1.46 | 0.71 |
| | Sph | — | — | 48.99 | 5.88 | 44.19 | 0.79 | 0.16 | 1.44 | 0.68 |
| | CS | — | — | 41.39 | 6.50 | 51.89 | 0.14 | 0.08 | 1.88 | 0.94 |
| | CL | — | — | 42.77 | 6.28 | 50.84 | 0.03 | 0.08 | 1.76 | 0.89 |
| | BFm-300 | 51.8 | — | 60.04 | 3.09 | 35.18 | 1.52 | 0.18 | 0.62 | 0.44 |
| | BSph-300 | 41.6 | — | 60.47 | 2.76 | 35.37 | 1.24 | 0.17 | 0.55 | 0.44 |
| | BCS-220 | 47.7 | — | 61.25 | 3.40 | 35.10 | 0.18 | 0.08 | 0.67 | 0.43 |
| Activated carbon | FmZC-400 | 36.4 | 3.47 | 83.44 | 2.44 | 12.96 | 1.01 | 0.14 | 0.35 | 0.12 |
| | SphZC-400 | 32.1 | 3.33 | 83.24 | 2.40 | 13.30 | 0.91 | 0.14 | 0.35 | 0.12 |
| | CLZC-400 | 28.1 | 3.37 | 88.57 | 2.39 | 8.84 | 0.14 | 0.06 | 0.32 | 0.07 |
| | BFmZC-400 | 57.2 | 3.39 | 77.69 | 2.81 | 17.52 | 1.69 | 0.29 | 0.43 | 0.17 |
| | BSphZC-400 | 61.3 | 3.11 | 76.62 | 2.47 | 19.22 | 1.53 | 0.15 | 0.39 | 0.19 |
| | BCSZC-400 | 47.8 | 3.11 | 85.48 | 2.43 | 11.81 | 0.21 | 0.07 | 0.34 | 0.10 |
| | FmZC-600 | 31.2 | 3.76 | 90.04 | 1.39 | 7.26 | 1.12 | 0.19 | 0.19 | 0.06 |
| | SphZC-600 | 25.5 | 3.58 | 90.22 | 1.37 | 7.14 | 1.11 | 0.17 | 0.18 | 0.06 |
| | CLZC-600 | 27.2 | 3.49 | 93.58 | 1.24 | 4.97 | 0.14 | 0.08 | 0.16 | 0.04 |
| | BFmZC-600 | 46.8 | 3.68 | 90.22 | 1.44 | 6.61 | 1.52 | 0.22 | 0.19 | 0.05 |
| | BSphZC-600 | 38.1 | 3.71 | 89.33 | 1.39 | 7.41 | 1.69 | 0.17 | 0.19 | 0.06 |
| | BCSZC-600 | 47.3 | 3.18 | 92.28 | 1.33 | 6.10 | 0.22 | 0.07 | 0.17 | 0.05 |
| | Norit GSX | — | 4.10 | 87.49 | 0.47 | 11.43 | 0.39 | 0.22 | 0.06 | 0.10 |

a. Yield is defined as the weight of products after activation, acid washing, and drying (excluding losses during transfer and filtration), per weight of raw materials used. Yield is the average of at least 3 subsamples.
b. Elemental content was calculated on the basis of triplicate sample analysis.
c. Oxygen content was determined by the weight difference of mean values, normalized by the 5 elements analyzed.

**Table S2** FTIR assignments of the boreal peats feedstocks and the obtained porous carbons.

| Wavenumber ($cm^{-1}$) | Assignment | Reference |
|---|---|---|
| 3392, 3369, 3343, 3335 | O-H stretching of hydroxyl groups in carbohydrates, such as cellulosic structures | [1] |
| 2918 | asymmetric C-H stretching of $CH_2$ in aliphatic hydrocarbons from plant wax or lipids | [2] |
| 2851, 2850 | symmetric C-H stretching of $CH_2$ in aliphatic hydrocarbons from plant wax or lipids | [2] |
| 1731, 1716, 1711, 1699, 1695, 1694 | C=O stretching of carbonyl groups in ketones, aldehydes, lactones, organic acids and aromatic esters | [1-3] |
| 1610, 1609, 1601, 1597, 1590, 1586, 1574, 1558, 1557 | C=C aromatic rings vibrations in conjunction with C=O stretching from aromatics such as lignins and quinones | [1, 4] |
| 1514 | aromatic C=C stretching from lignin backbones | [3] |
| 1421, 1368, 1367 | C-H and O-H deformation of lignins and aliphatic structures, indicative of structural carbohydrates | [2] |
| 1251, 1247,1243, 1239, 1228, 1216, 1169 | C-O stretching of phenolic OH groups and indicative of lignin structures and cellulosic materials | [4] |
| 1151, 1150 | C-O-C asymmetric stretching in cellulose and hemi-cellulose | [4] |
| 1031 | C-O stretching of polysaccharides | [2] |

**Table S3** Langumir, Freundlich and Redlich-Peterson isotherm parameters for *p*-nitrophenol adsorption on different sorbents at 20 ºC.

| | Langmuir | | | | Freundlich | | | Redlich-Peterson | | | |
|---|---|---|---|---|---|---|---|---|---|---|---|
| Material | $k_L$ (L/mg) | $q_m$ (mg/g) | $R_L$ | $R^2$ | $k_F$ (mg/g)·(L/mg)$^{1/n}$ | n | $R^2$ | $k_{RP}$ (L/g) | $\alpha_R$ (L/mg)$^{1/\beta}$) | β | $R^2$ |
| FmZC-400 | 0.0125 | 573.09 | 0.0356 | 0.9484 | 65.52 | 3.32 | 0.9808 | 25.97 | 0.22 | 0.78 | 0.9957 |
| FmZC-600 | 0.0460 | 527.31 | 0.0100 | 0.9159 | 132.30 | 4.94 | 0.9886 | 2349.55 | 16.78 | 0.81 | 0.9912 |
| BFmZC-400 | 0.0120 | 537.47 | 0.0401 | 0.8909 | 58.09 | 3.21 | 0.9826 | 98.44 | 1.45 | 0.71 | 0.9845 |
| BFmZC-600 | 0.0231 | 663.79 | 0.0212 | 0.6723 | 124.65 | 4.13 | 0.9569 | 3.25E+10 | 2.61E+08 | 0.76 | 0.9569 |
| SphZC-400 | 0.0087 | 624.75 | 0.0514 | 0.9570 | 68.93 | 3.35 | 0.9784 | 26.79 | 0.24 | 0.77 | 0.9846 |
| SphZC-600 | 0.0616 | 534.95 | 0.0080 | 0.9082 | 167.93 | 5.86 | 0.9800 | 1508.04 | 8.31 | 0.84 | 0.9823 |
| BSphZC-400 | 0.0148 | 608.73 | 0.0327 | 0.8262 | 65.89 | 3.15 | 0.9563 | 2.85E+09 | 4.32E+07 | 0.68 | 0.9563 |
| BSphZC-600 | 0.0105 | 858.71 | 0.0453 | 0.6854 | 100.37 | 3.32 | 0.9393 | 1.99E+09 | 1.98E+07 | 0.70 | 0.9393 |
| BCSZC-400 | 0.0211 | 630.73 | 0.0231 | 0.8847 | 98.48 | 3.74 | 0.9854 | 173.75 | 1.42 | 0.76 | 0.9904 |
| BCSZC-600 | 0.0680 | 612.84 | 0.0068 | 0.8503 | 173.69 | 5.25 | 0.9960 | 17669.49 | 98.56 | 0.81 | 0.9971 |
| CLZC-400 | 0.0344 | 623.68 | 0.0143 | 0.9474 | 120.20 | 4.15 | 0.9670 | 61.33 | 0.29 | 0.84 | 0.9926 |
| CLZC-600 | 0.0641 | 612.38 | 0.0077 | 0.9091 | 167.10 | 5.12 | 0.9830 | 288.82 | 1.41 | 0.83 | 0.9898 |
| Norit GSX | 0.0062 | 571.41 | 0.0741 | 0.7567 | 60.11 | 3.32 | 0.9669 | 1.70E+10 | 2.83E+08 | 0.70 | 0.9669 |

**Table S4** Parameters of kinetic models for *p*-nitrophenol adsorption onto selected sorbents at 20 °C.

| Material | $q_{exp}$ (mg/g) | Pseudo-first-order model | | | Pseudo-second-order model | | | | Intra-particle diffusion model | |
|---|---|---|---|---|---|---|---|---|---|---|
| | | $k_1$ ($min^{-1}$) | $q_e$ (mg/g) | $R^2$ | $k_2$ (g $mg^{-1}min^{-1}$) | $q_e$ (mg/g) | $k_2q_e$ ($min^{-1}$) | $R^2$ | $k_d$ (mg/g·$min^{0.5}$) | $R^2$ |
| FmZC-400 | 51.08 | 0.0118 | 24.50 | 0.7393 | 0.0037 | 49.26 | 0.183 | 0.9994 | 2.90 | 0.7355 |
| FmZC-600 | 53.26 | 0.0166 | 20.78 | 0.6991 | 0.0045 | 53.19 | 0.237 | 0.9993 | 3.00 | 0.7181 |
| BFmZC-400 | 48.82 | 0.0179 | 18.32 | 0.8129 | 0.0058 | 49.02 | 0.282 | 0.9998 | 2.58 | 0.6656 |
| BFmZC-600 | 53.05 | 0.0303 | 12.88 | 0.7203 | 0.0074 | 53.76 | 0.397 | 0.9998 | 2.99 | 0.5950 |
| BCSZC-400 | 52.49 | 0.0213 | 32.71 | 0.9095 | 0.0018 | 54.64 | 0.098 | 0.9988 | 3.61 | 0.8431 |
| BCSZC-600 | 54.06 | 0.0143 | 30.59 | 0.7799 | 0.0019 | 54.35 | 0.103 | 0.9978 | 3.60 | 0.8162 |
| Norit GSX | 57.59 | 0.7973 | 9.46 | 0.8718 | 0.5986 | 57.80 | 34.6 | 0.9999 | 15.68 | 0.5481 |

a Experimental equilibrium uptake of *p*-nitrophenol, obtained after 24 hrs.

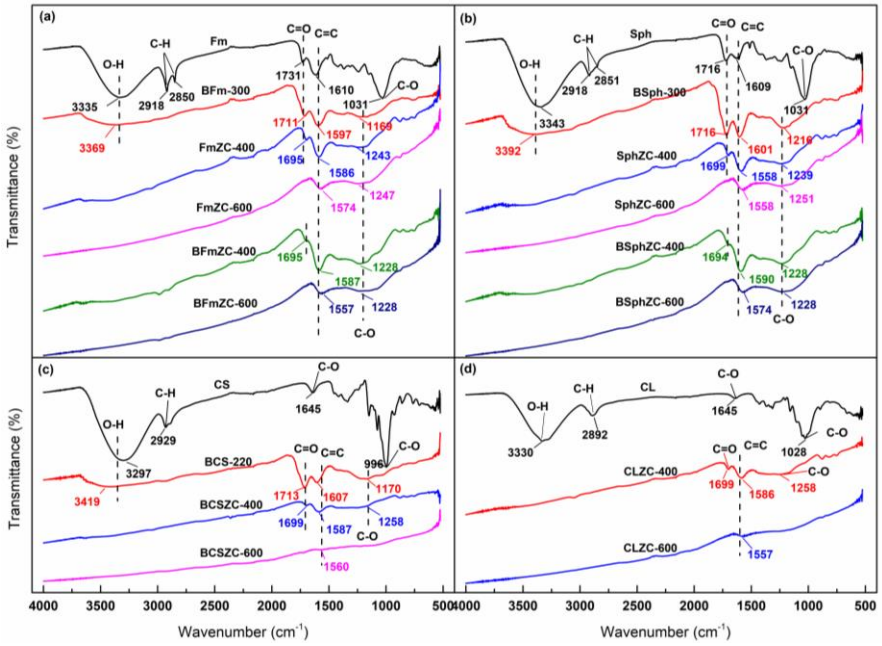


**Fig. S1.** FTIR spectra of (a) *feather moss* and its derived porous carbons, (b) *sphagnum* and its derived porous carbons, (c) corn starch and its derived porous carbons, (d) cellulose and its derived porous carbon.

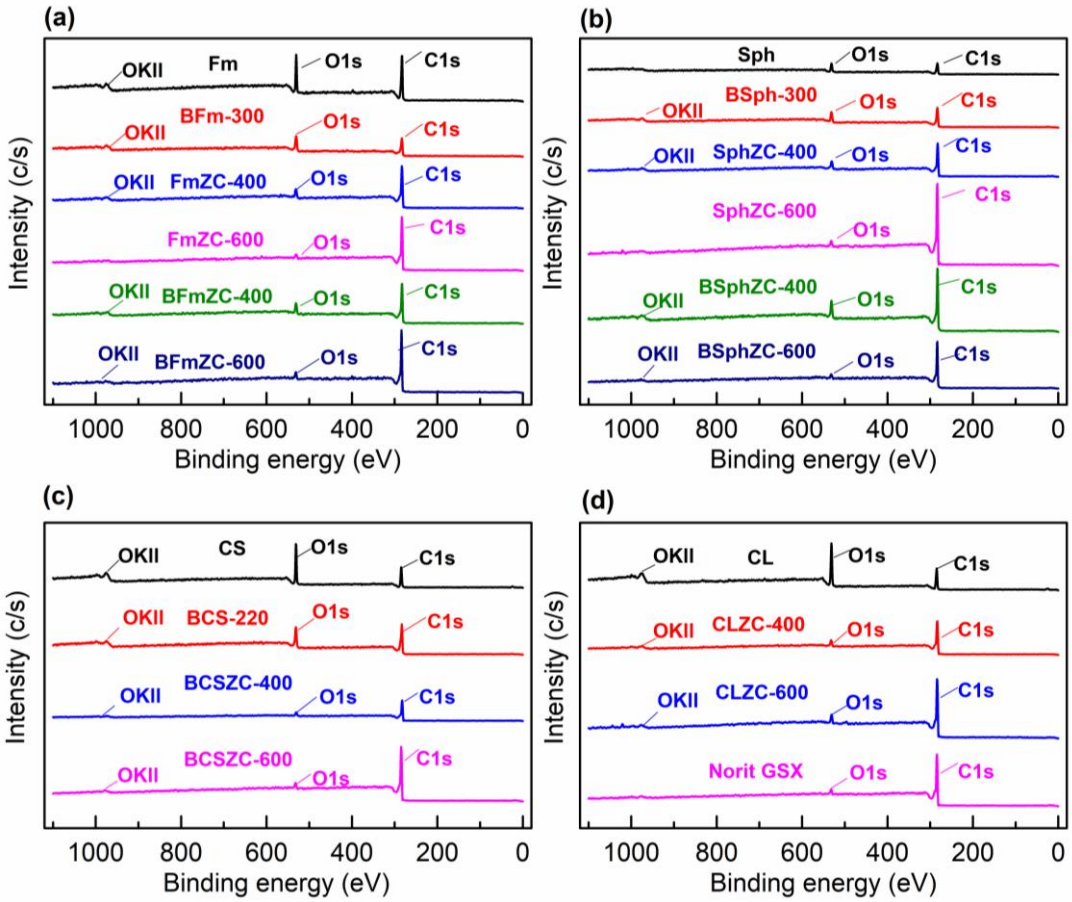


**Fig. S2.** XPS full scan of (a) *feather moss* and its derived porous carbons, (b) *sphagnum* and its derived porous carbons, (c) corn starch and its derived porous carbons, (d) cellulose and its derived porous carbons, and Norit GSX.

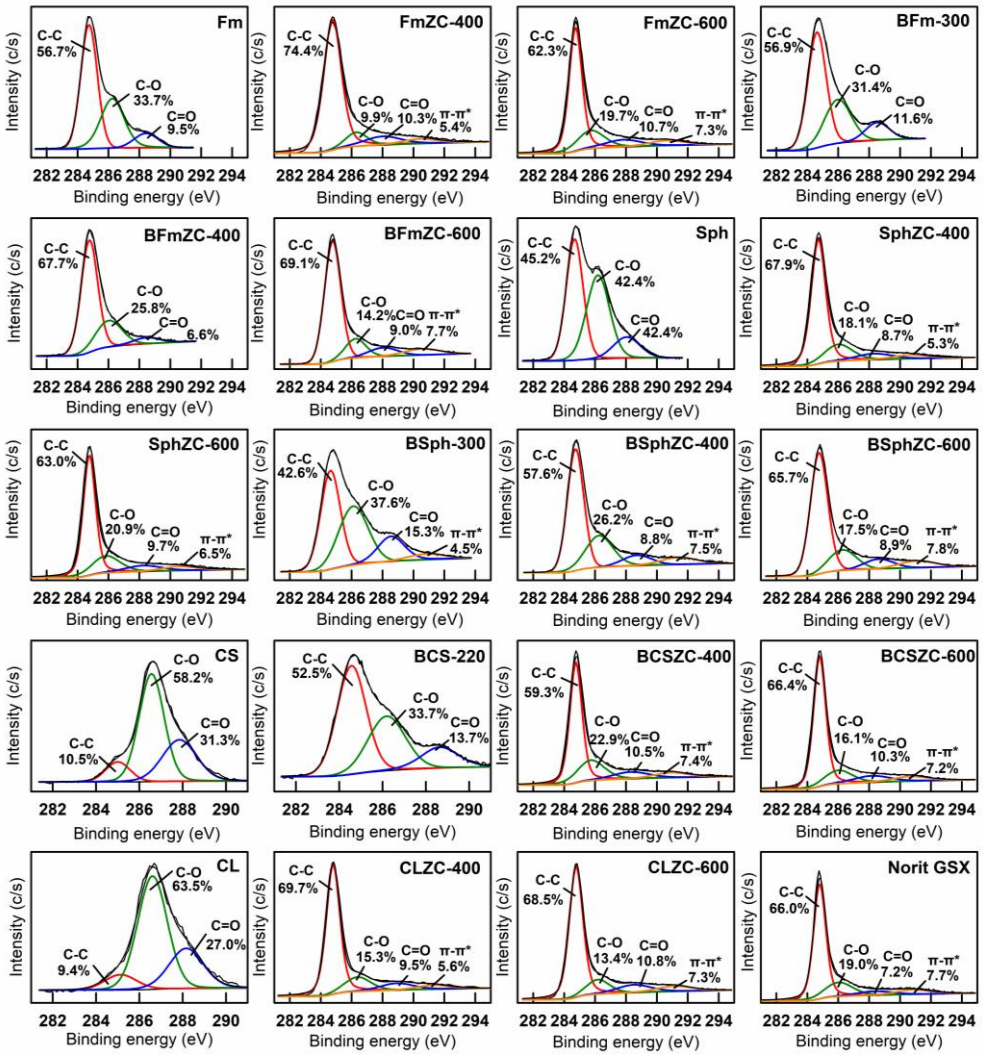


**Fig. S3.** XPS fitting curves of C1s and percentage fractions of different carbon groups for biomass precursors and different sorbents.

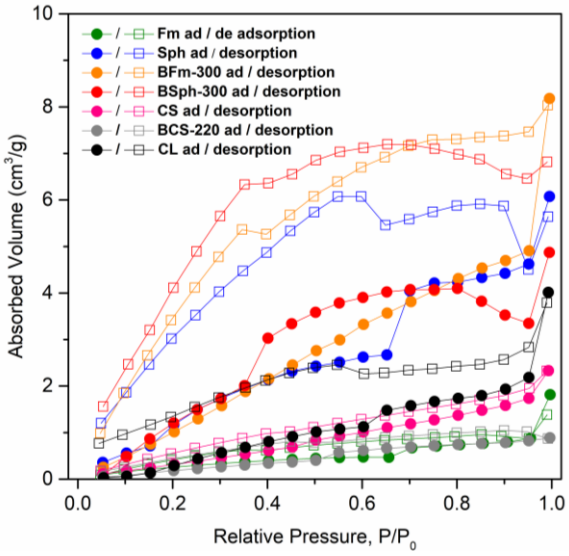


**Fig. S4.** BET $N_2$ adsorption-desorption isotherms of the precursors.

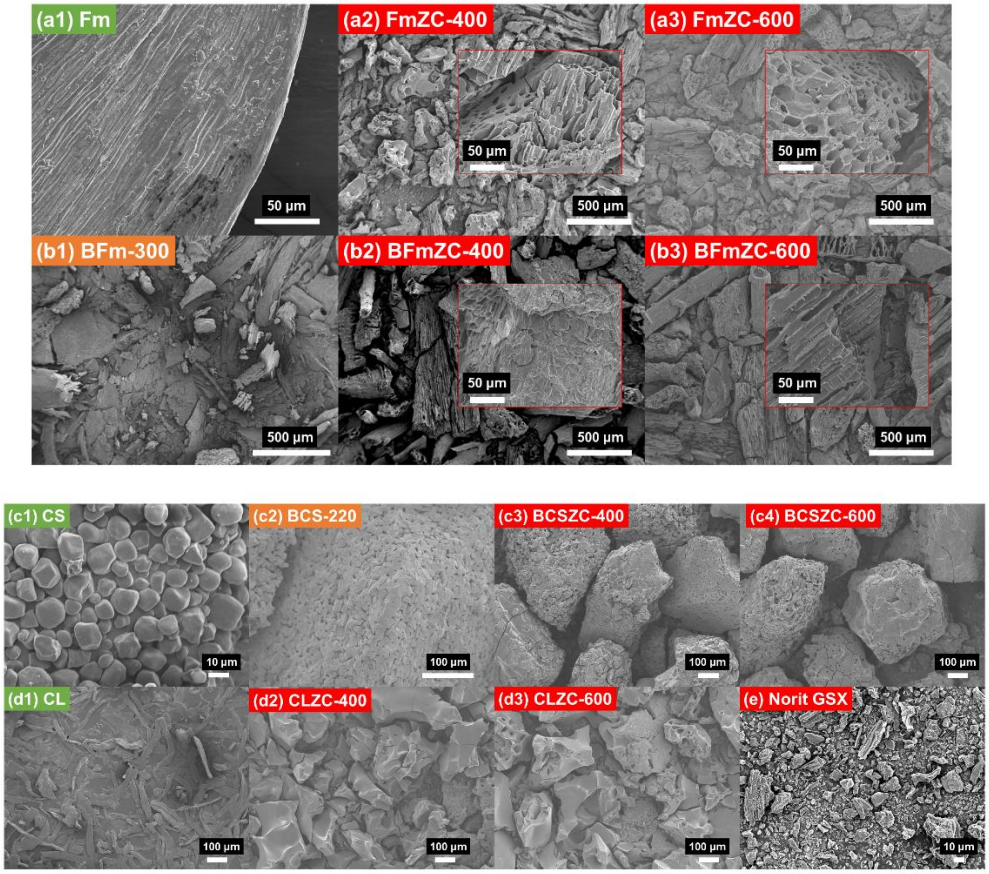


**Fig. S5.** SEM images of pre- and post-heat *feather moss*, corn starch and cellulose precursors and their derived sorbents. All micrographs were obtained at 5 eV.

## References

[1] R.R.E. Artz, S.J. Chapman, A.H. Jean Robertson, J.M. Potts, F. Laggoun-Defarge, S. Gogo, L. Comont, J.R. Disnar, A.J. Francez, FTIR spectroscopy can be used as a screening tool for organic matter quality in regenerating cutover peatlands, Soil Biology and Biochemistry, 40 (2008) 515-527.
[2] C. Cocozza, V. D'Orazio, T.M. Miano, W. Shotyk, Characterization of solid and aqueous phases of a peat bog profile using molecular fluorescence spectroscopy, ESR and FT-IR, and comparison with physical properties, Organic Geochemistry, 34 (2003) 49-60.
[3] M.M. Tfaily, W.T. Cooper, J.E. Kostka, P.R. Chanton, C.W. Schadt, P.J. Hanson, C.M. Iversen, J.P. Chanton, Organic matter transformation in the peat column at Marcell Experimental Forest: Humification and vertical stratification, Journal of Geophysical Research: Biogeosciences, 119 (2014) 661-675.
[4] M. Traoré, J. Kaal, A. Martínez Cortizas, Differentiation between pine woods according to species and growing location using FTIR-ATR, Wood Science and Technology, 52 (2018) 487-504.

## Chapter 4 Supporting Method Article

**Fast synthesis of high surface area bio-based porous carbons for organic pollutant removal**

Reprinted from *Y. Wu, N. Zhang, C.-F. de Lannoy, Fast synthesis of high surface area bio-based porous carbons for organic pollutant removal, MethodsX 8 (2021) 101464.* Open access, with permission from Elsevier.

## 1 Abstract

A fast, facile and one-pot chemical activation method was used to develop porous carbons with high surface area and excellent phenolic micropollutant adsorption performance from renewable precursors. This method was applied to three precursors: naturally abundant, but often underestimated wildfire-damaged boreal peats, corn starch, and cellulose. Porous carbon formation was accomplished through precursor impregnation with $ZnCl_2$ powder and their simultaneous pyrolysis under inert $N_2$ flow at 400 or 600 °C for 1 h. The maximum adsorption capacities of these bio-sorbents towards a model contaminant, *p*-nitrophenol, in simulated wastewater were equal to or superior than using a commercial activated carbon (CAC), Norit GSX (> 530 mg/g) over wide initial concentration ranges (20–2000 mg/L). *p*-nitrophenol adsorption best fitted Freundlich and Redlich-Peterson isotherms, suggesting multilayer chemisorption. Low concentration *p*-nitrophenol (20 mg/L) adsorption into the bio-sorbents was rapid in the first 4 h, and could reach high removals (> 98%). The method presented here yielded bio-sorbents with similarly high adsorption performance regardless of the precursor type, while avoiding energy-intensive processing steps during sorbent production. This study gives a useful alternative for manufacturing new sorbents from other upcycled carbonaceous and/or bio-based materials to remove micropollutants and heavy metals.

•Fast, single-step chemical activation for manufacturing bio-based porous carbons.

•Efficient adsorption towards aqueous phenolic micropollutant from batch studies.

•A competitive substitute of charcoal activated carbons for water purification.

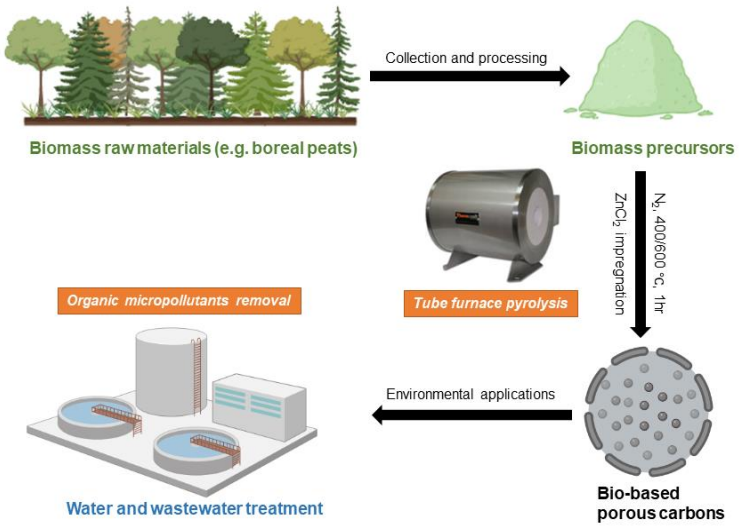


## 2. Background

Adsorption has been used for decades in water and wastewater treatment industries because of its simple design, ease of operation, and effectiveness, *i.e.*, the rapid removal of various inorganic and organic contaminants. Activated carbons (ACs), known to possess high surface areas, are maturely used in adsorption processing units. However, utilization of nonrenewable precursors, such as coals, along with traditional energy-consuming activation methods, cannot guarantee cheap manufacture in large quantities. Over the past several decades, production of bio-based sorbents from cheap, renewable agricultural and forestry wastes, and biowastes have been sufficiently investigated for the removal of varieties of aqueous contaminants, including pharmaceuticals [1, 2], pesticides [3], phenols [4], dyes [5] and natural organic matter [6]. However, not all these precursors are suitable for industrial-scale production. For instance, fruit and vegetable residues usually require multistep processing [3, 4, 7], and face low output during treatment, storage and transportation. Agricultural byproducts can be obtained in larger quantities during crop

harvesting and agro-industrial processing, but their supply is highly regional and seasonal. For instance, rice husk can be readily acquired by rice milling, but it is only available in the harvesting seasons in major rice-grown countries, such as China. Moreover, bio-based sorbents often neither achieve the high surface area nor the adsorptive performance of commercial CACs [8]. Furthermore, synthesis methods need to be improved. Various approaches have been developed to make bio-based sorbents, such as pyrolysis [2], carbonization and activation [1, 4], and hydrothermal reaction [2, 9]. These methods typically require relatively high temperature, long reaction time and multiple operating steps. Based on these limitations, the use of sustainably obtained biomaterials for conversion into efficient bio-based sorbents using rapid and facile synthesis methods will significantly benefit water treatment industries.

In the present study, we provide a feasible solution to address these challenges through utilizing the wildfire-damaged peats from the vast boreal regions of North America to produce porous carbons. Boreal peatland peats are organic soils, which serve important regional ecological functions, but have long been underestimated for environmental applications. Annual generation of surface peats could be considerable, as boreal peatlands cover 4,000,000 $km^2$ of terrestrial area in North America and Eurasia. These peats are also a large reservoir for terrestrial carbon. Boreal peats suffer from frequent peat fires and droughts, which are becoming more frequent due to climate change [10]. Damaged surface peats contribute to water runoff, have been shown to impact the water quality of downstream communities, and can impede the regrowth of valuable boreal forests after forest fires. Damaged peats, however, represent an opportunity to harness the energy of

forest fires for converting widely available organic material into precursors for bio-sorbents. We herein report the facile conversion of wildfire-impacted boreal peats, along with typical peat constituents (starch and cellulose), into highly porous bio-sorbents. This method involved *in-situ* $ZnCl_2$ chemical activation, which only required moderately high temperature (400 or 600 °C) with a short treatment duration (1 h). Applications of the as-prepared porous carbons for environmental pollution control, *i.e.*, the adsorption of a notorious micropollutant, *p*-nitrophenol from simulated wastewater was also discussed to reveal both their mechanisms of adsorption and their great potential for water treatment.

## 3. Method details

### Collection and treatment

Unburned surface boreal peats, including *feather moss* and *sphagnum* peats, were cored in PVC columns (H = 15 cm) from the Pelican Mountain Research Site (55°36' N, 113°35' W), Alberta, Canada. These two species were chosen as precursors because they are the most dominant moss species in the boreal spruce peatlands. Large twigs, plant roots and wood debris were manually removed. *Sphagnum* peat sampling and processing steps are shown in Fig. 1 as an example. Live *feather moss* was easily separated from underlying decomposed peats. *Sphagnum*, however, had no clear boundary with the underlying decomposed peat. Hence, the entire 15 cm *sphagnum* peat soils were picked as the feedstock. *Feather moss* and *sphagnum* samples were dried at 105 °C overnight in an oven to constant weight, ground and sieved (Fisher, dia. 8 inch) to less than 2 mm size. Post-burn peats were simulated through heating *feather moss* and *sphagnum* samples in a muffle furnace (Fisher Scientific, USA) at 300 °C for 30 min. 300°C was selected because this

was within reasonable range of temperatures that peat fires occur (*i.e.*, 250–300 °C) [10]. Moreover, we picked corn starch (Sigma-Aldrich) and cellulose (Sigma-Aldrich) as precursors, due to their low cost and abundance in North America, as well as their potential to partly mimic peat constituents, *i.e.*, polysaccharidic and lignocellulosic substances. Corn starch and cellulose were also oven-dried at 105°C overnight to constant weight. Preliminary experiments indicated that raw starch swelled significantly upon heat treatment and formed tar products with very low surface area after chemical activation. However, a previous study obtained high surface area spherical carbons through KOH activation from heat-stabilized cassava starch [11]. Here a similar approach was taken, where corn starch was first stabilized in a muffle furnace at 220 °C for 16 h to eliminate starch chain hydroxyl groups and melt the crystallites. The stabilized starch was further pulverized by a coffee grinder, then passed through a 2 mm sieve. Cellulose was not further treated prior to the activation. The biomass feedstocks, including unburned *feather moss*, unburned *sphagnum*, 300 °C lab-burned *feather moss*, 300 °C lab-burned *sphagnum*, 220 °C heat-stabilized corn starch and cellulose, were respectively labelled as Fm, Sph, BFm-300, BSh-300, BCS-220 and CL.

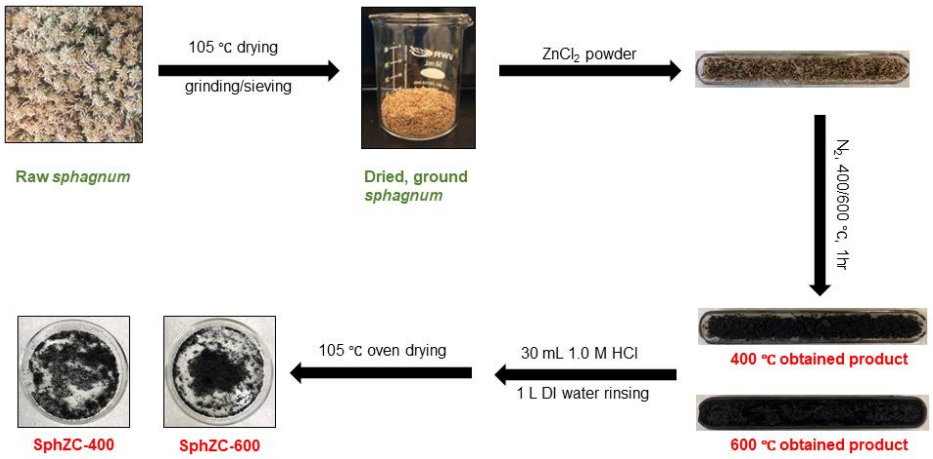


**Fig. 1.** A schematic presentation of main processing steps for obtaining *sphagnum* derived porous carbons.

**Chemical activation**

Fm, Sph, BFm-300, BSph-300, BCS-220 and CL were respectively impregnated with $ZnCl_2$ (anhydrous, ≥97%, Sigma-Aldrich) at a mass ratio of 1:3. All impregnated samples were well-stirred by a glass rod before chemical activation. Certain masses of these mixtures were loaded onto a quartz boat (100 × 15 × 75 mm), which was then transferred into a quartz tube. Before the pyrolysis, the tube furnace (Thermocraft Inc., USA) was preset to 200 °C. Samples were heated up to 400 °C at a rate of 7 °C/min and maintained for 1 h, or 600 °C at a rate of 13 °C/min and maintained for 1 h, under constant nitrogen flow (100 mL/min). After the reaction, the 400 °C treated samples were directly removed from the chamber, whereas the 600 °C treated samples were allowed cooling in the chamber for 20 min under $N_2$ flow before removing. The products were washed with 30 mL 1.0 M HCl (Sigma-Aldrich) followed by 1 L DI water until constant effluent pH, followed by drying overnight at 105 °C in an oven. The obtained porous carbons were respectively labelled as FmZC-T, SphZC-T, BFmZC-T, BSphZC-T, BCSZC-T and CLZC-

T, where T (°C) refers to the activation temperature. The detailed physicochemical characterizations of the as-prepared biomass porous carbons were described in our previous publication [8].

### *p*-nitrophenol adsorption

#### Batch adsorption

Batch adsorption experiments were performed on a multiposition stir plate (BT lab systems, USA) by continuous stirring of synthetic phenolic wastewater at 20 °C with addition of sorbents. To keep the pH constant for whole adsorption periods, the synthetic wastewater was prepared at phosphate buffer solutions. Briefly, every 1.165 g $NaH_2PO_4 \cdot H_2O$ and 3.097 g $Na_2HPO_4 \cdot 7H_2O$ were dissolved in 1 L DI water to afford the phosphate buffer solution (pH = 7, Molarity=20 mM). Preliminary tests indicated that this buffer condition was promising, as a pH deviation of only less than 0.3 was found for the tested *p*-nitrophenol concentration ranges (20–2000 mg/L) before or after adsorption. The sorbed *p*-nitrophenol on various biomass porous carbons was calculated by the following equation.

$$q_t = \frac{V(C_0 - C_t)}{m} \quad (1)$$

where $q_t$ is the adsorption capacity at time t (mg/g); $C_0$ and $C_t$ are the *p*-nitrophenol concentration at initial and a certain time t, respectively; V is the solution volume (L); m is the sorbent weight (g). When the adsorption reaches equilibrium, the equilibrium concentration of *p*-nitrophenol can be referred to $C_e$ (mg/L), such that the equilibrium adsorption capacity $q_e$ (mg/g) can be expressed as follows.

$$q_e = \frac{V(C_0 - C_e)}{m} \quad (2)$$

The concentration of *p*-nitrophenol was determined by UV–vis spectrometry performed on a DU800 UV–vis spectrophotometer (Beckman Coulter, USA). Before adsorption experiments, calibration curve for *p*-nitrophenol was established in the buffered solution, and a maximum absorbance wavelength at 400 nm was applied for the measurements.

**Adsorption isotherm**

25 mL buffered *p*-nitrophenol simulated wastewaters at various concentrations (20–2000 mg/L) were transferred into 50 mL conical flasks, followed by addition of 10 mg sorbents and stirring at 200 rpm at 20 °C for 24 h to allow adsorption equilibrium. Suspensions were afterwards filtered by 25 μm PVDF membranes, and diluted at proper magnifications (*e.g.*, 4, 20, 50, 100 times) if necessary, for UV–vis spectrophotometer measurements. Freundlich, Langmuir and Redlich-Peterson isotherms were used to model *p*-nitrophenol adsorption behaviors. These isotherm types are expressed as follows.

(1) Freundlich isotherm

$$q_e = k_F C_e^{1/n} \quad (3)$$

(2) Langmuir isotherm

$$q_e = \frac{q_m k_L C_e}{1 + k_L C_e} \quad (4)$$

(3) Redlich-Peterson isotherm

$$q_e = \frac{k_{RP} C_e}{1 + \alpha_R C_e^{\beta}} \quad (5)$$

where $k_L$ (L/mg) is the Langmuir constant; kF ((mg/g)·(L/mg)1/n) is the adsorption capacity; $k_{RP}$ (L/g) is the Redlich-Peterson constant; 1/n is an empirical constant; $\alpha_R$ and β are constants; $C_e$ (mg/L) is the equilibrium *p*-nitrophenol concentration; $q_e$ (mg/g) and $q_m$ (mg/g) are the equilibrium adsorption capacity and maximum adsorption capacity, respectively.

Representative modeled adsorption isotherms were plotted in Fig. 2 as well as described in our previous publication [8]. The Langmuir model suggests monolayer adsorption, assuming identical adsorptive sites with unform energy level [12]. The Freundlich model by comparison is based on multi-layer adsorption involving chemisorption mechanism onto heterogeneous surfaces [12]. The Redlich-Peterson model combines both the Langmuir and Freundlich models which can be applied in homogeneous or heterogeneous systems [13]. This hybrid model approaches ideal monolayer adsorption at low sorbate concentrations, but approximates multilayer adsorption at high sorbate concentrations [13]. By fitting data into these models, a mechanistic understanding of sorbent-sorbate interaction can be obtained. Freundlich model and Redlich-Peterson model fittings have the highest $R^2$ values, suggesting that *p*-nitrophenol adsorption involved multilayer chemisorption.

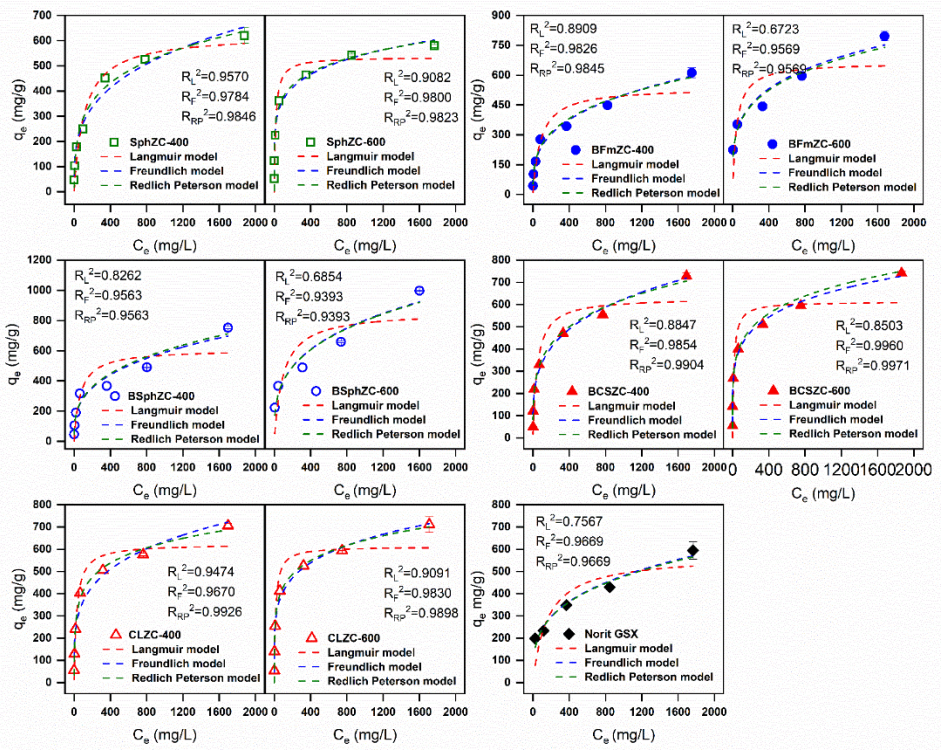


**Fig. 2.** Adsorption isotherms of *p*-nitrophenol onto selected bio-based porous carbons and Norit GSX at 20 ºC. $R_L^2$, $R_F^2$ and $R_{RP}^2$ represent the fitted determination coefficient of Langmuir, Freundlich and Redlich Peterson model, respectively.

## Kinetics

25 mL 20 mg/L buffered *p*-nitrophenol simulated wastewaters were dosed with 10 mg sorbents and stirred on a multiposition stir plate at 200 rpm at 20 °C for different time durations (0–4 h). Suspensions were then taken and filtered by 0.2 μm PVDF membranes, for UV–vis spectrophotometer measurements. Preliminary studies indicated that adsorption of 20 mg/L *p*-nitrophenol for 4 h on each sorbent can yield a removal efficiency of greater than 98%. After 4 h, the adsorption continued to occur but at an extremely slow rate. Therefore, the adsorption capacity at 24 h was considered as the equilibrium adsorption capacity. Pseudo-first-order model, pseudo-second-order model [14] and intra-

particle diffusion model [15] were used to evaluate the adsorption kinetic behavior. The equations can be expressed as follows.

(1) Pseudo-first-order model

$$\ln(q_e - q_t) = \ln q_e - k_1 t \quad (6)$$

(2) Pseudo-second-order model

$$\frac{t}{q_t} = \frac{1}{k_2 q_e^2} + \frac{t}{q_e} \quad (7)$$

(3) Intra-particle diffusion model

$$q_t = k_d t^{1/2} + C \quad (8)$$

where $k_1$ ($min^{-1}$) is the pseudo-first-order rate constant; $k_2$ ($g \cdot mg^{-1} \cdot min^{-1}$) is the pseudo-second-order rate constant; $k_d$ (mg/g·min0.5) is the intra-particle diffusion rate constant; $q_e$ (mg/g) and $q_t$ (mg/g) are the adsorption capacity at equilibrium and at time t (min); C is a constant.

Linear fitting of kinetic models for selected sorbents were plotted in Fig. 3. It is clear that a pseudo-second-order model was the optimal fit for the kinetic adsorption data, as indicated by the high $R^2$ values (> 0.99), which were much higher than that of the pseudo-first-order model ($R^2$ < 0.91) and the intra-particle diffusion model ($R^2$ < 0.84). This indicated that *p*-nitrophenol adsorption onto the activated carbons was mainly controlled by available adsorptive sites and adsorbate concentration in the system [16]. Worth noting, the scatter points of the intra-particle diffusion model (Fig. 3c) for the selected bio-based porous carbons had gradually decreased slopes, suggesting the adsorption can be described

by multiple adsorption rates, which accorded with the decreased adsorption rate after 4 h in the kinetic test.

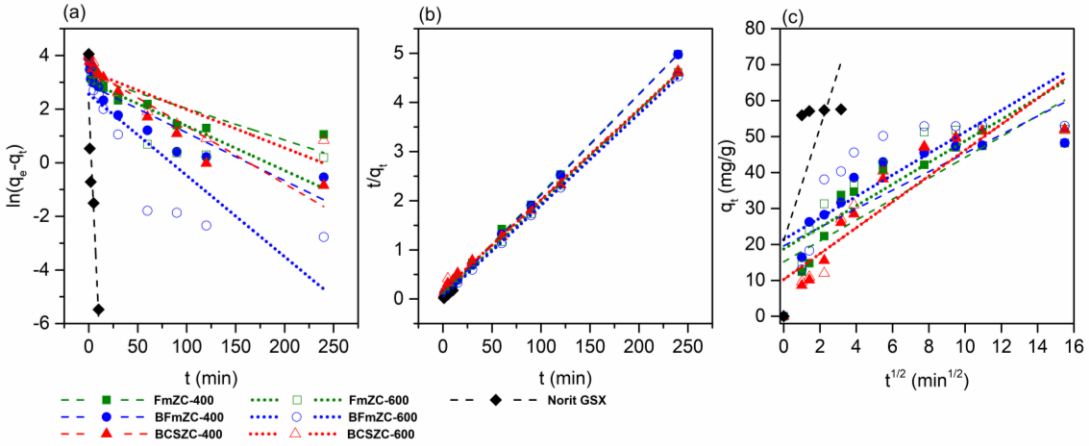


**Fig. 3.** Adsorption kinetics modeling of *p*-nitrophenol onto selected bio-based porous carbons and Norit GSX at 20 ºC in linearized forms. (a) Pseudo-first-order model; (b) Pseudo-second-order model; (c) Intra-particle diffusion model.

## Conclusion

This research demonstrates a simple, one-step chemical activation method using $ZnCl_2$ as an activation agent to obtain high surface area carbon-based sorbents from wildfire-impacted boreal peats, corn starch and cellulose precursors. The feedstocks can be easily-accessed in large quantities in North America, and their pretreatments prior to pyrolysis are simple and accessible to nearly all labs and most industrial producers. We also investigated the adsorption of *p*-nitrophenol onto the sorbents and fitted both Freundlich and Redlich-Peterson isotherms to these adsorption curves. The details of these fits and the equations used for these fits are presented herein. We suggest that fitting multiple isotherms is important for probing the adsorptive mechanism. Furthermore, analyzing both steady-state adsorption and kinetic adsorption is important for understanding the efficacy of these sorbents in comparison to commercial ACs. We suggest that both steady-state and kinetic

studies should be conducted, along with proper model fitting, for all bio-based sorbents being developed in the field so as to establish proper comparisons across this wide range of materials. In this way advantages and disadvantages of new sorbent materials can be sufficiently evaluated. These peat-based sorbents had excellent adsorption performance towards a typical phenolic model contaminant, *i.e.*, *p*-nitrophenol, in simulated wastewater, comparable or higher than that obtained from a common market-sale CAC, Norit GSX. Because the manufacturing route for the biomass sorbents was easy and efficient, we encourage that other carbonaceous materials, such as agricultural wastes, be collected and treated for producing new bio-based sorbents following a similar approach. In addition, attempts to treat other organic molecules (*e.g.*, azo dyes and pharmaceuticals), and heavy metals can be made on the basis of these biomass sorbents in future studies.

## Acknowledgements

The authors would like to acknowledge Dr. David Latulippe and Indranil Sarkar for their preliminary research work on biomass activation, and Maddison Konway for her help with the method development.

## References

[1] H.M. Jang, E. Kan, Engineered biochar from agricultural waste for removal of tetracycline in water, Bioresource technology, 284 (2019) 437-447.
[2] H.N. Tran, F. Tomul, N.T.H. Ha, D.T. Nguyen, E.C. Lima, G.T. Le, C.-T. Chang, V. Masindi, S.H. Woo, Innovative spherical biochar for pharmaceutical removal from water: Insight into adsorption mechanism, Journal of hazardous materials, 394 (2020) 122255.
[3] Y. Wang, S.-l. Wang, T. Xie, J. Cao, Activated carbon derived from waste tangerine seed for the high-performance adsorption of carbamate pesticides from water and plant, Bioresource Technology, 316 (2020) 123929.
[4] S.F. Lütke, A.V. Igansi, L. Pegoraro, G.L. Dotto, L.A. Pinto, T.R. Cadaval Jr, Preparation of activated carbon from black wattle bark waste and its application for phenol adsorption, Journal of Environmental Chemical Engineering, 7 (2019) 103396.
[5] X.C. Nguyen, T.T.H. Nguyen, T.H.C. Nguyen, Q. Van Le, T.Y.B. Vo, T.C.P. Tran, D.D. La, G. Kumar, V.K. Nguyen, S.W. Chang, Sustainable carbonaceous biochar adsorbents derived from

agro-wastes and invasive plants for cation dye adsorption from water, Chemosphere, (2021) 131009.
[6] M. Kończak, A. Siatecka, M.A. Nazarkovsky, B. Czech, P. Oleszczuk, Sewage sludge and solid residues from biogas production derived biochar as an effective bio-waste adsorbent of fulvic acids from water or wastewater, Chemosphere, 278 (2021) 130447.
[7] A. Pandiarajan, R. Kamaraj, S. Vasudevan, S. Vasudevan, OPAC (orange peel activated carbon) derived from waste orange peel for the adsorption of chlorophenoxyacetic acid herbicides from water: adsorption isotherm, kinetic modelling and thermodynamic studies, Bioresource technology, 261 (2018) 329-341.
[8] Y. Wu, N. Zhang, C.-F. de Lannoy, Upcycling wildfire-impacted boreal peats into porous carbons that efficiently remove phenolic micropollutants, Journal of Environmental Chemical Engineering, 9 (2021) 105305.
[9] T.H. Tran, A.H. Le, T.H. Pham, D.T. Nguyen, S.W. Chang, W.J. Chung, D.D. Nguyen, Adsorption isotherms and kinetic modeling of methylene blue dye onto a carbonaceous hydrochar adsorbent derived from coffee husk waste, Science of the Total Environment, 725 (2020) 138325.
[10] Y. Wu, N. Zhang, G. Slater, J.M. Waddington, C.-F. de Lannoy, Hydrophobicity of peat soils: Characterization of organic compound changes associated with heat-induced water repellency, Science of The Total Environment, 714 (2020) 136444.
[11] D. Jin, X. Yang, M. Zhang, B. Hong, H. Jin, X. Peng, J. Li, H. Ge, X. Wang, Z. Wang, A novel high surface area spherical carbon from cassava starch, Materials Letters, 139 (2015) 262-264.
[12] J. Yu, H. Feng, L. Tang, Y. Pang, J. Wang, J. Zou, Q. Xie, Y. Liu, C. Feng, J. Wang, Insight into the key factors in fast adsorption of organic pollutants by hierarchical porous biochar, Journal of Hazardous Materials, 403 (2021) 123610.
[13] M.A. Al-Ghouti, D.A. Da'ana, Guidelines for the use and interpretation of adsorption isotherm models: A review, Journal of hazardous materials, 393 (2020) 122383.
[14] Y.S. Ho, G. McKay, Pseudo-second order model for sorption processes, PROCESS BIOCHEMISTRY, 34 (1999) 451-465.
[15] W.J. Weber Jr, J.C. Morris, Kinetics of adsorption on carbon from solution, Journal of the sanitary engineering division, 89 (1963) 31-59.
[16] N.A. Mohammed, R.A. Abu-Zurayk, I. Hamadneh, A.H. Al-Dujaili, Phenol adsorption on biochar prepared from the pine fruit shells: Equilibrium, kinetic and thermodynamics studies, Journal of environmental management, 226 (2018) 377-385.

## Chapter 6 Supplementary Information

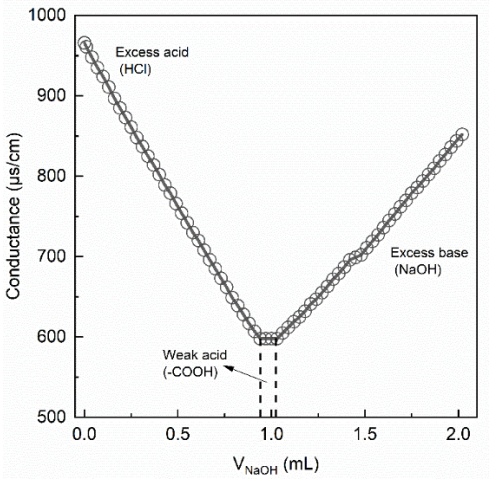


**Fig. S1.** Conductometric titration of GO suspension. $m_{GO}$ = 5 mg, $C_{NaOH}$ = 0.1 mg/L.

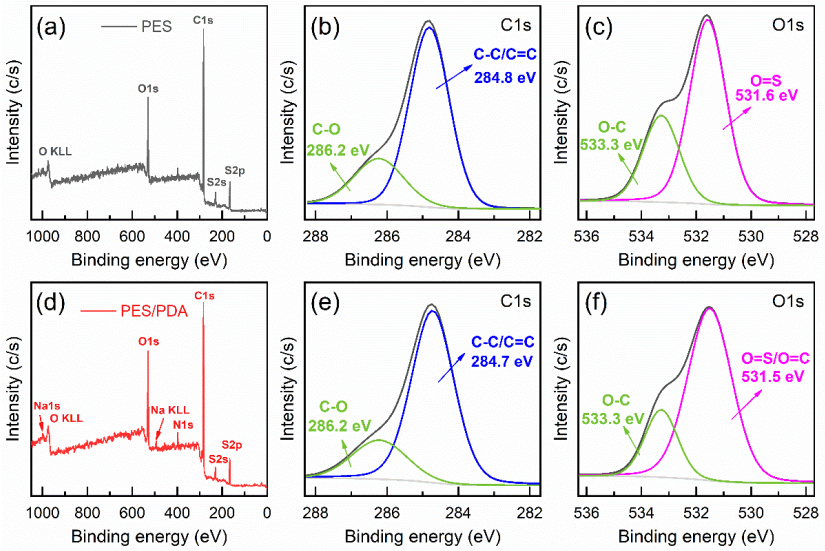


**Fig. S2.** XPS survey spectra, C1s spectra and O1s spectra of PES membrane (a, b and c) and PES/PDA membrane (d, e and f).

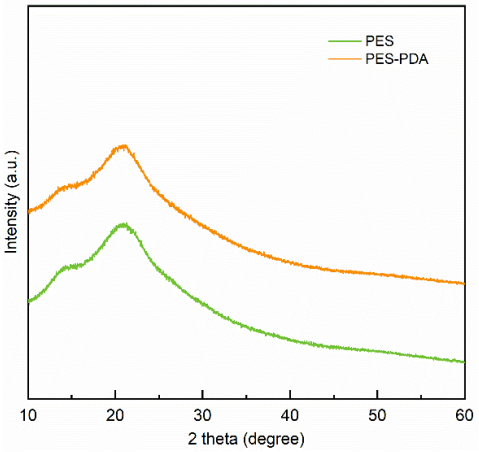


**Fig. S3.** XRD spectra of PES membrane and PES/PDA membrane.

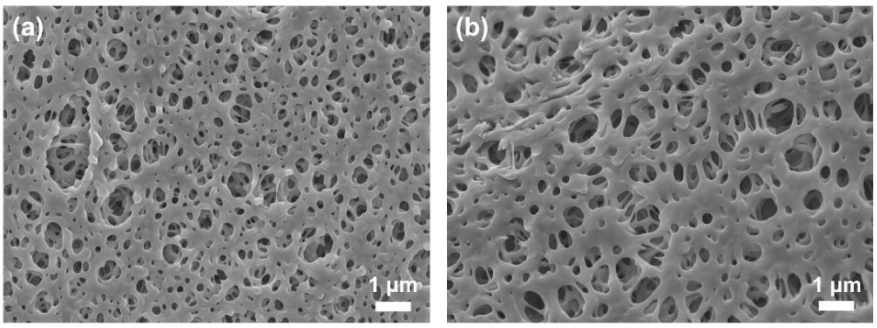


**Fig. S4.** SEM surface morphologies of (a) PES membrane and (b) PES/PDA membrane.

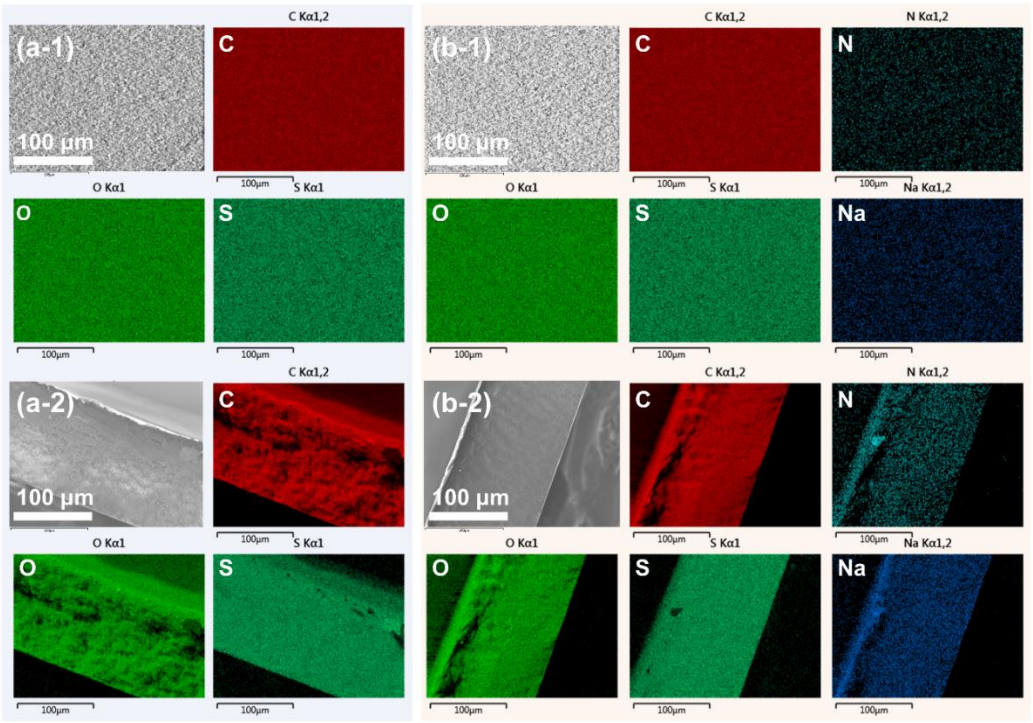


**Fig. S5.** SEM/EDS surface and cross section images of PES membrane (a-1 and a-2) and PES/PDA membrane (b-1 and b-2).

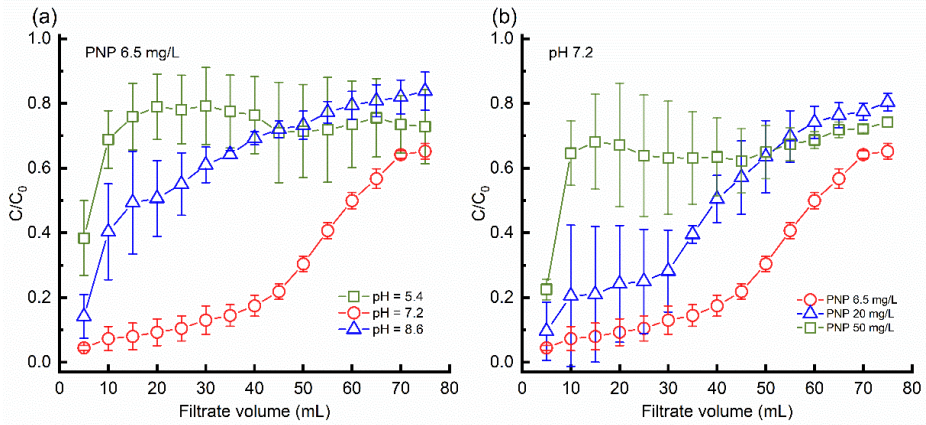


**Fig. S6.** PNP relative concentration ($C/C_0$) profile as a function of filtrate volume by PES/PDA/rGO – Fe membrane (rGO mass equals to 6 mg) at (a) different aqueous pH and (b) different PNP feed concentration. Error bars represent standard deviations of triplicate measurements.

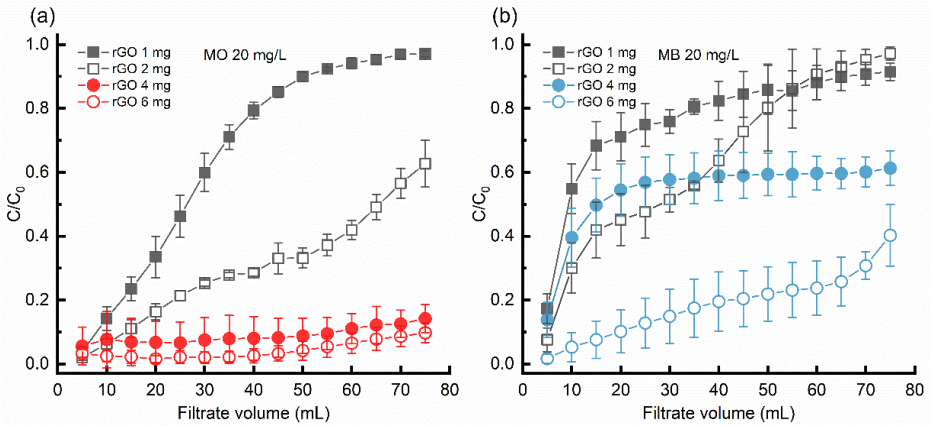


**Fig. S7.** (a) MO and (b) MB relative concentration ($C/C_0$) profile as a function of filtrate volume by PES/PDA/rGO – Fe membranes at pH 7.2. Error bars represent standard deviations of triplicate measurements.